# Localized Surface Plasmon Resonances of Gold Nanocrystals: Refractive Index Sensitivity, Plasmon Coupling and Photothermal Conversion

CHEN, Huanjun

A Thesis Submitted in Partial Fulfillment
of the Requirements for the Degree of
Doctor of Philosophy
in
Physics

The Chinese University of Hong Kong
July 2010

Thesis/Assessment Committee

Professor LIN, Hai Qing (Chair)
Professor WANG, Jianfang (Thesis Supervisor)
Professor ONG, Hock Chun Daniel (Committee Member)
Professor LI, Baojun (External Examiner)

# Abstract

Noble metal nanocrystals have attracted much interest due to their rich optical properties, which arise from the localized surface plasmon resonances, the collective oscillations of free electrons confined on the nanoscale. Under resonant excitation by light, noble metal nanocrystals exhibit extremely large light scattering and absorption, as well as large near-field enhancements. These fascinating properties bring about a variety of applications, including plasmonic sensing, plasmonic waveguiding, surface-enhanced Raman scattering, plasmon-enhanced fluorescence, photothermal cancer therapy, and plasmonic-enhanced energy harvesting. Among various noble metal nanocrystals, gold nanocrystals exhibit high chemical stability and large biological compatibility. Moreover, their plasmon resonance wavelengths can be synthetically tuned from the visible to near infrared spectral regions. In this thesis, a systematic study on the localized surface plasmon resonances of gold nanocrystals is presented, both experimentally and theoretically.

The refractive index sensitivity of gold nanocrystals is a key factor in their practical sensing applications. I will first introduce the systematic studies on the dependence of the index sensitivity on the shapes and sizes of gold nanocrystals that have varying plasmon resonance wavelengths. The index sensitivity has been found to generally increase as the plasmon resonance wavelength for a fixed nanocrystal shape becomes longer and as the curvature of the nanocrystals gets larger. I have further studied the dependence of the index sensitivity on the different shapes of gold nanocrystals that have the same longitudinal plasmon resonance wavelength. The refractive index sensitivities have been found to vary with the nanocrystal shape. Finite-difference time-domain (FDTD)

calculations have been performed on these nanocrystals to reveal the origin of this dependence. A linear relationship is found between the index sensitivity and the product of the electric polarizability with the curvature. On the basis of these studies, a novel plasmonic optical fiber device has further been fabricated to detect small changes in the local dielectric environment.

Assembly of noble metal nanocrystals gives rise to extraordinary plasmonic properties that are distinct from those of isolated ones. We have prepared clusters that are composed of two-dimensionally-ordered gold nanocubes on flat substrates and investigated their plasmonic properties. It is found that the plasmon resonances of the nanocube clusters are highly dependent on both the number and ordering of the nanocubes in the clusters. FDTD calculations reveal that the rich plasmon modes in the clusters originate from the interparticle couplings in the cluster and the couplings between the entire clusters and the substrate.

When fabricating plasmonic devices, such as waveguides, optical switches, plasmonic sensors, and plasmon-enhanced solar cells, one needs to attach metal nanocrystals onto different substrates. The interactions between gold nanocrystals and the substrates can strongly modify the plasmonic responses of the nanocrystals and therefore need to be taken into account when designing of various plasmonic devices. We have further investigated the coupling between gold nanocrystals and substrates with different dielectric properties, including insulating, semiconducting, and metallic ones. It is found that the substrates play an important role in both the scattering patterns and scattering spectra of the supported gold nanocrystals. Specifically, Fano-type resonances can be observed for large nanocrystals sitting on silicon substrates that have a large dielectric constant.

Photothermal conversion of gold nanocrystals can be applied in the areas of photothermal

polymerization, photothermal imaging, drug release from capsules, and photothermal therapy. We have investigated the photothermal conversion properties of different gold nanocrystals and their composites. The studies show that the plasmon wavelength, particle volume, shell coating, and assembly of gold nanocrystals all play important roles in their photothermal conversion efficiency.

I believe that my research work has provided an in-depth fundamental understanding of the localized surface plasmon resonances of gold nanocrystals and will have a number of implications for the applications of metallic nanostructures in optics, optoelectronics, and biotechnology.

# 摘要

金屬納米結構具有表面離子體共振激元（局域在納米尺度內的電子集體振盪模式），該特徵使得金屬納米結構在光場激發下表現出一系列奇特的性質。處於共振激發時，金屬納米結構表現出極大的散射截面和吸收截面。據估計，該散射截面和吸收截面分別比傳統的染料分子的發射截面和吸收截面大 5 個數量級。另外，電磁場會局域在金屬納米結構的周圍，形成極大的局域場增強效應（電場強度的增強可高達 $10^6$）。金屬納米結構中表面等離激元引起的這些效應已被廣泛應用于納米感測器、表面等離子體共振波導、表面增強拉曼散射、等離激元增強螢光、光熱治療以及基於表面等離激元增強的新型太陽能電池等領域。近 20 年來，金屬納米結構已經吸引了眾多研究者對其進行了深入的研究。特別是金納米結構，由於其具有化學穩定性好、生物相容性強的優點，更備受關注。另一方面，得益於近年來發展的基於種子生長法的化學合成手段，金納米結構的表面等離子體共振波長（以下簡稱等離子體波長）可以實現從可見到近紅外波段的連續可調，滿足了許多應用領域的需要。本論文主要是對金納米結構表面等離子體共振的幾個基礎問題進行了系統的研究。

首先，本論文研究了金納米顆粒的折射率靈敏度。金納米顆粒的一個重要應用是製作基於表面等離子體共振的生物感測器，而表徵這類感測器傳感性能的一個重要參數就是傳感單元的折射率靈敏度（refractive index sensitivity）。由於金納米顆粒的折射率靈敏度強烈依賴於其結構特徵。我們在論文中對具有不同尺寸、形狀、以及不同等離子體波長的金納米顆粒進行了系統的折射率靈敏度表徵。研究表明，對於具有相似形貌的納米顆粒，折射率靈敏度隨著等離子體波長的增加而升高；而對於不同形貌的納米顆粒，具有較大曲率半徑的納米顆粒

表現出更高的靈敏度。我們進一步對具有相同等離子體波長的不同形貌和尺寸的納米顆粒進行了研究，結果表明折射率靈敏度正比于納米顆粒在共振波長處的極化強度與其曲率半徑的乘積。基於這些結果，我們將不同尺寸的金納米顆粒沉積到商用光纖上面，製作了基於光纖激發的等離子體感測器原型器件。

其次，我們研究了基於金納米立方體的有序二維團簇的表面等離子體共振耦合效應。研究結果表明，相對于單個金納米立方體來說，二維有序團簇表現出更加豐富的共振性質，其共振模式的波長和共振模式數目強烈依賴於組成該團簇的納米立方體的個數和排列方式。時域有限差分（FDTD）計算分析表明，二維有序納米團簇的共振模式起源於團簇裏面各個納米立方體之間的共振耦合，以及整個團簇跟襯底之間的共振耦合。

由於在器件的製作過程中，涉及到將納米顆粒沉積到不同的襯底上面，因此，本論文也同時研究了絕緣襯底、半導體襯底和金屬襯底分別跟金納米顆粒的相互作用。結果表明，襯底的存在將會極大地影響納米顆粒的共振波長以及遠場散射圖案。當具有較大尺寸的顆粒（長度約 190 nm，直徑約 120 nm）沉積到具有較大介電常數（比如矽片）上面時，兩者之間的耦合作用將會導致 Fano 振盪的出現。

最後，由於金納米顆粒的光熱效應在光熱治療、藥物釋放、光熱成像以及光致熱聚合等方面具有廣泛的應用，本論文還對金納米顆粒及其複合體系的光熱轉化效率進行了系統的研究。研究結果表明，金納米顆粒的等離子體波長、顆粒的尺寸、顆粒的包覆物以及顆粒的聚合均會對其光熱轉化效率產生至關重要的影響。

本論文的研究結果有助於人們更為深入的瞭解局域表面等離子體的物理本質，並且在一定程度上揭示了相關金屬納米材料在光學、光電子學和生物技術等領域的應用前景。

# Acknowledgements

I would like to give my deep appreciation to many people that have helped me during my thesis work. This thesis would not be what it is today without the great guidance and help from them.

Most of all, I would like to express my greatest gratitude to my dear supervisor, Professor Jianfang Wang. Professor Wang gave me the great opportunity to join in his group and lead me into such a beautiful and interesting research field. His profound knowledge in physics and chemistry has well guided me along the research. His expertise and patience have considerably helped me to overcome the obstacles encountered in my studies. His rigorous attitude towards scientific research and optimistic attitude towards life are affecting me and making me a better researcher and a better person. I am very lucky and proud to be one of his students.

I would also like to appreciate Professor Hai-Qing Lin. Professor Lin gave lots of theoretical help to my thesis research. I have particularly learnt a lot from the discussions with him every week. This thesis won't come out without the guidance and valuable suggestions from him.

Every achievement in my scientific research is based on the close collaboration among different individuals. I can not make any progress without the help from my group members. I would like to appreciate Mr. Kat Choi Woo. Most of the FDTD calculations in this thesis cannot be done without his kind and effective help. I would like to thank Dr. Zhenhua Sun and his wife, Dr. Zhihong Bao, from whom I have learnt lots of experimental synthetic techniques and chemistry. I

would also like to thank Mr. Tian Ming, Mr. Lei Shao, Mr. Lei Zhao, Mr. Feng Wang, Mr. Manda Xiao, Miss Zhao Jin, and Miss Caihong Fang, who have helped me a lot in my experiments and never hesitate to give me their hands whenever I have trouble in my life and thesis writing.

I would also like to give my appreciation to our previous group members Dr. Zhi Yang, Miss Xiaoshan Kou, and Miss Li Li for their encouragement and assistance. And of course, especially to Dr. Weihai Ni, who taught me a lot when I knew nothing about this field.

I would like to thank Yeuk Lan, Mandy, and other ladies in the general office for their assistance, and thank Mr. Andrew Li, Mr. Man Hau Yeung, Mr. Wai Kit Chao, and other technical staffs in the physics department, who take time to help me to solve the troubles related to my experiments.

I would also like to thank my friends, Mr. Jihui Zhang, Dr. Weiguang Xie, Mr. Jiepeng Liu, Mr. Fangfei Ming, Mr. Shihang Yang, Mr. Yin Tao, Mr. Xiaojing Wang, Dr. Mingjie Zheng, and Dr. Yao Liang, for their kind help in my research and pleasure time sharing in the university life.

Finally, I would like to give my special gratitude to my parents. I cannot move any further without their constant support, understanding, and patience. Moreover, I have to say sorry for not spending enough time on staying together with them during these years' studies.

# Contents

# List of figures

# List of tables

# Chapter 1

# Introduction

To start this thesis, I would like to give a brief overview of the localized surface plasmon resonance in noble metal nanostructures. This introduction includes basic knowledge of the localized surface plasmon resonance and their related applications. This is to show why it is important and necessary to carry out the studies in my thesis research. A brief outline of the thesis is presented at the end of this chapter.

## 1.1 Surface Plasmons of Noble Metals and Their Nanostructures

Noble metals, as their names suggests, have been regarded as one of the most precious matters in the world. Since their first extraction in the 5th century B. C., they have been equivalent to wealth. Many stories were born along with them, such as the famous novel, *The Cup of Gold*, written by John Steinbeck. The stories become more enriched when they are divided into fragments with sizes approaching the wavelengths of light, i.e. nanostructures. Dating back to their appearance thousands of years ago, though not fully understood, noble metal nanostructures came into people's life with 'color'. Figure 1.1 shows two striking examples of noble metal nanocrystals in beautiful art works. By embedding gold (Au) nanoparticles into glass, the Lycurgus cup, which was made in the 4th century A.D. (Figure 1.1.1A) appears green when shined on by daylight while red when viewed in transmitted light. These nanoparticles can also be painted onto windows and walls to construct amazing art works in churches, which have won great admiration for centuries

(Figure 1.1.1B).

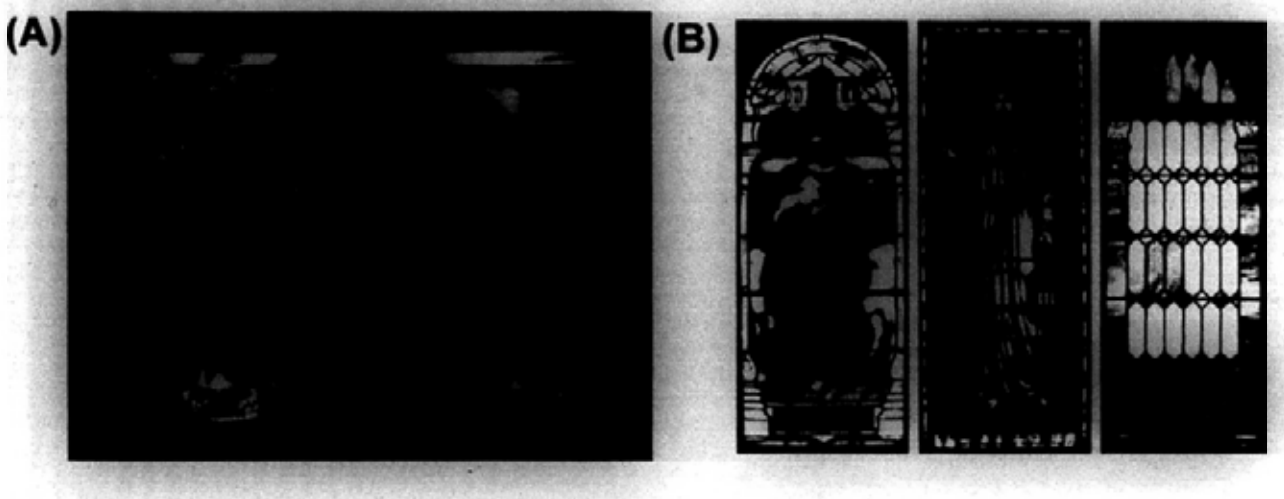


Figure 1.1.1. (A) The Lycurgus cup. (B) The stained glass in Bourne United Methodist Church.

The first scientific effort to study noble metal nanostructures was performed by Michael Faraday in 1847, which can be considered as the birth of nanoscience [1]. The red solution of colloidal Au (Figure 1.1.2) was prepared by the reduction of chloroaurate ( $AuCl_4^-$ ) using phosphorus in $CS_2$ solutions.

Figure 1.1.2. Faraday's colloidal solutions of gold.

The origins of the rich colors in noble metal nanostructures have attracted many people's attention while no mature theoretical description appeared until the appearance of Maxwell equations, the classical theory for investigating light–matter interactions. Mie developed the first analytical formalism for calculating the electromagnetic response of objects with a spherical shape [2]. Under this formalism, the scattering/absorption and the electromagnetic field distribution around the object can be obtained by the expansion of a series of partial waves. Specifically, if the materials have dispersive dielectric properties, electromagnetic resonances will occur at specific frequencies, giving rise to scattering or absorption maxima and different colors of the objects. The Mie theory was first utilized in explaining the colorful appearance of spherical noble metal nanocrystals and agreed with experimental results. After that, several approximate models have been developed to describe the optical response of particles with nonspherical shapes. Among them, the Gans theory, which is based on electrostatic approximation, is a simple and very effective method for calculating

the scattering/absorption cross sections of ellipsoidal nanoparticles [3]. The above two theories will be discussed in more detail in Chapter 2.

Not until the development of quantum physics did people realize that the specific scattering/absorption resonances in noble metal nanostructures were related to the collective oscillations of electrons in the conduction band of metals. These collective oscillations are given a name of *plasmons* or *plasmon resonances* [4]. Plasmons can be excited by different techniques [4 – 6]. Because in many researches and applications, plasmons are mainly excited by light, they are referred to as electromagnetic resonances due to collective electron oscillations. As the absorption in metals is very high, the plasmons are generally confined at the interface between the metal and dielectric, which are known as *surface plasmons* or *surface plasmon resonances (SPRs)* [5]. Maxwell equations can be utilized to describe the electromagnetic response of surface plasmons, which are characterized by an electromagnetic surface wave that propagates along the interface. The propagation distances usually range from several nanometers to hundreds of microns, depending on the types of metal and the excitation wavelength. Therefore they are also known as *propagating surface plasmons (PSPs)*, which decay exponentially into the space perpendicular to the interface and have their maximum intensity at the interface. As their dispersion relation $\omega(\vec{k})$ lies below that of free-space light, there is a momentum mismatch between the PSPs and free-space light. The excitation by light therefore needs special techniques to overcome the momentum mismatch [6]. Due to the same reason, the propagating surface plasmons cannot be directly converted into free-space light emission. Therefore they are also known as 'nonradiative' surface plasmons.

The plasmons will be significantly different from the propagating ones if the collective oscillations of the free electrons are confined in three dimensions. Under the external excitation, the boundary of a nanoparticle will place an additional restoring force on the electrons other than the

positive background, leading to an oscillation that is confined in the small region of the nanoparticle. This confined oscillation is named as the *localized surface plasmon* [7]. If the frequency of the excitation field is close to the eigenfrequency of the collective electron oscillation, the oscillation strength reaches its maximum. This phenomenon is known as the *localized surface plasmon resonance (LSPR)*. The localized surface plasmons can be directly excited by and converted into light due to their localized nature. Therefore they are also called 'radiative' surface plasmons.

Compared to its propagating counterpart, the localized surface plasmon resonance has several features that have gained much attention. First of all, as mentioned above, there is no need to utilize special techniques for their excitation. The localized nature of this type of resonance provides an effective way to directly convert far-field signals into near-field ones and vice versa for measurements, characterizations, and tests. Second of all, the small volumes of metal nanostructures can avoid Ohmic losses. The Ohmic loss due to resistive heating is a big problem in the applications of propagating surface plasmons [8, 9]. Introducing a gain medium adjacent to the plasmon active region is a possible solution but rather complex [10 – 12]. On the other hand, the Ohmic loss can be substantially suppressed in localized surface plasmon resonance nanostructures due to the reduced volume of metal. Moreover, the small volume can also meet with the ultracompact characteristic of modern optoelectronic devices. Third of all, the resonance wavelengths of metal nanostructures are highly dependent on their shapes, sizes, compositions, and spatial arrangements. Therefore, the localized surface plasmon resonances can be facilely tuned from the violet into infrared spectral regions. Although traditional physical methods such as electron-beam lithography can give an excellent control of the geometries of nanostructures, they are limited to dimensions larger than 10 nm. The seed-mediated growth method developed in recent years is a milestone in synthesizing metal nanocrystals with uniform size distributions of tens of nanometers [13 – 17]. Combining these

physical and chemical methods to design and fabricate metal nanostructures will be one of the key ingredients of future applications of plasmonics. Fourth of all, the excitation of localized surface plasmons can lead to extremely large electromagnetic field confinement in the vicinity of metal nanocrystals [18, 19]. This confinement can give rise to remarkable near-field enhancements around metal nanocrystals, leading to a new phenomenon named as plasmon enhanced spectroscopy [20 – 22]. The near-field enhancement can also favor the coupling between two adjacent nanocrystals and lead to the development of many interesting sub-wavelength devices for signal processing in future optoelectronic circuits.

In the last twenty years, the field of localized surface plasmon resonance in metal nanostructures has undergone a significant expansion and has become one of the most active research areas within the nanoscience community. Exciting developments have been made at an unusually fast pace and this field has now developed into a relatively mature research area with ample exciting and new research opportunities, as evinced from the vast number of papers (Figure 1.1.3) published on plasmonics in metal nanostructures over the past two decades. In particular, the number of papers has increased significantly in the last ten years. Localized surface plasmonies is multidisciplinary. People working in this field include physicists, chemists, biologists, and engineers. They are constantly pushing the env elope to develop new fundamentals of science as well as potential applications in this active area. Several important subfields have emerged, with each representing an exciting direction for utilizing the above virtues of localized surface plasmon resonances. These subfields include localized surface plasmon based biosensing and therapy, plasmon-enhanced energy harvesting and conversion, and plasmonic circuits. As the research in my thesis is highly related to these fields, I will give a brief overview on them in the following discussions.

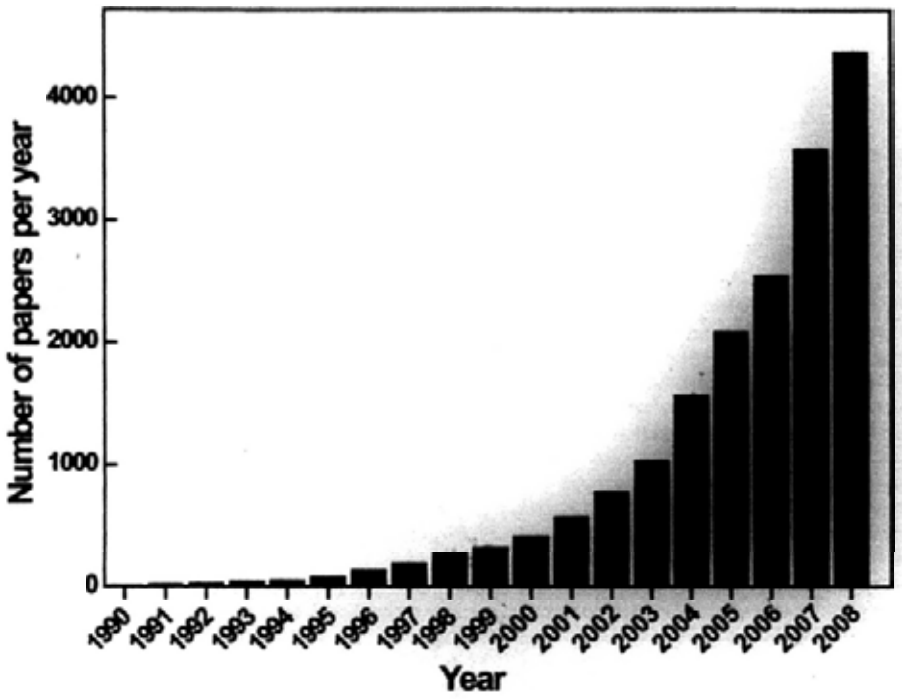


Figure 1.1.3. Increase in the number of publications on the localized surface plasmon resonance of metal nanostructures from 1990–2008 (Source: ISI Web of Knowledge).

## 1.2 Health Issue: Diagnosis and Therapy

The greenhouse effect, land desertification, ozone depletion, and environmental pollution—all of these familiar phrases appearing on almost everyday's television news and newspapers are threatening people's lives; Some have even led to the outcome of different diseases. Besides joint efforts by governments of different countries to save the Earth, early diagnosis and effective therapy of the diseases in human bodies are also strongly desired for today's health concerns.

Clinical diagnosis currently places a rapidly increasing demand for low-cost, easy-operation, and ultrasensitive biosensors with real-time and high spatial resolution performances. A typical biosensor is a device composed of a biological recognition layer designed to bind to a specific

substance and a physical transducer that can translate the biochemical interaction into a quantifiable signal [23]. Among different signal transduction methods, the optical sensors, in particular those based on surface plasmon resonances in thin metal films, have been most extensively employed [24]. The physical mechanism of this type of biosensors is the strong dependence of the PSPs on the refractive index of the surrounding environment. Binding of analytes will increase the refractive index of the dielectric environment in the vicinity to the metal surface, leading to red shifts of the PSPs. The PSPs-based biosensors have been widely used to monitor a broad range of analyte-surface binding interactions including the adsorption of small molecules [25 – 27], ligand–receptor binding [28 – 31], protein adsorption on self-assembled monolayers [32, 33], antibody–antigen binding [34], DNA and RNA hybridization [35 – 38], and protein–DNA interactions [39]. However, as mentioned above, the special techniques for the excitation of PSPs are cumbersome for the implementation of this type of sensors in large biosensor arrays. Moreover, real-time sensing or kinetic measurements using PSPs are severely mass-transport limited by diffusion to time scales on the order of $10^3$–$10^4$ s for analytes at bulk concentrations of $C_{bulk}$ < $10^{-6}$–$10^{-7}$ M [24]. These two fundamental challenges have hindered the PSPs in developing large-scale, multiplexed biosensors composed of highly miniaturized signal transducer elements. Biosensors based on noble metal nanostructures, on the other hand, are expected to provide solutions to the above problems. LSPRs related to metal nanostructures can be directly excited and out-coupled for measurements. The smaller surface area of nanostructures can reduce non-specific interactions and enable more targeted binding. Moreover, the smaller volume of nanostructures can also overcome the mass transport limit.

There are generally two types of sensors depending on the origins of the changes of the LSPR signals: refractive index sensors and aggregation sensors [23]. The first one is similar to the PSPs

sensor, which is based on the strong dependence of the LSPRs of metal nanostructures on the refractive index of the surrounding environment. Van Duyne et al. developed the first plasmonic biosensor to detect amyloid-$\beta$ derived diffusible ligands (ADDLs), a ligand that is believed to be responsible for the Alzheimer's disease, by using silver (Ag) nanoparticle arrays [40]. A detection limit of down to ~1 pM was obtained (Figure 1.2.1). Following the same principle, Au nanoparticles were attached onto glass substrates and used to detect the hormone stanozolol with a detection limit of the pM level [41], which can be considered as the first examples of "real life" applications of LSPR based biosensors. In a recent study, biotin-functionalized Au nanocrystals have been utilized to detect the streptavidin. A detection limit of as low as 19 nM can be reached in serum [42]. In order to fulfill the future requirements of real-time, parallel monitoring, and high miniaturization, LSPR sensors need to be pushed to their detection limit and explored for multiplex sensing. One crucial step is to design and fabricate metal nanocrystals with excellent sensing behaviors. The refractive index sensitivity, which denotes the plasmon shift as the refractive index of the surrounding medium is increased by 1, of metal nanocrystals is a key parameter that will ultimately determine their sensing performance. Finding out the major factors that determine the refractive index sensitivity of noble metal nanocrystals is therefore essential to fully realize the potential of plasmonic sensors. I have systematically studied the influence of the plasmon wavelengths, sizes, and shapes of metal nanocrystals on their refractive index sensitivities, which will be discussed in Chapter 4.

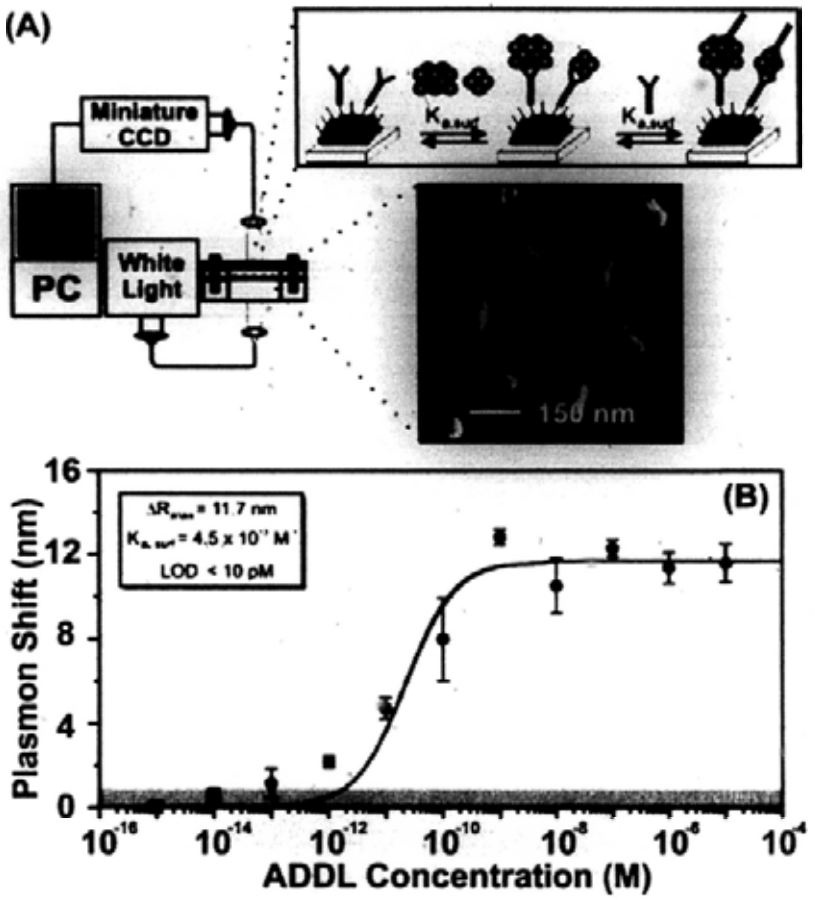


Figure 1.2.1. (A) Schematic showing a localized plasmon-based biosensor for the detection of ADDLs using Ag nanoparticles. (B) Plasmon shift (ΔR) as a function of the ADDLs concentration during the binding of ADDLs to an anti-ADDL antibody-functionalized Ag nanobiosensor.

The other type of LSPR sensors is based on the aggregation of colloidal metal nanocrystals. The core mechanism of this type of sensors is the plasmon coupling between different nanocrystals. By bringing two metal nanocrystals close together, their LSPRs couple with each other via Coulomb interactions, giving rise to changes in the extinction and scattering spectra. This sensing strategy was originally proposed by the Alivisatos group and Mirkin group [43, 44]. The detection can be realized by mixing two metal nanocrystal colloids, each capped, for example, with a different and non-complementary single stranded DNA (ssDNA). The addition of a third oligonucleotide, which is

complementary to both immobilized ssDNA (one at each end) can induce the aggregation through hybridization between the complementary oligonucleotides. Such aggregation is accompanied by drastic color changes of the colloidal solution, which can be even visualized with the naked eye [45 – 47]. This idea has even been employed to monitor DNA conformation changes upon hybridization. The plasmon coupling between two metal nanocrystals linked via ssDNA can act as a "plasmon ruler" to determine the change in the separation distance between two particles due to DNA hybridization [48, 49]. Biosensors using colloidal aggregation are not restricted to DNA. Protein recognition has also been demonstrated [50]. A more detailed discussion of this technique can be found in a recent review paper [23]. For this type of LSPR sensors, one crucial problem is to quantitatively calibrate the plasmon changes due to the aggregation of metal nanocrystals. Several excellent studies have experimentally and theoretically revealed the dependence of plasmon shifts on the distance between two neighboring nanocrystals [51 – 67]. Although they are closer to practical situations, the plasmon changes in aggregates composed of more than two nanocrystals are seldom explored.

The sensing techniques mentioned above are related to the direct measurements of the SPR or LSPR signals. There are also other traditional sensing techniques used to detect and identify molecules on the basis of their own fingerprints, such as Raman and fluorescence spectroscopy. The discovery of the LSPR in metal nanocrystals also revives these traditional analytical techniques. The remarkable near-field enhancement around metal nanocrystals under the excitation of their LSPRs will lead to enormous enhancements of Raman and fluorescence signals. For example, when molecules are adsorbed onto a plasmonic nanostructure or move to within a few nanometers of its surface, the Raman scattering signal (approximately proportional to $|\mathbf{E}|^4$) can be enhanced by a factor of $10^6$–$10^8$ for an ensemble of molecules [68, 69], and by as much as $10^{14}$–$10^{15}$ for single

molecules [70 - 72]. This phenomenon is known as surface-enhanced Raman scattering (SERS). Moreover, the electromagnetic field enhancement can even be large in the gap region of metal nanocrystal aggregates, forming so-called "hot-spots". Recently, a quantitative measurement of the distribution the SERS enhancement sites demonstrates that the "hot-spots" with local field intensity enhancement factors larger than $10^9$ in an aggregate account for only 63 sites in 1,000,000 of the total sites, but contribute 24% of the overall SERS intensity [20]. In all of these regards, assembling metal nanocrystals into well-defined SERS nanostructures are greatly desired [21]. On the other hand, previous studies have shown that the maximum Raman enhancement occurs when the plasmon resonance wavelengths of metal nanostructures lie between the excitation wavelength and the vibrationally shifted wavelength [73, 74]. This emphasizes that it is very important to study the plasmon resonance in metal nanocrystal aggregates so as to choose the right excitation laser wavelengths for achieving the best SERS detection performance. In Chapter 5 of this thesis I will introduce the study on plasmon coupling properties in clusters composed of Au nanocrystals with different numbers and orderings.

Metal nanocrystals also have promising perspectives in providing an effective therapeutic strategy in addition to the diagnostic biosensors mentioned above. "To do no harm" is at the heart of physicians' creed. However, current standard medical therapies, especially those used in cancer treatments, are far from being innocuous, painless, and nontoxic. They are usually associated with too many acute and chronic side effects. Furthermore, cancer cure rates for most types of human malignancies have improved only minimally or even not at all over the last three decades [75]. Novel treatment approaches that can improve cure rates while minimizing toxicity are sorely needed. Hyperthermal therapy, on the other hand, is a promising candidate that has gained more and more attention, especially for treating cancers. Its basic idea is to employ energy sources together with

proper absorbers that can be delivered to target regions to generate local heating. This local heating can raise the temperature far above the normal body temperature and induce the death of cancer cells [75]. Specifically, when the energy source is a laser, the hyperthermal therapy is referred to as the photothermal therapy. Traditional light absorbers such as organic dyes usually undergo photo-bleaching and limit heat generation. On the other hand, metal nanocrystals, especially the Au nanocrystals, can act as promising energy absorbers for photothermal therapy. Excitation of localized surface plasmon resonances in metal nanocrystals can give rise to extremely large light absorption. It is reported that Au nanospheres with sizes around 40 nm show an absorption cross section 5 orders higher than conventional absorbing dyes when excited at their plasmon resonances [76, 77]. This superior ability to efficiently convert light into heat can be readily employed for photothermal therapy [76]. Moreover, the LSPRs of metal nanocrystals can be facilely tailored into the near infrared range, in which light can penetrate 6–9 mm into tissue without being absorbed by hemoglobin or other chromophores [78]. By taking all of these properties into consideration, it is possible to target metal nanocrystals into desired locations for their *in vivo* therapeutic applications. The first use of Au nanocrystals in photothermal therapy was realized by Halas and co-workers [79 – 81]. In their studies, Au–silica nanoshells were used to target breast carcinoma cells with HER2 antibodies. Near-infrared irradiation of the nanoshells led to a rise in the temperature of the target regions between 40 to 50 °C, which selectively destroyed the carcinoma cells. In a recent study, Bhatia et al. have also established the potential for Au nanorods to provide photothermal heating of tumors to ablative temperatures *in vivo* [82]. This type of application needs scientists to systematically investigate the photothermal conversion properties of metal nanocrystals and correlate the size, shape, and local environment of nanocrystals with their photothermal response. These studies can help design metal nanostructure-based phototherapy agents with improved

efficiencies. The detailed studies of the photothermal conversion efficiencies of different Au nanostructures will be presented in Chapter 7.

## 1.3 Energy Harvesting: Plasmon Enhanced Solar Cells

Nowadays, over 85 % of energy demands are met by the combustion of coal, oil, and natural gas, as shown in Figure 1.3.1. All of them are non-renewable sources of energy. It is anticipated that with current provided reserves and usages, coal, oil, and natural gas will be run out in 148, 43, and 61 years, respectively [83]. In addition, most of these energy sources are located in limited countries and areas and can not be accessed everywhere on the Earth. Consequentially, there have been wars for these energy-supplying regions, like the Gulf War in 1991. Furthermore, the burning of fossil fuels results in a net increase of 10.65 billion tones of atmospheric carbon dioxide per year [83], leading to the well-known greenhouse effect and other environmental problems. Energy has now become a vital problem for the fast development of human society. A global movement toward the development of highly-efficient, renewable, and green energy is therefore of great necessity to help meet the increased energy demands. Among different candidates like nuclear, hydroelectric, wind, and geothermal energy, solar energy is one of the most promising choices. It is estimated that the energy from the sunlight striking the Earth in 1 h (14 TW) is more than all the energy consumed on the planet in a year (12.8 TW in 1998) [84]. Since the 1970s, solar energy technology has attracted more and more attention, and the global photovoltaic market is undergoing a rapid growth. By 2008, the market has already produced a total of 5559 MW, and is expected to rise above 20 GW by 2015 [84, 85]. The total global consumption of energy in 2050 is estimated to be 28 TW. Therefore there is still plenty of room for solar energy technology. The current industry is already a 10-billion-dollar industry and 1-billion-dollar venture capital market [84]. Most financial analysts are painting a

bullish forecast for the solar business, spurred on by encouraging industry statistics and favorable government actions.

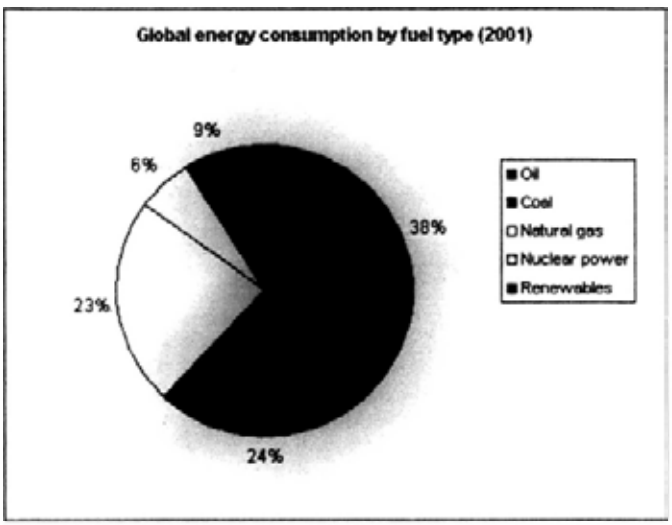


Figure 1.3.1. Statistics on global energy consumption by fuel type in 2001. (Source: Energy Information Administration, U.S.A.)

The core of the solar energy technique is the development of highly efficient solar cells at low cost. One key issue of today's solar cell industry is the high cost of solar energy absorbers. Absorbers in solar cells must be "optically thick" to allow near-complete light absorption and photocarrier current collection. Nowadays the solar-cell market is based on crystalline silicon wafers with thicknesses between 180–300 μm due to their poor absorption above 600 nm [86]. Much of the price of solar cells is due to the costs of silicon materials and their processing. Therefore, thin-film solar cells (1–2 μm thick absorber layers) with special techniques to increase light absorbance are very important for today's solar cell industry. Due to their large-scale geometries, conventional light trapping techniques such as using a pyramidal surface texture to increase the scattering of light into the absorbers, are not suitable for thin-film solar cells [87, 88]. Metal nanostructures, on the other

hand, open a new way for achieving light trapping in thin-film solar cells. In a recent comprehensive review paper by Atwater, three strategies are proposed for trapping light in thin-film solar cells. Two of them are related to the use of metal nanocrystals [86]. First of all, due to their large scattering cross-sections under the excitation of the LSPR, metal nanocrystals can be used as strong scattering elements to couple and trap freely propagating plane waves from the Sun into an absorbing-semiconductor-thin film (Figure 1.3.2A). Moreover, the adhesion of nanocrystals onto a substrate with a large dielectric constant (such as silicon wafers) can significantly increase the forward scattering of the electromagnetic field into the substrate, which is favored for the light-trapping purpose [89]. Second of all, the near-field enhancement around metal nanocrystals is so strong that the nanocrystals can be used as subwavelength antennas. These nanoantennas can be embedded into the semiconductor layer and increase its effective absorption cross section (Figure 1.3.2B), leading to increased charge generations.

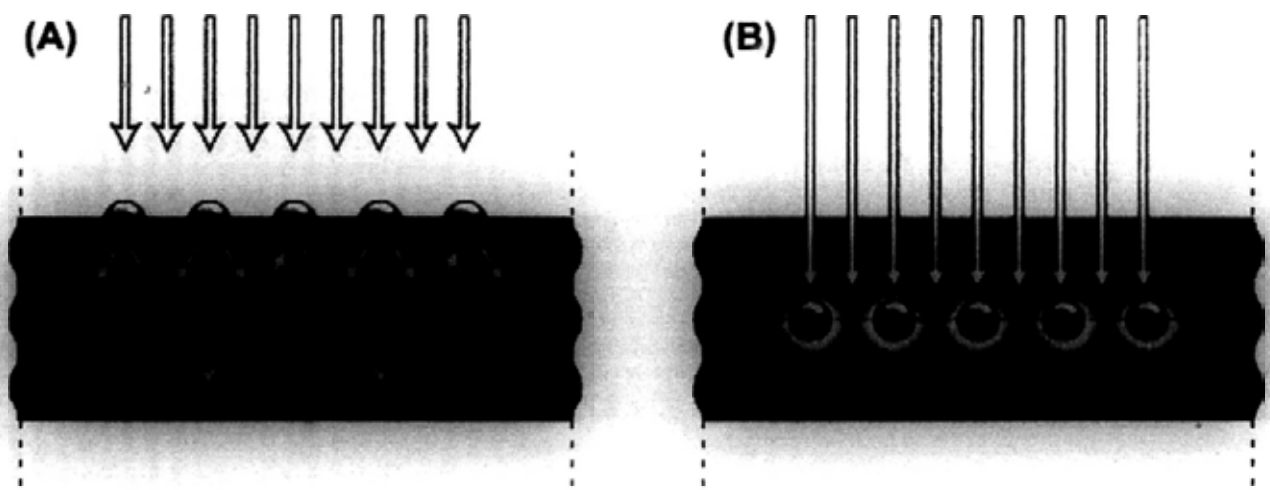


Figure 1.3.2. Plasmonic light-trapping geometries for thin-film solar cells. (A) Light trapping by scattering from metal nanocrystals at the surface of the solar cell. Light is preferentially scattered and trapped into the semiconductor thin film by multiple and high-angle scattering, causing an

increase in the effective optical path length in the cell. (B) Light trapping by the excitation of localized surface plasmons in metal nanoparticles embedded in the semiconductor. The near-field enhancement of the nanocrystal can favor the absorption of the active materials.

The use of metal nanocrystals for enhancing light scattering into the absorbers have been studied in single-crystalline silicon [90], amorphous silicon [91, 92], silicon-on-insulator [93], quantum well [94], and GaAs [95] solar cells. Specifically, it is predicted that a 30-fold enhancement of the light trapping can be realized for Ag hemispheres with 100 nm diameter on silicon [96]. On the other hand, enhanced efficiencies due to the near-field enhancement of metal nanocrystals have been demonstrated for solar cells doped with Ag nanoparticles [97, 98]. For organic bulk heterojunction solar cells, the efficiency can be enhanced by a factor of 1.7 [99, 100]. In a recent report an enhancement factor of as much as 3 times has been observed for charge generation in organic photovoltaic films on top of a layer of Ag nanoprisms [101]. Inorganic solar cells have also shown increased photocurrents owing to near-field effects, such as CdSe/Si heterostructures [102] and silicon [103]. Nowadays microelectronic techniques can be employed to fabricate large-scale metal nanocrystal patterns in a controlled manner. Figure 1.3.3 shows several examples of large-area metal nanocrystal patterns for plasmon-enhanced solar cells [86]. All of these make plasmon-enhanced solar cells a very promising technique to meet future explosive energy needs.

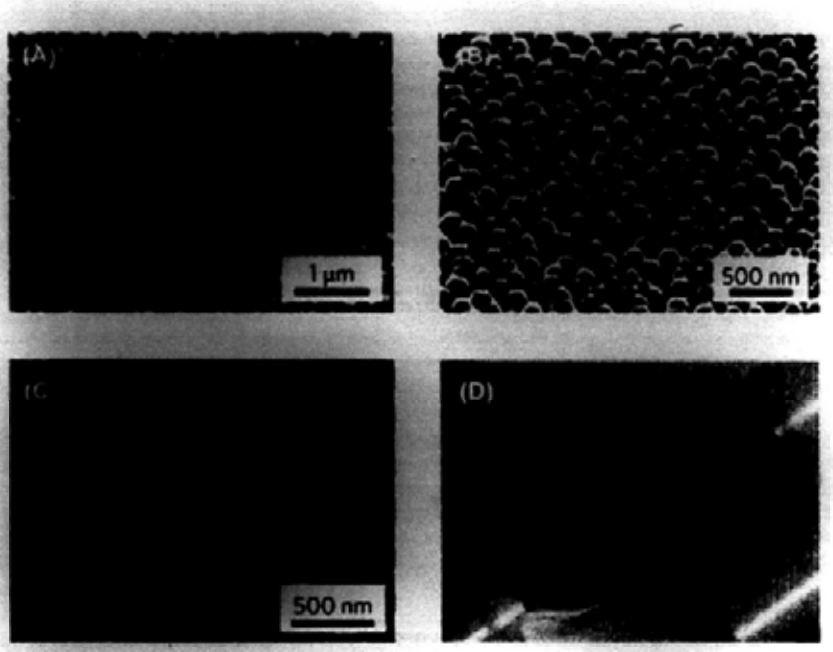


Figure 1.3.3. Large-area metal nanocrystal patterns for plasmon-enhanced solar cells. (A) – (C), Scanning electron microscopy images of arrays of Ag nanocrystals on silicon. (D) Wafer-scale metal nanocrystal patterns.

However, like other frontier technologies, there are still many questions regarding the underlying physical mechanisms. For example, the enhanced light scattering of metal nanocrystals is strongly dependent on both shape and size [96, 105]. This should be taken into account in practical applications in order to design the optimum nanocrystal structure for the enhancement of photovoltaic efficiency. Therefore the dependence of the scattering cross sections on the geometries of the nanocrystals should be well studied both experimentally and theoretically. Moreover, the resonance peak, near-field enhancement, and far-field scattering intensity of the nanocrystals can be modified enormously in the presence of a dielectric or conducting substrate [105 – 117]. These modifications will certainly affect their enhancement of the solar cell efficiency. Therefore the coupling between metal nanocrystals and substrates with different dielectric responses should be studied profoundly, because most of the examples mentioned in this section talk about adhering the

nanocrystals onto a substrate. However, only until recently has some attention been paid to the coupling between metal nanocrystals and substrates with different dielectric properties [105 – 117]. There have been only a few reports regarding the LSPR behaviors of metal nanocrystals on silicon substrates, which are most widely used in the current solar cell industry. These questions will be considered in my thesis and discussed in Chapters 6 and 7.

## 1.4 Plasmonic Circuits: the Next Generation of Communication Networks

The ability of plasmonic metal nanostructures to confine electromagnetic fields well below the classical diffraction limit gives rise to a new branch of optoelectronic circuits—the plasmonic circuit. Nowadays communication networks are built on electronic circuits that are based on semiconductors devices and optical circuits that are based on dielectric waveguides and components. However, semiconductor electronics has been limited in speed by the interconnect delay time [8, 118]. Optical interconnects such as fiber optic cables that carry digital data with a capacity > 1000 times that of electronic interconnects can overcome this interconnect-delay limit. Unfortunately, the size of the traditional optical components can not be reduced into nanoscale due to the diffraction limit, preventing the combinations of these two technologies onto the same chip [8, 119]. Surface plasmons that can transmit optical signals through the collective electron oscillations can serve as a bridge between the traditional electronic and photonic circuits, thus providing a solution for combining the superior technical advantages of photonics and electronics and fabricating devices with both nanoscale sizes and high processing speed onto one chip. Figure 1.4.1 shows clearly the importance and promising future of the plasmonic circuits [119].

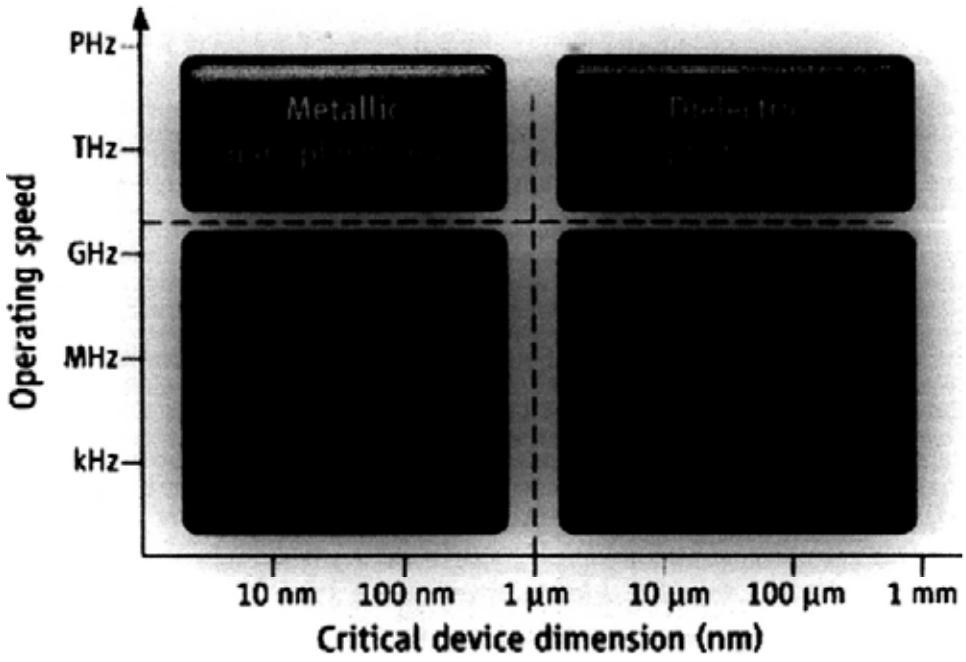


Figure 1.4.1. The different domains in terms of operating speed and device size rely on the unique material properties of semiconductors (electronics), insulators (photonics), and metals (plasmonics). The dashed lines indicate the physical limitations of different technologies. Semiconductor electronics is limited in speed by interconnect delay time to about 10 GHz. Dielectric photonics is limited in size by the fundamental laws of diffraction to about 1 μm. Plasmonics can serve as a bridge between photonics and electronics.

Propagating surface plasmons associated with the metal-dielectric interface were first utilized for the fabrication of plasmonic waveguides. Berini presented the first theoretical study on the possibility of using thin metal stripes embedded in a homogeneous dielectric host to guide optical signals by PSPs [120]. Charbonneau et al. then performed the first experimental verification. By using Au stripe of 20-nm thickness and 8-μm width embedded in glass, optical signals can be guided over several millimeters at 1.55 μm [121]. Furthermore, a 200-nm-wide and 50-nm-thick Au nanowire was shown to have a two dimensional subwavelength guiding feature for a

800-nm-wavelength excitation. The propagation length reached a few micrometers [122]. Since then, PSP-based plasmonic waveguides with different geometries have been studied comprehensively [8, 9]. A major disadvantage in PSP-based plasmonic waveguides is the high Ohmic loss in metal nanostructures, which has limited the maximum propagation length of optical signals in these nanostructures. One solution for this problem is to utilize metal nanocrystal arrays. As has been mentioned previously, the small volume of metal nanocrystals can reduce the resistive heating substantially while the optical signal can be transmitted via the coupling between the nanocrystals in an array. Maier et al. demonstrated that by using a linear closely spaced Ag nanoparticle chain, the optical signal at 570 nm can be transported over a distance of 500 nm [123]. Moreover, they further fabricated a two-dimensional Au nanoparticle array (Figure 1.4.2) on a silicon-on-insulator wafer using lithography. This structure showed a propagation length of longer than 50 μm for a 1.5-μm-wavelength excitation [124]. All these exciting results indicate that metal nanocrystals will certainly make great contributions to the next generation of communication based on plasmonic circuits.

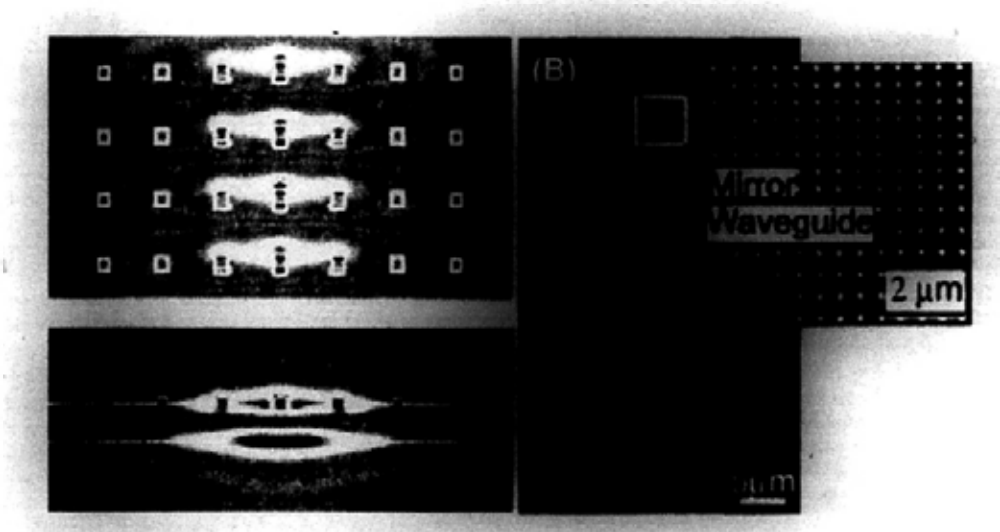


Figure 1.4.2. (A) Simulated electric field intensity distribution of a plasmon waveguide mode in top (upper plot) and side view (lower plot). (B) Scanning electron microscopy image of a fabricated

plasmon waveguide on an undercut Si membrane. The waveguide is terminated by mirrors at both ends.

All of the designs and fabrications of metal nanocrystal-based plasmonic circuits are based on our understandings of the LSPRs of metal nanocrystal aggregates or arrays. Therefore, the coupling behaviors between different nanocrystals need to be systematically studied. Specifically, the question of how plasmon coupling depends on the numbers and orderings of individual nanocrystals should be addressed and well understood. Moreover, as most optoelectronic components are fabricated on silicon-based substrates, the coupling between the plasmon resonances and the substrates will certainly influence the guiding performance of the nanocrystals. Studying the coupling between the silicon substrate and metal nanocrystals is therefore important for designing the nanostructures utilized in future plasmonic circuits. I have performed some preliminary studies in my thesis research, which will be introduced in Chapter 5 and Chapter 6.

The above brief introductions have shown several exciting technological applications that have been made possible by metal nanocrystals. Among various metal nanocrystals, Au nanocrystals have received much attention in recent years due to several attractive virtues. They are chemically stable and biocompatible. Their surface can be easily functionalized with a variety of chemical and biological molecules. Moreover, the localized plasmon resonance wavelengths of Au nanocrystals can be synthetically tailored to range from the visible to the near-infrared spectral regions. Therefore I focused on the studies of localized surface plasmon resonances in Au nanocrystals in my thesis research. The outline of the thesis is given below.

## 1.5 Thesis Outline

In my research, I mainly focused on the study of the refractive index sensitivity, plasmon coupling, and photothermal conversion of Au nanocrystals. The contents are organized as follows.

Chapter 2 will give a brief introduction to the theoretical background of the localized surface plasmon resonances in noble metal nanocrystals, including Maxwell electrodynamics, the solid state theory for describing the dielectric properties of noble metal nanocrystals, and several common numerical methods used for calculating the plasmonic properties of noble metal nanostructures.

Chapter 3 describes the experimental preparation methods of Au nanostructures and characterization methods of their plasmonic properties. Experimental studies are presented in Chapters 4–7.

Chapter 4 discusses the refractive index sensing behaviors of Au nanocrystals. The dependence of the index sensitivity of Au nanocrystals on their shapes, sizes, and localized plasmon wavelengths will be studied.

Chapter 5 presents studies on the plasmon coupling in clusters composed of two-dimensionally ordered Au nanocubes. In these studies, Au nanocubes were deposited onto the substrate to form clusters with different nanocube numbers and arrangements. Their scattering spectra were systematically studied.

In Chapter 6, the influence of adjacent substrates on the plasmonic properties of Au nanocrystals were discussed. Au nanorods were deposited onto substrates with different dielectric properties, including insulating, semiconducting, and metallic substrates. Substrates were found to have great impacts on the far-field scattering patterns and the spectra of Au nanorods.

The photothermal conversion properties of Au nanocrystals and their composites will be discussed in Chapter 7. In this chapter, the effects of the plasmon wavelengths, particle volumes,

shell coatings, and the assembly of Au nanocrystals on their photothermal conversion will be studied both experimentally and theoretically.

Finally, conclusions will be given in Chapter 8.

## References

[1] M. Faraday, Experimental Relations of Gold (and Other Metals) to Light. *Phil. Trans. R. Soc.*, 147: 145, 1857.

[2] G. Mie. Beitäge Zur Optik Trüber Medien, Speziel Kolloidaler Metallösungen–Contribution to the Optics of Suspended Media, Specifically Colloidal Metal Suspensions. *Ann. Phys.*, 25: 377, 1908.

[3] R. Gans, Über Die form Ultramikroskopischer Teilchen. *Ann. Phys.*, 37: 881, 1912.

[4] H. Raether, Excitation of Plasmons and Interband Transitions by Electrons. Springer-Verlag Berlin Heidelberg, New York, US, 1980.

[5] H. Raether, Surface Plasmons on Smooth and Rough Surface. Springer-Verlag Berlin Heidelberg, New York, US, 1988.

[6] A. V. Zayats, I. I. Smolyaninov, A. A. Maradudin, Nano-Optics of Surface Plasmon Polaritons. *Phys. Rep.*, 408: 131, 2005.

[7] G. C. Schatz, R. P. Van Duyne, Handbook of Vibrational Spectroscopy. Wiley New York, US, 2002.

[8] E. Ozbay, Plasmonics: Merging Photonics and Electronics at Nanoscale Dimensions. *Science*, 311: 189, 2006.

[9] S. A. Maier, Plasmonics: Fundamentals and Applications. Springer Science+Business Media LLC, 2007.

[10] M. P. Nezhad, K. Tetz, Y. Fainman, Gain Assisted Propagation of Surface Plasmon Polaritons on Planar Metallic Waveguides. *Opt. Express*, 12: 4072, 2004.

[11] S. A. Maier, Gain-Assisted Propagation of Electromagnetic Energy in Subwavelength Surface Plasmon Polariton Gap Waveguides. *Opt. Commun.*, 258: 295, 2006.

[12] M. Ambati, S. H. Nam, E. Ulin-Avila, D. A. Genov, G. Bartal, X. Zhang, Observation of Stimulated Emission of Surface Plasmon Polaritons. *Nano Lett.*, 8: 3998, 2008.

[13] B. Nikoobakht, M. A. El-Sayed, Preparation and Growth Mechanism of Gold Nanorods (NRs) Using Seed-Mediated Growth Method. *Chem. Mater.*, 15: 1957, 2003.

[14] T. K. Sau, C. J. Murphy, Seeded High Yield Synthesis of Short Au Nanorods in Aqueous Solution. *Langmuir*, 20: 6414, 2004.

[15] C.-K. Tsung, X. S. Kou, Q. H. Shi, J. P. Zhang, M. H. Yeung, J. F. Wang, G. D. Stucky, Selective Shortening of Single-Crystalline Gold Nanorods by Mild Oxidation. *J. Am. Chem. Soc.*, 128: 5352, 2006.

[16] X. S. Kou, S. Z. Zhang, Z. Yang, C.-K. Tsung, G. D. Stucky, L. D. Sun, J. F. Wang, C. H. Yan, Glutathione- and Cysteine-Induced Transverse Overgrowth on Gold Nanorods. *J. Am. Chem. Soc.*, 129: 6402, 2007.

[17] W. H. Ni, X. S. Kou, Z. Yang, J. F. Wang, Tailoring Longitudinal Surface Plasmon Wavelengths, Scattering and Absorption Cross Sections of Gold Nanorods. *ACS Nano*, 2: 677, 2008.

[18] H. X. Xu, E. J. Bjerneld, M. Käll, L. Börjesson, Spectroscopy of Single Hemoglobin Molecules by Surface Enhanced Raman Scattering. *Phys. Rev. Lett.*, 83: 4357, 1999.

[19] J. A. Schuller, E. S. Barnard, W. S. Cai, Y. C. Jun, J. S. White, M. L. Brongersma, Plasmonics for Extreme Light Concentration and Manipulation. *Nat. Mater.*, 9: 193, 2010.

[20] Y. Fang, N.-H. Seong, D. D. Dlott, Measurement of the Distribution of Site Enhancements in Surface-Enhanced Raman Scattering. *Science*, 321: 388, 2008.

[21] D.-K. Lim, K.-S. Jeon, H. M. Kim, J.-M. Nam, Y. D. Suh, Nanogap-Engineerable Raman-Active Nanodumbbells for Single-Molecule Detection. *Nat. Mater.*, 9: 60, 2010.

[22] A. Kinkhabwala, Z. F. Yu, S. H. Fan, Y. Avlasevich, K. Müllen, W. E. Moerner, Large

Single-Molecule Fluorescence Enhancements Produced by a Bowtie Nanoantenna. *Nat. Photonics*, 3: 654, 2009.

[23] B. Sepúlveda, P. C. Angelomé, L. M. Lechuga, L. M. Liz-Marzán, LSPR-Based Nanobiosensors. *Nano Today*, 4: 244, 2009.

[24] A. J. Haes, R. P. Van Duyne, A Nanoscale Optical Biosensor: Sensitivity and Selectivity of an Approach Based on the Localized Surface Plasmon Resonance Spectroscopy of Triangular Silver Nanoparticles. *J. Am. Chem. Soc.*, 124: 10596, 2002.

[25] L. S. Jung, C. T. Campbell, T. M. Chinowsky, M. N. Mar, S. S. Yee, Quantitative Interpretation of the Response of Surface Plasmon Resonance Sensors to Adsorbed Films. *Langmuir*, 14: 5636, 1998.

[26] L. S. Jung, C. T. Campbell, Sticking Probabilities in Adsorption of Alkanethiols from Liquid Ethanol Solution onto Gold. *J. Phys. Chem. B*, 104: 11168, 2000.

[27] L. S. Jung, C. T. Campbell, Sticking Probabilities in Adsorption from Liquid Solutions: Alkylthiols on Gold. *Phys. Rev. Lett.*, 84: 5164, 2000.

[28] L. S. Jung, K. E. Nelson, P. S. Stayton, C. T. Campbell, Binding and Dissociation Kinetics of Wild-Type and Mutant Streptavidins on Mixed Biotin-Containing Alkylthiolate Monolayers. *Langmuir*, 16: 9421, 2000.

[29] V. H. Perez-Luna, M. J. O'Brien, K. A. Opperman, P. D. Hampton, G. P. Lopez, L. A. Klumb, P. S. Stayton, Molecular Recognition between Genetically Engineered Streptavidin and Surface-Bound Biotin. *J. Am. Chem. Soc.*, 121: 6469, 1999.

[30] D. A. Mann, M. Kanai, D. J. Maly, L. L. Kiessling, Probing Low Affinity and Multivalent Interactions with Surface Plasmon Resonance: Ligands for Concanavalin A. *J. Am. Chem. Soc.*, 120: 10575, 1998.

[31] M. Hendrix, E. S. Priestley, G. F. Joyce, C.-H. Wong, Direct Observation of Aminoglycoside–RNA Interactions by Surface Plasmon Resonance. *J. Am. Chem. Soc.*, 119: 3641, 1997.

[32] M. Mrksick, J. R. Grunwell, G. M. Whitesides, Biospecific Adsorption of Carbonic Anhydrase to Self-Assembled Monolayers of Alkanethiolates That Present Benzenesulfonamide Groups on Gold. *J. Am. Chem. Soc.*, 117: 12009, 1995.

[33] J. Rao, L. Yan, B. Xu, G. M. Whitesides, Using Surface Plasmon Resonance to Study the Binding of Vancomycin and Its Dimer to Self-Assembled Monolayers Presenting D-Ala-D-Ala. *J. Am. Chem. Soc.*, 121: 2629, 1999.

[34] C. E. H. Berger, T. A. M. Beumer, R. P. H. Kooyman, J. Greve, Surface Plasmon Resonance Multisensing. *Anal. Chem.*, 70: 703, 1998.

[35] R. J. Heaton, A. W. Peterson, R. M. Georgiadis, Electrostatic Surface Plasmon Resonance: Direct Electric Field-Induced Hybridization and Denaturation in Monolayer Nucleic Acid Films and Label-Free Discrimination of Base Mismatches. *Proc. Natl. Acad. Sci. U.S.A.*, 98: 3701, 2001.

[36] R. Georgiadis, K. P. Peterlinz, A. W. Peterson, Kinetic Control of Hybridization in Surface Immobilized DNA Monolayer Films. *J. Am. Chem. Soc.*, 122: 7837, 2000.

[37] C. E. Jordan, A. G. Frutos, A. J. Thiel, R. M. Corn, Surface Plasmon Resonance Imaging Measurements of DNA Hybridization Adsorption and Streptavidin/DNA Multilayer Formation at Chemically Modified Gold Surfaces. *Anal. Chem.*, 69: 4939, 1997.

[38] B. P. Nelson, T. E. Grimsrud, M. R. Liles, R. M. Goodman, Surface Plasmon Resonance Imaging Measurements of DNA and RNA Hybridization Adsorption onto DNA Microarrays. *Anal. Chem.*, 73: 1, 2001.

[39] J. M. Brockman, A. G. Frutos, R. M. Corn, A Multistep Chemical Modification Procedure To

Create DNA Arrays on Gold Surfaces for the Study of Protein–DNA Interactions with Surface Plasmon Resonance Imaging. *J. Am. Chem. Soc.*, 121: 8044, 1999.

[40] A. J. Haes, L. Chang, W. L. Klein, R. P. Van Duyne, Detection of a Biomarker for Alzheimer's Disease from Synthetic and Clinical Samples Using a Nanoscale Optical Biosensor. *J. Am. Chem. Soc.*, 127: 2264, 2005.

[41] M. P. Kreuzer, R. Quidant, G. Badenes, M.-P. Marco, Quantitative Detection of Doping Substances by a Localized Surface Plasmon Sensor. *Biosens. Bioelectron.*, 21: 1345, 2006.

[42] S. M. Marinakos, S. Chen, A. Chilkoti, Plasmonic Detection of a Model Analyte in Serum by a Gold Nanorod Sensor. *Anal. Chem.*, 79: 5278, 2007.

[43] A. P. Alivisatos, K. P. Johnsson, X. G. Peng, T. E. Wilson, C. J. Loweth, M. P. Bruchez, P. G. Schultz, Organization of 'Nanocrystal Molecules' Using DNA. *Nature*, 382: 609, 1996.

[44] C. A. Mirkin, R. L. Letsinger, R. C. Mucic, J. J. Storhoff, A DNA-Based Method for Rationally Assembling Nanoparticles into Macroscopic Materials. *Nature*, 382: 607, 1996.

[45] R. Elghanian, J. J. Storhoff, R. C. Mucic, R. L. Letsinger, C. A. Mirkin, Selective Colorimetric Detection of Polynucleotides Based on the Distance-Dependent Optical Properties of Gold Nanoparticles. *Science*, 277: 1078, 1997.

[46] J. J. Storhoff, R. Elghanian, R. C. Mucic, C. A. Mirkin, R. L. Letsinger, One-Pot Colorimetric Differentiation of Polynucleotides with Single Base Imperfections Using Gold Nanoparticle Probes. *J. Am. Chem. Soc.*, 120: 1959, 1998.

[47] J. J. Storhoff, A. A. Lazarides, R. C. Mucic, C. A. Mirkin, R. L. Letsinger, G. C. Schatz, What Controls the Optical Properties of DNA-Linked Gold Nanoparticle Assemblies? *J. Am. Chem. Soc.*, 122: 4640, 2000.

[48] C. Sönnichsen, B. M. Reinhard, J. Liphardt, A. P. Alivisatos, A Molecular Ruler Based on

Plasmon Coupling of Single Gold and Silver Nanoparticles. *Nat. Biotechnol.*, 23: 741, 2005.

[49] B. M. Reinhard, M. Siu, H. Agarwal, A. P. Alivisatos, J. Liphardt, Calibration of Dynamic Molecular Rulers Based on Plasmon Coupling between Gold Nanoparticles. *Nano Lett.*, 5: 2246, 2005.

[50] N. T. K. Thanh, Z. Rosenzweig, Development of an Aggregation-Based Immunoassay for Anti-Protein A Using Gold Nanoparticles. *Anal. Chem.*, 74: 1624, 2002.

[51] K.-H. Su, Q.-H. Wei, X. Zhang, J. J. Mock, D. R. Smith, S. Schultz, Interparticle Coupling Effects on Plasmon Resonances of Nanogold Particles. *Nano Lett.*, 3: 1087, 2003.

[52] P. Nordlander, C. Oubre, E. Prodan, K. Li, M. I. Stockman, Plasmon Hybridization in Nanoparticle Dimers. *Nano Lett.*, 4: 899, 2004.

[53] L. Gunnarsson, T. Rindzevicius, J. Prikulis, B. Kasemo, M. Käll, S. L. Zou, G. C. Schatz, Confined Plasmons in Nanofabricated Single Silver Particle Pairs: Experimental Observations of Strong Interparticle Interactions. *J. Phys. Chem. B*, 109: 1079, 2005.

[54] B. Khlebtsov, A. Melnikov, V. Zharov, N. Khlebtsov, Absorption and Scattering of Light by a Dimer of Metal Nanospheres: Comparison of Dipole and Multipole Approaches. *Nanotechnology*, 17: 1437, 2006.

[55] P. K. Jain, M. A. El-Sayed, Surface Plasmon Coupling and Its Universal Size Scaling in Metal Nanostructures of Complex Geometry: Elongated Particle Pairs and Nanosphere Trimers. *J. Phys. Chem. C*, 112: 4954, 2008.

[56] C. Tabor, R. Murali, M. Mahmoud, M. A. El-Sayed, On the Use of Plasmonic Nanoparticle Pairs as a Plasmon Ruler: The Dependence of the Near-Field Dipole Plasmon Coupling on Nanoparticle Size and Shape. *J. Phys. Chem. A*, 113: 1946, 2009.

[57] K. L. Shuford, K. A. Meyer, C. C. Li, S. O. Cho, W. B. Whitten, R. W. Shaw, Computational

and Experimental Evaluation of Nanoparticle Coupling. *J. Phys. Chem. A*, 113: 4009, 2009.

[58] T. Atay, J.-H. Song, A. V. Nurmikko, Strongly Interacting Plasmon Nanoparticle Pairs: From Dipole–Dipole Interaction to Conductively Coupled Regime. *Nano Lett.*, 4: 1627, 2004.

[59] P. K. Jain, W. Y. Huang, M. A. El-Sayed, On the Universal Scaling Behavior of the Distance Decay of Plasmon Coupling in Metal Nanoparticle Pairs: A Plasmon Ruler Equation. *Nano Lett.*, 7: 2080, 2007.

[60] H. Wang, N. J. Halas, Plasmonic Nanoparticle Heterodimers in a Semiembedded Geometry Fabricated by Stepwise Upright Assembly. *Nano Lett.*, 6: 2945, 2006.

[61] J. B. Lassiter, J. Aizpurua, L. I. Hernandez, D. W. Brandl, I. Romero, S. Lal, J. H. Hafner, P. Nordlander, N. J. Halas, Close Encounters between Two Nanoshells. *Nano Lett.*, 8: 1212, 2008.

[62] P. K. Jain, S. Eustis, M. A. El-Sayed, Plasmon Coupling in Nanorod Assemblies: Optical Absorption, Discrete Dipole Approximation Simulation, and Exciton-Coupling Model. *J. Phys. Chem. B*, 110: 18243, 2006.

[63] B. Willingham, D. W. Brandl, P. Nordlander, Plasmon Hybridization in Nanorod Dimers. *Appl. Phys. B: Laser Opt.*, 93: 209, 2008.

[64] Z. H. Sun, W. H. Ni, Z. Yang, X. S. Kou, L. Li, J. F. Wang, pH-Controlled Reversible Assembly and Disassembly of Gold Nanorods. *Small*, 4: 1287, 2008.

[65] C. Tabor, D. Van Haute, M. A. El-Sayed, Effect of Orientation on Plasmonic Coupling between Gold Nanorods. *ACS Nano*, 3: 3670, 2009.

[66] M.-W. Chu, V. Myroshnychenko, C. H. Chen, J.-P. Deng, C.-Y. Mou, F. J. García de Abajo, Probing Bright and Dark Surface-Plasmon Modes in Individual and Coupled Noble Metal Nanoparticles Using an Electron Beam. *Nano Lett.*, 9: 399, 2009.

[67] I. Romero, J. Aizpurua, G. W. Bryant, F. J. García de Abajo, Plasmons in Nearly Touching

Metallic Nanoparticle: Singular Response in the Limit of Touching Dimers. *Opt. Express*, 14: 9988, 2006.

[68] D. L. Jeanmaire, R. P. Van Duyne, Surface Raman Spectroelectrochemistry. Part I. Heterocyclic, Aromatic, and Aliphatic Amines Adsorbed on the Anodized Silver Electrode. *J. Electroanal. Chem. Interface Electrochem.*, 84: 1, 1977.

[69] A. D. McFarland, M. A. Young, J. A. Dieringer, R. P. Van Duyne, Wavelength-Scanned Surface-Enhanced Raman Excitation Spectroscopy. *J. Phys. Chem. B*, 109: 11279, 2005.

[70] S. Nie, S. R. Emory, Probing Single Molecules and Single Nanoparticles by Surface-Enhanced Raman Scattering. *Science*, 275: 1102, 1997.

[71] J. A. Dieringer, R. B. L. Ii, K. A. Scheidt, R. P. Van Duyne, A Frequency Domain Existence Proof of Single-Molecule Surface-Enhanced Raman Spectroscopy. *J. Am. Chem. Soc.*, 129: 16249, 2007.

[72] K. Kneipp, Y. Wang, H. Kneipp, L. T. Perelman, I. Itzkan, R. R. Dasari, M. S. Feld, Single Molecule Detection Using Surface-Enhanced Raman Scattering (SERS). *Phys. Rev. Lett.*, 78: 1667, 1997.

[73] K. A. Willets, R. P. Van Duyne, Localized Surface Plasmon Resonance Spectroscopy and Sensing. *Annu. Rev. Phys. Chem.*, 58: 267, 2007.

[74] C. L. Haynes, R. P. Van Duyne, Plasmon-Sampled Surface-Enhanced Raman Excitation Spectroscopy. *J. Phys. Chem. B*, 107: 7426, 2003.

[75] P. Cherukuri, E. S. Glazer, S. A. Curley, Targeted Hyperthermia Using Metal Nanoparticles. *Adv. Drug Delivery Rev.*, 62: 339, 2010.

[76] D. Pissuwan, S. M. Valenzuela, M. B. Cortie, Therapeutic Possibilities of Plasmonically Heated Gold Nanoparticles. *Trends Biotechnol.* 24: 62, 2006.

[77] P. K. Jain, K. S. Lee, I. H. El-Sayed, M. A. El-Sayed, Calculated Absorption and Scattering Properties of Gold Nanoparticles of Different Size, Shape, and Composition: Applications in Biological Imaging and Biomedicine. *J. Phys. Chem. B*, 110: 7328, 2006.

[78] R. Weissleder, A Clearer Vision for *in vivo* Imaging. *Nat. Biotechnol.*, 19: 316, 2001.

[79] C. Loo, A. Lin, L. Hirsch, M.-H. Lee, J. Barton, N. Halas, J. West, R. Drezek, Nanoshell-Enabled Photonics-Based Imaging and Therapy of Cancer. *Technol. Cancer Res. Treat.*, 3: 33, 2004.

[80] L. R. Hirsch, R. J. Stafford, J. A. Bankson, S. R. Sershen, B. Rivera, R. E. Price, J. D. Hazle, N. J. Halas, Nanoshell-Mediated Near-Infrared Thermal Therapy of Tumors under Magnetic Resonance Guidance. *Proc. Natl. Acad. Sci. U. S. A.*, 100: 13549, 2003.

[81] D. P. O'Neal, L. R. Hirsch, N. J. Halas, J. D. Payne, J. L. West, Photo-Thermal Tumor Ablation in Mice Using Near Infrared-Absorbing Nanoparticles. *Cancer Lett.*, 209: 171, 2004.

[82] G. von Maltzahn, A. Centrone, J.-H. Park, R. Ramanathan, M. J. Sailor, T. A. Hatton, S. N. Bhatia, SERS-Coded Gold Nanorods as a Multifunctional Platform for Densely Multiplexed Near-Infrared Imaging and Photothermal Heating. *Adv. Mater.*, 21: 3175, 2009.

[83] Wikipedia, http://en.wikipedia.org/wiki/Fossil_fuel.

[84] N. G. Dhere, Toward GW/Year of CIGS Production within the Next Decade. *Sol. Energy Mater. Sol. Cells*, 91: 1376, 2007.

[85] H. M. Liou, Overview of the Photovoltaic Technology Status and Perspective in Taiwan. *Renewable Energy. Renewable Sustainable Energy Rev.*, 14: 1202, 2010.

[86] H. A. Atwater, A. Polman, Plasmonics for Improved Photovoltaic Devices. *Nat. Mater.*, 9: 205, 2010.

[87] E. Yablonovitch, G. D. Cody, Intensity Enhancement in Textured Optical Sheets for Solar Cells.

*IEEE Trans. Electr. Dev.*, 29: 300, 1982.

[88] H. W. Deckman, C. B. Roxlo, E. Yablonovitch, Maximum Statistical Increase of Optical Absorption in Textured Semiconductor Films. *Opt. Lett.*, 8: 491, 1983.

[89] J. Mertz, Radiative Absorption, Fluorescence, and Scattering of a Classical Dipole near a Lossless Interface: a Unified Description. *J. Opt. Soc. Am. B*, 17: 1906, 2000.

[90] D. M. Schaadt, B. Feng, E. T. Yu, Enhanced Semiconductor Optical Absorption via Surface Plasmon Excitation in Metal Nanoparticles. *Appl. Phys. Lett.*, 86: 063106, 2005.

[91] D. Derkacs, S. H. Lim, P. Matheu, W. Mar, E. T. Yu, Improved Performance of Amorphous Silicon Solar Cells via Scattering from Surface Plasmon Polaritons in nearby Metallic Nanoparticles. *Appl. Phys. Lett.*, 89: 093103, 2006.

[92] P. Matheu, S. H. Lim, D. Derkacs, C. McPheeters, E. T. Yu, Metal and Dielectric Nanoparticle Scattering for Improved Optical Absorption in Photovoltaic Devices. *Appl. Phys. Lett.*, 93: 113108, 2008.

[93] S. Pillai, K. R. Catchpole, T. Trupke, M. A. Green, Surface Plasmon Enhanced Silicon Solar Cells. *J. Appl. Phys.*, 101: 093105, 2007.

[94] D. Derkacs, W. V. Chen, P. M. Matheu, S. H. Lim, P. K. L. Yu, E. T. Yu, Nanoparticle-Induced Light Scattering for Improved Performance of Quantum-Well Solar Cells. *Appl. Phys. Lett.*, 93: 091107, 2008.

[95] K. Nakayama, K. Tanabe, H. A. Atwater, Plasmonic Nanoparticle Enhanced Light Absorption in GaAs Solar Cells. *Appl. Phys. Lett.*, 93: 121904, 2008.

[96] K. R. Catchpole, A. Polman, Design Principles for Particle Plasmon Enhanced Solar Cells. *Appl. Phys. Lett.*, 93: 191113, 2008.

[97] B. P. Rand, P. Peumans, S. R. Forrest, Long-Range Absorption Enhancement in Organic

Tandem Thin-Film Solar Cells Containing Silver Nanoclusters. *J. Appl. Phys.*, 96: 7519, 2004.

[98] S. S. Kim, S.-I. Na, J. Jo, D. Y. Kim, Y.-C. Nah, Plasmon Enhanced Performance of Organic Solar Cells Using Electrodeposited Ag Nanoparticles. *Appl. Phys. Lett.*, 93: 073307, 2008.

[99] A. J. Morfa, K. L. Rowlen, T. H. Reilly, M. J. Romero, J. Van de Lagemaat, Plasmon-Enhanced Solar Energy Conversion in Organic Bulk Heterojunction Photovoltaics. *Appl. Phys. Lett.*, 92: 013504, 2008.

[100] N. C. Lindquist, W. A. Luhman, S. H. Oh, R. J. Holmes, Plasmonic Nanocavity Arrays for Enhanced Efficiency in Organic Photovoltaic Cells. *Appl. Phys. Lett.*, 93: 123308, 2008.

[101] A. P. Kulkarni, K. M. Noone, K. Munechika, S. R. Guyer, D. S. Ginger, Plasmon-Enhanced Charge Carrier Generation in Organic Photovoltaic Films Using Silver Nanoprisms. *Nano Lett.*, 10: 1501, 2010.

[102] R. B. Konda, R. Mundle, H. Mustafa, O. Bamiduro, A. K. Pradhan, U. N. Roy, Y. Cui, A. Burger, Surface Plasmon Excitation via Au Nanoparticles in n-CdSe/*p*-Si Heterojunction Diodes. *Appl. Phys. Lett.*, 91: 191111, 2007.

[103] C. Hägglund, M. Zäch, B. Petersson, B. Kasemo, Electromagnetic Coupling of Light into a Silicon Solar Cell by Nanodisk Plasmons. *Appl. Phys. Lett.*, 92: 053110, 2008.

[105] K. R. Catchpole, A. Polman, Plasmonic Solar Cells. *Opt. Express*, 16: 21793, 2008.

[106] M. W. Knight, Y. P. Wu, J. B. Lassiter, P. Nordlander, N. J. Halas, Substrates Matter: Influence of an Adjacent Dielectric on An Individual Plasmonic Nanoparticle. *Nano Lett.*, 9: 2188, 2009.

[107] P. Nordlander, E. Prodan, Plasmon Hybridization in Nanoparticles near Metallic Surfaces. *Nano Lett.*, 4: 2209, 2004.

[108] T. Okamoto, I. Yamaguchi, Optical Absorption Study of the Surface Plasmon Resonance in Gold Nanoparticles Immobilized onto a Gold Substrate by Self-Assembly Technique. *J. Phys. Chem.*

*B*, 107: 10321, 2003.

[109] F. Le, N. Z. Lwin, J. M. Steele, M. Käll, N. J. Halas, P. Nordlander, Plasmons in the Metallic Nanoparticle–Film System As a Tunable Impurity Problem. *Nano Lett.*, 5: 2009, 2005.

[110] V. V. Gozhenko, L. G. Grechko, Electrodynamics of Spatial Clusters of Spheres: Substrate Effects. *Phys. Rev. B*, 68: 125422, 2003.

[111] G. Lévêque, O. J. F. Martin, Optical Interactions in a Plasmonic Particle Coupled to a Metallic Film. *Opt. Express*, 14: 9971, 2006.

[112] G. Lévêque, O. J. F. Martin, Tunable Composite Nanoparticle for Plasmonics. *Opt. Lett.*, 31: 2750, 2006.

[113] Y. P. Wu, P. Nordlander, Finite-Difference Time-Domain Modeling of the Optical Properties of Nanoparticles near Dielectric Substrates. *J. Phys. Chem. C*, 114: 7302, 2010.

[115] F. Moreno, B. García-Cámara, J. M. Saiz, F. González, Interaction of Nanoparticles with Substrates: Effects on the Dipolar Behaviour of the Particles. *Opt. Express*, 16: 12487, 2008.

[116] J. J. Mock, R. T. Hill, A. Degiron, S. Zauscher, A. Chilkoti, D. R. Smith, Distance-Dependent Plasmon Resonant Coupling between a Gold Nanoparticle and Gold Film. *Nano Lett.*, 8: 2245, 2008.

[117] S.-H. Guo, S.-J. Tsai, H.-C. Kan, D.-H. Tsai, M. R. Zachariah, R. J. Phaneuf, The Effect of an Active Substrate on Nanoparticle-Enhanced Fluorescence. *Adv. Mater.*, 20: 1424, 2008.

[118] M. J. Kobrinsky, B. A. Block, J.-F, Zheng, B. C. Barnett, E. Mohammed, M. Reshotko, F. Robertson, S. List, I. Young, K. Cadien, On-Chip Optical Interconnects. *Intel Technol. J.*, 8: 129, 2004.

[119] M. L. Brongersma, V. M. Shalaev, The Case for Plasmonics. *Science*, 328: 440, 2010.

[120] P. Berini, Plasmon–Polariton Waves Guided by Thin Lossy Metal Films of Finite Width:

Bound Modes of Symmetric Structures. *Phys. Rev. B*, 61:10484, 2000.

[121] R. Charbonneau, P. Berini, E. Berolo, E. Lisicka-Shrzek, Experimental Observation of Plasmon–Polariton Waves Supported by a Thin Metal Film of Finite Width. *Opt. Lett.*, 25: 844, 2000.

[122] J. R. Krenn, J. C. Weeber, Surface Plasmon Polaritons in Metal Stripes and Wires. *Phil. Trans. R. Soc. Lond. A*, 362: 739, 2004.

[123] S. A. Maier, P. G. Kik, H. A. Atwater, S. Meltzer, E. Harel, B. E. Koel, A. A. G. Requicha, Local Detection of Electromagnetic Energy Transport below the Diffraction Limit in Metal Nanoparticle Plasmon Waveguides. *Nat. Mater.*, 2: 229, 2003.

[124] S. A. Maier, M. D. Friedman, P. E. Barclay, O. Painter, Experimental Demonstration of Fiber-Accessible Metal Nanoparticle Plasmon Waveguides for Planar Energy Guiding and Sensing. *Appl. Phys. Lett.*, 86: 071103, 2005.

# Chapter 2

# Theoretical Background

In quantum mechanics, surface plasmon is the quanta of electron collective oscillations. Full descriptions of the optical response of the surface plasmon require the quantization of the electromagnetic field and study the electron–electron, electron–photon interactions in the framework of quantum field theory. However, in most cases the classical electrodynamic theory that is based on Maxwell equations can give a very good description. In classical electrodynamics, surface plasmons can be characterized as surface waves that are confined at different interfaces. The optical responses are mainly determined by the dielectric properties of the materials at both sides of the interfaces, the different boundary conditions of the interfaces, and the properties of the excitation light source. In this chapter, the Maxwell's equations and the solid state theory for describing the dielectric properties of metals will first be discussed. The electrodynamic theory for calculating the optical response of spherical nanoparticles and the quasi-static approximation approach will be given in the second part. Finally, numerical methods for calculating the plasmonic properties of metal nanocrystals will be introduced.

## 2.1 Maxwell Equations

Maxwell equations are the basis for describing the electrodynamic processes in macroscopic systems (here macroscopic means that the systems are composed of many atoms and quantum effects can be neglected). In this formalism, the electric field (**E**) and the magnetic field (**B**) are not

independent and are related by the following four partial differential equations,

$$\nabla \cdot \mathbf{D} = \rho_f \tag{2.1.1}$$

$$\nabla \times \mathbf{E} + \frac{\partial \mathbf{B}}{\partial t} = 0 \tag{2.1.2}$$

$$\nabla \cdot \mathbf{B} = 0 \tag{2.1.3}$$

$$\nabla \times \mathbf{H} = \mathbf{J}_F + \frac{\partial \mathbf{D}}{\partial t} \tag{2.1.4}$$

The electric displacement (**D**) and magnetic field intensity (**H**) are determined by the polarization and magnetization properties of the system,

$$\mathbf{D} = \varepsilon_0 \mathbf{E} + \mathbf{P} \tag{2.1.5}$$

$$\mathbf{B} = \frac{\mathbf{H}}{\mu_0} - \mathbf{M} \tag{2.1.6}$$

where the quantities **P** and **M** are polarization (electric dipole moment per unit volume) and magnetization (magnetic dipole moment per unit volume). In most cases of our studies, the response of the system is linear and the **P** and **M** can be expressed as,

$$\mathbf{P} = \varepsilon_0 \chi_e \mathbf{E} \tag{2.1.7}$$

$$\mathbf{M} = \mu_0 \mu_M \mathbf{H} \tag{2.1.8}$$

Under these considerations, equations (2.1.5) and (2.1.6) become,

$$\mathbf{D} = \varepsilon_0 \mathbf{E} + \mathbf{P} = \varepsilon_0 (1 + \chi_e) \mathbf{E} = \varepsilon_0 \varepsilon_r \mathbf{E} \tag{2.1.9}$$

$$\mathbf{B} = \mu_0 \mathbf{H} + \mu_0 \mathbf{M} = \mu_0 (1 + \chi_M) \mathbf{H} = \mu_0 \mu_M \mathbf{H} \tag{2.1.10}$$

The phenomenological parameters $\varepsilon_r$ and $\mu_M$ are defined as the permittivity and permeability and usually frequency-dependent. Combining the above equations, one can get to the following universal equations describing the electromagnetic wave transmitting through a linear media,

$$\nabla(\nabla\cdot\mathbf{E})-\nabla^2\mathbf{E}+\mu_0\frac{\partial}{\partial t}[\nabla\times(\mu_M\mathbf{H})]=0 \tag{2.1.11}$$

$$\nabla(\nabla\cdot\mathbf{H})-\nabla^2\mathbf{H}-\nabla\times\mathbf{J}_F-\varepsilon_0\frac{\partial}{\partial t}[\nabla\times(\varepsilon_r\mathbf{E})]=0 \tag{2.1.12}$$

If the system is homogeneous and has no free charges, the above equations are reduced to,

$$\nabla^2\mathbf{E}-\varepsilon_0\varepsilon_r\mu_0\mu_M\frac{\partial^2\mathbf{E}}{\partial t^2}=0 \tag{2.1.13}$$

$$\nabla^2\mathbf{H}-\varepsilon_0\varepsilon_r\mu_0\mu_M\frac{\partial^2\mathbf{H}}{\partial t^2}=0 \tag{2.1.14}$$

As the Maxwell equation is linear, a general solution can be expressed as the sum of many harmonic components via Fourier transformation. We therefore only consider the time-harmonic solution of equations (2.1.13) and (2.1.14), which has a dependence on the time as *exp(-iωt)*. On the basis of this consideration, equations (2.1.13) and (2.1.14) become,

$$\nabla^2\mathbf{E}+\varepsilon_0\varepsilon_r\mu_0\mu_M\omega^2\mathbf{E}=0 \tag{2.1.15}$$

$$\nabla^2\mathbf{H}+\varepsilon_0\varepsilon_r\mu_0\mu_M\omega^2\mathbf{H}=0 \tag{2.1.16}$$

Classically, localized surface plasmon resonance-related problems of different metallic nanoparticles can be regarded as the solutions of equation (2.1.15) and (2.1.16) with different dielectric constant and under different boundary conditions. Nanoparticles with spherical and ellipsoidal boundaries are two common examples that have gained much attention. As a result, Mie theory and Gans theory have been developed for these two types of nanoparticles, respectively. In the following sections, the theory of the permittivity of metals, the Mie theory, and the Gans theory will be further discussed.

## 2.2 Theoretical Description of the Dielectric Function of Metals

The complex permittivity, or the dielectric function, $\varepsilon_r$, of the metals can be written as,

$$\varepsilon_r = \varepsilon' + i\varepsilon'' \tag{2.2.1}$$

The modulus of $\varepsilon_r$ determines the magnitude of the polarization while the phase of $\varepsilon_r$ controls the phase lag of the metal's response to the external field. The dissipation mechanisms are all included in the $\varepsilon''$ term. A full description of $\varepsilon_r$ requires the use of quantum theories for solids, which is a complicated and arduous task because both the electron–electron interaction and electron–lattice interaction need to be taken into account. In 1900, Drude constructed a famous phenomenological theory, which has been known as the Drude model, for the free electrons in metals [1, 2]. The theory is very simple yet gains surprisingly successful in describing metal's conductance and optical properties. In the Drude model the conduction electrons are treated as electron gas. They collide with the positive-ion background. Moreover, the electrons are assumed to be independent (neglecting the electron–electron interactions between the collisions) and free (neglecting the electron–ion interactions between the collisions). Under these considerations, the movement of the electrons in the metal under an external field can be treated in the framework of Newtonian mechanics,

$$\frac{d\mathbf{p}(t)}{dt} = -\frac{\mathbf{p}(t)}{\tau} - e\mathbf{E}(t) \tag{2.2.2}$$

Here $\tau$ is the relaxation time that characterizes the collision process, $\boldsymbol{p}$ is the momentum of the electrons. Because the electric field associated with the optical excitation is time-harmonic, the solution to eqution (2.2.2) is a time-harmonic steady-state solution,

$$-\omega^2 m\mathbf{x} - im\omega\frac{\mathbf{x}}{\tau} = -e\mathbf{E} \tag{2.2.3}$$

Here $m$ is the mass of a free electron. Equation (2.2.3) can be rearranged as,

$$\mathbf{x} = -\frac{e}{m}\frac{1}{\omega^2 + \frac{i\omega}{\tau}}\mathbf{E} \tag{2.2.4}$$

From the definition of polarization one can see that,

$$\mathbf{P} = ne\mathbf{x} = \varepsilon_0\chi_e\mathbf{E} = -\frac{ne^2}{m}\frac{1}{\omega^2 + \frac{i\omega}{\tau}}\mathbf{E} \tag{2.2.5}$$

Thus the dielectric function $\varepsilon_r$ can be expressed as,

$$\varepsilon_r = 1 - \frac{ne^2}{\varepsilon_0 m}\frac{1}{\omega^2 + \frac{i\omega}{\tau}} \tag{2.2.6}$$

In practical calculation, a more general form is often used,

$$\varepsilon_r = 1 - \frac{\omega_p^2}{\omega^2 + i\gamma\omega} \tag{2.2.7}$$

where $\omega_p = \sqrt{\frac{ne^2}{\varepsilon_0 m}}$ is the plasma frequency of the metal and $\gamma$ represents the collision relaxation.

In the Drude model, the dielectric properties of metals at a specific frequency are mainly determined by the conduction electron density $n$, the conduction electron mass $m$, and the relaxation constant $\gamma$. In real metals, the positive-ion background not only acts as scattering centers, but also provides a periodic potential to the electrons, leading to different energy band structures of the metals. Therefore an extension of the ideal Drude model is needed so that it can be employed to describe the real metals. First, the conduction electrons are dominated by the electrons in the $s$ band. Their masses will be modified according to the band structures and replaced by the effective mass $m^*$ [3]. Second, the filled $d$ band close to the Fermi surface will cause a highly polarized environment, leading to a residual polarization background. The correction for this effect can be done by replacing the constant "1" in equation (2.2.7) by a background dielectric constant $\varepsilon_\infty$

(usually between 1 and 10 and often referred to as high-frequency dielectric constant) [4]. Now equation (2.2.7) becomes,

$$\varepsilon_r = \varepsilon_\infty - \frac{\omega_p^2}{\omega^2 + i\gamma\omega} \tag{2.2.8}$$

$$\omega_p = \sqrt{\frac{ne^2}{\varepsilon_0 m^*}} \tag{2.2.9}$$

The effective mass, the background dielectric constant, and the relaxation constant can be obtained by fitting the Drude model to the experimentally determined dielectric data of metals. The parameters for some common metals are listed in Table 2.2.1 [3, 5, 6].

Table 2.2.1. Conduction electron density and plasma parameters of several metals.

| | Au | Ag | Cu |
|---|---|---|---|
| $m^*$ (in free electron mass $m_e$) | 0.99 | 0.96 | 1.49 |
| $\varepsilon_\infty$ | 9.5 | 5.0 | |
| $\hbar\gamma$ (meV) | 69 | 99 | 96 |
| $\hbar\omega_p$ (eV) | 9.1 | 9.5 | 8.8 |
| $n$ ($10^{28}$ cm$^{-3}$) | 5.9 | 5.76 | 8.45 |

The validity of the Drude model is corroborated for Au and Ag in Figure 2.2.1. Clearly, this model agrees excellently with the experiments in the low-energy (infrared region) part of the dielectric function. At energies above 2 eV for Au and 3 eV for Ag, the model deviates from the experiments due to the interband transitions of the bound electrons in these energy ranges [4, 7].

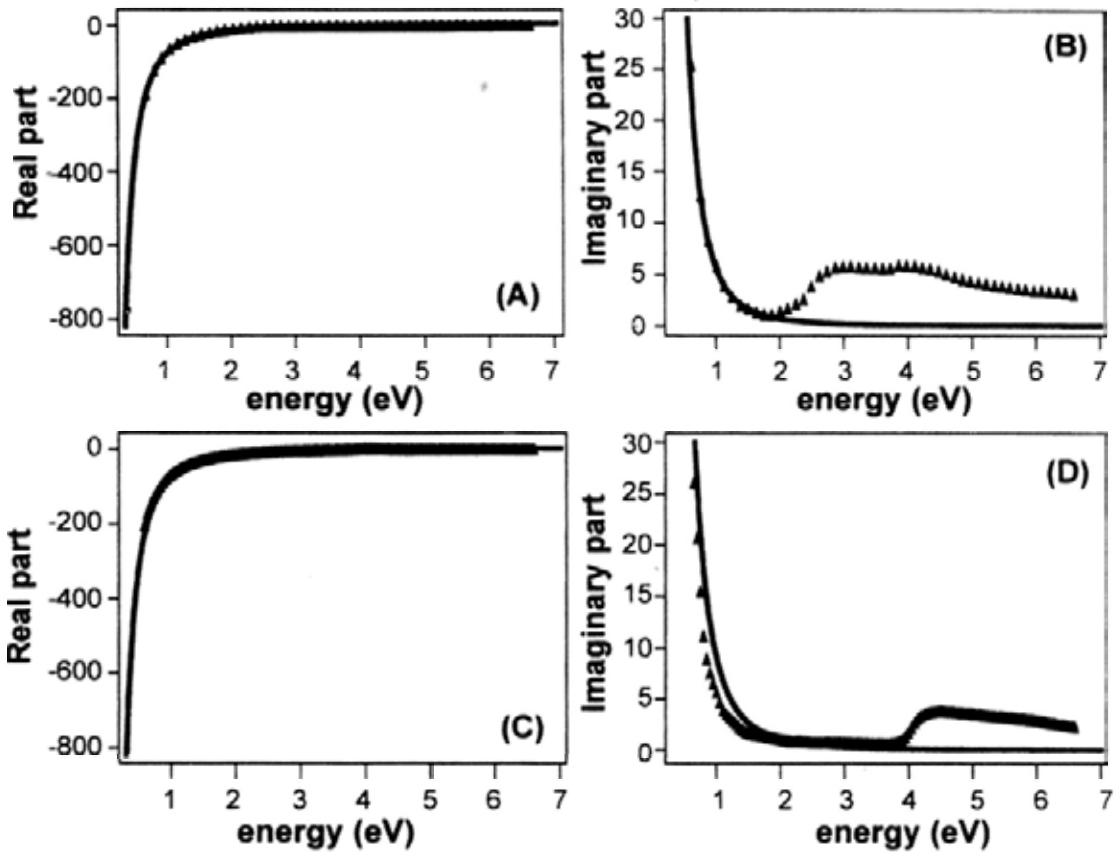


Figure 2.2.1 Dielectric functions of Au and Ag. (A) Real part of Au. (B) Imaginary part of Au. (C) Real part of Ag. (D) Imaginary part of Ag. The triangles are the experimental data determined by Johnson and Christy [5], and the solid lines are the dielectric function calculated by the Drude model by using the parameters for Au and Ag shown in Table 2.2.1

The deviation can be corrected by modifying equation (2.2.3) with a Lorentz oscillator model, which is as a classical model often employed for describing resonance absorptions [7 – 11].

$$m\ddot{\mathbf{x}} + m\gamma\dot{\mathbf{x}} + m\omega_0^2\mathbf{x} = -e\mathbf{E}(t) \tag{2.2.10}$$

In equation (2.2.10), $\omega_0$ is the resonance frequency, and $\gamma$ is the relaxation constant, representing the intrinsic width of the absorption peak. The solution of equation (2.2.10) is,

$$\mathbf{x} = -\frac{e}{m}\frac{\mathbf{E}}{\omega_0^2 - \omega^2 - i\gamma\omega} \tag{2.2.11}$$

Because there usually exist more than one interband transitions that involve different energy bands, the solution to each transition should be added together in order to model the dielectric response of metals accurately. This consideration leads to the following expression for the dielectric function,

$$\varepsilon_r = \varepsilon_\infty - \frac{\omega_p^2}{\omega^2 + i\gamma\omega} + \sum_i \frac{A_i}{\omega_i^2 - \omega^2 - i\gamma_i\omega} \tag{2.2.12}$$

This treatment is also mathematically feasible, as a sum over an infinite number of Lorentz functions can reproduce any well-behaved function that obeys the Kramers–Kronig relation, such as the dielectric function of metals [11]. In recent years, several groups have proved that by employing two to five Lorentz terms, the dielectric function of Au and Ag can be well reproduced [8 – 11]. Another distinct advantage of this treatment is that the Drude model and Lorentz model can be easily incorporated into the time-domain numerical methods for electrodynamic calculations, for example, the finite-difference time-domain method. We will revisit this point in the discussion of electrodynamic numerical calculations.

On the other hand, as the size of metals reaches the mean free path of the electrons (38 nm for Au and 52 nm for Ag), the scattering of the electrons by the surface of the metals will become important. The contribution of the surface electron scattering can be taken into account by including a correction term into the relaxation time of the Drude model. The Lorentz terms are for the bound electrons in the metal. The bound electrons will not undergo the surface scattering). Euler gave the first calculation of the surface scattering-induced relaxation in spherical particles. The relaxation time for spherical particles is described by [13],

$$\tau = \tau_D + \frac{R}{v_F} \tag{2.2.13}$$

where $\tau_D$ is the Drude relaxation time, $v_F$ is the Fermi velocity of the electrons in the metal (1–2 nm/fs for most of metals at room temperature) [3] , and $R$ is the radius of the spherical particles. The

expression of the relaxation time for nonspherical particles becomes,

$$\tau = \tau_D + A\frac{R_{\text{eff}}}{v_F} \tag{2.2.14}$$

$R_{eff}$ is the effective radius of the sphere whose volume equals to that of the nonspherical particles, and $A$ is a proportional parameter ranging from 0 to 1 [13]. If the particle size is further reduced and becomes a cluster composed of hundreds of atoms, the dielectric function will no longer be adequate to describe the optical properties of the particle. In this circumstance, quantum effects will become dominant, which is out of the scope of this thesis.

After the formalism of the dielectric functions of metals have been established, the remaining question is to solve the Maxwell equations under specific boundary conditions. I will discuss this in the next section.

## 2.3 Mie Theory

In 1908, Mie developed the most beautiful analytical theory for calculating the electrodynamic response of particles with a spherical shape [14]. The starting point of Mie theory is equations (2.1.15) and (2.1.16). As both these two equations and the boundary conditions are linear, one need only consider the fundamental solutions. The general solutions can be obtained by superposing these fundamental solutions. Suppose that a plane wave with a specific frequency and polarization is incident on a homogeneous, isotropic sphere of radius $a$ and refractive index $n$. The sphere is surrounded by a homogeneous medium with refractive index of $n_m$. The standard approach for searching for the solution to equations (2.1.15) and (2.1.16) is by first expanding the incident electromagnetic field, the scattered field, and the field inside the sphere into infinite series of vector spherical harmonics with unknown coefficients. These coefficients can then be determined by

fulfilling the boundary conditions on the surface of the sphere. Thereafter the near-field distribution, the far-field distribution, and the angular distribution of the scattering can be obtained. Specifically, the absorption cross section ($C_{abs}$), the scattering cross section ($C_{sca}$), and the extinction cross section ($C_{ext}$) can be obtained via the following expressions [7, 14, 15],

$$C_{sca} = \frac{2\pi}{k^2}\sum_{n=1}^{\infty}(2n+1)\left(|a_n|^2 + |b_n|^2\right) \tag{2.3.1}$$

$$C_{ext} = \frac{2\pi}{k^2}\sum_{n=1}^{\infty}(2n+1)\mathrm{Re}(a_n + b_n) \tag{2.3.2}$$

$$C_{abs} = C_{ext} - C_{sca} \tag{2.3.3}$$

Here $k$ is the wave vector defined as $k = \frac{2\pi n_m}{\lambda}$. The coefficients $a_n$ and $b_n$ are calculated according to the following expressions,

$$a_n = \frac{m\psi_n(mx)\psi_n'(x) - \psi_n(x)\psi_n'(mx)}{m\psi_n(mx)\xi_n'(x) - \xi_n(x)\psi_n'(mx)} \tag{2.3.4}$$

$$b_n = \frac{\psi_n(mx)\psi_n'(x) - m\psi_n(x)\psi_n'(mx)}{\psi_n(mx)\xi_n'(x) - m\xi_n(x)\psi_n'(mx)} \tag{2.3.5}$$

$$x = ka = \frac{2\pi n_m a}{\lambda} \tag{2.3.6}$$

$$m = \frac{k_1}{k} = \frac{n}{n_m} \tag{2.3.7}$$

The functions $\psi_n$ and $\xi_n$ are related to the Riccati-Bessel functions through,

$$\psi_n(\rho) = \rho j_n(\rho) \tag{2.3.8}$$

$$\xi_n(\rho) = \rho h_n^{(1)}(\rho) \tag{2.3.9}$$

In practical calculations, the infinite summations in equations (2.3.1) and (2.3.2) are usually truncated to a particular $n$ value, which is dependent on the radius of the sphere. Figure 2.3.1 shows

the scattering, absorption, and extinction cross sections of two different Au nanospheres in water calculated by Mie theory. The smaller sphere with a diameter of 50 nm shows a dipole resonance at 530 nm while the larger one with a diameter of 200 nm exhibits a dipole mode at 780 nm and a quadruple mode at 560 nm.

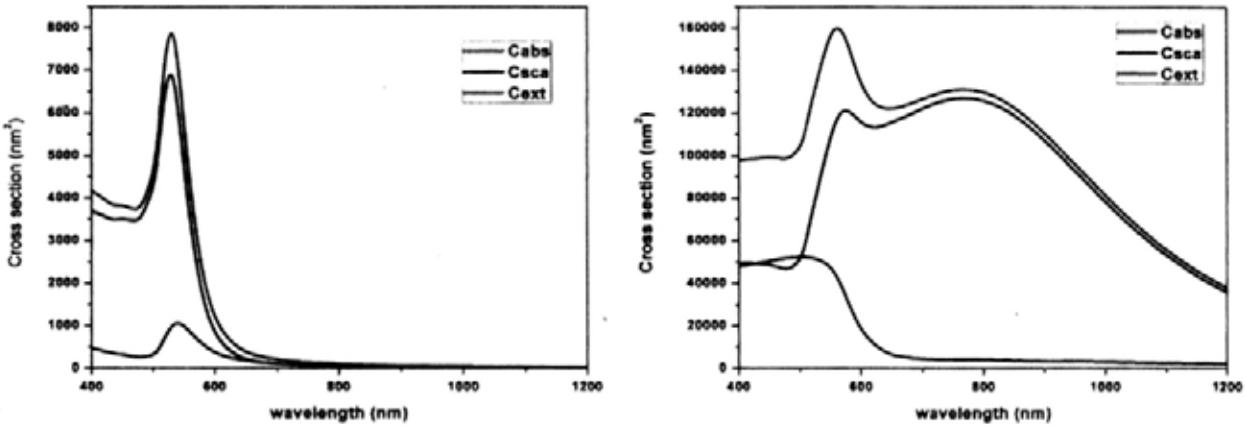


Figure 2.3.1. Calculation of the absorption, scattering, and extinction cross sections by Mie theory for two Au nanospheres with diameters of 50 nm (left) and 200 nm (right). The two spheres are embedded in water.

## 2.4 Quasi-Static Approximation

Mie theory is applicable for spherical nanoparticles. The solutions of equations (2.1.15) and (2.1.16) for non-spherical nanoparticles are very complicated and there have been no analytical solutions without any approximations. Quasi-static approximation is effective for calculating the optical response of particles with sizes much smaller than the wavelength of light. Under this approximation, the electromagnetic field is treated to be the same throughout the entire particle. It is then solely determined by the scalar potential. Equations (2.1.15) and (2.1.16) can therefore be changed into Laplace's equation [7, 15]. The problem now turns into finding the solutions of Laplace's equation under different boundary conditions. The validity of this approximation can be

corroborated by considering Mie theory for particles with small sizes. The expressions of the Mie coefficients shown in equations (2.3.4) and (2.3.5) indicate that they are mainly contributed by the first few terms when the radius of the sphere is much smaller than the incident wavelength ( $x << 1$ ). Figure 2.4.1 shows the magnitudes of the Mie coefficients for a sphere with a radius of 25 nm. We can see that only the first term dominates the summations in equations (2.3.1) to (2.3.3).

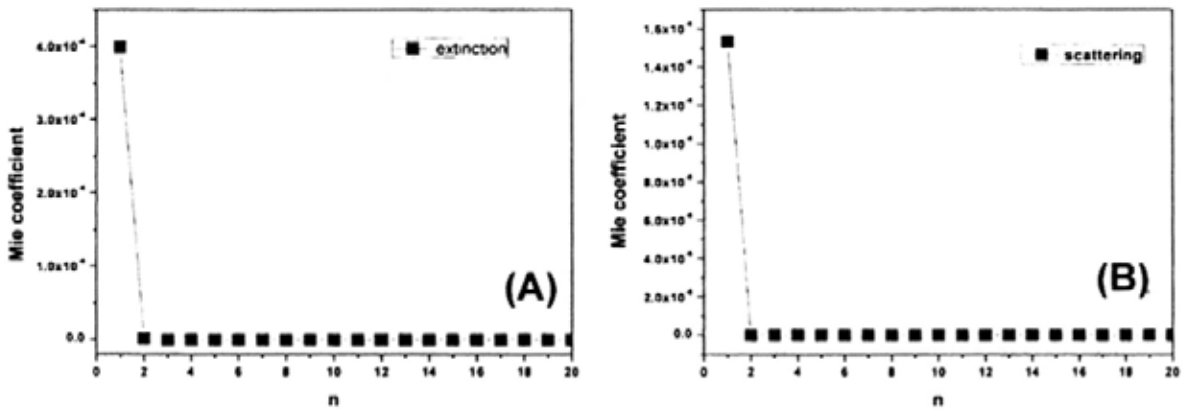


Figure 2.4.1. The Mie coefficients in the summation of (A) the extinction cross section and (B) scattering cross section.

A simple analysis shows that the first term leads to the expressions for the absorption and scattering cross sections of a small sphere with radius $a$ as [7],

$$C_{abs} = \pi a^2 4x \mathrm{Im}\left(\frac{\varepsilon_1 - \varepsilon_m}{\varepsilon_1 + 2\varepsilon_m}\right) \tag{2.4.1}$$

$$C_{sca} = \pi a^2 \frac{8}{3} x^4 \left|\frac{\varepsilon_1 - \varepsilon_m}{\varepsilon_1 + 2\varepsilon_m}\right|^2 \tag{2.4.2}$$

where $\varepsilon_m$ and $\varepsilon_1$ are the dielectric functions of the surrounding environment and the metal sphere. Equations (2.4.1) and (2.4.2) is the same as those obtained for a sphere with a dipole moment of

$4\pi a^3 \varepsilon_m \frac{\varepsilon_1 - \varepsilon_m}{\varepsilon_1 + 2\varepsilon_m}$ under the quasi-static approximation and the condition that the absorption of the sphere is much larger than its scattering. This criterion is often fulfilled in most noble metal nanoparticles with small sizes. Frequently encountered nanoparticles in experiments are non-spherical. Gans considered ellipsoidal nanoparticles under the quasi-static approximation [16]. By solving Laplace's equation in the ellipsoidal coordinate system, the scattering, absorption, and extinction cross sections of the ellipsoid excited along different axes can be obtained as [7, 16],

$$C_{sca,i} = \frac{k^4}{6\pi} |\alpha_i|^4 \tag{2.4.3}$$

$$C_{abs,i} = k \, \mathrm{Im}(\alpha_i) \tag{2.4.4}$$

$$C_{ext,i} = C_{sca,i} + C_{abs,i} \tag{2.4.5}$$

$$\alpha_i = 4\pi abc \frac{\varepsilon_1 - \varepsilon_m}{3\varepsilon_m + 3L_i(\varepsilon_1 - \varepsilon_m)} \tag{2.4.6}$$

The parameter $i$ stands for different axes, the parameter $L_i$ is the depolarization factor, which can be calculated via,

$$L_1 = \frac{abc}{2} \int_0^\infty \frac{dq}{(a^2 + q) f(q)} \tag{2.4.7}$$

$$L_2 = \frac{abc}{2} \int_0^\infty \frac{dq}{(b^2 + q) f(q)} \tag{2.4.8}$$

$$L_3 = 1 - L_1 - L_2 \tag{2.4.9}$$

$$f(q) = \left\{(q + a^2)(q + b^2)(q + c^2)\right\}^{1/2} \tag{2.4.10}$$

Here $a$, $b$, and $c$ are the half lengths of the ellipsoid along the three major axes. Equations (2.4.3)–(2.4.6) have been widely used in the calculations of the plasmonic properties of Au and Ag nanorods and nanodisks, which can approximately be treated as ellipsoids or oblates. The localized

plasmon resonance peaks can be well predicted by Gans theory [17 – 20]. These anisotropic metallic particles usually exhibit two types of resonance modes. One is associated with the excitation along the longitudinal axis and assigned as the longitudinal localized surface plasmon resonance. The other one is associated with the excitation along the transverse axis and assigned as the transverse localized surface plasmon resonance.

As the size of the nanoparticle becomes larger and larger, the contributions from the higher order components, such as the quadruplolar and octupolar ones, cannot be neglected. In this case, the quasi-static approximation breaks down, because it only considers the dipolar response. This point can be seen more clearly in Figure 2.4.2. The extinction cross section of a Au sphere calculated by equation (2.4.1) and (2.4.2) deviates largely from that by Mie theory when the sphere radius is larger than 25 nm. Moreover, in recent years nanocrystals with complex geometries and nanostructures composed of several metal nanocrystals have gained more and more attentions. The accurate description of the plasmonic properties of these nanostructures has to rely on numerical approaches, which will be discussed in the following section.

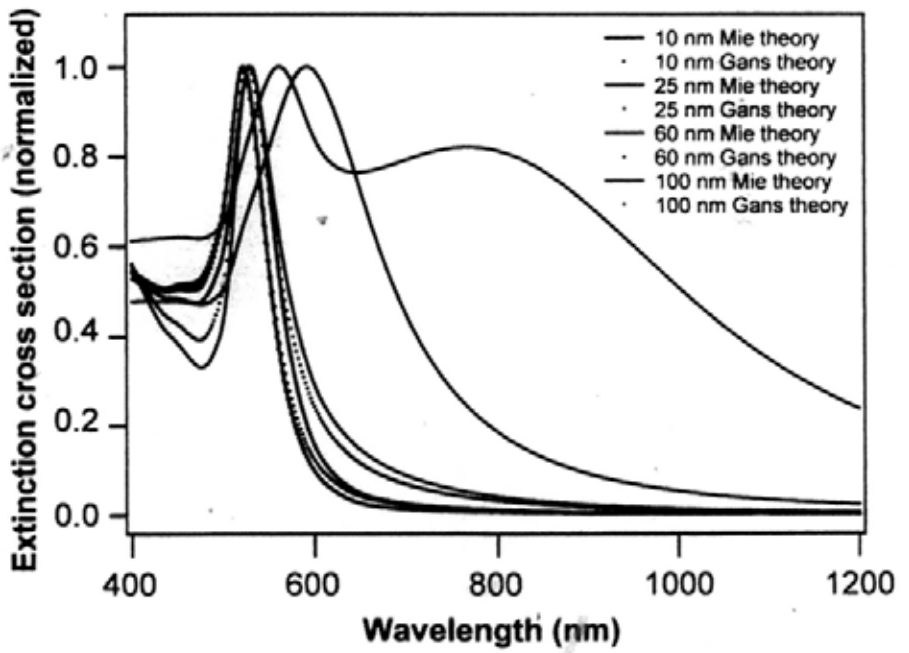

Figure 2.4.2. Comparison of the extinction cross sections of Au nanospheres with different radius calculated by Mie theory (solid lines) and Gans theory (dashed lines).

## 2.5 Numerical Methods for Simulating the Localized Surface Plasmon Resonance Properties of Metal Nanostructures

Mie theory is restricted to spherical particles embedded in a non-absorbing background. However, many nanoparticles encountered in experiments have complex geometries. Moreover, nanoparticles are often assembled together for fabrication of plasmonic devices. Accurate description of their plasmonic properties is therefore very important for their applications. Numerical approaches provide powerful tools for calculating the optical responses of objects with arbitrary shapes and sizes other than the analytical approaches. There are mainly two types of numerical methods for electrodynamic calculations. One is carried out in the frequency domain. The discrete dipole approximation (DDA) and the couple dipole method (CDM) are two typical examples of this type [21, 22]. In these methods, an arbitrarily shaped particle is treated as a three-dimensional assembly of dipoles on a cubic grid located at positions $\mathbf{r}_j$ ($j$ = 1, … , $N$). Each dipole cell is assigned a complex polarizability $\alpha$, which can be computed from the complex dielectric function of the bulk material and the number of dipoles in a unit volume. The electromagnetic scattering problem is then solved on the basis of this array of the point dipoles. Each dipole has a polarization $\mathbf{P}_j=\alpha_j\mathbf{E}_j$, where $\mathbf{E}_j$ is the total electric field at $\mathbf{r}_j$. It consists of the incident wave $\mathbf{E}_{inc,j}$ plus the contribution of the other $N$–1 dipoles,

$$\mathbf{E}_j = \mathbf{E}_{inc,j} - \sum_{k \neq j} A_{jk}\mathbf{P}_k \tag{2.5.1}$$

In equation (2.5.1) $-\mathbf{A}_{jk}\mathbf{P}_k$ is the electric field at $\mathbf{r}_j$ caused by the dipole $\mathbf{P}_k$ at location $\mathbf{r}_k$ and it

includes the retardation effects. Each element $A_{jk}$ is a 3×3 matrix,

$$A_{jk} = \frac{\exp(ikr_{jk})}{r_{jk}} \times \left[ k^2 \left( \hat{r}_{jk} \hat{r}_{jk} - \mathrm{I}_3 \right) + \frac{ikr_{jk} - 1}{r_{jk}^2} \left( 3\hat{r}_{jk} \hat{r}_{jk} - \mathrm{I}_3 \right) \right] \tag{2.5.2}$$

where $k=\omega/c$, $r_{jk}=|\mathbf{r}_j-\mathbf{r}_k|$, $\hat{r}_{jk} = (\mathbf{r}_j - \mathbf{r}_k)/r_{jk}$, and $\mathbf{I}_3$ is the 3×3 identity matrix. The phase retardation has been included in equation (2.5.2). Defining $A_{jj} \equiv \alpha_j^{-1}$ reduces the scattering problem to finding the polarizations $\{\mathbf{P}_j\}$ that satisfy a system of $3N$ complex linear equations,

$$\sum_{k=1}^{N} A_{jk} \mathbf{P}_k = \mathbf{E}_{inc,j} \tag{2.5.3}$$

Once the above equation is solved for the unknown polarizations $\{\mathbf{P}_j\}$, the extinction and absorption cross sections $C_{ext}$ and $C_{abs}$ may be evaluated,

$$\begin{cases} C_{ext} = \dfrac{4\pi k}{|\mathbf{E}_0|^2} \displaystyle\sum_{j=1}^{N} \mathrm{Im}\left( \mathbf{E}_{inc,j}^{*} \cdot \mathbf{P}_j \right) \\ C_{abs} = \dfrac{4\pi k}{|\mathbf{E}_0|^2} \displaystyle\sum_{j=1}^{N} \left\{ \mathrm{Im}\left[ \mathbf{P}_j \cdot \left( \alpha_j^{-1} \right)^{*} \mathbf{P}_j^{*} \right] - \frac{2}{3} k^3 |\mathbf{P}_j|^2 \right\} \\ C_{sca} = C_{ext} - C_{abs} \end{cases} \tag{2.5.4}$$

These methods were first developed by Draine and Flatau. There are some open source codes available for the calculations. The major drawback of these methods is that they rely on the linear algebra. Redundant calculations have to be performed in order to solve equations (2.5.1)–(2.5.4). This will become more pronounce when someone tries to improve the accuracy of the calculations by increasing the numbers of the dipoles consisted of the objects. Even if the calculations are performed on a high-performance computer, they are still limited to fewer than $10^6$ electromagnetic unknowns [6]. There are also some other frequency domain methods such as the T-matrix method [23], finite element method (FEM) [24], boundary element method (BEM) [25, 26]. The detailed introduction of these methods can be found in recent excellent reviews [27, 28].

The other type is performed in both the time domain and the frequency domain and among them the finite-difference time-domain (FDTD) method is the most widely used one [6, 29, 30]. FDTD was first developed by Yee in 1966 [31]. The FDTD calculation is a time-marching method. It is based on Maxwell equations. The key point is to replace all the derivatives in Maxwell's equations with finite discrete grids–the Yee cells. The Yee cell is the basic element of an interlocked grid with the electric field **E** representing an unknown on the edges of one grid and the magnetic field **H** the unknowns on the other grid, corresponding to the faces of the grid. Figure 2.5.1 shows a typical Yee cell, with (i, j, k) representing a specific grid point in the space.

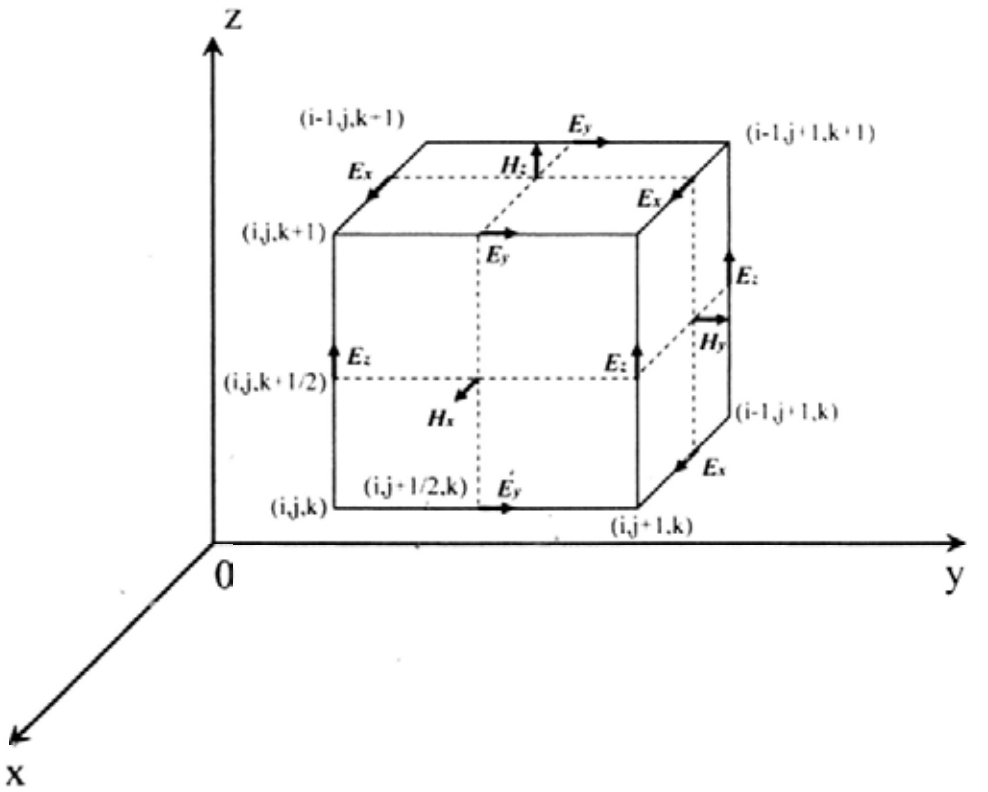


Figure 2.5.1. Schematic showing a Yee cell used in the FDTD calculations.

**E** and **H** are offset in both the space and time, allowing one to use the central differences and

making the algorithm second-order accurate. For example, the one-dimensional discrete form of Maxwell equations can be expressed as,

$$\varepsilon(k)E_x^{n+1}(k) = \varepsilon(k)E_x^n(k) - \frac{\Delta t}{\Delta z}\left[H_y^{n+1/2}\left(k+\frac{1}{2}\right) - H_y^{n+1/2}\left(k-\frac{1}{2}\right)\right] \tag{2.5.5}$$

$$\mu\left(k+\frac{1}{2}\right)H_y^{n+1/2}\left(k+\frac{1}{2}\right) = \mu\left(k+\frac{1}{2}\right)H_y^{n-1/2}\left(k+\frac{1}{2}\right) - \frac{\Delta t}{\Delta z}\left[E_x^n(k+1) - E_x^n(k)\right] \tag{2.5.6}$$

where $k$ is the spatial coordinate and the $n$ superscript denotes time. It is then straightforward to solve the above equations iteratively and get the distribution of **E** and **H** at different time step. The frequency-related properties such as the scattering and absorption cross section can then be obtained through Fourier transform [29, 30, 32]. In order to calculate the optical responses of dispersive objects, we need to transform the dispersion into the time domain. This is usually done by including the electric displacement **D** into the discretized equation, which can be expressed as,

$$\mathbf{D}^{n+1} = \mathbf{D}^n + \Delta t(\nabla \times \mathbf{H})^{n+1/2} \tag{2.5.7}$$

The dispersion of the material is described by a specific model, such as the Drude model or the Lorentz model. Based on Fourier transform, the transformation of the dispersion into the time domain is carried out by using the relation between **E** and **D** and by replacing the complex frequency $-i\omega$ with the calculator $\partial/\partial t$. Equations (2.5.8) and (2.5.9) show this procedure by using the Drude model as an example.

$$\mathbf{D}(\omega) = \varepsilon(\omega)\mathbf{E}(\omega) = \varepsilon_0\left(\varepsilon_\infty - \frac{\omega_p^2}{\omega^2 + i\gamma\omega}\right)\mathbf{E}(\omega) \tag{2.5.8}$$

$$\left(\frac{\partial^2}{\partial t^2} - \gamma\frac{\partial}{\partial t}\right)\mathbf{D} = \varepsilon_0\varepsilon_\infty\left(\frac{\partial^2}{\partial t^2} - \gamma\frac{\partial}{\partial t}\right)\mathbf{E} + \varepsilon_0\omega_p^2\mathbf{E} \tag{2.5.9}$$

The solutions of the Maxwell equations are then obtained by iteratively calculating the **E**, **D**, and **H**

on the basis of the above equations.

On the other hand, practical calculation can not be carried out in an infinite space. FDTD therefore employs a perfectly matched layer (PML) technique to model the propagation of the electromagnetic wave into the infinite. Numerically, the PML technique is to place a boundary around the simulated object. This boundary can totally absorb the electromagnetic energy around the simulated object. Detailed descriptions of the FDTD formalisms can be found in several famous literatures [6, 29 – 31].

The FDTD method provides several advantages: (1) It is fully explicit and uses no linear algebra, which can reduces the computational overhead needed to solve a particular problem. This characteristic enables it to process as many as $10^9$ electromagnetic unknowns [6]. (2) It is based on time-domain, the calculation yields a full spectrum with a single run. (3) The time-marching aspect of this algorithm allows for observing the electromagnetic field distribution at any time of the simulation. (4) The discretizing-based algorithm can be easily parallelized among different computers to enable the calculation of large and complex objects. However, some of these virtues are also the drawbacks of the FDTD method. In the time-marching procedure the response of the materials at a given time depends on the field at all of the former time steps. This requires very large memories for the calculations. Furthermore, FDTD requires calculating the electromagnetic field not only inside the object but also in the entire space outside the object. Therefore, a substantial amount of calculations have to be incorporated. In addition, the accuracy of the calculations is determined by the size of the grid and the time step. The use of a smaller grid size and time step can improve the calculation results, but will consume much more calculation time and memories.

Nowadays there are several excellent commercial packages for electrodynamic numerical calculations based on the above mentioned algorithms [32 – 38]. These well-developed softwares

have not only improved the understanding of the plasmonic properties of noble metal nanostructures but also facilitated the designing of the novel photonic devices.

## References

[1] P. Drude. Zur Elektronentheorie Der Metalle. *Annalen der Physik*, 306: 566, 1900.

[2] C. Kittel, Introduction to Solid State Physics. 8th ed. Hoboken, NJ: Wiley, c2005.

[3] N. W. Ashcroft, N. D. Mermin, Solid State Physics. New York: Holt, Rinehart and Winston, 1976.

[4] S. A. Maier, Plasmonics: Fundamentals and Applications. Springer Science+Business Media LLC, 2007.

[5] P. B. Johnson, R. W. Christy, Optical Constants of the Noble Metals. *Phys. Rev. B*, 6: 4370, 1972.

[6] C. Oubre, P. Nordlander, Optical Properties of Metallodielectric Nanostructures Calculated Using the Finite Difference Time Domain Method. *J. Phys. Chem. B*, 108: 17740, 2004.

[7] C. Bohren, D. Huffman, Absorption and Scattering of Light by Small Particles. New York: Wiley, 1983.

[8] A. Vial, A.-S. Grimault, D. Macías, D. Barchiesi, M. L. de la Chapelle, Improved Analytical Fit of Gold Dispersion: Application to the Modeling of Extinction Spectra with a Finite-Difference Time-Domain method. *Phys. Rev. B*, 71: 085416, 2005.

[9] F. Hao, P. Nordlander, Efficient Dielectric Function for FDTD Simulation of the Optical Properties of Silver and Gold Nanoparticles. *Chem. Phys. Lett.*, 446: 115, 2007.

[10] T. Laroche, C. Girard, Near-Field Optical Properties of Single Plasmonic Nanowires. *Appl. Phys. Lett.*, 89: 233119, 2006.

[11] M. Moskovits, I. Srnová-Šloufová, B. Vlčková, Bimetallic Ag–Au Nanoparticles: Extracting Meaningful Optical Constants from the Surface-Plasmon Extinction Spectrum. *J. Chem. Phys.*, 116: 10435, 2002.

[12] J. Euler, Infrared Properties of Metals and the Mean Free Paths of Conduction Electrons, *Z.*

*Physik.*, 137: 318, 1954.

[13] U. Kreibig, Electronic Properties of Small Silver Particles: the Optical Constants and Their Temperature Dependence. *J. Phys. F: Metal Phys*, 4: 999, 1974.

[14] G. Mie. Beitäge Zur Optik Trüber Medien, Speziel Kolloidaler Metallösungen–Contribution to the Optics of Suspended Media, Specifically Colloidal Metal Suspensions. *Ann. Phys.*, 25: 377, 1908.

[15] U. Kreibig, M. Vollmer, Optical Properties of Metal Clusters. Berlin: Springer-verlag; New York: Springer-Verlag, c1995.

[16] R. Gans, Über Die form Ultramikroskopischer Teilchen. *Ann. Phys.*, 37: 881, 1912.

[17] S. Link, M. B. Mohamed, M. A. El-Sayed, Simulation of the Optical Absorption Spectra of Gold Nanorods as a Function of Their Aspect Ratio and the Effect of the Medium Dielectric Constant. *J. Phys. Chem. B*, 103: 3073, 1999.

[18] K.-S. Lee, M. A. El-Sayed, Gold and Silver Nanoparticles in Sensing and Imaging: Sensitivity of Plasmon Response to Size, Shape, and Metal Composition. *J. Phys. Chem. B*, 110: 19220, 2006.

[19] C. L. Nehl, J. H. Hafner, Shape-Dependent Plasmon Resonances of Gold Nanoparticles, *J. Mater. Chem.*, 18: 2415, 2008.

[20] W. H. Ni, X. S. Kou, Z. Yang, J. F. Wang, Tailoring Longitudinal Surface Plasmon Wavelengths, Scattering and Absorption Cross Sections of Gold Nanorods, *ACS Nano*, 2: 677, 2008.

[21] V. A. Markel, Coupled-Dipole Approach to Scattering of Light from a One-Dimensional Periodic Dipole Structure. *J. Mod. Opt.*, 40: 2281, 1993.

[22] B. T. Draine, P. J. Flatau, Discrete-Dipole Approximation for Scattering Calculations, *J. Opt. Soc. Am. A*, 11: 1491, 1994.

[23] P. C. Waterman, Matrix Formulation of Electromagnetic Scattering. *Proc. IEEE* 53: 803, 1965.

[24] S. Gilbert, F. George, An Analysis of The Finite Element Method. Prentice Hall. 1973.

[25] F. J. García de Abajo, A. Howie, Relativistic Electron Energy Loss and Electron-Induced Photon Emission in Inhomogeneous Dielectrics. *Phys. Rev. Lett.*, 80: 5180, 1998.

[26] F. J. García de Abajo, A. Howie, Retarded Field Calculation of Electron Energy Loss in Inhomogeneous Dielectrics. *Phys. Rev. B*, 65: 115418, 2002.

[27] T. Wriedt, A Review of Elastic Light Scattering Theories. *Part. Part. Syst. Charact.*, 15: 67, 1998.

[28] M. A. Yurkin, A. G. Hoekstra, The Discrete Dipole Approximation: An Overview and Recent Developments. *J. Quant. Spectrosc. Radiat. Transfer*, 106: 558, 2007.

[29] A. Taflove, Computational Electrodynamics: the Finite Difference Time-Domain Method. Artech House, Boston 1995.

[30] D. M. Sullivan. Electromagnetic Simulation Using the FDTD Method. IEEE Press, Piscataway, NJ, 2000.

[31] K. Yee: Numerical Solution of Initial Boundary Value Problems Involving Maxwell's Equations in Isostropic Media. *IEEE Trans. Antennas Propag.*, AP-14: 302, 1966.

[32] FDTD Solutions Reference Guide, Release 6.10. Lumerical Solutions, Inc, Canada, 2007.

[33] OptiFDTD Software, Optiwave, Inc., Ottawa, Canada.

[34] FDTD Solutions Software, Lumerical, Inc.,Vancouver, Canada.

[35] FDTD Solutions™, Breault Research Organization, Tucson, AZ, USA.

[36] EZ-FDTD+ Software, Electromagnetic Simulation Company, Four Oaks, NC, USA.

[37] B. T. Draine, P. J. Flatau, DDSCAT 6.1.

[38] COMSOL Multiphysics, COMSOL Group, Stockholm, Sweden.

# Chapter 3

# Preparation of Gold Nanocrystals and Characterization Methods

Au nanocrystals are used in my research. They are synthesized by the Ag ion-assisted seed-mediated method in the presence of stabilizing surfactants. A detailed introduction of this method will first be given in §3.1. The localized plasmon wavelengths (LPWs) of the as-grown nanocrystals are usually limited. We have developed two methods for synthetically tuning the LPWs of the Au nanocrystals. They are anisotropic oxidation and transverse overgrowth, which will be discussed in §3.2. In §3.3, I will present the experimental methods employed for the characterization of the plasmonic properties of Au nanostructures. The setups include the UV–visible–NIR spectrophotometry used for the extinction measurements of colloidal Au nanocrystals and single-particle scattering imaging and spectroscopy implemented for the studying of individual Au nanostructures on substrates.

## 3.1 Seed-Mediated Growth of Gold Nanocrystals

The growth of Au nanocrystals is based on the seed-mediated growth approach that was developed by El-Sayed and Murphy [1, 2]. Typically, a Au (III) complex ion ($HAuCl_4$) is initially reduced by a strong reducing agent of sodium borohydride ($NaBH_4$) to form Au seeds in water with the presence of the stabilizing agent cetyltrimethylammonium bromide (CTAB) or sodium citrate

(TSC). The seeds have been found to be crucial in the growth. The growth with single-crystalline Au nanocrystal seeds that are stabilized by CTAB gives single-crystalline Au nanorods and nanocubes, while the growth with multiply-twinned nanocrystal seeds that are stabilized with citrate yields nanospheres, nanobranches, and nanobipyramids [3, 4]. The seeds grow into nanocrystals in the presence of more metal salts, micelle-forming cationic surfactants, and additional but milder reducing agents of ascorbic acid (AA). Moreover, $AgNO_3$ is added during some growth processes in order to improve the yields of the Au nanocrystals [1, 2, 5 – 7]. Several typical Au nanocrystals of different sizes and shapes are given here as examples, including nanospheres, nanocubes, nanobranches, nanorods with two different longitudinal LPWs (LLPWs: 800 nm and 950 nm), and nanobipyramids.

For the growth of the Au nanospheres, the seed solution was prepared by the addition of an aqueous $HAuCl_4$ solution (0.25 mL, 0.01 M) and TSC (0.25 mL, 0.01 M) into deionized (DI) water (9.5 mL). After the solution was mixed by inversion, a freshly prepared, ice-cold aqueous $NaBH_4$ solution (0.3 mL, 0.1 M) was added and followed by rapid inversion-mixing for 2 min. The resulting TSC-stabilized Au nanocrystal seed solution was kept at room temperature and used 2–5 h after preparation. The seed-mediated growth was divided into two steps. First, $HAuCl_4$ (0.225 mL, 0.01 M) and DI water (1.575 mL) were added into CTAB (7.2 mL, 0.1 M) in a plastic tube, followed by gentle inversion-mixing. A freshly prepared AA solution (0.05 mL, 0.1 M) was then added, followed by the addition of 1.0 mL seed solution. The resulting solution was stirred for 30 min. In the next step, $HAuCl_4$ (0.225 mL, 0.01 M), DI water (1.575 mL), and CTAB (7.2 mL, 0.1 M) were mixed together and then added with 0.05 mL AA solution (0.1 M). 1 mL of the as-prepared solution in the first step was subsequently added and the resulting solution was kept at room temperature for 8 h. The obtained nanosphere sample has a mean diameter of (15 ± 1) nm and exhibits a LPW at 527 nm

in water. Figure 3.1.1A shows the transmission electron microscopy (TEM) image of a nanosphere sample. Its extinction spectrum is shown by the black line in Figure 3.1.1G.

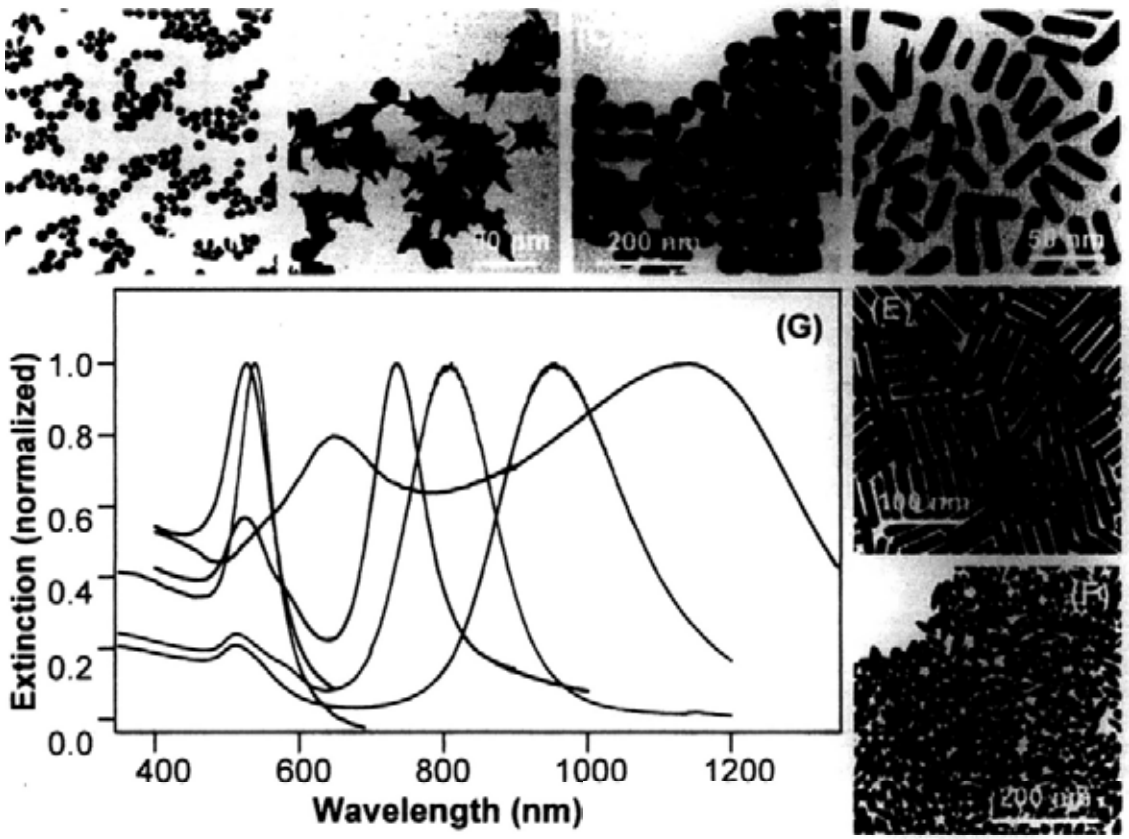


Figure 3.1.1. TEM images and extinction spectra of the different Au nanocrystals. (A) Au nanospheres. (B) Au nanobranches. (C) Au nanocubes. (D) Au nanorods with LLPW of 810 nm. (E) Au nanorods with LLPW of 957 nm. (F) Au nanobipyramids. (G) Extinction spectra of the nanospheres (black line), nanocubes (green line), nanobranches (red line), nanorods with LLPW of 810 nm (blue line), nanorods with LLPW of 957 nm (brown line), and nanobipyramids (pink line).

The Au nanobranches were grown with citrate-stabilized seeds. For the preparation of the seeds, aqueous solutions of $HAuCl_4$ (0.125 mL, 0.01 M) and TSC (0.25 mL, 0.01 M) were added into water (9.625 mL), and then a freshly prepared, ice-cold aqueous $NaBH_4$ solution (0.15 mL, 0.01 M)

was added under vigorous stirring. The resulting seed solution was kept at room temperature for at least 2 h before use. The growth solution of the Au nanobranches was prepared by the sequential addition of $HAuCl_4$ (1.8 mL, 0.01 M), $AgNO_3$ (0.27 mL, 0.01 M), and AA (0.3 mL, 0.1 M) into an aqueous tetradecyltrimethylammonium bromide (TTAB) solution (42.75 mL, 0.1 M). The seed solution (40 μL) was then added. The entire reaction solution was mixed by gentle inversion for 10 s and then left undisturbed overnight. The obtained Au nanobranch sample exhibits a LLPW at 1140 nm (Figure 3.1.1B and the red line in Figure 3.1.1G). The average length of the tips on the nanobranches is (80 ± 14) nm.

For the growth of the Au nanocubes and nanorods with LLPW at 850 nm, the seeds were prepared by the addition of a freshly prepared, ice-cold aqueous $NaBH_4$ solution (0.3 mL, 0.01 M) into an aqueous mixture solution composed of $HAuCl_4$ (0.125 mL, 0.01 M) and CTAB (3.75 mL, 0.1 M), followed by rapid inversion-mixing for 2 min. The resulting seed solution was kept at room temperature for 1 h (for the growth of the nanocubes) or 2 h (for the growth of the nanorods) before use.

The Au nanocubes were grown following a procedure modified from that reported by Sau and Murphy [8]. The growth solution was prepared by the sequential addition of CTAB (6.4 mL, 0.1 M), $HAuCl_4$ (0.8 mL, 0.01 M), and AA (3.8 mL, 0.1 M) into water (32 mL). 20 μL of the CTAB-stabilized seed solution diluted 10 times with water was then added into the growth solution. The resulting solution was mixed by gentle inversion for 10 s and then left undisturbed overnight. The average edge length of the Au nanocubes is (57 ± 2) nm. The nanocube sample exhibits a LPW at 546 nm, as shown in Figure 3.1.1C and by the green line in Figure 3.1.1G.

The growth of the Au nanorods with an ensemble LLPW of 810 nm followed essentially the similar procedure. The growth solution was made by the sequential addition of $HAuCl_4$ (1.8 mL,

0.01 M), $AgNO_3$ (0.27 mL, 0.01 M), and AA (0.288 mL, 0.1 M) into CTAB (42.75 mL, 0.1 M). Then 250 μL of the seed solution was added and the whole solution was left undisturbed overnight. The obtained nanorod sample has a mean diameter and length of (10 ± 2) nm and (38 ± 5) nm, respectively (Figure 3.1.1D and the blue line in Figure 3.1.1G).

For the growth of the Au nanorods with an ensemble LLPW at 957 nm, the seed solution was prepared by the addition of $NaBH_4$ (0.6 mL, 0.01 M) into a mixture composed of $HAuCl_4$ (0.25 mL, 0.01 M) and CTAB (9.75 mL, 0.1 M). The seed solution was kept at room temperature for 2 h before use. The growth solution was made by the sequential addition of $HAuCl_4$ (2 mL, 0.01 M), $AgNO_3$ (0.6 mL, 0.01 M), HCl (0.8 mL, 1.0 M), and AA (0.32 mL, 0.1 M) into CTAB (40 mL, 0.1 M). After the resultant solution was mixed by swirling for 30 s, 0.3 mL of the seed solution was added. The reaction solution was gently inversion-mixed for 2 min and then left undisturbed overnight. The obtained nanorods have a mean diameter and length of (12 ± 1) nm and (64 ± 6) nm, respectively (Figure 3.1.1E). The brown line in Figure 3.1.1G shows their ensemble extinction spectrum in water.

The Au nanobipyramids were grown using citrate-stabilized seeds [9]. For the preparation of the seeds, aqueous solutions of $HAuCl_4$ (0.125 mL, 0.01 M) and TSC (0.25 mL, 0.01 M) were first added into DI water (9.625 mL), and then a freshly prepared, ice-cold solution of $NaBH_4$ (0.15 mL, 0.01 M) was added under vigorous stirring. The resulting seed solution was kept at room temperature for 2 h before use. The growth solution was made by the sequential addition of $HAuCl_4$ (1.2 mL, 0.01 M), AA (0.402 mL, 0.1 M), and $AgNO_3$ (0.06 mL, 0.01 M) into cetyltributylammonium bromide (CTBAB) (28.5 mL, 0.01 M). Then 0.45 mL of the seed solution was added into the growth solution, followed by gentle inversion-mixing for 10 s. The resulting solution was left undisturbed overnight in an isothermal oven at 65 °C. The obtained Au nanobipyramid sample has a LLPW of 729 nm. Their diameters and lengths are averaged at (19 ± 1)

nm and (55 ± 5) nm, respectively (Figure 3.1.1F and the pink line in Figure 3.1.1G).

## 3.2 Anisotropic Oxidation and Transverse Overgrowth

The localized plasmon wavelengths of the Au nanorods and nanobipyramids can only be roughly controlled with the seed-mediated approach. In addition, they vary from batch to batch owing to the inherent experimental fluctuations. Two methods have thus been developed for synthetically tailoring the plasmon wavelengths continuously from the near-infrared into visible spectral range. One is the anisotropic shortening, where $O_2$ or $H_2O_2$ are employed to oxidize the Au nanocrystals. During the oxidation, the nanocrystal length is gradually reduced while the diameter remains unchanged and therefore the LLPWs of the nanocrystals blue-shift (Figure 3.2.1) [9 – 11]. The oxidation of a typical Au nanorod sample with LLPW at 810 nm is given here as an example. The oxidation is initiated by adding $H_2O_2$. Specifically, 100 μL HCl (1 M) was firstly added into 10 mL Au nanorods solution to adjust the pH to ~3. 100 μL of $H_2O_2$ (35 wt %) was then added into the starting Au nanorod solution (The volume ratio of $H_2O_2$ to the starting nanorod solution was kept at 1:100). The following reaction would take place as the oxidant was added, leading to the shortening of the nanorods.

$$2Au + 8Br^- + 3H_2O_2 + 6H^+ \rightarrow 2[AuBr_4]^- + 6H_2O \qquad (3.2.1)$$

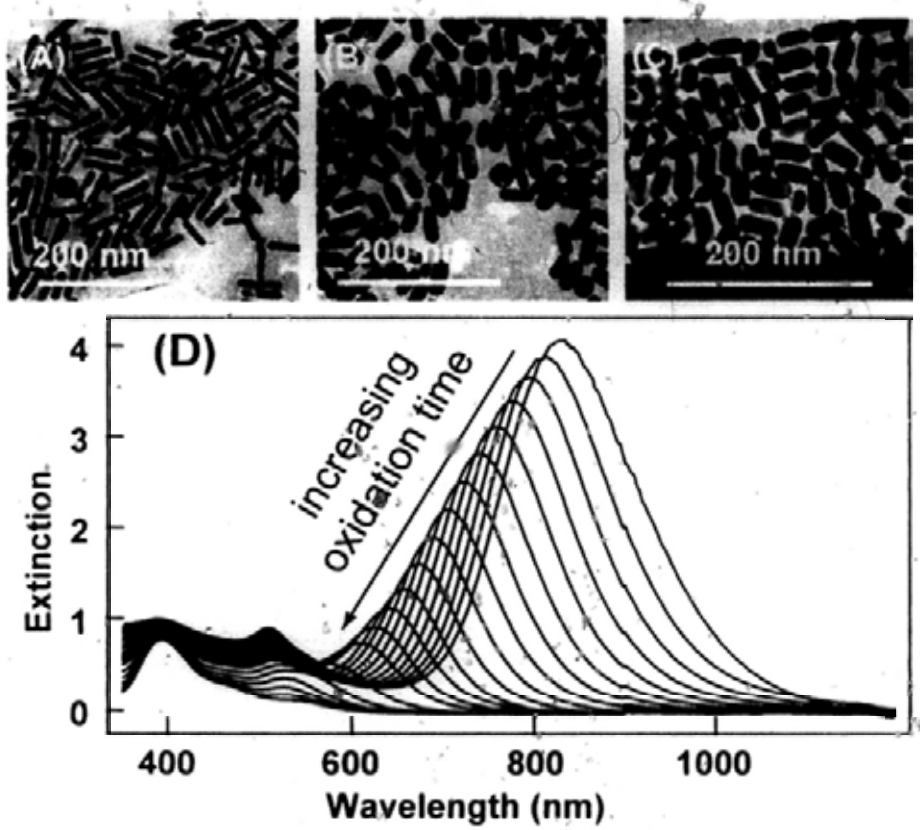


Figure 3.2.1. Anisotropic oxidation process. (A) – (C) TEM images of the Au nanorods obtained from the oxidation process. (D) Evolvement of the extinction spectra of the nanorod sample during the oxidation.

The oxidation process was monitored by taking extinction spectra (which will be discussed in the following section) as a function of time. Figure 3.2.1 shows the evolvement of the plasmon peak during the oxidation, which blue-shifts gradually from 810 nm to 500 nm and disappears finally. The Au nanorods with desired LLPWs can be obtained at intermediate stages of the oxidation by centrifugation and redispersion of the resulting precipitates into water. The oxidation can also be initiated by bubbling $O_2$ as the oxidant, which initiates the following reaction,

$$4Au + 8Br^- + O_2 + 4H^+ \rightarrow 4[AuBr_2]^- + 2H_2O \qquad (3.2.2)$$

The other tuning method is transverse overgrowth, where small thiol molecules are selectively bonded to the nanocrystal ends to block the longitudinal growth [10, 12]. During the overgrowth, as more Au precursor is supplied, the nanocrystals grow fatter while their lengths remain nearly unchanged. As a result, the aspect ratios of the nanocrystals become smaller and the LLPWs become shorter. Figure 3.2.2 shows the overgrowth of a specific nanorod sample with a starting LLPW at 810 nm. A stock solution for the overgrowth was firstly made by mixing together CTAB (42.75 mL, 0.1 M), $HAuCl_4$ (1.8 mL, 0.01 M), $AgNO_3$ (0.27 mL, 0.01 M), and AA (0.288 mL, 0.1 M). Before overgrowth, the pH of the starting nanorod solution was adjusted to ~3 by HCl (1.0 M) and then a glutathione solution (GSH) (150 μL, 0.01 M) was added into 15 mL of the starting solution. After the resulting mixture was kept at room temperature for 2 h, 25 mL of the stock solution was added to initiate the overgrowth. Extinction spectra were taken consecutively to monitor the overgrowth process. When the desired longitudinal plasmon wavelength was reached, the produced nanorods were washed by centrifugation and redispersion in 0.1 M CTAB solution.

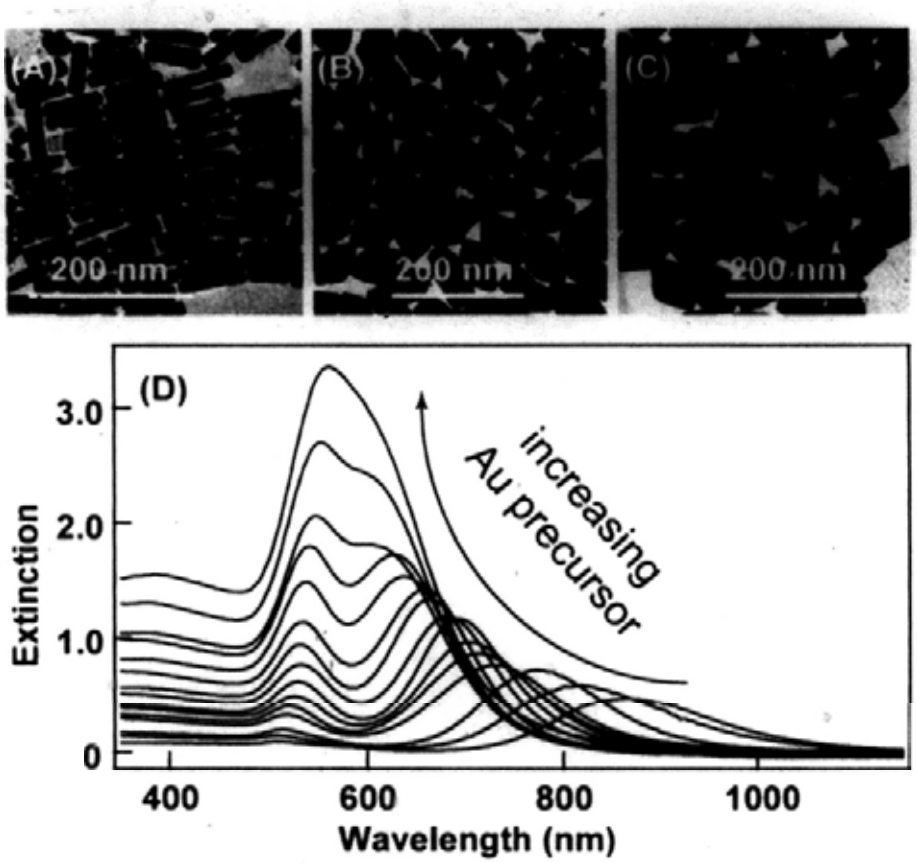


Figure 3.2.2. Transverse overgrowth process of a Au nanorod sample. (A) – (C) TEM images of the Au nanorods obtained from the overgrowth process. (D) Evolvement of the extinction spectra during the overgrowth.

## 3.3 Experimental Setups

Two methods were employed in my research to measure the plasmonic properties of different Au nanostructures. One is transmission spectrometry, which measures extinction—the sum of absorption and scattering. This method is simple and inexpensive. It is suitable for ensemble metal nanocrystals dispersed in solutions or deposited on planar substrates. The other one is single-particle dark-field imaging and spectrometry, which measures scattering only. Single-particle measurements can remove the average effect in the ensemble measurement and enable higher spatial resolution.

## UV–Visible–NIR Extinction Spectroscopy

Excitation of the localized surface plasmon resonance of Au nanocrystals leads to large light absorption and scattering around the resonance peaks. The resulting transmission light thus shows a large reduction in the light intensity. Measuring the extinction spectra of the nanocrystal sample can reveal its plasmonic information such as the plasmon resonance wavelength and the plasmon peak width. The basic idea of the extinction spectroscopy is as follows. Suppose a nanostructure ensemble is placed in a light beam. The power of the transmitted light can be measured by a detector placed just behind the nanostructure ensemble. The detector also records the power of the light directly from the light source (the incident light) in the absence of the nanostructure ensembles through a reference light path. The presence of the nanostructure ensemble can lead to the scattering and absorption of the light, which results in the attenuation of the transmitted light. The ratio of the transmitted power $I$ to the incident power $I_0$ is denoted as the transmissivity $T$. The extinction of the nanostructure ensemble $N\sigma_{ext}$ can therefore be determined by the measurement of the transmissivity $T$,

$$T = \frac{I}{I_0} = \exp(-N\sigma_{ext}l) \tag{3.3.1}$$

where $N$ is the number of the nanostructures per volume, $\sigma_{ext}$ is the extinction cross section of a single nanostructure, and $l$ is the interaction length. Measuring the transmissivity $T$ at different wavelengths will generate the extinction spectrum of the nanostructure ensemble. Equation (3.3.1) can be rewritten in the form of the optical density ($O.D.$) as:

$$O.D. = -\log_{10}\left(\frac{I}{I_0}\right) = \frac{N\sigma_{ext}l}{\log_e(10)} \tag{3.3.2}$$

The extinction measurement in my thesis was performed on a Hitachi U-3501 UV–visible–NIR spectrophotometer.

## Single-Particle Scattering Imaging and Spectroscopy

There are two disadvantages in the ensemble extinction measurements: (1) Inhomogeneous size and shape distributions of the ensemble samples will lead to additional broadening of the plasmon peak width, preventing an accurate measurement of the plasmon resonance peak and detailed study of different plasmonic damping mechanisms in metallic nanostructures. (2) The ensemble measurement will average out many plasmonic properties. For example, the random orientations in the ensemble hinder a detailed study of the polarization dependent properties of elongated Au nanostructures. These drawbacks can be overcome by performing single-particle measurements.

Single-particle detection approaches are usually employed when particles need to be investigated separately. The detection of the scattering/emitting light from individual particles is possible due to white light sources such as halogen lamps combined with highly sensitive detectors such as charge-coupled devices (CCDs) and photomultiplier tubes (PMTs). By using the technique of dark-field microscopy (Figure 3.3.1), the scattered light from individual sub-wavelength particles can be imaged in diffraction-limited patterns, and spectrally analyzed if the background is sufficiently suppressed. The suppression efficiency of the background directly determines the quality of the image and the signal-to-noise ratio of the spectrum. Several approaches can be applied to efficiently suppress the background, including the total internal reflection using prisms and fibers, reflection dark-field using specially designed dark-field objectives, and transmission dark-field using dark-field condensers. The reflection dark-field technique with dark-field objectives is very convenient in comparison with the other methods. A schematic of this kind of dark-field microscopy is illustrated in Figure 3.3.1A, where the parallel light from a light source is reflected from the side to the center of the field of view by a ring-shaped mirror (circular mirror) at the end of the objective. Part of the excitation light is reflected at the sample surface. The other part transmits through or is

absorbed by the sample. The scattered light by the investigated object is then collected by the same objective and then directed to the detector. The reflected light at a larger angle is blocked from the optical detection system due to the limited numerical aperture (NA) of the objective. Typical NAs of dark-field objectives are 0.5–0.8. This type of microscopes is used primarily to inspect non-transparent surfaces of minerals and structured semiconductors. Besides the ability to inspect non-transparent substrates, another advantage is that it does not require any immersion oil on or below the sample.

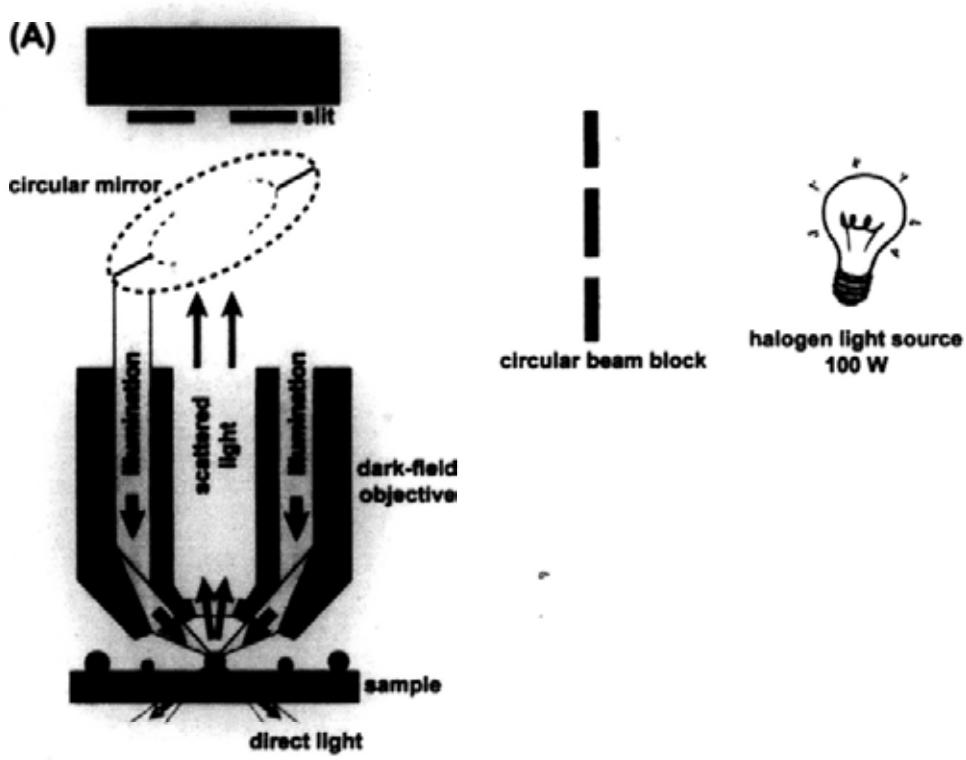


Figure 3.3.1. (A) Scheme of the dark-field technique used in studying the localized surface plasmon resonances of Au nanostructures. (B) Photographs of our dark-field optical system.

Our single-particle scattering imaging and spectroscopy system (Figure 3.3.1B) is built on an Olympus BX60 optical microscope that is integrated with an Acton SpectraPro 2300i spectrometer and a Princeton Instruments Pixis 512B CCD [13]. The CCD can be thermoelectrically cooled to −70 °C. A silver mirror is placed on the upper outlet of the microscope to reflect the light from the microscope to the entrance slit of the spectrometer. A chromatic aberration-corrected lens is placed between the entrance slit and the silver mirror to amplify the image from the microscope by 4 fold and exactly project it to the focus plane at the entrance slit of the spectrometer. Controlled by the software (WinSpec32), the spectrometer can be operated in the imaging mode using a mirror on the terret to identify and select particles of interest. The spectrometer replaces the mirror with a grating when the system is switched to the spectroscopy mode. The light from the images of each particle at

the entrance slit is then horizontally dispersed onto the CCD. The scattering spectra of different particles aligned vertically along the entrance slit can be recorded simultaneously. They are vertically stacked in the recorded spectral image according to the vertical positions of the particles in the slit, as shown in Figure 3.3.2.

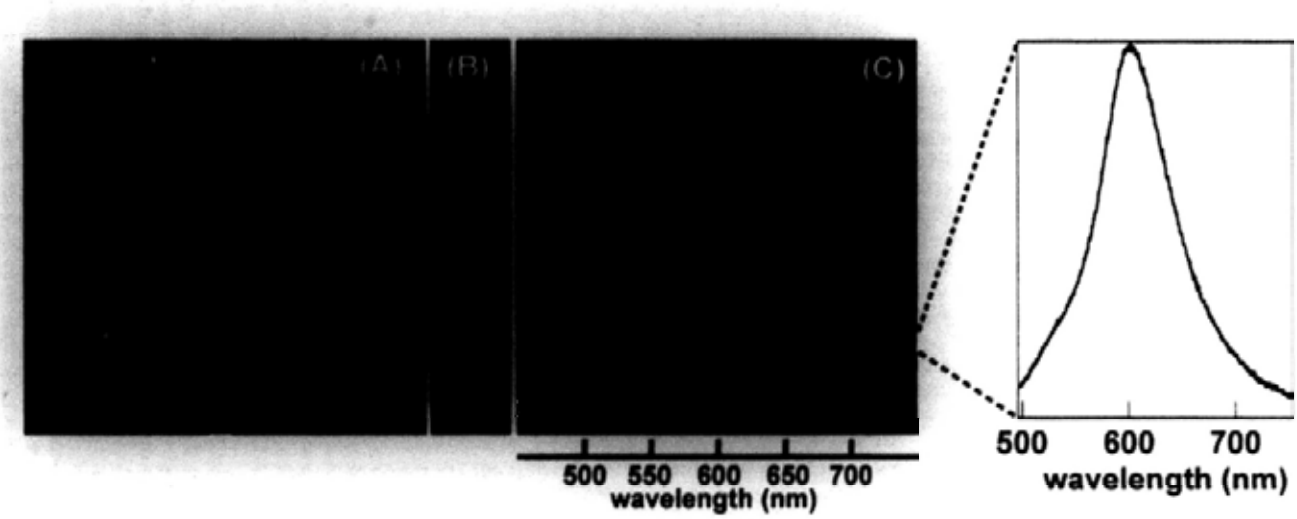


Figure 3.3.2. Recording of single-particle scattering images and spectra. (A) A typical single-particle scattering image. The image is recorded on Au nanorods excited by the white light from the halogen bulb shown in Figure 3.3.1A. The bright spots in the image represent the scattering light from individual Au nanorods. The white rectangle represents the entrance slit. (B) The particles in the entrance slit. The scattered light from the particles out of the slit is blocked. (C) The spectral image of the particles in (B). The spectral images are vertically stacked according to the vertical positions of the particles in the slit. The integrated spectrum of one particular particle is shown on the right.

The region of interest (ROI) can be chosen on the recording image in the software (the white rectangular region in Figure 3.3.2C) to integrate the vertical stacks and then generate the scattering spectrum of the particle. The background spectra are taken from the adjacent regions containing no

particles. The scattering spectra from individual particles are thereafter corrected by subtracting the background spectra and divided by a white-light scattering spectrum from the halogen lamp (Figure 3.3.2C, right).

## References

[1] B. Nikoobakht, M. A. El-Sayed, Preparation and Growth Mechanism of Gold Nanorods (NRs) Using Seed-Mediated Growth Method. *Chem. Mater.*, 15: 1957, 2003.

[2] T. K. Sau, C. J. Murphy, Seeded High Yield Synthesis of Short Au Nanorods in Aqueous Solution. *Langmuir*, 20: 6414, 2004.

[3] M. Z. Liu, P. Guyot-Sionnest, Mechanism of Silver(I)-Assisted Growth of Gold Nanorods and Bipyramids. *J. Phys. Chem. B*, 109: 22192, 2005.

[4] X. S. Kou, S. Z. Zhang, C.-K. Tsung, M. H. Yeung, Q. H. Shi, G. D. Stucky, L. D. Sun, J. F. Wang, Growth of Gold Nanorods and Bipyramids Using CTEAB Surfactant. *J. Phys. Chem. B*, 110: 16377, 2006.

[5] L. F. Gou, C. J. Murphy, Fine-Tuning the Shape of Gold Nanorods. *Chem. Mater.*, 17: 3668, 2005.

[6] N. R. Jana. Gram-Scale Synthesis of Soluble, Near-Monodisperse Gold Nanorods and Other Anisotropic Nanoparticles. *Small*, 1: 875, 2005.

[7] X. C. Jiang, A. Brioude, M. P. Pileni, Gold Nanorods: Limitations on Their Synthesis and Optical Properties. *Colloids Surf. A*, 277: 201, 2006.

[8] T. K. Sau, C. J. Murphy, Room Temperature, High-Yield Synthesis of Multiple Shapes of Gold Nanoparticles in Aqueous Solution. *J. Am. Chem. Soc.*, 126: 8648, 2004.

[9] X. S. Kou, W. H. Ni, C.-K. Tsung, K. Chan, H.-Q. Lin, G. D. Stucky, J. F. Wang, Growth of Gold Bipyramids with Improved Yield and Their Curvature-Directed Oxidation. *Small*, 3: 2103, 2007.

[10] W. H. Ni, X. S. Kou, Z. Yang, J. F. Wang, Tailoring Longitudinal Surface Plasmon Wavelengths, Scattering and Absorption Cross Sections of Gold Nanorods. *ACS Nano*, 2: 677, 2008.

[11] C.-K. Tsung, X. S. Kou, Q. H. Shi, J. P. Zhang, M. H. Yeung, J. F. Wang, G. D. Stucky, Selective Shortening of Single-Crystalline Gold Nanorods by Mild Oxidation. *J. Am. Chem. Soc.*, 128: 5352, 2006.

[12] X. S. Kou, S. Z. Zhang, Z. Yang, C.-K. Tsung, G. D. Stucky, L. D. Sun, J. F. Wang, C. H. Yan, Glutathione- and Cysteine-Induced Transverse Overgrowth on Gold Nanorods. *J. Am. Chem. Soc.*, 129: 6402, 2007.

[13] W. H. Ni, Plasmonic Spectroscopy of Metallic Nanostructures. Ph. D Thesis, Department of Physics, The Chinese University of Hong Kong, 2008.

# Chapter 4

# Refractive Index Sensitivity of Gold Nanocrystals

Environmental protection and cleaning and clinical diagnosis currently place a rapidly increasing demand for low-cost, easy-operation, and ultrasensitive sensors. The refractive index localized plasmonic sensors are considered as very promising candidates and expected to make important contributions in these areas. The physical basis of this type of sensors is the strong dependence of the plasmon resonance of metal nanocrystals on the changes of the surrounding dielectric environment. Specifically, the adsorption of analytes such as organic molecules or metal ions will simply increase the refractive index of the nanoenvironment surrounding metal nanocrystals, leading to an increased screening of the Coulombic restoring force that acts on the free electrons in the metal nanocrystals. The reduced restoring force therefore results in a redshift in the localized plasmon resonance. This type of plasmonic sensors has recently received much attention and been demonstrated in a number of experiments. For example, the plasmon shift response to self-assembled alkanethiol monolayers is found to be linear with a slope of 5.2 and 3 nm per carbon atom for Au nanorings and Ag nanoparticle arrays, respectively [1, 2]. Such high sensitivities have allowed for the fabrication of optical biosensors for the detection of proteins [3, 4], antibodies [5], and the biomarker for Alzheimer's disease [6, 7]. Therefore to find out the major factors that determine the refractive index sensitivities of noble metal nanocrystals is essential for fully realizing

the potential of the plasmonic sensors.

A number of experimental and theoretical studies have been made on the measurement of the refractive index sensitivities of metal nanocrystals at both ensemble [8 – 10] and single-particle levels [11 – 17]. Previous studies have shown that the index sensitivity generally increases as the localized plasmon wavelength is increased for a given nanocrystal metal material. For example, Au nanospheres with a plasmon wavelength of 550 nm have an index sensitivity around 75 nm/RIU (refractive index unit) [18], while both Au nanorings with a plasmon wavelength of 1300 nm and Au nanocrescents with a plasmon wavelength of 2640 nm show index sensitivities of 880 nm/RIU [1, 16]. Most of these investigations have focused on one particular type of metal nanocrystals per study. The question of how the refractive index sensitivity varies with the nanocrystal shape and size has remained unanswered. Resolving this question requires systematic measurements and comparison of the refractive index sensitivities of metal nanocrystals with various shapes, sizes, and plasmon resonance wavelengths. In §4.1, I will first introduce the characterization of the refractive index sensing behaviors of Au nanocrystals with different shapes, sizes, and localized plasmon wavelengths. It is found that the refractive index sensitivity generally increases as the apexes of the nanocrystals become sharper and their plasmon wavelengths become longer. In §4.2, I will present the study on the refractive index sensitivity of Au nanocrystals with varying shapes and sizes but the same plasmon wavelength. The index sensitivity is found to exhibit an approximately linear dependence on the product of the nanocrystal polarizability and end curvature.

On the other hand, many sensing applications need to attach Au nanocrystals onto the substrates. Optical fibers are an attractive candidate due to the fact that they are usually compact, lightweight, minimally invasive, and can be multiplexed effectively. The use of optical fibers for plasmon excitation could combine together the attractive sensing features of metal nanocrystals and

optical fibers and lead to the development of real-time, low-cost, ultrasensitive, and multiplexed sensors. A few previous studies have demonstrated plasmon excitation by the evanescent wave from optical fibers [19 – 22], but only spherical nanoparticles have been employed, and only the ensemble response to the index change has been characterized. In addition, the index sensitivities of spherical metal nanocrystals are much smaller than those of elongated ones. On the basis of the results in §4.1 and §4.2, I further deposited Au nanorods onto the side surface of a commercial optical fiber and studied the excitation of the surface plasmon of Au nanorods by optical fibers in §4.3. The plasmon excitation produces strong scattered light from Au nanorods, allowing for single-particle imaging and spectroscopy. The refractive index sensitivity of individual Au nanorods is found to increase linearly with the LLPWs and can reach 200 nm/RIU for nanorods with LLPW of 688 nm. The ensemble index sensitivities of the longitudinal and transverse localized plasmon resonances of Au nanorods with an ensemble LLPW of 663 nm are further determined to be 140 and 30 nm/RIU, respectively, by measuring the transmission spectra at the fiber output end.

## 4.1 Shape- and Size-Dependent Refractive Index Sensitivity of Gold Nanocrystals with Different Localized Surface Plasmon Wavelengths

Ten types of Au nanocrystals were prepared according to the methods stated in Chapter 3. Specifically, nanospheres, nanocubes, nanobranches, nanorods with LLPW of 846 nm, and nanobipyramids with LLPW of 1096 nm were synthesized directly with the seed-mediated method. The prepared Au nanorods and nanobipyramids were used as precursors for anisotropic shortening to obtain nanocrystals with shorter LLPWs. Figure 4.1.1 shows typical TEM images of the Au nanocrystals with different shapes and sizes.

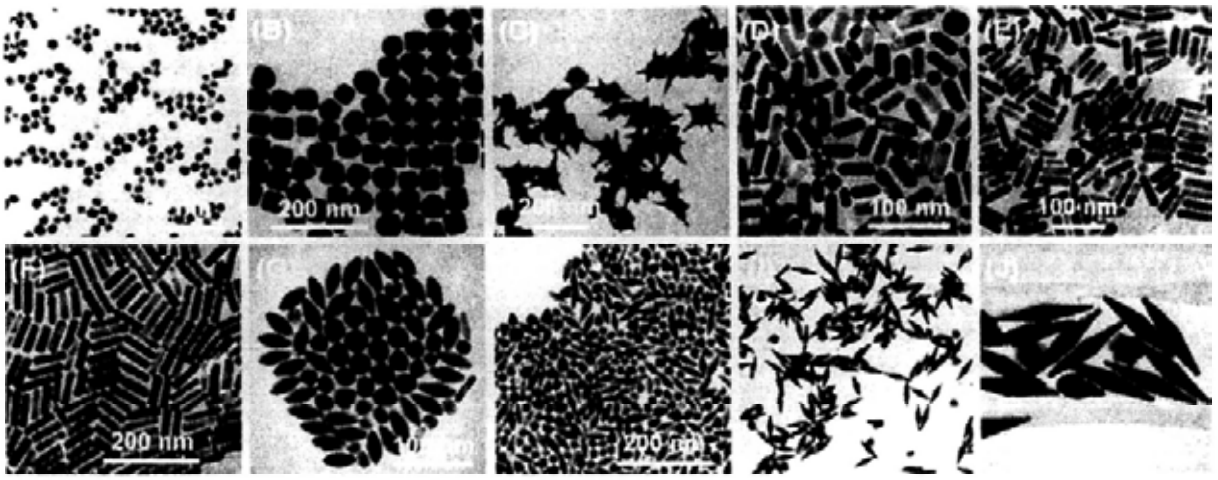


Figure 4.1.1. Representative TEM images of the Au nanocrystals of different shapes and sizes. (A) Nanospheres. (B) Nanocubes. (C) Nanobranches. (D) Nanorods (aspect ratio = 2.4 ± 0.3). (E) Nanorods (aspect ratio = 3.4 ± 0.5). (F) Nanorods (aspect ratio = 4.6 ± 0.8). (G) Nanobipyramids (aspect ratio = 1.5 ± 0.3). (H) Nanobipyramids (aspect ratio = 2.7 ± 0.2). (I) Nanobipyramids (aspect ratio = 3.9 ± 0.2). (J) Nanobipyramids (aspect ratio = 4.7 ± 0.2).

The yields of these nanocrystals are shape-dependent, ranging from 50% to 95%. Each nanocube has six facets and eight slightly rounded corners. Each nanobipyramid contains two sharp tips and ten side surfaces. Nanobranches contain sharp tips of varying lengths. The number of the branched tips per nanobranch ranges from two to eight. The sizes of about 200 particles per sample were measured from their TEM images, and the averages are listed in Table 4.1.1 [23]. These Au nanocrystals cover a wide size range, from 15 to 190 nm, and their size distributions are relatively narrow. For the nanocubes, the edge length was measured. For the nanobipyramids, the diameter was measured at the middle. For the nanobranches, the length from the center to the branched tip was measured and averaged over different branches.

Table 4.1.1. Sizes, plasmon wavelengths, and refractive index sensitivities of the variously-shaped Au nanocrystals.

| Au nanocrystals | length[a] (nm) | diameter[a] (nm) | aspect ratio[a, b] | plasmon wavelength[c] (nm) | index sensitivity[a, d] (nm/RIU) | figure of merit |
|---|---|---|---|---|---|---|
| nanospheres | | 15 (1) | | 527 | 44 (3) | 0.6 |
| nanocubes | 44 (2) | | | 538 | 83 (2) | 1.5 |
| nanobranches | 80 (14) | | | 1141 | 703 (19) | 0.8 |
| nanorods | 40 (6) | 17 (2) | 2.4 (0.3) | 653 | 195 (7) | 2.6 |
| nanorods | 55 (7) | 16 (2) | 3.4 (0.5) | 728 | 224 (4) | 2.1 |
| nanorods | 74 (6) | 17 (2) | 4.6 (0.8) | 846 | 288 (8) | 1.7 |
| nanobipyramids | 27 (4) | 19 (7) | 1.5 (0.3) | 645 | 150 (5) | 1.7 |
| nanobipyramids | 50 (6) | 18 (1) | 2.7 (0.2) | 735 | 212 (6) | 2.8 |
| nanobipyramids | 103 (7) | 26 (2) | 3.9 (0.2) | 886 | 392 (7) | 4.2 |
| nanobipyramids | 189 (9) | 40 (2) | 4.7 (0.2) | 1096 | 540 (6) | 4.5 |

[a] The numbers in the parentheses are standard deviations. [b] It is the ratio between the length and the diameter. [c] Measured when the Au nanocrystals are dispersed in aqueous solutions. For the nanobranches, it is the longer plasmon wavelength. For the nanorods and nanobipyramids, it is the LLPW. [d] For the nanobranches, it is the refractive index sensitivity of the longer-wavelength plasmon peak. For the nanorods and nanobipyramids, it is the index sensitivity of the longitudinal plasmon resonances.

Figure 4.1.2 shows the extinction spectra of the Au nanocrystals that are stabilized with cationic surfactants in aqueous solutions. The Au nanospheres and nanocubes have one surface plasmon peak. The Au nanobranches, nanorods, and nanobipyramids exhibit two major surface plasmon peaks. We focus in our experiments on their longitudinal localized plasmon resonances.

The surface plasmon peaks of these Au nanocrystals, except nanobranches, are relatively sharp, with their full widths at half-maximum (FWHM) values ranging from 50 to 140 nm. The nanobranches have a broad longitudinal plasmon peak, mainly because their tip lengths vary widely within a single nanobranch and among different nanobranches. In addition, a small extinction peak is sometimes observed between the transverse and longitudinal plasmon peaks on the extinction spectra of the Au nanobipyramids. This small peak is ascribed to the presence of a small percentage of Au nanorods that are grown together with the Au nanobipyramids [24]. The surface plasmon wavelengths of these nanocrystals are also listed in Table 4.1.1. They range from 525 to 1150 nm.

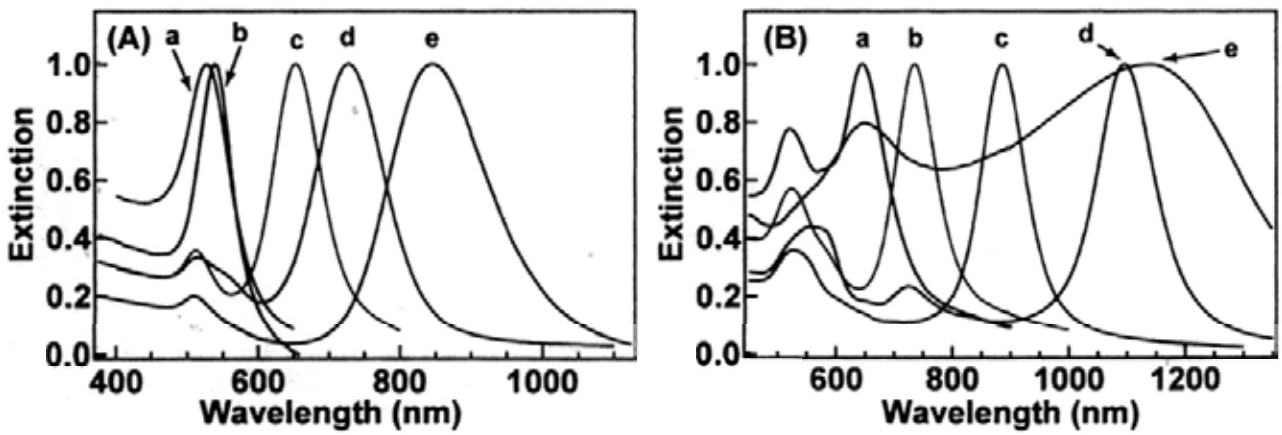


Figure 4.1.2. Normalized extinction spectra of the Au nanocrystals with different shapes and sizes. (A) Spectra (a) – (e) correspond to the nanospheres, nanocubes, and nanorods with aspect ratios of 2.4 ± 0.3, 3.4 ± 0.5, and 4.6 ± 0.8, respectively. (B) Spectra (a) – (e) correspond to the nanobipyramids with aspect ratios of 1.5 ± 0.3, 2.7 ± 0.2, 3.9 ± 0.2, and 4.7 ± 0.2, and the nanobranches, respectively.

Au nanocrystals stabilized with cationic quaternary ammonium surfactants are positively charged, because the ammonium surfactants form a bilayer on the surfaces of the nanocrystals, with

the ammonium headgroups of one monolayer facing the nanocrystal surfaces [25]. The presence of the surfactant bilayer makes Au nanocrystals very stable when dispersed in aqueous solutions. In order to study the response of their surface plasmon peaks to the refractive index of the surrounding medium, we have tried dispersing Au nanocrystals into organic solvents of varying refractive indices. When water-immiscible organic solvents, such as chloroform and toluene, are used to disperse Au nanocrystals that are precipitated by centrifugation, Au nanocrystals aggregate together, probably because the surfactant bilayer is destroyed in these solvents. When water-miscible solvents, such as methanol and ethanol, are added into aqueous dispersions of Au nanocrystals above a certain volume percentage (~30 vol % for methanol and ethanol), the aggregation of Au nanocrystals occurs immediately. After trying a variety of organic solvents, I have finally found that water–glycerol mixtures can be used to disperse cationic surfactant-stabilized Au nanocrystals without causing aggregation. The volume percentage of glycerol can be up to 100% for the dispersion of Au nanocrystals. In my experiments, the highest volume percentage of glycerol that was used is 90%, because pure glycerol is too viscous. The refractive index of the liquid mixture is calculated according to the Lorentz-Lorenz equation [26],

$$\frac{n_{12}^2 - 1}{n_{12}^2 + 2} = \varphi_1 \frac{n_1^2 - 1}{n_1^2 + 2} + \varphi_2 \frac{n_2^2 - 1}{n_2^2 + 2} \qquad (4.1.1)$$

where $n_{12}$ is the refractive index of the liquid mixture, $n_1$ and $n_2$ are the indices of water (1.3334) and glycerol (1.4746), respectively, and $\varphi_1$ and $\varphi_2$ are the volume fractions of the two components. The calculated refractive index of the liquid mixture as a function of the volume percentage of glycerol can be fitted well by a straight line, as shown in Figure 4.1.3A.

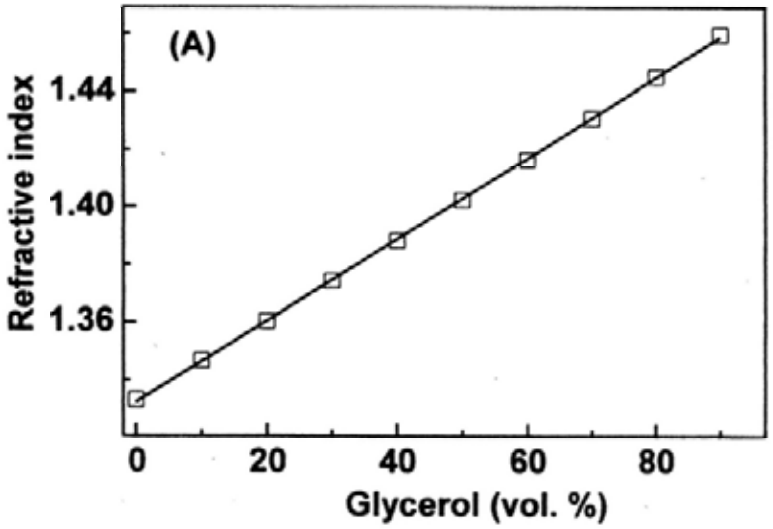
(A)
Refractive index
1.44
1.40
1.36
0
20
40
60
80
Glycerol (vol. %)

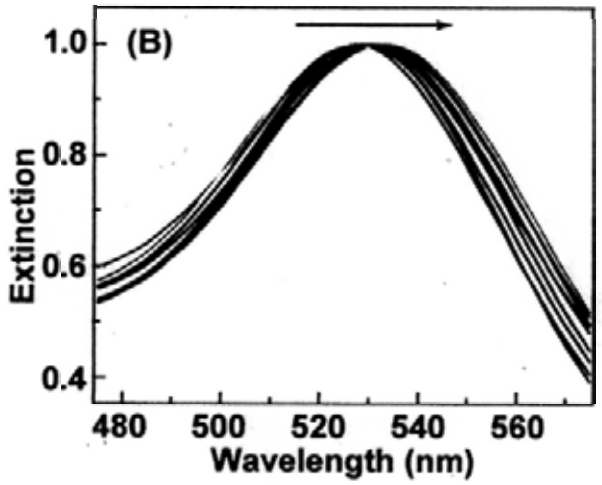
(B)
Extinction
1.0
0.8
0.6
0.4
480
500
520
540
560
Wavelength (nm)

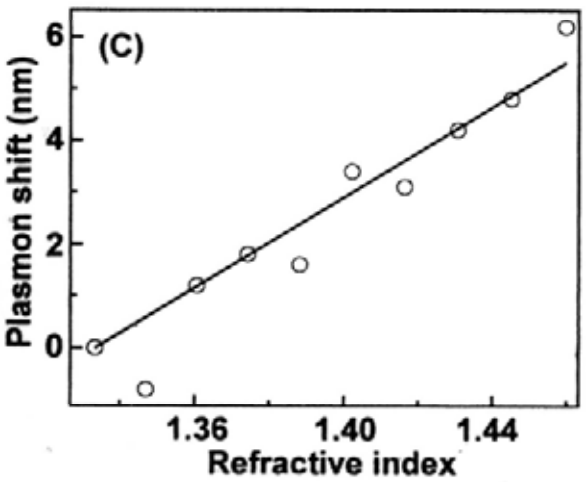
(C)
Plasmon shift (nm)
6
4
2
0
1.36
1.40
1.44
Refractive index

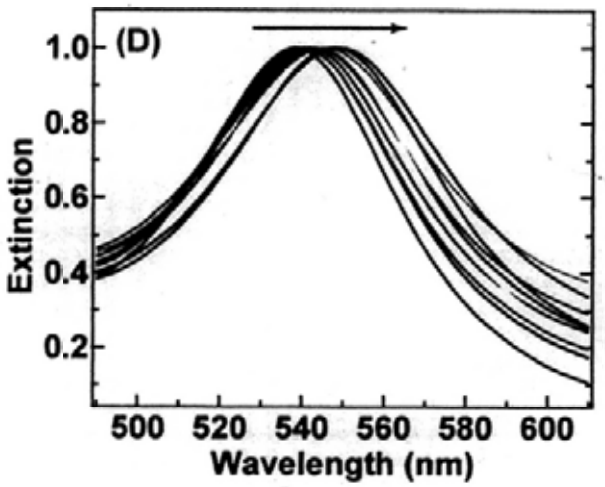
(D)
Extinction
1.0
0.8
0.6
0.4
0.2
500
520
540
560
580
600
Wavelength (nm)

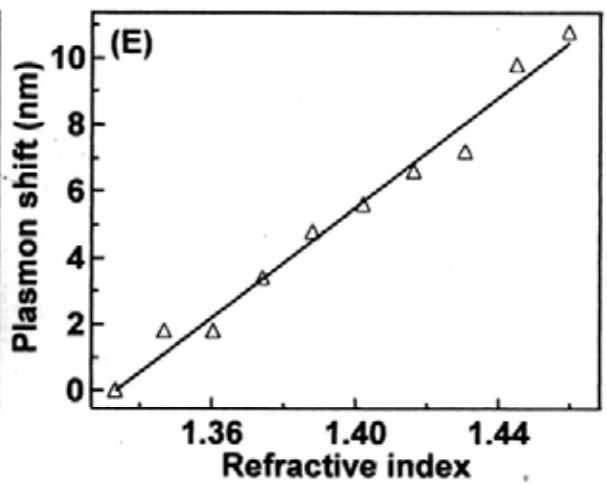
(E)
Plasmon shift (nm)
10
8
6
4
2
0
1.36
1.40
1.44
Refractive index

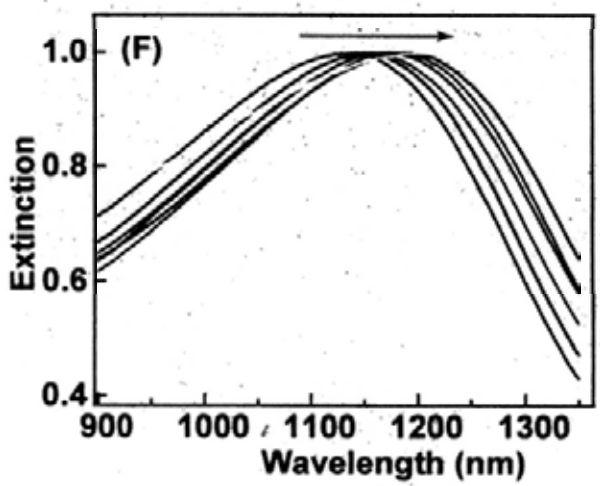
(F)
Extinction
Wavelength (nm)

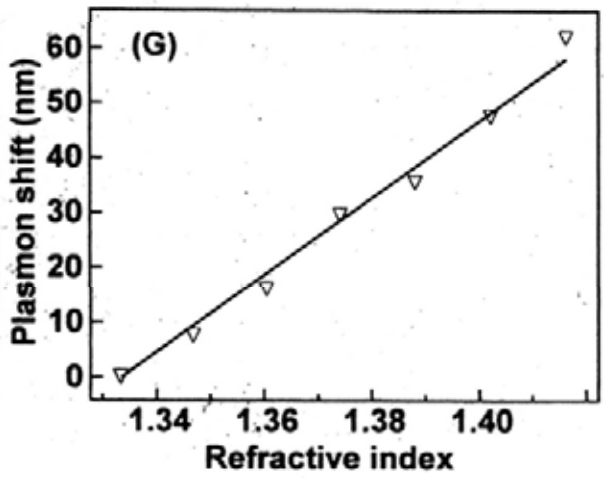
(G)
Plasmon shift (nm)
Refractive index

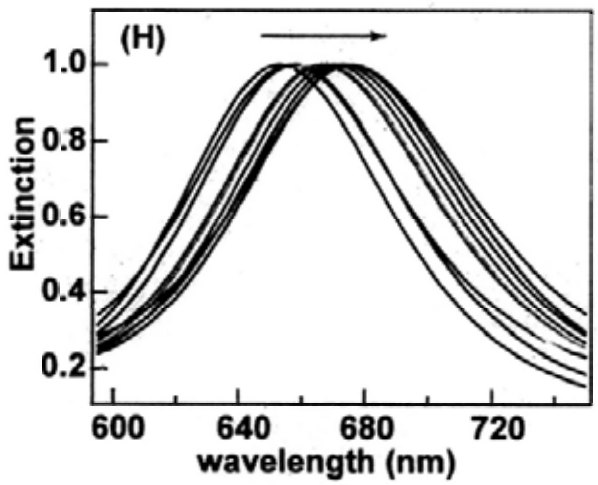
(H)
Extinction
wavelength (nm)

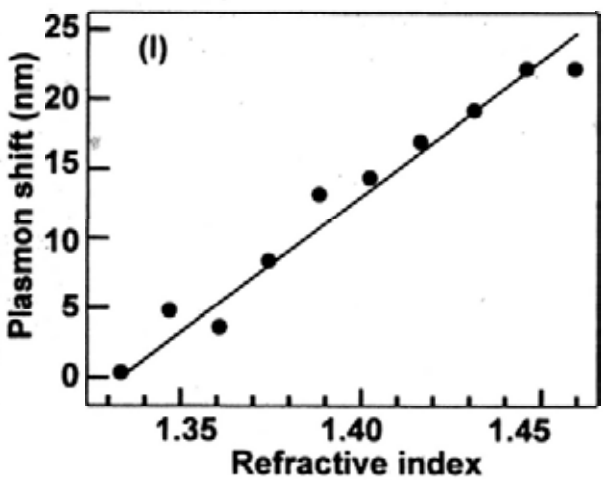
(I)
Plasmon shift (nm)
Refractive index

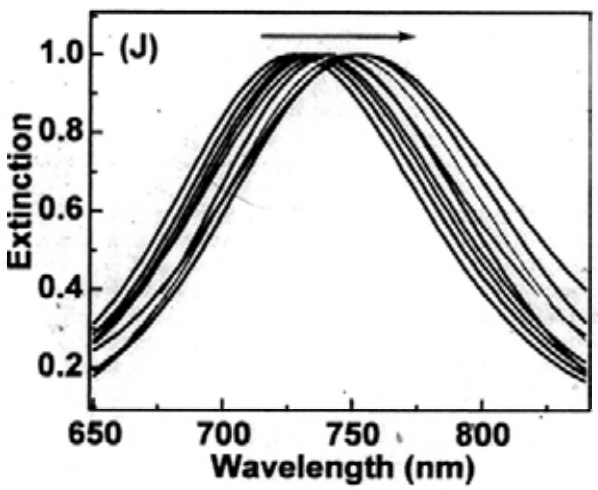
(J)
Extinction
Wavelength (nm)

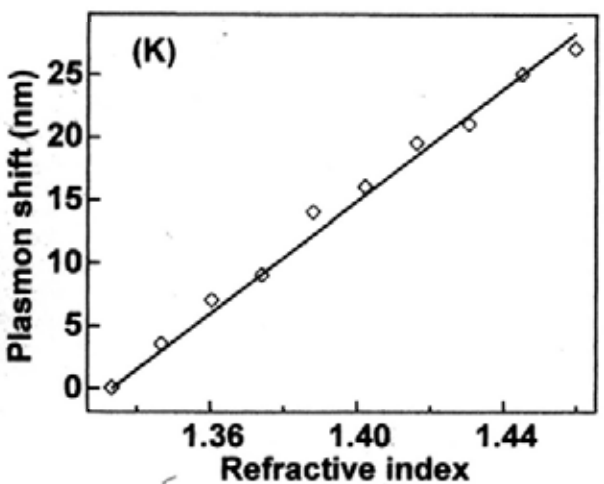
(K)
Plasmon shift (nm)
Refractive index

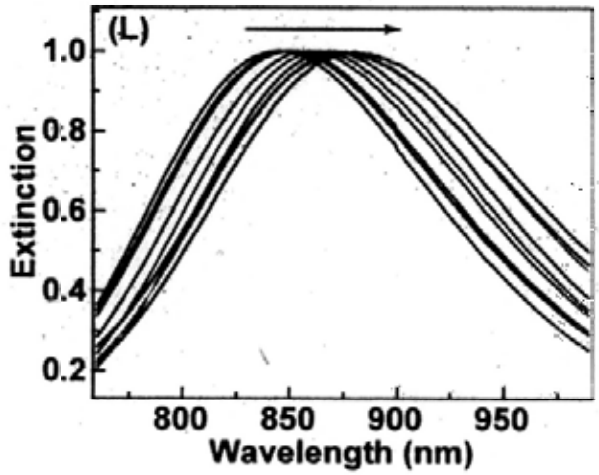
(L)
Extinction
Wavelength (nm)
1.0
0.8
0.6
0.4
0.2
800
850
900
950

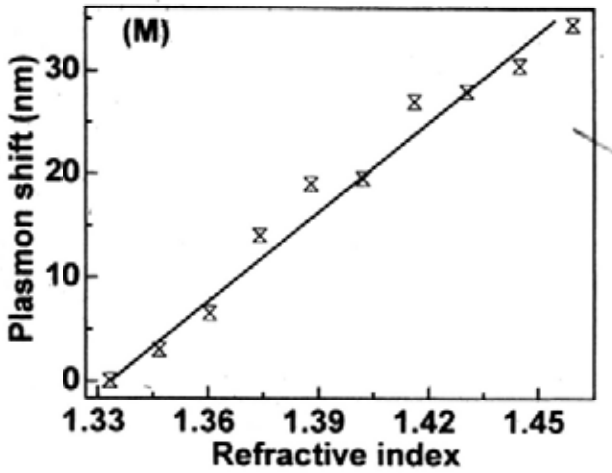
(M)
Plasmon shift (nm)
Refractive index
30
20
10
0
1.33
1.36
1.39
1.42
1.45

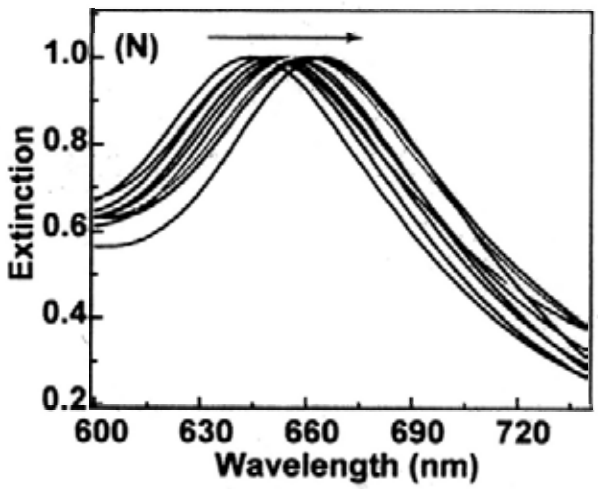
(N)
Extinction
Wavelength (nm)
1.0
0.8
0.6
0.4
0.2
600
630
660
690
720

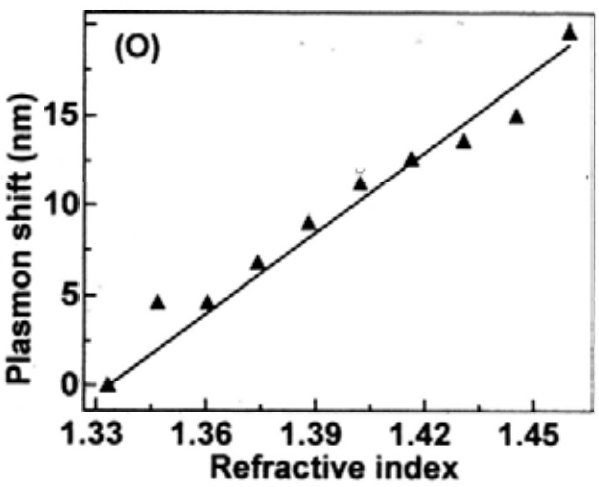
(O)
Plasmon shift (nm)
Refractive index
15
10
5
0
1.33
1.36
1.39
1.42
1.45

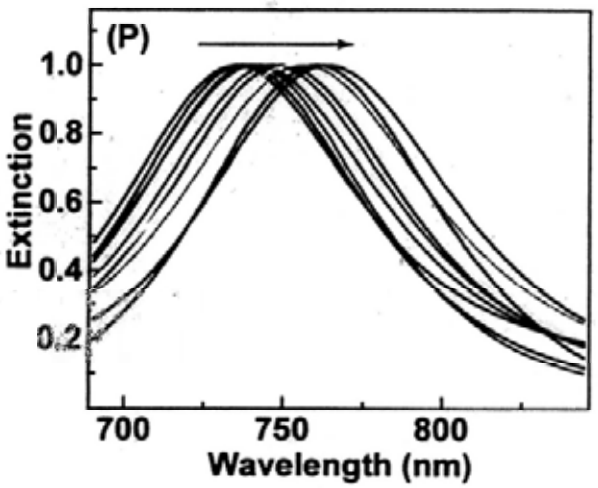
(P)
Extinction
Wavelength (nm)
1.0
0.8
0.6
0.4
0.2
700
750
800

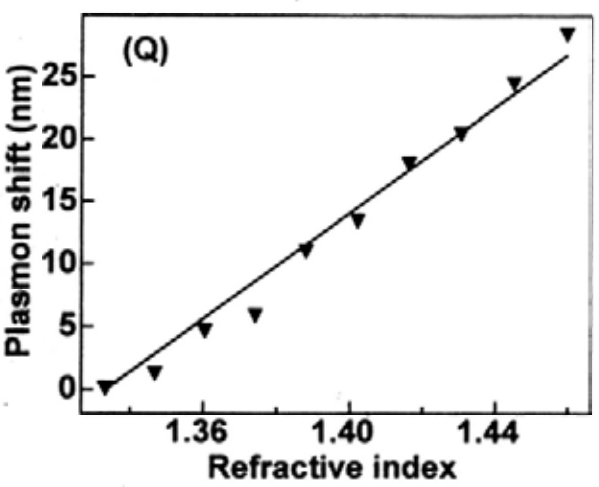
(Q)
Plasmon shift (nm)
Refractive index
25
20
15
10
5
0
1.36
1.40
1.44

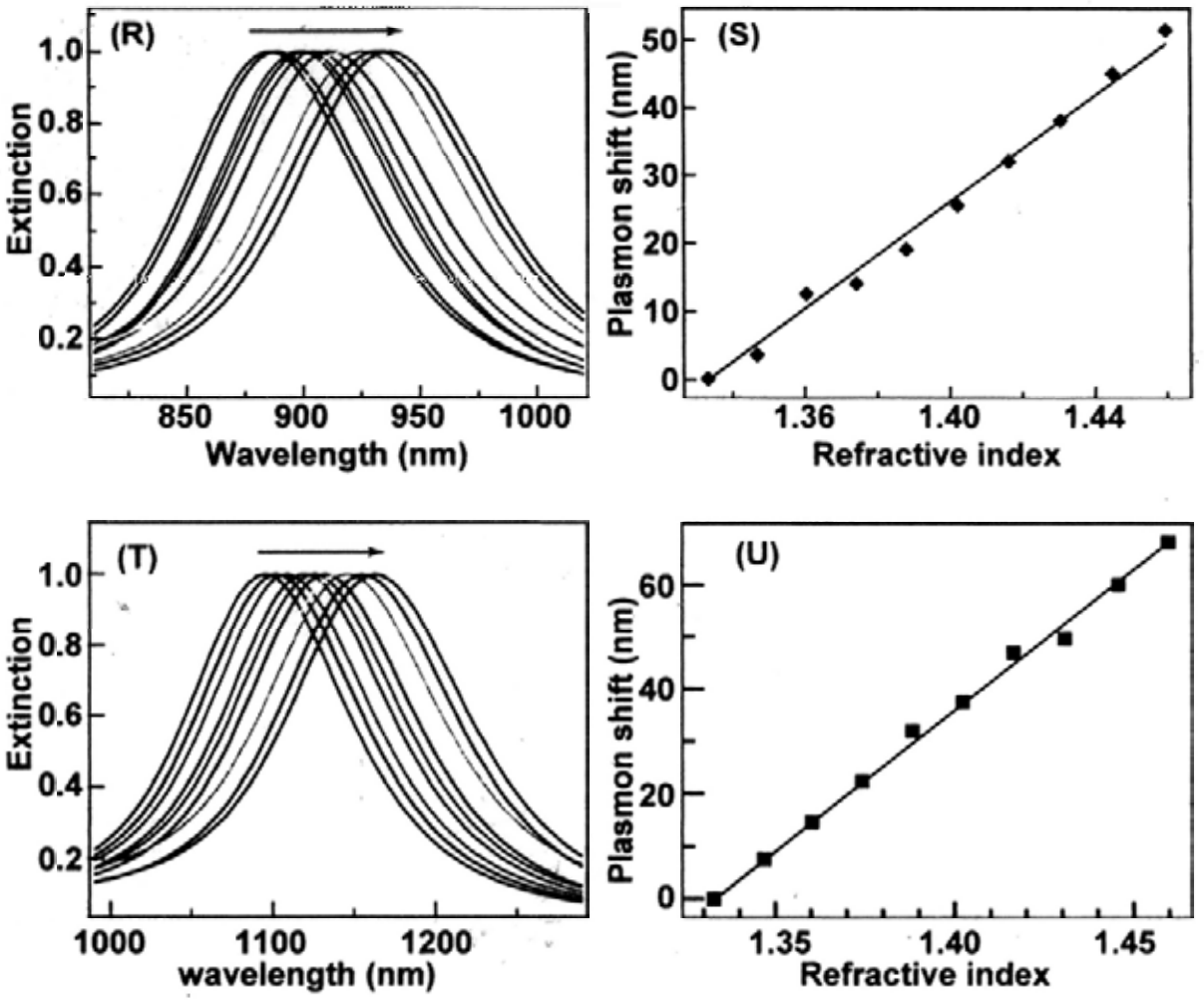


Figure 4.1.3. (A) Dependence of the refractive index of water–glycerol mixtures on the volume percentage of glycerol. The line is a linear fit. From (B) to (U), Left side: normalized extinction spectra of the Au nanocrystals dispersed in water–glycerol mixtures of varying compositions. The arrows indicate the direction of increasing volume percentage of glycerol. Right side: dependence of the longitudinal plasmon resonance shift on the refractive index of the liquid mixture. The lines are linear fits. (B, C) Nanospheres. (D, E) Nanocubes. (F, G) Nanobranches. (H, I) Nanorods with an aspect ratio of 2.4 ± 0.3. (J, K) Nanorods with an aspect ratio of 3.4 ± 0.5. (L, M) Nanorods with an aspect ratio of 4.6 ± 0.8. (N, O) Nanobipyramids with an aspect ratio of 1.5 ± 0.3. (P, Q) Nanobipyramids with an aspect ratio of 2.7 ± 0.2. (R, S) Nanobipyramids with an aspect ratio of 3.9 ± 0.2. (T, U) Nanobipyramids with an aspect ratio of 4.7 ± 0.2.

Figure 4.1.3 shows the extinction spectra of these ten Au nanocrystals dispersed in water–glycerol mixtures of varying volume ratios (Figure 4.1.3B, D, F, H, J, L, N, P, R, and T). As the volume percentage of glycerol is increased, the localized plasmon resonances of the nanocrystals generally shift towards the red direction. The localized plasmon resonance wavelengths can be readily obtained from the extinction spectra. Figure 4.1.3 also shows the plots of the plasmon shift, which is the difference between the plasmon wavelengths obtained when the Au nanocrystals are dispersed in the liquid mixture and water, respectively, versus the refractive index of the medium for all of the ten nanocrystals (Figure 4.1.3C, E, G, I, K, M, O, Q, S, and U). All of these plots can be fitted well linearly. The slopes are the refractive index sensitivities. The results are summarized in Table 4.1.1. Several observations can be made from the refractive index sensitivities listed in Table 4.1.1. (1) The Au nanospheres with the shortest plasmon wavelength exhibit the smallest refractive index sensitivity of 44 nm/RIU, while the Au nanobranches with the longest wavelength possess the largest index sensitivity of 703 nm/RIU. The index sensitivities of both the nanorods and nanobipyramids increase as their plasmon wavelengths are increased. These findings indicate that the index sensitivities are generally larger for Au nanocrystals with longer plasmon wavelengths. (2) We have deliberately chosen Au nanorods and nanobipyramids with similar longitudinal plasmon wavelengths (653 versus 645 nm, 728 versus 735 nm, and 846 versus 886 nm) and found that the sensitivities of the Au nanobipyramids increase faster than those of the corresponding Au nanorods with increasing longitudinal plasmon wavelengths. This result suggests that the shape and size of Au nanocrystals are also important factors in determining the refractive index sensitivity. (3) In general, the index sensitivity increases as the apexes of the Au nanocrystals get sharper. The Au nanobranches with the sharpest tips exhibit the highest index sensitivity, up to 703 nm/RIU. The index sensitivities can be further increased by making metal nanostructures of sharper apexes, as

have been demonstrated with nanorices (801 nm/RIU) and nanocrescents (up to 880 nm/RIU) [16, 27]. (4) The figure of merit (FOM), defined as the refractive index sensitivity divided by the FWHM of the plasmon resonance peak, of the Au nanobipyramids are much larger than those of the other Au nanocrystals. It is because nanobipyramids have larger index sensitivities and more uniform sizes than the nanorods. Because most portable optical sensing devices detect light intensity changes at fixed wavelengths, narrower plasmon resonance peaks can generally lead to larger intensity changes for a fixed plasmon shift and therefore give improved sensing performance. In this regard, the Au nanobipyramids should therefore be more advantageous than the Au nanorods when nanocrystal ensembles are employed for plasmonic sensing.

The above observations suggest that both the plasmon wavelengths and geometrical parameters play important roles in determining the index sensitivities of Au nanocrystals. However, as the plasmon wavelengths of metal nanocrystals are strongly dependent on their shapes and sizes and the relationship between them is often very complex, it has been difficult to differentiate the effects of the plasmon resonance wavelength and the nanocrystal shape on the refractive index sensitivity. The question of how the index sensitivities of metal nanocrystals depend specifically on their shapes has remained unanswered. We therefore measured and compared the refractive index sensitivities of Au nanocrystals with different shapes and sizes but the same longitudinal plasmon wavelength.

## 4.2 Shape- and Size-Dependent Refractive Index Sensitivity of Gold Nanocrystals with the Same Localized Surface Plasmon Wavelength

Seven Au nanocrystals with a common longitudinal plasmon wavelength of 730 nm were prepared. They are named as large nanorods, medium nanorods, dogbone-like nanorods, peanut-like nanorods, small nanorods, nanobipyramids, and large nanobipyramids. Specifically, the large

nanorods, dogbone-like nanorods, and nanobipyramids were grown directly by the seed-mediated method. The medium nanorods and small nanorods were obtained from the anisotropic oxidation. The starting nanorods exhibit LLPWs of 955 and 810 nm, respectively. The large nanobipyramids were also made by the anisotropic oxidation from starting nanobipyramids with a LLPW at 886 nm. The peanut-like nanorods were synthesized by the transverse overgrowth where the starting nanorods have a LLPW at 955 nm.

Figure 4.2.1 shows the representative scanning electron microscopy (SEM) and transmission electron microscopy (TEM) images of the nanocrystals in seven different shapes. The medium (Figure 4.2.1E) and small nanorods (Figure 4.2.1H) are cylindrical in the middle section and capped with two half spheres at both ends. The large nanorods are faceted at the side, as revealed by SEM imaging (Figure 4.2.1A). The cross section of the large nanorods in the middle section is believed to be octagonal, according to previous high-resolution TEM characterizations [28]. The nanobipyramids (Figure 4.2.1C) and large nanobipyramids (Figure 4.2.1D) possess ten side surfaces per particle and their ends are rounded. The dogbone-like nanorods have two fatter ends and a thinner middle section (Figure 4.2.1F). The peanut-like nanorods are similar to the dogbone-like nanorods in geometry, except that the fatter ends of the peanut-like nanorods are more rounded (Figure 4.2.1G). The yields of the large, medium, small, dogbone-like, and peanut-like nanorods in terms of the particle number are ~90%, and those of the nanobipyramids and large nanobipyramids are ~60%.

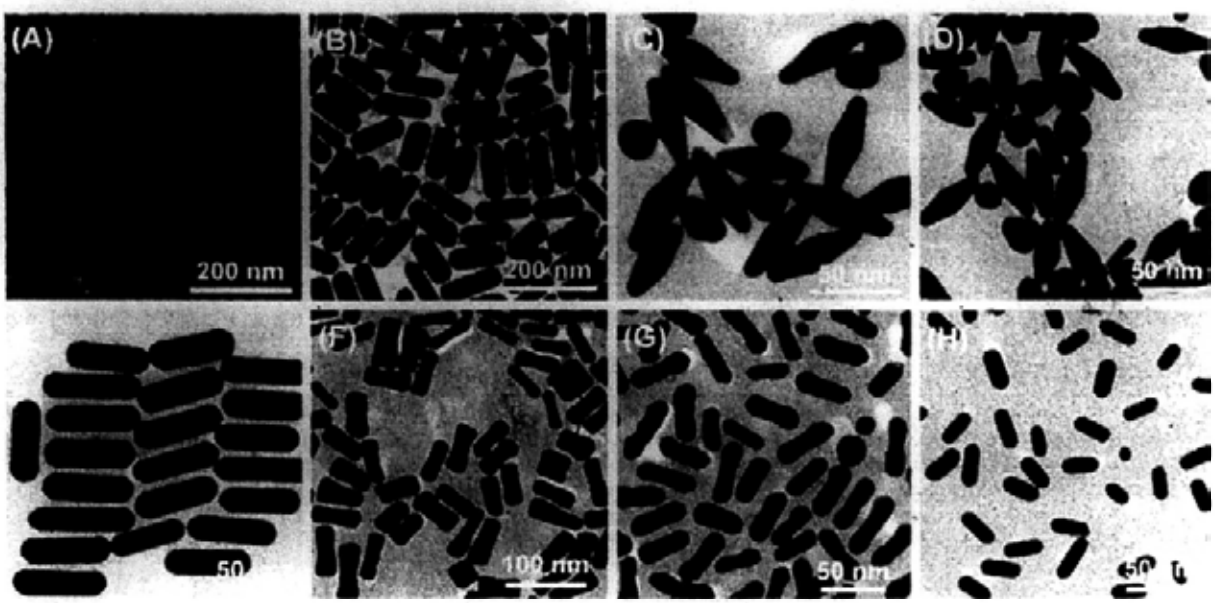


Figure 4.2.1. (A) SEM image of the large Au nanorods. (B) TEM image of the large Au nanorods. (C – H) TEM images of the nanobipyramids, large nanobipyramids, medium nanorods, dogbone-like nanorods, peanut-like nanorods, and small nanorods, respectively.

The sizes of these nanocrystals measured from their TEM images are listed in Table 4.2.1. The length was measured between the two farthest ends, and the diameter was measured at the middle waist. The sizes of these nanocrystals are relatively uniform. The percent errors, which are the standard deviations divided by the average values, are in the ranges of 4–10%, 6–15%, and 4–14% for the diameter, length, and aspect ratio, respectively. The particle volume ranges from 2 000 to 157 000 $nm^3$ and increases in the order of the small nanorods, peanut-like nanorods, nanobipyramids, large nanobipyramids, medium nanorods, dogbone-like nanorods, and large nanorods.

Table 4.2.1. Sizes and plasmon resonance wavelengths of the gold nanocrystals.

| Au nanocrystals | diameter[a] (nm) | length (nm) | aspect ratio | volume ($nm^3$) | curvature ($10^{-3}$ $nm^{-1}$) | LLPW (nm) | FWHM (nm) |
|---|---|---|---|---|---|---|---|
| large nanorods | 44 (2) | 108 (7) | 2.5 (0.2) | 157 000 | 42 (4) | 732 | 116 |
| nanobipyramids | 19 (1) | 55 (5) | 2.9 (0.2) | 11 000 | 200 (10) | 729 | 91 |
| large nanobipyramids | 24 (1) | 67 (4) | 2.8 (0.1) | 17 000 | 125 (5) | 729 | 61 |
| medium nanorods | 20 (1) | 61 (5) | 3.1 (0.3) | 18 000 | 87 (3) | 733 | 94 |
| dogbone-like nanorods | 20 (2) | 56 (5) | 2.8 (0.4) | 21 000 | 100 (9) | 732 | 125 |
| peanut-like nanorods | 14 (1) | 43 (4) | 3.2 (0.4) | 7 000 | 160 (15) | 734 | 116 |
| small nanorods | 10 (1) | 26 (4) | 2.6 (0.3) | 2 000 | 122 (7) | 733 | 98 |

[a] The numbers in the parentheses are standard deviations. The dimensions of the Au nanocrystals, including their diameters, lengths, aspect ratios, and curvatures, were averaged over ~250 nanocrystals per sample.

Because it is well-known that the maximum local electric field enhancement of metal nanocrystals depends strongly on the local curvature, the average local curvatures of the nanocrystals were also measured and included in Table 4.2.1. The curvature of each nanocrystal sample was measured at its sharpest points, which were assumed to be spherically truncated. Spherical crowns were first drawn on the TEM images of the Au nanocrystals to model the shapes and sizes of their sharpest points, as shown in Figure 4.2.2. The base radius $a$ and height $h$ of each crown were then measured. The curvature was calculated according to $\sigma = 2h/(a^2 + h^2)$. The sharpest points of the dogbone-like nanorods are located at the circular edge at the end, while those of the other nanocrystals are located at both apexes.

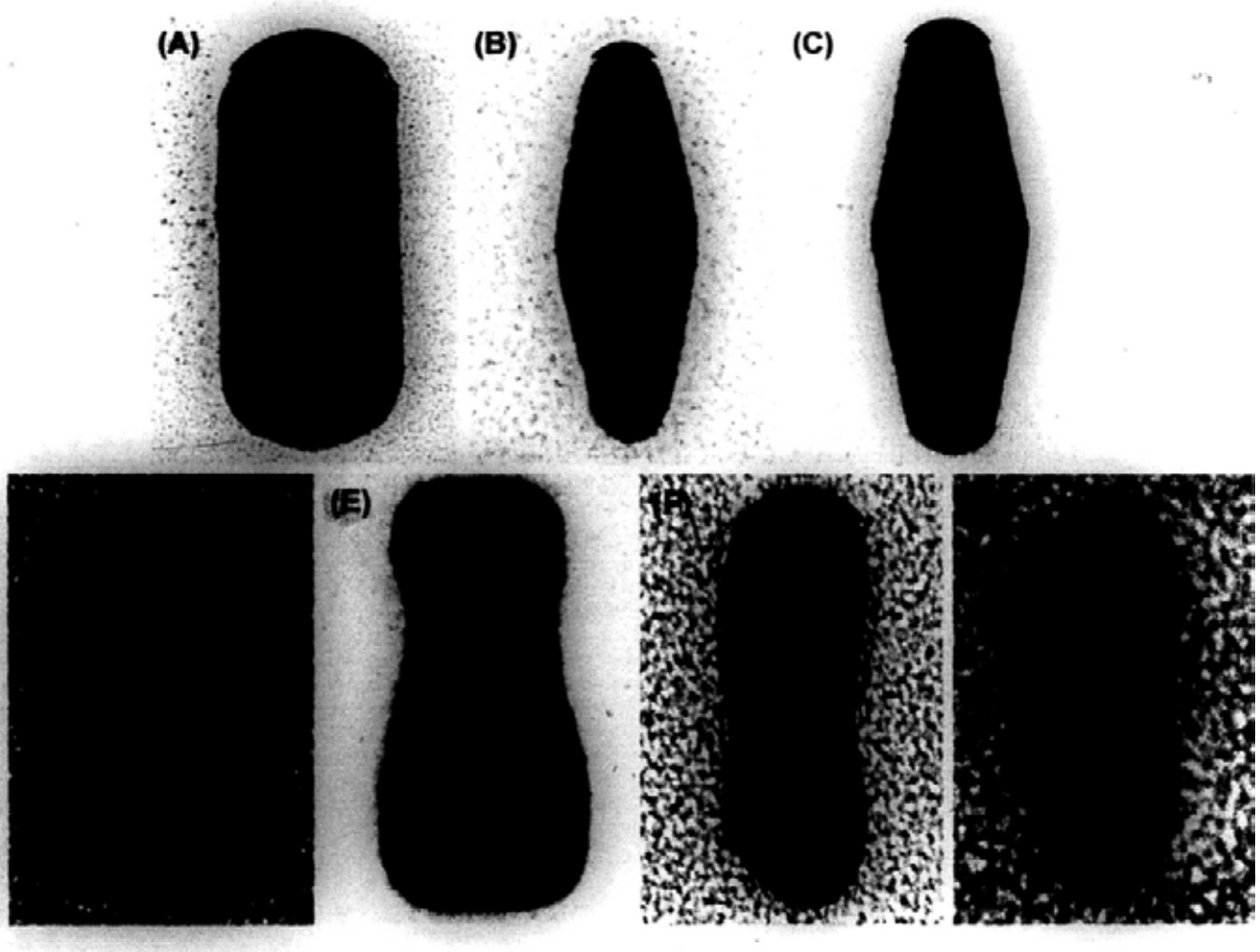


Figure 4.2.2. Representative spherical crowns drawn on the TEM images of the Au nanocrystals for the measurement of their end curvatures. (A) Large nanorod. (B) Nanobipyramid. (C) Large nanobipyramid. (D) Medium nanorod. (E) Dogbone-like nanorod. (F) Peanut-like nanorod. (G) Small nanorod.

Figure 4.2.3 shows the experimental normalized extinction spectra of seven differently shaped Au nanocrystal samples that are dispersed in aqueous solutions. Their LLPWs measured from the extinction peaks range from 729 to 734 nm and are very close to each other (Table 4.2.1). The FWHMs of the longitudinal extinction peaks are in the range of 60–125 nm, with the large nanobipyramids exhibiting the smallest peak width and the dogbone-like nanorods exhibiting the

largest one. The difference in the peak width is mainly caused by the extent of the inhomogeneous size distribution, which varies among the Au nanocrystal samples because they were prepared under different conditions. The Au nanocrystals were dispersed in water–glycerol mixtures to measure the refractive index sensitivities of their longitudinal localized plasmon resonance.

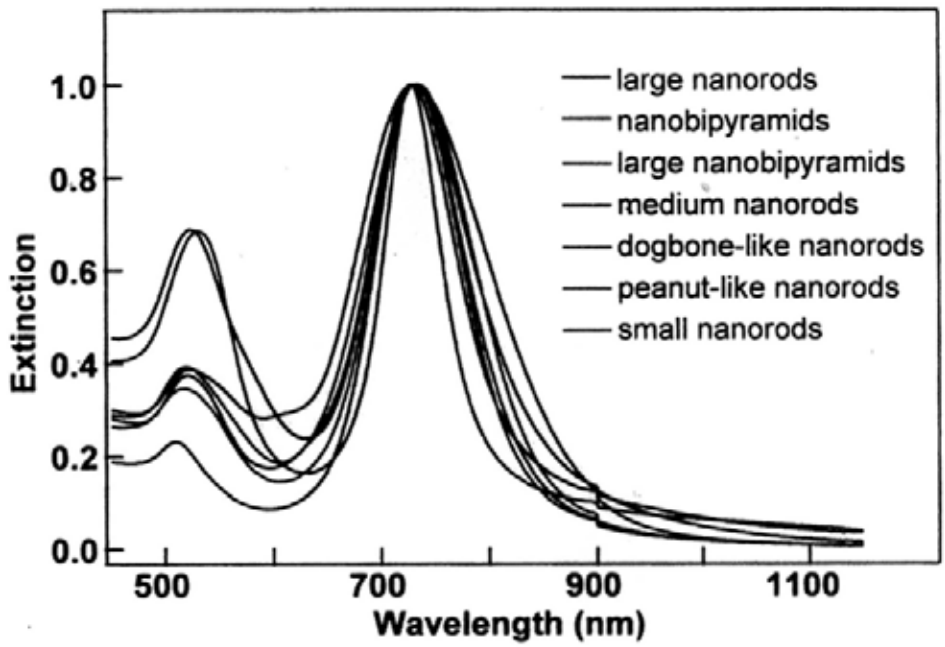


Figure 4.2.3. Normalized extinction spectra of differently-shaped Au nanocrystals dispersed in water.

Figure 4.2.4 shows the extinction spectra of the seven nanocrystal samples dispersed in the liquid mixtures of increasing volume percentage of glycerol. Similarly, the longitudinal plasmon resonance peaks of the nanocrystals shift toward longer wavelengths as the refractive index of the liquid mixture is increased (Figure 4.2.4A, C, E, G, I, K, and M).

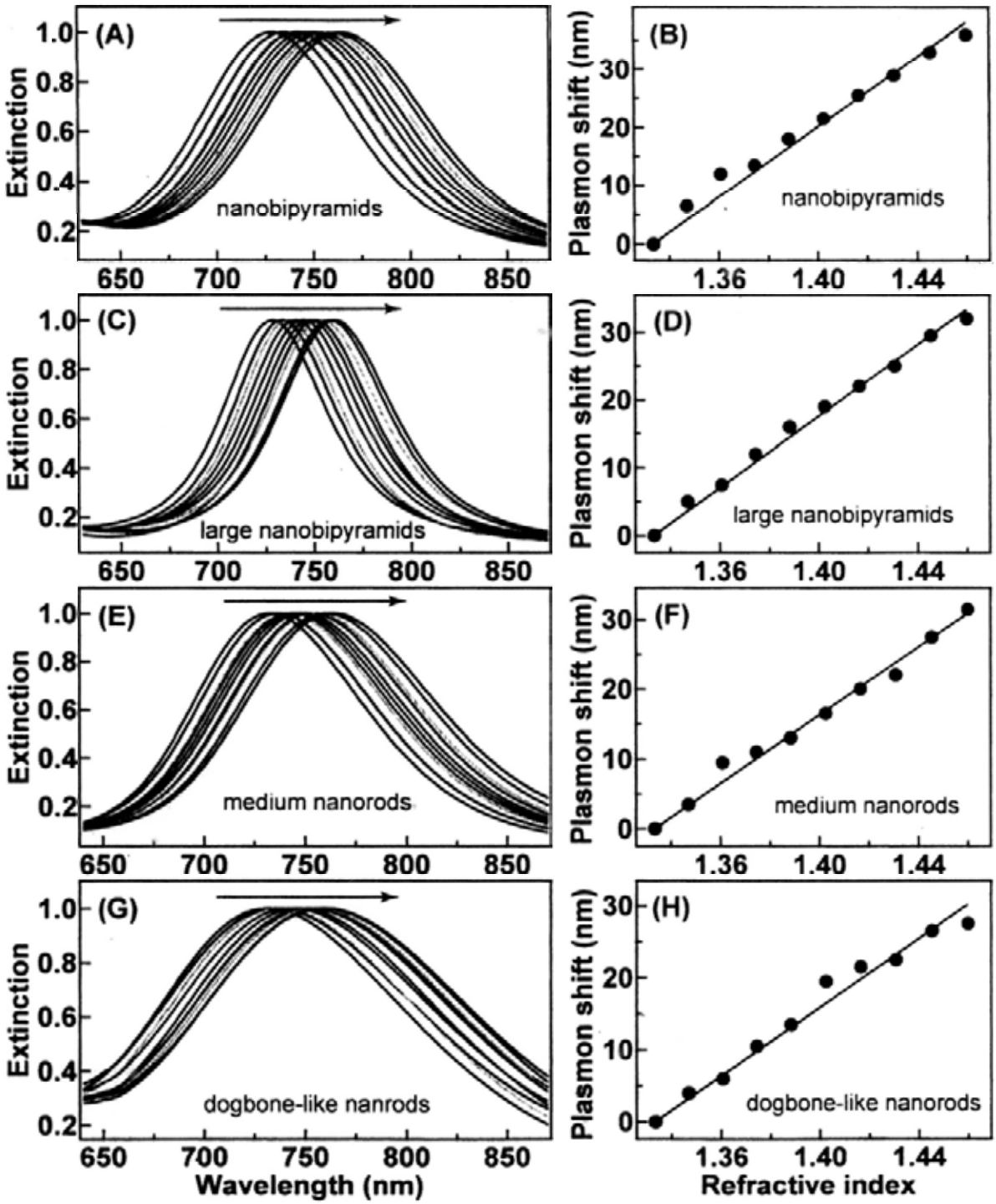
(A)
nanobipyramids
(B)
nanobipyramids
(C)
large nanobipyramids
(D)
large nanobipyramids
(E)
medium nanorods
(F)
medium nanorods
(G)
dogbone-like nanrods
(H)
dogbone-like nanorods
Extinction
Plasmon shift (nm)
Wavelength (nm)
Refractive index

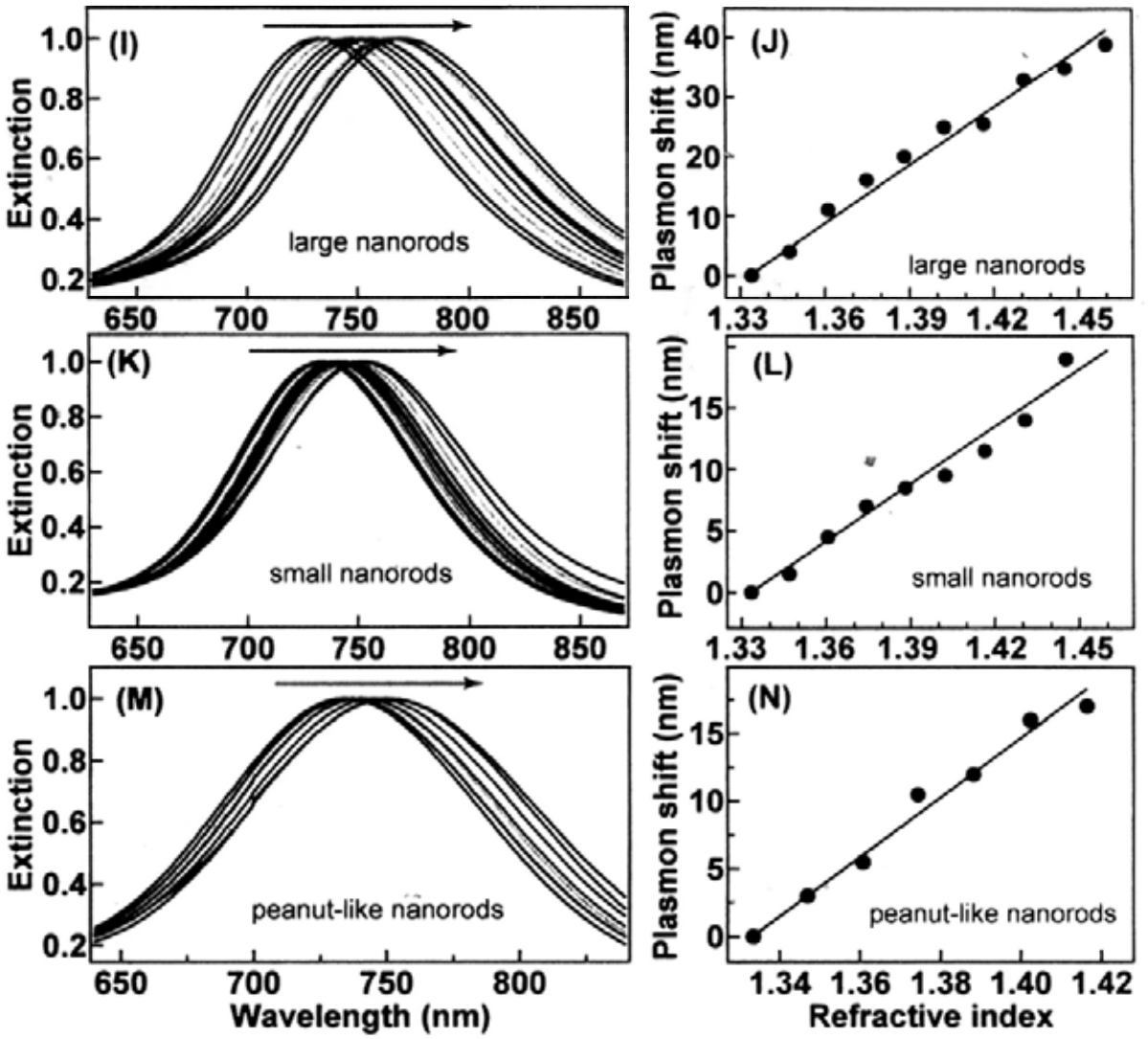


Figure 4.2.4. Left side: normalized extinction spectra of the Au nanocrystals dispersed in water–glycerol mixtures of varying compositions. The arrows indicate the direction of increasing volume percentage of glycerol. Right side: dependence of the longitudinal plasmon shift on the refractive index of the liquid mixture. The lines are linear fits. (A, B) Nanobipyramids. (C, D) Large nanobipyramids. (E, F) Medium nanorods. (G, H) Dogbone-like nanorods. (I, J) Large nanorods. (K, L) Small nanorods. (M, N) Peanut-like nanorods.

The refractive index sensitivities of these nanocrystals can be obtained by linear fitting of their plasmon shifts against the refractive index of the liquid mixtures (Figure 4.2.4B, D, F, H, J, L, and

N). The determined index sensitivities as well as the FOMs are given in Table 4.2.2 for all of the nanocrystal samples. It shows that the Au nanocrystals in different shapes exhibit different refractive index sensitivities even though their LLPWs are all around 730 nm. The index sensitivities range from 156 to 326 nm/RIU and increase in the order of the small nanorods, peanut-like nanorods, dogbone-like nanorods, medium nanorods, large nanobipyramids, nanobipyramids, and large nanorods. The highest index sensitivity is more than twice larger than the lowest one. These results suggest that the refractive index sensitivities of noble metal nanocrystals are highly dependent on their shapes and sizes even though their plasmon resonance wavelengths are the same.

Table 4.2.2. Refractive index sensitivities, figures of merit, and plasmonic properties of the gold nanocrystals.

| Au nanocrystals | sensitivity (nm/RIU) | FOM | intensity enhancement[a] | decay length[b] (nm) | polarizability[c] ($10^6$ nm) |
|---|---|---|---|---|---|
| large nanorods | 326 | 2.8 | 840 | 2.8 | 14.5 |
| nanobipyramids | 301 | 3.3 | 5 200 | 2.3 | 2.5 |
| large nanobipyramids | 264 | 4.3 | 3 500 | 3.2 | 3.9 |
| medium nanorods | 244 | 2.6 | 1 600 | 4.3 | 5.3 |
| dogbone-like nanorods | 238 | 1.9 | 1 900 | 3.6 | 3.0 |
| peanut-like nanorods | 220 | 1.9 | 940 | 3.8 | 1.6 |
| small nanorods | 156 | 1.6 | 1 300 | 4.3 | 0.7 |

[a] The maximum electric field intensity enhancement. [b] The length where the electric field intensity enhancement falls to $1/e$ of the maximum value along the direction perpendicular to the nanocrystal surface. [c] Polarizability $|\alpha| = \frac{\sqrt{6\pi C_{scat}}}{k^2}$, with $C_{scat}$ being the scattering cross section obtained from FDTD calculations and $k$ being the wavevector. Both $C_{scat}$ and $k$ values at the longitudinal

plasmon resonance wavelength are used. The resultant polarizability therefore also refers to the value at this wavelength.

In a previous theoretical study, the index sensitivity has been found to be dependent solely on the plasmon resonance wavelength and independent of the shape and size for single-component noble metal nanocrystals [29]. In that study, metal nanocrystals in the shapes of highly regular cylinders, disks, and spherical shells are considered. They have either circular or spherical symmetries. The plasmon resonance condition is determined by the depolarization parameter, the real dielectric function of the metal, and the refractive index of the surrounding medium. This resonance condition leads to the exclusive dependence of the index sensitivity on the refractive index of the medium and the real dielectric function of the metal. In my studies, the Au nanocrystals are truncated and have more complex geometries. Their longitudinal plasmon resonance wavelengths are dependent not only on the aspect ratio, but also on the specific shape (Table 4.2.1). The resonance condition of these nanocrystals is much more complicated and cannot be described with a simple relationship. It is therefore very important to investigate and identify the determining factors for the refractive index sensitivity of noble metal nanocrystals that have different shapes but the same plasmon resonance wavelength.

The index sensitivities of noble metal nanocrystals are fundamentally determined by how easily the free electron cloud in metal nanocrystals is displaced relative to the positive atomic lattice by light. The easier it is to displace the free electron cloud in metal nanocrystals, the more severe the index increase-caused screening of the Coulombic restoring force becomes. The displacement pattern of the free electron cloud in metal nanocrystals depends not only on the net polarizability but also on the specific shape. Metal nanocrystals of complex shapes usually exhibit much higher charge

densities in the surface regions with sharp curvatures. Because there are no analytic solutions for the polarizabilities of metal nanocrystals with complex shapes, we performed FDTD calculations to obtain the polarizabilities of the Au nanocrystals and investigated the effects of different factors on the refractive index sensitivity by taking into account the geometrical shape as well. I employed a software package, FDTD Solutions, developed by Lumerical Solutions, Inc. to perform the FDTD calculations on the different Au nanocrystals. The dielectric function of Au was formulated with the Drude model with parameters chosen to match the experimental dielectric data as close as possible (The related parameters were already listed in Table 4.2.1). In the calculation, an electromagnetic pulse with its wavelength ranging from 600 to 900 nm was launched into a box containing the target Au nanocrystal to simulate a propagating plane wave interacting with the nanocrystal. The Au nanocrystal and its surrounding medium inside the box were divided into meshes of 0.5 nm in size. The electric field of the pulse was set along the length axis of the nanocrystal. The surrounding medium was taken as water with a refractive index of 1.333. The sizes and shapes of the Au nanocrystals in calculation were set to be as close as possible to those measured from the TEM images. Specifically, the medium and small nanorods were modeled as cylinders capped with two half spheres at both ends. The peanut-like nanorods were modeled as a cylinder at the middle waist and two larger spheres at both ends. The larger spheres were cut to form four facets symmetrically relative to the length axis. The dogbone-like nanorods were also modeled as a cylinder at the middle waist and two larger spheres at both ends. The larger spheres were facetted only at the end. The large nanorods were modeled as an octagonal prism at the middle waist and two octagonal pyramids at both ends. The large nanobipyramids and nanobipyramids were modeled as two pentagonal pyramids with five facetted surfaces in the middle region and their apexes were modeled as spherical caps with five cut facets.

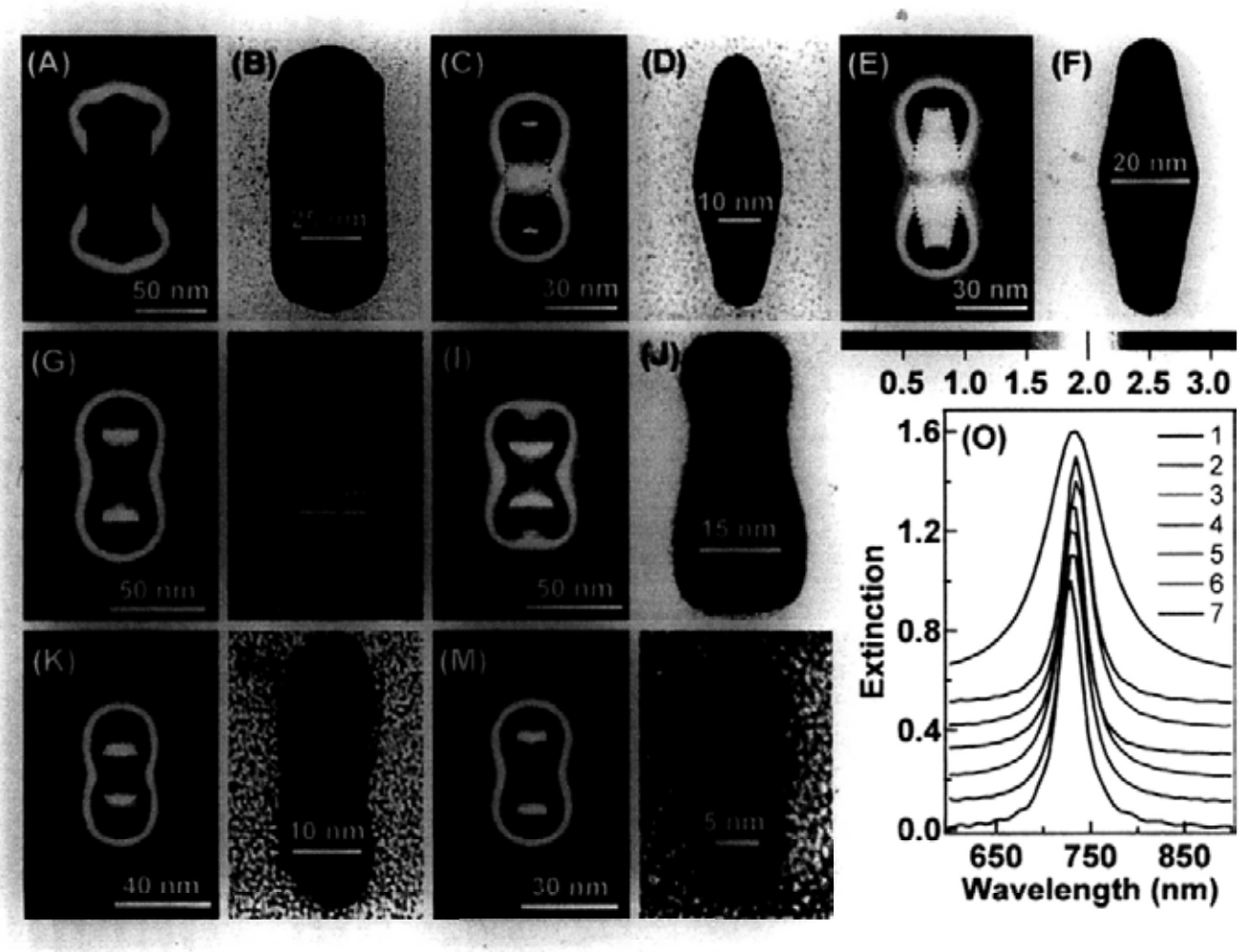


Figure 4.2.5. Electric field intensity enhancement contours (colored) and TEM images (gray) of the differently-shaped Au nanocrystals. (A, B) Large nanorods. (C, D) Nanobipyramids. (E, F) Large nanobipyramids. (G, H) Medium nanorods. (I, J) Dogbone-like nanorods. (K, L) Peanut-like nanorods. (M, N) Small nanorods. (O) Calculated extinction spectra of the Au nanocrystals embedded in water. The curves 1 to 7 represent the large nanorods, nanobipyramids, large nanobipyramids, medium nanorods, dogbone-like nanorods, peanut-like nanorods, and small nanorods, respectively. The field intensity enhancement is at the logarithmic scale.

Figure 4.2.5 shows the electric field intensity enhancement contours and the extinction spectra obtained from the FDTD calculations on the Au nanocrystals with seven different shapes. To better illustrate the shapes of the nanocrystals, the TEM images with each image containing a single nanocrystal are also provided. The extinction maxima for all of the seven samples are all located around 730 nm, suggesting that the numerical calculations agree well with the experiments. The electric field intensity enhancement is nonuniform around each nanocrystal. The enhancement at the end surfaces is generally much larger than that at the side surfaces. For the dogbone-like nanorod, the maximum enhancement is along the circular edge at the end, while for all of the other nanocrystals, the maximum enhancement is at the apex. The intensity enhancement decays rapidly away from the metal surface. From the field intensity enhancement contours, the maximum field intensity enhancement and the corresponding decay length of the enhancement are obtained and listed in Table 4.2.2. In addition, the FDTD calculations also give the scattering cross sections of the metal nanocrystals at their longitudinal plasmon resonance wavelengths. From the scattering cross sections, the polarizabilities are obtained and also included in Table 4.2.2. I plot the refractive index sensitivity as functions of different parameters of the Au nanocrystals in order to find out their effects on the index sensitivity. I first look at the geometrical parameters of the metal nanocrystals, including the particle volume and the local curvature, because in general, larger particle volumes lead to higher scattering cross sections and sharper local curvatures give larger local electric field enhancements. From the plots of the index sensitivity versus the particle volume (Figure 4.2.6A), no clear relationship is found. As the particle volume is increased from 2 000 to 20 000 $nm^3$, the index sensitivity varies between 150 and 300 nm/RIU without showing a clear trend. The particle volume of the large nanorods is 14 times that of the nanobipyramids, but the index sensitivity increases only from 301 to 326 nm/RIU. The particle volume of the nanobipyramids is smaller than that of the

dogbone-like nanorods, but the index sensitivity of the nanobipyramids is larger than that of the dogbone-like nanorods. There is no positive correlation between the index sensitivity and the local curvature either (Figure 4.2.6B). The effects of the parameters beyond the simple geometrical consideration on the index sensitivity need therefore to be further taken into account. I next look at the plasmon resonance-related properties, including the maximum electric field intensity enhancement, the product of the maximum field enhancement and the decay length, and the polarizability. Figure 4.2.6C shows the plot of the index sensitivity versus the maximum electric field intensity enhancement. It is postulated that larger electric field enhancements lead to higher polarization of the molecules in the surrounding medium. The polarized medium can partially neutralize the charge density at the metal surface and thus reduce the plasmon resonance energy. However, no positive correlation is observed between the index sensitivity and the maximum electric field intensity enhancement. In particular, the large nanorods possess the largest sensitivity but their field intensity enhancement is the smallest. The electric field intensity enhancement is usually the largest in the region adjacent to the metal surface. It decays rapidly away from the metal surface. Previous experiments on index change-based sensing have shown that the region within the range of 10–20 nm on the metal surface is the most sensitive [30, 31]. I therefore consider the product between the maximum field enhancement and the decay length. Figure 4.2.6D shows the plot of the index sensitivity versus this product. Again, no positive correlation is found. As mentioned above, the polarizability of metal nanocrystals plays an important role in the refractive index sensitivity. The index sensitivity is therefore plotted as a function of the polarizability, as shown in Figure 4.2.6E. There is no simple correlation between the index sensitivity and the polarizability, suggesting that there are also other factors taking effect on the index sensitivity. I therefore plot the index sensitivity as a function of the product between the nanocrystal

polarizability and the local curvature (Figure 4.2.6F). An approximate linear relationship is obtained. The index sensitivity increases as the polarizability–curvature product is increased, which is consistent with the above argument that both the polarizability and shape of metal nanocrystals play important roles on the index sensitivity.

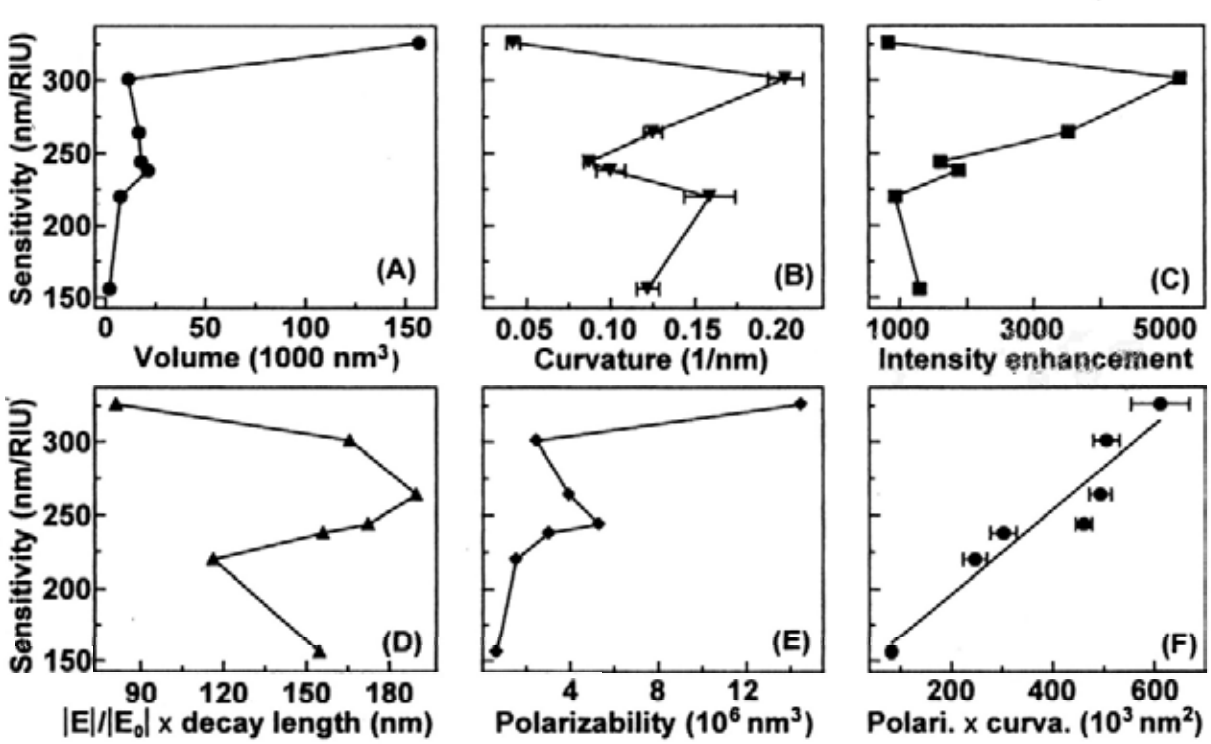


Figure 4.2.6. Relationship between the refractive index sensitivity and different parameters of the Au nanocrystals. (A) Nanocrystal volume. (B) End curvature. (C) Maximum electric field intensity enhancement. (D) Product of the maximum field enhancement and the decay length of the field intensity enhancement. (E) Polarizability. (F) Product of the polarizability and the end curvature.

The studies in the above two sections point out a potential direction for the design and synthesis of metal nanocrystals with superior refractive index sensing behaviors. Ideal nanocrystals for the use in the refractive index plasmonic sensing would have plasmon wavelengths in the

near-infrared region but shorter than the absorption wavelength of water. Moreover, they should also possess sharp curvatures and monodisperse shapes and sizes. On the other hand, it is also strongly desired to explore the possibility of employing these nanocrystals in fabricating the fundamental sensing devices. In the following section, I will demonstrate the utilizing of Au nanorods for fabricating optical fiber-based plasmonic sensors.

## 4.3 Optical Fiber-Excited Localized Surface Plasmon Resonance Sensor

Au nanorods are chosen to be deposited onto the core surface of an etched fiber, because their refractive index sensitivities are higher than the spherical Au nanocrystals and their yields are higher than those of Au nanobipyramids (§4.1). Commercial multimode optical fibers (Thorlabs, product code: AFS105/125Y, NA: 0.22) were used. The fibers are composed of a 105 μm pure fused silica core, a 125 μm doped fused silica cladding, and a 250 μm polyacrylate jacket. The polymer jacket was stripped off with a fiber stripper to open a window of ~6 cm in length, followed by chemical etching in aqueous 48 wt % hydrofluoric acid (HF) solutions. The etched fiber was rinsed with a copious amount of ethanol and blown dry with nitrogen. Figure 4.3.1A shows a SEM image of the optical fiber with a portion of the polymer jacket stripped off, and Figure 4.3.1B shows a SEM image of the fiber after being etched for 20 min. The remaining core is highly uniform along the fiber axis, with a diameter of 41 μm. The core diameter can be controlled by the etching time (Figure 4.3.1C – E). It decreases with increasing etching time (Figure 4.3.1F). In our experiment, the fiber cladding is completely removed and the diameter of the fiber core is controlled in the range of 40–50 μm.

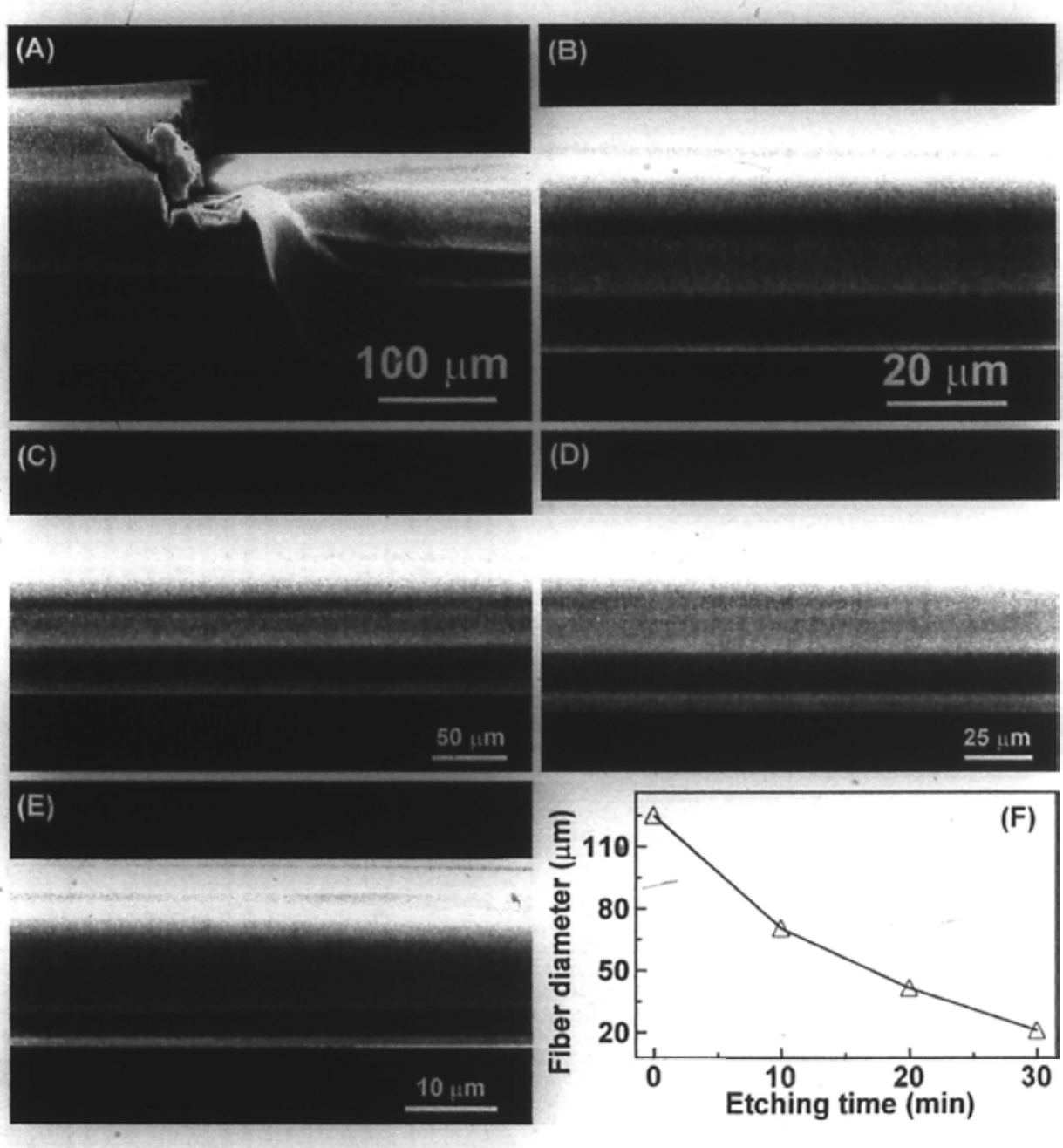


Figure 4.3.1. SEM images of the optical fibers. (A) SEM image of an optical fiber with polyacrylate jacket stripped. (B) SEM image of a chemically etched optical fiber. The diameter of the remaining core is 41 μm. (C – E) SEM images of the optical fibers that were etched with an aqueous 48 wt % HF solution for 0, 10, and 30 min, respectively. The stripes are due to charging during the SEM examination. (F) Dependence of the remaining core diameter on the etching time.

The Au nanorods were grown using the transverse overgrowth method. Their LLPWs can readily be controlled by varying the amount of the growth solution (Figure 4.3.2). They exhibit strong light scattering because of their large diameters [32], which is advantageous for scattering-based single-particle imaging and spectroscopy. For the deposition of the Au nanorods, the etched fiber core was first immersed into an ethanolic 10 vol % (3-mercaptopropyl)trimethoxysilane solution for 15 min to functionalize the core surface. The fiber was thereafter rinsed with ethanol and deionized water.

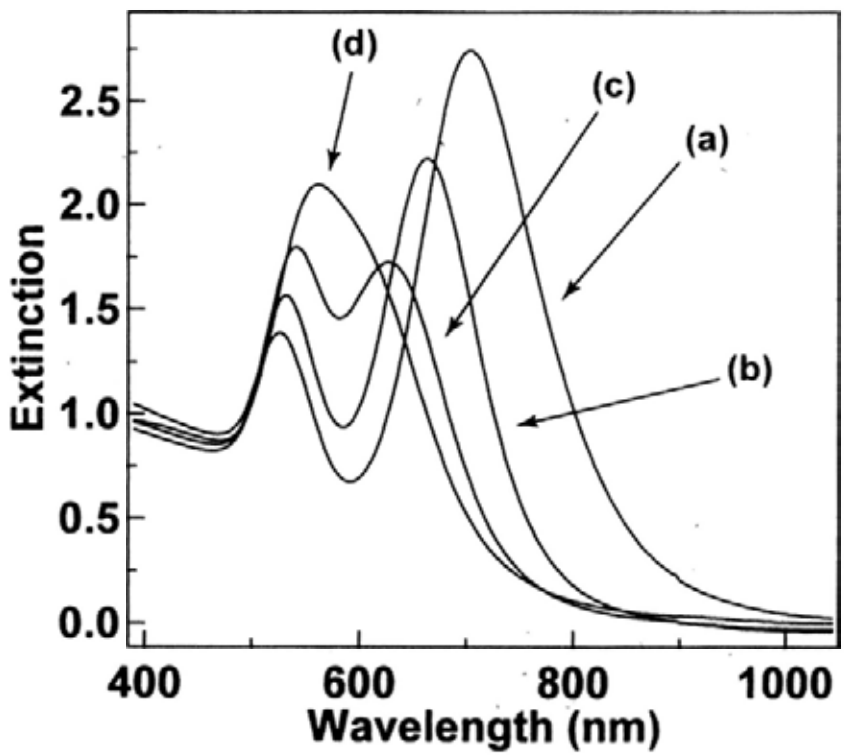


Figure 4.3.2. Extinction spectra of the Au nanorod samples that were obtained from the transverse overgrowth. The LLPWs of the nanorod samples (a) – (d) are 704, 663, 628, and 604 nm, respectively. The LLPW of the sample (d) is determined by double Gaussian fitting.

The transversely overgrown Au nanorods that were stabilized in aqueous 0.1 M CTAB solutions with an estimated particle concentration of ~0.2 nM were washed twice with water by centrifugation at 14 000 × g for 6 min to remove the excess surfactants and then dispersed into DI water to obtain a particle concentration of ~2 nM. The pH of the nanorod solution was adjusted to ~3 by adding HCl (0.1 M) to facilitate the deposition of the Au nanorods. The functionalized fiber core was immersed into the resulting nanorod solution for 30 s, followed immediately by rinsing with ethanol and water. The SEM images shown in Figure 4.3.3 indicate that the Au nanorods deposited onto the fiber core surface are well separated from each other without aggregation. Four overgrown nanorod samples were used. Their ensemble longitudinal plasmon wavelengths in water are 704, 663, 628, and 604 nm (Figure 4.3.2). Their average lengths/middle-section diameters are (85 ± 9)/(30 ± 4), (91 ± 8)/(38 ± 4), (97 ± 8)/(49 ± 5), and (99 ± 12)/(66 ± 8) nm, respectively.

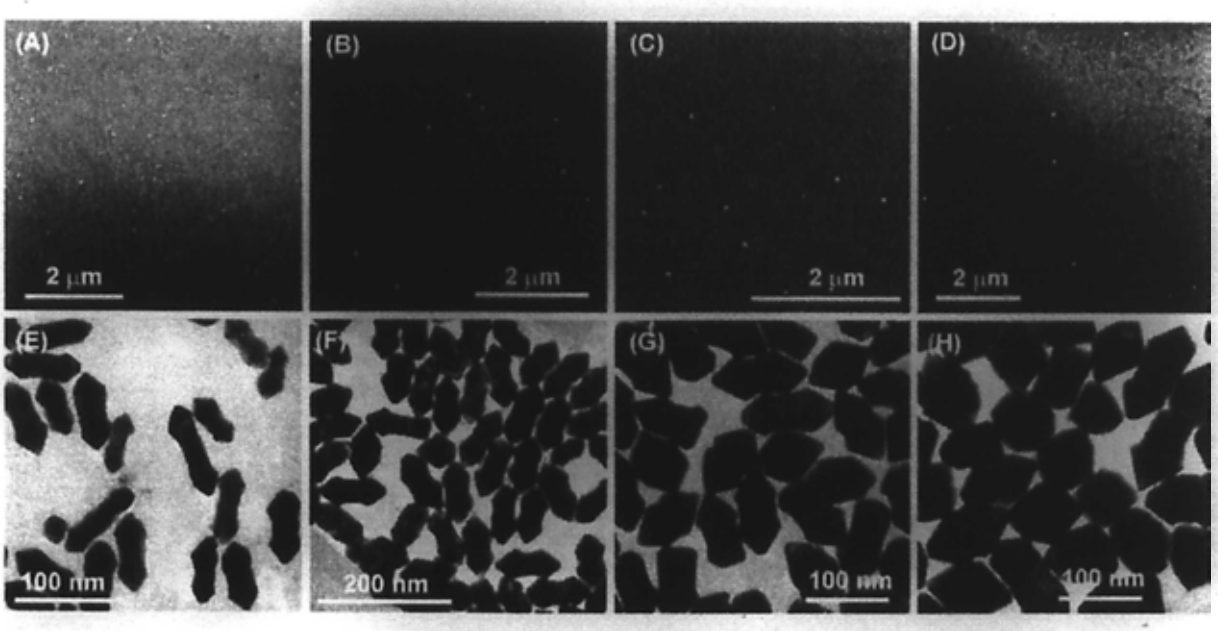


Figure 4.3.3. (A), (B), (C), and (D) SEM images of the Au nanorods deposited on the surface of the etched fiber core. The ensemble LLPWs of the nanorods when dispersed in water are 704, 663, 628, and 604 nm, respectively. Their corresponding TEM images are shown in (E), (F), (G), and (H),

respectively.

The fiber portion carrying the Au nanorods was mounted onto the sample stage under an objective (LMPlanFl, 100×, NA: 0.8) on an optical microscope (Olympus BX60) integrated with a spectrograph (Acton, model: SP-2300i) and a charge-coupled device (CCD, Princeton Instruments, PIXIS: 512B). The CCD was thermoelectrically cooled down to –50 °C. When one end of the optical fiber was coupled with a 200 W quartz tungsten halogen lamp (Oriel Instruments), a number of bright spots were observed on the fiber core surface. Their scattering intensity was so strong that they could even be recorded with a common digital camera (Nikon, Coolpix 4500) attached onto the eyepiece (Figure 4.3.4A). The surface number density of the Au nanorods can be controlled by varying the nanorod concentration and the fiber immersion time during deposition. Figure 4.3.4B and C show two representative CCD images of the nanorods that were deposited by immersing the fiber into the nanorod solutions of ~2 and ~20 nM, respectively, for 30 s. The resulting surface number densities are (7 ± 1) and (34 ± 4) per 100 $\mu m^2$. Moreover, the scattering color can be readily varied by using Au nanorods of different aspect ratios, as illustrated by a set of single-particle scattering spectra (Figure 4.3.4D) covering the wavelength from 560 to 660 nm. The high scattering cross sections and tunable scattering wavelengths allow for the studying of their sensing behaviors on the single-particle level.

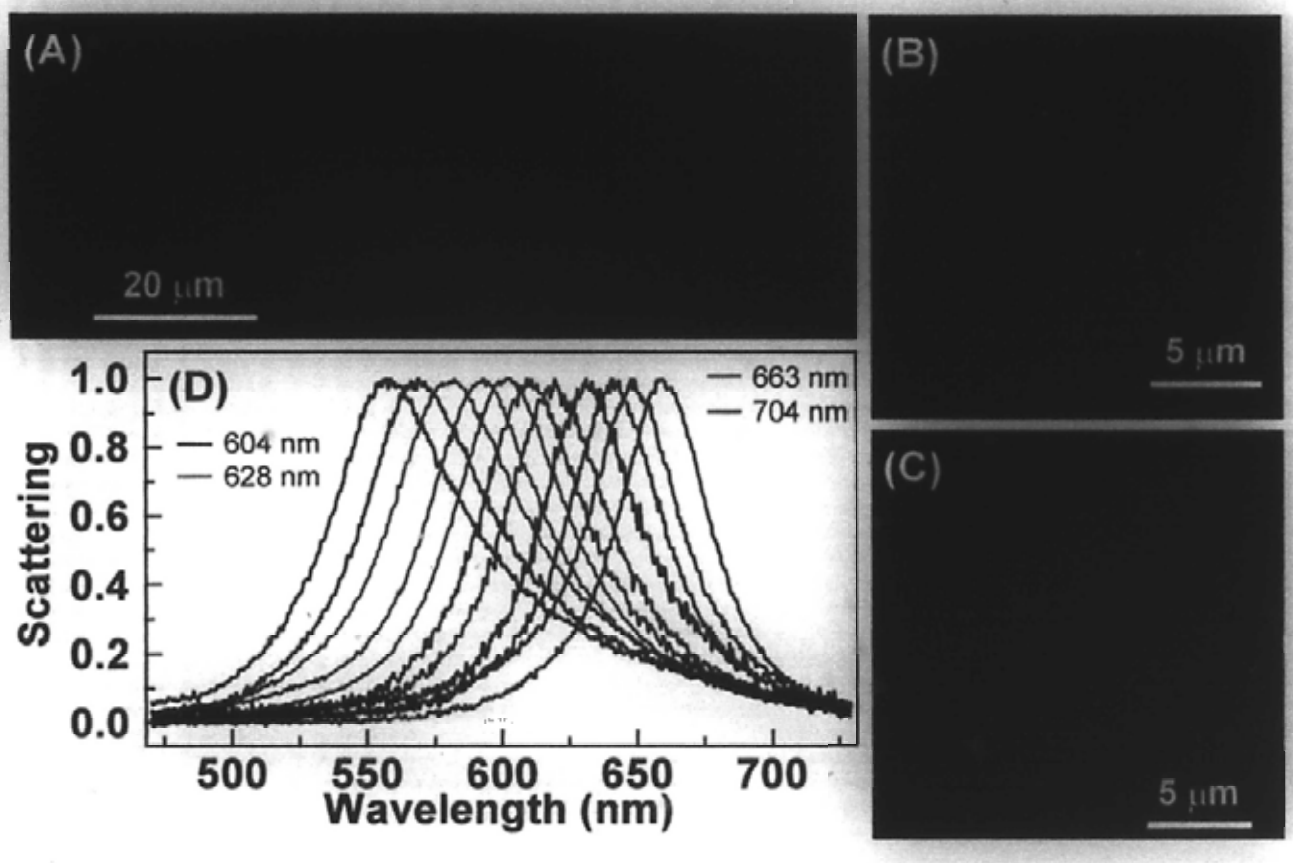


Figure 4.3.4. Single-particle scattering imaging and spectroscopy of Au nanorods. (A) True-color digital image (exposure time: 8 s) of the Au nanorods excited by the evanescent wave of an optical fiber. The blurred spots at the top and bottom are due to the defocus caused by the cylindrical shape of the fiber. (B) and (C) CCD images (exposure time: 5 s) of the same nanorod sample as in (A) at two different surface number densities. The color scales are different for the two images. The nanorod sample shown in (A) – (C) has an ensemble LLPW of 663 nm in water. (D) Representative normalized scattering spectra (exposure time: 60 s) of individual Au nanorods. The purple, green, blue, and red spectra are obtained from the four different nanorod samples. The optical fiber carrying the Au nanorods is kept in air.

The strong light scattering from the Au nanorods deposited on the unclad portion of the optical fiber results from the excitation of the longitudinal plasmon resonance of the nanorods by the

evanescent wave at the fiber core–air interface. For multimode fibers, the power fraction $\eta_p$ of the total light intensity in the evanescent wave can be calculated as [33],

$$\eta_p = \frac{4\sqrt{2}\lambda}{3\pi d\sqrt{n_1^2 - n_2^2}} \tag{4.3.1}$$

The penetration depth $\delta$, defined as the length where the intensity of the evanescent wave field decays to $1/e$, can be calculated from,

$$\delta = \frac{\lambda}{2\pi\sqrt{n_1^2 \sin^2\theta_i - n_2^2}} \tag{4.3.2}$$

In Equations (4.3.1) and (4.3.2), $\lambda$ is the wavelength of light, $d$ is the diameter of the fiber core, $n_1$ and $n_2$ are the refractive indices of the core and cladding, and $\theta_i$ is the incidence angle. If $n_1$ and $n_2$ are taken to be 1.46 for pure fused silica and 1.0 (1.33) for air (water), respectively, a 50 μm fiber core guiding 600 nm light contains 0.7% (1.2%) of the power in the evanescent wave. The minimal penetration depth corresponding to an incidence angle of 90° is calculated to be 90 (159) nm. The estimated penetration depth is comparable to the nanorod length and larger than the nanorod diameter, allowing for the excitation of the plasmon resonance of Au nanorods by the evanescent wave from the optical fiber.

A fluidic channel of ~0.2 mL in volume was fabricated by cutting poly(dimethylsiloxane) with a razor blade and sandwiching the channel between two glass slides (Fisher Scientific, catalog number: 12–544E, #1.5, 24 mm × 50 mm, 0.16–0.19 mm thick) in order to investigate the dependence of the resonance wavelength on the refractive index of the surrounding medium. The fiber carrying the Au nanorods in the unclad portion was placed close to the upper glass slide in the fluidic channel (Figure 4.3.5A) so that the scattering signal could be collected with a long working distance objective (LMPlanFl, 50 ×, NA: 0.5). Water–ethylene glycol mixtures were used to change the refractive index due to their lower viscosity compared with the water–glycerol mixtures,

allowing for the introduction of the mixture into the fluidic channel. The liquid mixture was introduced into the fluidic channel using a syringe. When a new mixture was introduced, the fluidic channel was flushed with a copious amount of the new mixture (~30 mL) in order to completely remove the previous mixture. Figure 4.3.5B shows a CCD image of the Au nanorods that are immersed in a water–ethylene glycol mixture and excited by the evanescent wave.

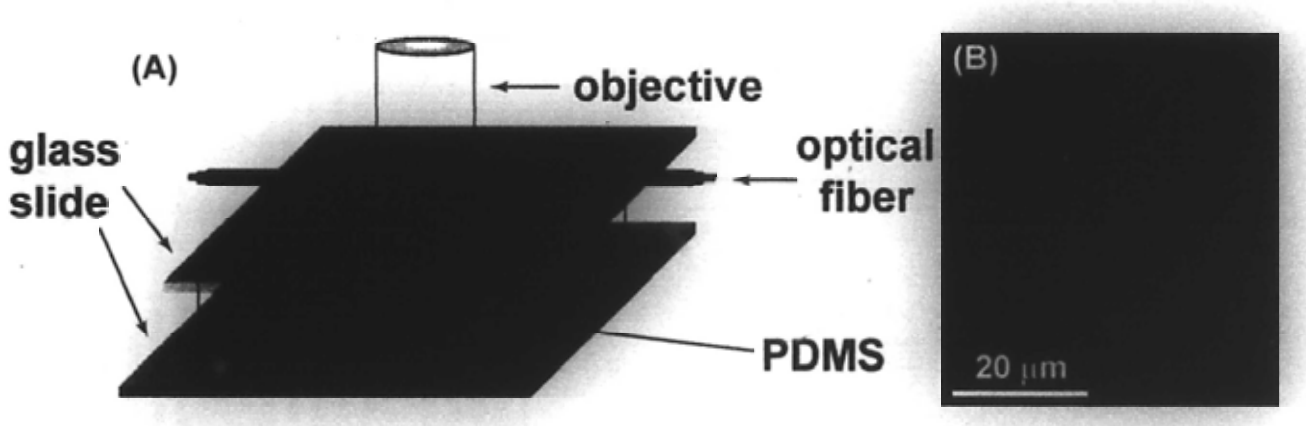


Figure 4.3.5. (A) Schematic showing the construction of the fluidic cell and the fiber-excited scattering imaging and spectroscopy of individual Au nanorods. (B) CCD scattering image (exposure time: 1 s) of the Au nanorods attached on an etched fiber core. The dashed lines indicate the edges of the fiber core.

As the volume percentage of ethylene glycol is increased, the scattering peak shifts steadily to longer wavelengths (Figure 4.3.6). According to the refractive index of the mixtures with different ethylene glycol volume ratios shown in Figure 4.3.6A, the index sensitivity is quantified by linear regression of the plot of the scattering peak wavelength as a function of the refractive index (Figure 4.3.6 right part). Linear regression yields slopes of 125–200 nm/RIU for the Au nanorods with LLPWs varying from 615 to 690 nm when dispersed in water. These index sensitivities are comparable to those (160–235 nm/RIU) determined for single Ag nanocrystals of various shapes,

including spheres, cubes, prisms, and rods [11, 12, 14, 34, 35]. The FOMs of the Au nanorods ranges from 2.2 to 3.8, which are comparable to those (1.6–3.3) measured for single triangular Ag nanoprisms [35]. Moreover, the index sensitivity and FOM of the Au nanorods are found to increase with the LLPW in an approximately linear fashion (Figure 4.3.6J). Several methods have been developed to make Au nanorods with high aspect ratios and thus large LLPWs [28, 36 – 38]. In addition, the plasmon resonance linewidth of Au nanorods has been found to decrease with increasing aspect ratios due to the reduction in the plasmon dephasing rate [39]. The index sensitivity and FOM can therefore be further increased by using Au nanorods of longer LLPWs. Au nanorods that have near-infrared LLPWs with high refractive index sensitivities and FOMs could offer opportunities for in vivo biological imaging and sensing because of the large penetration depth of near-infrared light (650–900 nm) into biological tissues [40].

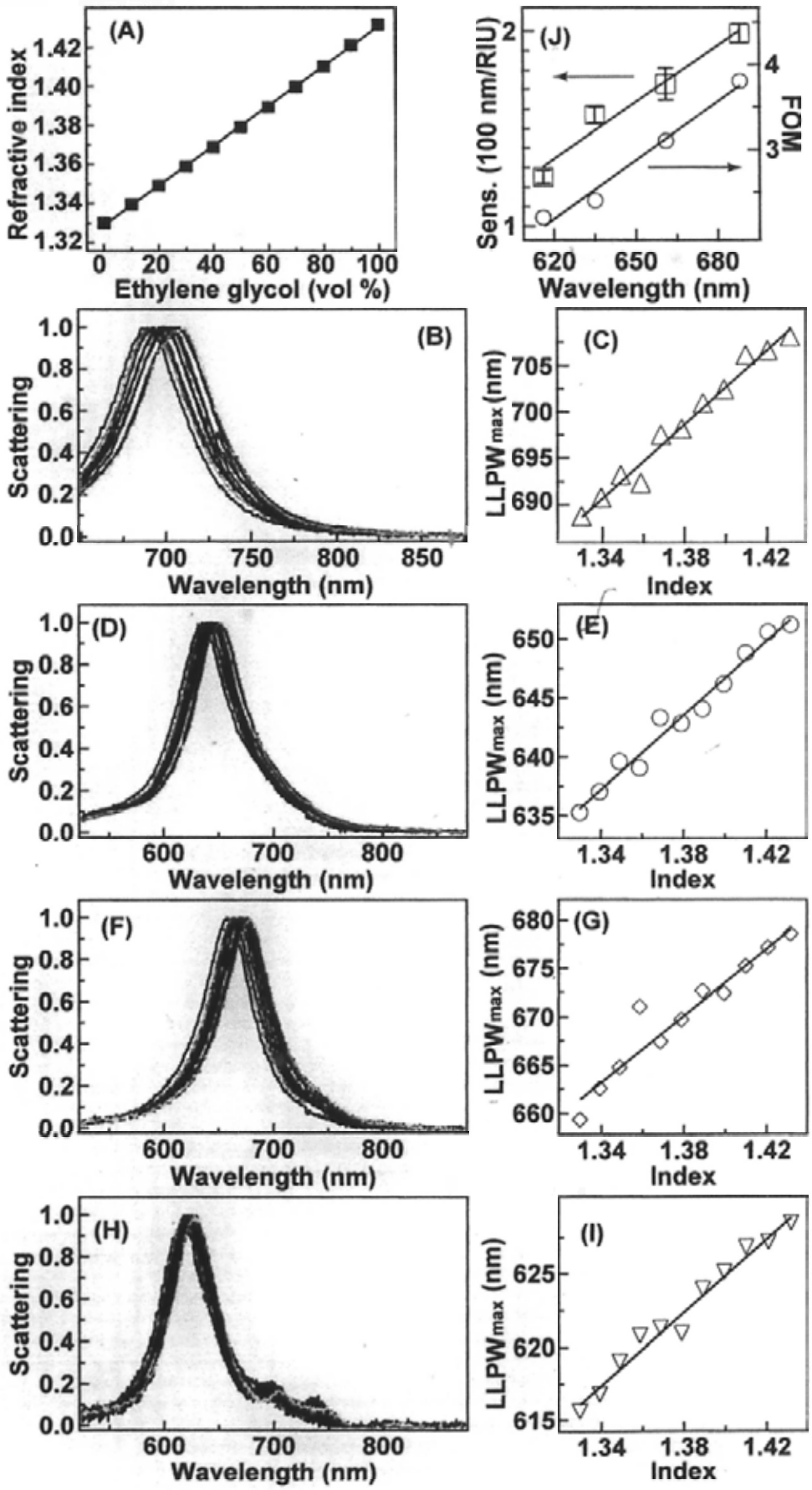
(A)
Refractive index
1.42
1.40
1.38
1.36
1.34
1.32
0
20
40
60
80
100
Ethylene glycol (vol %)
(J)
Sens. (100 nm/RIU)
2
1
FOM
4
3
620
650
680
Wavelength (nm)
(B)
Scattering
1.0
0.8
0.6
0.4
0.2
0.0
700
750
800
850
Wavelength (nm)
(C)
LLPW max (nm)
705
700
695
690
1.34
1.38
1.42
Index
(D)
Scattering
600
700
800
Wavelength (nm)
(E)
LLPW max (nm)
650
645
640
635
Index
(F)
Scattering
Wavelength (nm)
(G)
LLPW max (nm)
680
675
670
665
660
Index
(H)
Scattering
Wavelength (nm)
(I)
LLPW max (nm)
625
620
615
Index

Figure 4.3.6. (A) Dependence of the refractive index on the volume percentage of ethylene glycol for the water–ethylene glycol mixture. The line is a linear fit. (B), (D), (F), and (H), Normalized scattering spectra of four different Au nanorods in water–ethylene glycol mixtures of varying compositions. The exposure time for all of the spectra is 60 s. The two weak scattering peaks around 700 and 740 nm in (H) result from nearby nanorods. (C), (E), (G), and (I), Changes of the LLPW as a function of the refractive index of the surrounding medium for the four nanorods shown in (B), (D), (F), and (H), respectively. The lines are linear fits. The refractive index sensitivities determined for (B), (D), (F), and (H) are (199 ± 9), (157 ± 8), (173 ± 17), and (125 ± 7) nm/RIU, respectively. (J) Dependence of the index sensitivity (squares) and FOM (circles) on the LLPW of the Au nanorods. The LLPWs refer to the values when the Au nanorods are exposed to water.

One common type of operation configuration for optical fiber based sensors is the measurement of the transmission intensity loss. I therefore further measured the transmitted light spectra when the fiber carrying the Au nanorods was immersed in the liquid mixtures. For this measurement, one end of the fiber was positioned at the focus of a low-magnification objective (UMPlanFl, 20 ×, NA: 0.4), and the light from a tungsten halogen lamp (Ocean Optics, LS–1, 6.5 W) was coupled into the other end of the fiber (Figure 4.3.7A). The light from a central ~4 μm wide stripe area of the fiber end was collected by using a 0.35 mm wide entrance slit and dispersed onto the CCD. Figure 4.3.7B shows the acquired transmission spectra. As the index of the liquid mixture is increased, the transmitted light intensity integrated over the range of 500–900 nm decreases linearly (Figure 4.3.7C). Previous analysis has shown that the transmission intensity loss along the fiber can be ascribed to two major factors [41]. One is the change in the cladding index, which causes changes in the numerical aperture and critical angle for total internal reflection. The other is the absorption and scattering of

the Au nanorods that are excited by the evanescent wave. In order to reveal the contribution to the intensity loss by the deposited Au nanorods, the transmission spectrum obtained with the fiber exposed in air was used as a reference, and it was divided by the spectra obtained with the fiber immersed in the liquid mixtures. If there are no absorbing or scattering materials adsorbed on the etched fiber surface, the resulting spectra should exhibit no peaks because the variations of the refractive indices of the related materials (silica, air, water, and ethylene glycol) versus the light wavelength in the visible region are generally very smooth. However, two relatively sharp peaks are observed in the resulting spectra (Figure 4.3.7D). These two peaks result from the transverse and longitudinal surface plasmon resonances of the Au nanorods. The appearance of the plasmon resonance peaks of the Au nanorods indicates that the increase in the light intensity loss due to the plasmon resonance of the Au nanorods is larger than that due to the numerical aperture change as the index of the liquid mixture is increased. In addition, the appearance of both the transverse and longitudinal plasmon peaks is because both absorption and scattering contribute to the light intensity loss and absorption is dominant at the transverse longitudinal plasmon resonance wavelength (TLPW) for small-diameter Au nanorods [42, 43].

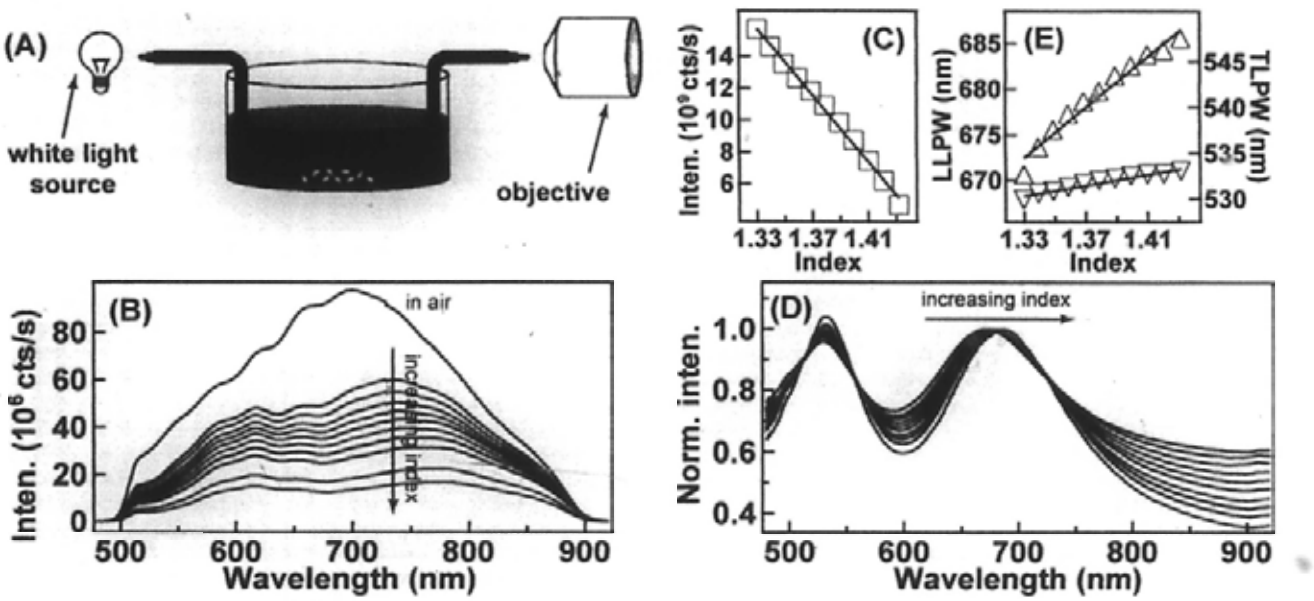


Figure 4.3.7. (A) Schematic showing the setup for measuring transmission spectra. (B) Transmission spectra (exposure time: 1.5–10 s) measured when the optical fiber carrying the Au nanorods is exposed to varying surrounding environments. The black spectrum is taken when the fiber is exposed in air, and the other spectra from the top to the bottom are acquired as the volume percentage of ethylene glycol is increased at a step of 10 vol %. (C) Transmission intensity integrated from 500 to 900 nm as a function of the refractive index. The line is a linear fit. (D) Corrected and normalized transmission spectra. (E) The dependence of the LLPW (upper triangles) and TLPW (lower triangles) on the index of the liquid mixture. The lines are linear fits, with index sensitivities of (138 ± 9) and (29 ± 2) nm/RIU, respectively. The nanorod sample used in this experiment has an ensemble LLPW of 663 nm when dispersed in water.

The transverse and longitudinal resonance increase linearly as the index of the liquid mixture is increased (Figure 4.3.7E). The slopes for the TLPW and LLPW are 29 and 138 nm/RIU, and the FOMs are 0.4 and 1.2, respectively. The larger slope and FOM exhibited by the LLPW suggest that the longitudinal plasmon resonance of the Au nanorods is more advantageous than the transverse

one for sensing applications. The index sensitivities and FOMs obtained from the transmission spectral measurement are ensemble average values. That the FOM of the LLPW obtained from the ensemble measurement is much smaller than those obtained from the single-particle measurement is mainly due to the inhomogeneous size distributions of the Au nanorods. The ensemble FWHM (~110 nm) of the Au nanorods is about twice that of single nanorods (55–65 nm). These results indicate that monodisperse Au nanorods are highly desired for optical fiber-based sensing applications based on the transmission spectral measurement.

## 4.4 Summary

In summary, I have systematically studied and compared the refractive index sensing behaviors of Au nanocrystals with various shapes, sizes, and plasmon resonance wavelengths. It is found that the refractive index sensitivity generally increases as the plasmon resonance wavelengths of the Au nanocrystals are increased. For a specific plasmon wavelength, Au nanocrystals with higher-curvature protrusions and larger polarizabilities exhibit higher refractive index sensitivities. Specifically, the refractive index sensitivities are found to increase linearly as the product between the curvature and the polarizability is increased. On the basis of these studies, I further deposited Au nanorods with different longitudinal plasmon wavelengths onto the core surface of an etched commercial optical fiber. The plasmonic resonance can be excited by the evanescent wave from the fiber, which enables the studies of the sensing behaviors of this optical fiber-based plasmonic sensor. It is found that the nanorod index sensitivity and FOM are linearly dependent on the LLPW and can reach up to 200 nm/RIU and 3.8, respectively. I have further characterized the response of the plasmon resonance of ensemble nanorods by measuring the transmitted light spectra. The ensemble index sensitivity and FOM of the longitudinal plasmon resonance are found to be 138 nm/RIU and

1.2, respectively. All these findings are believed to not only further the understanding of the mechanisms of the plasmonic sensing of metal nanocrystals but also facilitate the development of real-time, low-cost, ultrasensitive, and multiplexed sensors for industrial, environmental, and clinical applications.

## References

[1] E. M. Larsson, J. Alegret, M. Käll, D. S. Sutherland, Sensing Characteristics of NIR Localized Surface Plasmon Resonances in Gold Nanorings for Application as Ultrasensitive Biosensors. *Nano Lett.*, 7: 1256, 2007.

[2] M. D. Malinsky, K. L. Kelly, G. C. Schatz, R. P. Van Duyne, Chain Length Dependence and Sensing Capabilities of the Localized Surface Plasmon Resonance of Silver Nanoparticles Chemically Modified with Alkanethiol Self-Assembled Monolayers. *J. Am. Chem. Soc.*, 123: 1471, 2001.

[3] A. J. Haes, R. P. Van Duyne, A Nanoscale Optical Biosensor: Sensitivity and Selectivity of an Approach Based on the Localized Surface Plasmon Resonance Spectroscopy of Triangular Silver Nanoparticles. *J. Am. Chem. Soc.*, 124: 10596, 2002.

[4] C. R. Yonzon, E. Jeoung, S. L. Zou, G. C. Schatz, M. Mrksich, R. P. Van Duyne, A Comparative Analysis of Localized and Propagating Surface Plasmon Resonance Sensors: The Binding of Concanavalin A to a Monosaccharide Functionalized Self-Assembled Monolayer. *J. Am. Chem. Soc.*, 126: 12669, 2004.

[5] J. C. Riboh, A. J. Haes, A. D. McFarland, C. R. Yonzon, R. P. Van Duyne, A Nanoscale Optical Biosensor: Real-Time Immunoassay in Physiological Buffer Enabled by Improved Nanoparticle Adhesion. *J. Phys. Chem. B*, 107: 1772, 2003.

[6] A. J. Haes, W. P. Hall, L. Chang, W. L. Klein, R. P. Van Duyne, A Localized Surface Plasmon Resonance Biosensor: First Steps toward an Assay for Alzheimer's Disease. *Nano Lett.*, 4: 1029, 2004.

[7] A. J. Haes, L. Chang, W. L. Klein, R. P. Van Duyne, Detection of a Biomarker for Alzheimer's Disease from Synthetic and Clinical Samples Using a Nanoscale Optical Biosensor. *J. Am. Chem. Soc.*, 127: 2264, 2005.

[8] J. Yang, J.-C. Wu, Y.-C. Wu, J.-K. Wang, C.-C. Chen, Organic Solvent Dependence of Plasma Resonance of Gold Nanorods: A Simple Relationship. *Chem. Phys. Lett.*, 416: 215, 2005.

[9] C. X. Yu, J. Irudayaraj, Quantitative Evaluation of Sensitivity and Selectivity of Multiplex NanoSPR Biosensor Assays. *Biophys. J.*, 93: 3684, 2007.

[10] C. L. Wu, Q.-H. Xu, Stable and Functionable Mesoporous Silica-Coated Gold Nanorods as Sensitive Localized Surface Plasmon Resonance (LSPR) Nanosensors. *Langmuir*, 25: 9441, 2009.

[11] J. J. Mock, D. R. Smith, S. Schultz, Local Refractive Index Dependence of Plasmon Resonance Spectra from Individual Nanoparticles. *Nano Lett.*, 3: 485, 2003.

[12] A. D. McFarland, R. P. Van Duyne, Single Silver Nanoparticles as Real-Time Optical Sensors with Zeptomole Sensitivity. *Nano Lett.*, 3: 1057, 2003.

[13] G. Raschke, S. Brogl, A. S. Sucha, A. L. Rogach, T. A. Klar, J. Feldmann, B. Fieres, N. Petkov, T. Bein, A. Nichtl, K. Kürzinger, Gold Nanoshells Improve Single Nanoparticle Molecular Sensors. *Nano Lett.*, 4: 1853, 2004.

[14] L. J. Sherry, S.-H. Chang, G. C. Schatz, R. P. Van Duyne, B. J. Wiley, Y. N. Xia, Localized Surface Plasmon Resonance Spectroscopy of Single Silver Nanocubes. *Nano Lett.*, 5: 2034, 2005.

[15] C. Novo, A. M. Funston, I. Pastoriza-Santos, L. M. Liz-Marzán, P. Mulvaney, Influence of the Medium Refractive Index on the Optical Properties of Single Gold Triangular Prisms on a Substrate. *J. Phys. Chem. C*, 112: 3, 2008.

[16] R. Bukasov, J. S. Shumaker-Parry, Highly Tunable Infrared Extinction Properties of Gold Nanocrescents. *Nano Lett.*, 7: 1113, 2007.

[17] W. H. Ni, H. J. Chen, X. S. Kou, M. H. Yeung, J. F. Wang, Optical Fiber-Excited Surface Plasmon Resonance Spectroscopy of Single and Ensemble Gold Nanorods. *J. Phys. Chem. C*, 112: 8105, 2008.

[18] N. Nath, A. Chilkoti, A Colorimetric Gold Nanoparticle Sensor to Interrogate Biomolecular Interactions in Real Time on a Surface. *Anal. Chem.*, 74: 504, 2002.

[19] S.-F. Cheng, L.-K. Chau. Colloidal Gold-Modified Optical Fiber for Chemical and Biochemical Sensing. *Anal. Chem.*, 75: 16, 2003.

[20] K. Mitsui, Y. Handa, K. Kajikawa. Optical Fiber Affinity Biosensor Based on Localized Surface Plasmon Resonance. *Appl. Phys. Lett.*, 85: 4231, 2004.

[21] A. K. Sharma, B. D. Gupta. Fibre-Optic Sensor Based on Surface Plasmon Resonance with Ag–Au Alloy Nanoparticle Films. *Nanotechnology*, 17: 124, 2006.

[22] L.-K. Chau, Y.-F. Lin, S.-F. Cheng, T.-J. Lin. Fiber-Optic Chemical and Biochemical Probes Based on Localized Surface Plasmon Resonance. *Sens. Actuators B*, 113: 100, 2006.

[23] H. J. Chen, X. S. Kou, Z. Yang, W. H. Ni, J. F. Wang, Shape- and Size-Dependent Refractive Index Sensitivity of Gold Nanoparticles. *Langmuir*, 24: 5233, 2008.

[24] X. S. Kou, W. H. Ni, C.-K. Tsung, K. Chan, H.-Q. Lin, G. D. Stucky, J. F. Wang, Growth of Gold Bipyramids with Improved Yields and Their Curvature-Directed Oxidation. *Small*, 3: 2103, 2007.

[25] B. Nikoobakht, M. A. El-Sayed, Evidence for Bilayer Assembly of Cationic Surfactants on the Surface of Gold Nanorods. *Langmuir*, 17: 6368, 2001.

[26] R. Mehra, Application of Refractive Index Mixing Rules in Binary Systems of Hexadecane and Heptadecane with N-Alkanols at Different Temperatures. *Proc. Indian Acad. Sci. (Chem. Sci.)*, 115: 147, 2003.

[27] H. Wang, D. W. Brandl, F. Le, P. Nordlander, N. J. Halas, Nanorice: A Hybrid Plasmonic Nanostructure. *Nano Lett.*, 6: 827, 2006.

[28] X. S. Kou, S. Z. Zhang, C.-K. Tsung, Z. Yang, M. H. Yeung, G. D. Stucky, L. D. Sun, J. F. Wang, C. H. Yan, One-Step Synthesis of Large-Aspect-Ratio Single-Crystalline Gold Nanorods by Using CTPAB and CTBAB Surfactants. *Chem. Eur. J.*, 13 : 2929, 2007.

[29] M. M. Miller, A. A. Lazarides, Sensitivity of Metal Nanoparticle Surface Plasmon Resonance to the Dielectric Environment. *J. Phys. Chem. B*, 109: 21556, 2005.

[30] A. V. Whitney, J. W. Elam, S. L. Zou, A. V. Zinovev, P. C. Stair, G. C. Schatz, R. P. Van Duyne, Localized Surface Plasmon Resonance Nanosensor: A High-Resolution Distance-Dependence Study Using Atomic Layer Deposition. *J. Phys. Chem. B*, 109: 20522, 2005.

[31] S. M. Marinakos, S. H. Chen, A. Chilkoti, Plasmonic Detection of a Model Analyte in Serum by a Gold Nanorod Sensor. *Anal. Chem.*, 79: 5278, 2007.

[32] P. K. Jain, K. S. Lee, I. H. El-Sayed, M. A. El-Sayed. Calculated Absorption and Scattering Properties of Gold Nanoparticles of Different Size, Shape, and Composition: Applications in Biological Imaging and Biomedicine. *J. Phys. Chem. B*, 110: 7238, 2006.

[33] D. Gloge. Weakly Guiding Fibers. *Appl. Opt.*, 10: 2252, 1971.

[34] L. J. Sherry, R. C. Jin, C. A. Mirkin, G. C. Schatz, R. P. Van Duyne. Localized Surface Plasmon Resonance Spectroscopy of Single Silver Triangular Nanoprisms. *Nano Lett.*, 6: 2060, 2006.

[35] G. Raschke, S. Kowarik, T. Franzl, C. Sönnichsen, T. A. Klar, J. Feldmann, A. Nichtl, K. Kurzinger. Biomolecular Recognition Based on Single Gold Nanoparticle Light Scattering. *Nano Lett.*, 3: 935, 2003.

[36] B. Nikoobakht, M. A. El-Sayed. Preparation and Growth Mechanism of Gold Nanorods (NRs)

Using Seed-Mediated Growth Method. *Chem. Mater.*, 15: 1957, 2003.

[37] C.-K. Tsung, X. S. Kou, Q. H. Shi, J. P. Zhang, M. H. Yeung, J. F. Wang, G. D. Stucky. Selective Shortening of Single-Crystalline Gold Nanorods by Mild Oxidation. *J. Am. Chem. Soc.*, 128: 5352, 2006.

[38] X. S. Kou, S. Z. Zhang, C.-K. Tsung, M. H. Yeung, Q. H. Shi, G. D. Stucky, L. D. Sun, J. F. Wang, C. H. Yan. Growth of Gold Nanorods and Bipyramids Using CTEAB Surfactant. *J. Phys. Chem. B*, 110: 16377, 2006.

[39] C. Sönnichsen, T. Franzl, T. Wilk, G. von Plessen, J. Feldmann. Drastic Reduction of Plasmon Damping in Gold Nanorods. *Phys. Rev. Lett.*, 88: 077402, 2002.

[40] R. A. Weissleder. Clearer Vision for *in vivo* Imaging. *Nat. Biotechnol.*, 19: 316, 2001.

[41] J.-P. Conzen, J. Bürck, H.-J. Ache. Characterization of a Fiberoptic Evanescent-Wave Absorbency Sensor for Nonpolar Organic Compounds. *Appl. Spectrosc.*, 47: 753, 1993.

[42] K.-S. Lee, M. A. El-Sayed. Dependence of the Enhanced Optical Scattering Efficiency Relative to that of Absorption for Gold Metal Nanorods on Aspect Ratio, Size, End-Cap Shape, and Medium Refractive Index. *J. Phys. Chem. B*, 109: 20331, 2005.

[43] W. H. Ni, X. S. Kou, Z. Yang, J. F. Wang, Tailoring Longitudinal Surface Plasmon Wavelengths, Scattering and Absorption Cross Sections of Gold Nanorods. *ACS Nano*, 2: 677, 2008.

# Chapter 5

# Plasmon Coupling in Clusters Composed of Two-Dimensionally Ordered Gold Nanocubes

The results in the previous chapter show that for sensing applications it is strongly desired to have metal nanocrystals with longer plasmon wavelengths, more highly curvatured protrusions, and larger polarizabilities. Assembly of individual Au nanocrystals into complex superstructures provides an effective and promising approach, because metallic assemblies usually exhibit redshifted plasmon resonances and much larger polarizabilities [1 – 5]. Therefore studying the plasmonic coupling behaviors of Au nanocrystals is essential for the fabrication of novel and powerful plasmonic sensors. Moreover, assembling noble-metal nanostructures and studying the plasmonic properties of the resultant superstructures have several implications. First, when two metal nanocrystals are brought closely together, their plasmon resonances will be coupled together. The local electric field in the junction region is largely enhanced when the superstructure is irradiated at the coupled plasmon wavelength. The junction regions can therefore function as ''hot spots'' for plasmon-enhanced spectroscopies [6 – 10]. Because both the coupled plasmon wavelength and local field enhancement are exponentially sensitive to the interparticle

spacing [2, 11 – 13], the development of reproducible methods for the formation of metal nanostructure assemblies with well-controlled gaps is essential for the practical applications of plasmon-enhanced spectroscopies. Second, highly ordered, large scale assemblies of noble metal nanostructures can exhibit collective plasmonic properties that are distinct from those of isolated ones. For example, ordered arrays of Au nanorods can emit highly efficient multiphoton-excited photoluminescence, which can be ascribed to the giant enhancement and coupling of the longitudinal plasmon resonances of periodically, closely spaced Au nanorods [14, 15]. Ordered Au nanorod arrays can also exhibit strong resonance coupling with adsorbed molecular dyes [16]. The coupling strength can be easily engineered by varying the spectral overlap and spacing between the nanorod arrays and dye aggregates. Moreover, monodisperse Ag nanocrystals have been assembled into highly ordered, macroscopic plasmonic crystals. The interplay between the photonic states established by the periodic order and the plasmon resonances of Ag nanocrystals gives rise to tunable optical pass bands [17, 18]. Third, clusters composed of ordered noble metal nanocrystals are intermediate between isolated metal nanocrystals and bulk metals. Propagation of surface plasmon resonance modes supported at metal/dielectric interfaces can be tailored for the fabrication of miniaturized photonic circuits at length scales much smaller than those currently achieved [19, 20]. Studying the plasmonic properties of clusters composed of assembled metal nanocrystals can therefore help in understanding the transition from the localized plasmon resonance associated with isolated nanocrystals to the propagating one associated with metal/dielectric interfaces.

Previous experiments on the plasmon coupling have mainly focused on the investigation of the dependence of the plasmon shift on the spacing between two metal nanostructures [2, 11 – 13, 21 – 28]. The plasmon shift has been found to decay nearly exponentially with the interparticle spacing. In addition, the relationship between the plasmon shift and interparticle spacing has been employed

as a plasmonic ruler to measure and monitor dynamic distance changes in biology [3, 29, 30]. Most of these studies employed electron-beam lithography for fabricating the assemblies. Although electron-beam lithography offers controllability of the interparticle spacing over a wide range, due to its resolution limit the size and interparticle spacing of metal nanocrystals can only be varied above ~10 nm, which precludes the studies of the plasmon coupling near the limit of touching nanocrystals. Theoretical investigations have shown that two nearly touching nanocrystals exhibit rich plasmonic behaviors, including plasmon hybridization and splitting, inhibition of dipolar oscillations, the appearance of multipolar resonance modes, and the occurrence of singular behaviors [1, 31]. In addition, previous plasmon coupling studies have exclusively focused on noble metal nanostructure dimers with varying gaps. Until very recently did some reports mention that the coupling between Au nanorod dimers would depend on the specific orientation of the two nanorods [32 – 34]. However, only a few special cases have been considered in that report and there still have been no systematic investigations on the dependence of the plasmon coupling on the number of nanocrystals and their spatial arrangement. I therefore performed the studies on the plasmon coupling in clusters composed of two-dimensionally ordered gold nanocubes with different numbers and arrangement.

In §5.1, I will first describe the methods for the assembly and pattern matching of two-dimensionally ordered Au nanocube clusters. Then the plasmonic properties of the two-dimensionally ordered Au nanocube clusters will be studied both experimentally and theoretically in §5.2. It is found that these clusters exhibit rich plasmonic properties that are highly dependent on the number and ordering of the Au nanocubes. In §5.3 the nanocubes will further be welded together by thermal annealing. The plasmonic properties of the welded Au nanocubes are found to significantly differ from those before thermal treatment, suggesting that the gaps play a very important role in the plasmon coupling of Au nanostructures.

## 5.1 Assembly and Pattern Matching of Two-Dimensionally Ordered Gold Nanocube Clusters

Au nanocubes are chosen because they can readily assemble together on flat substrates owing to their flat faces. Moreover, finite-difference time-domain (FDTD) calculations indicate that the electric field enhancement in the junction region of Au nanocube dimers is much more uniform than that of Au nanosphere dimers (Figure 5.1.1). Such highly uniform field enhancements will be beneficial to plasmon-enhanced spectroscopies.

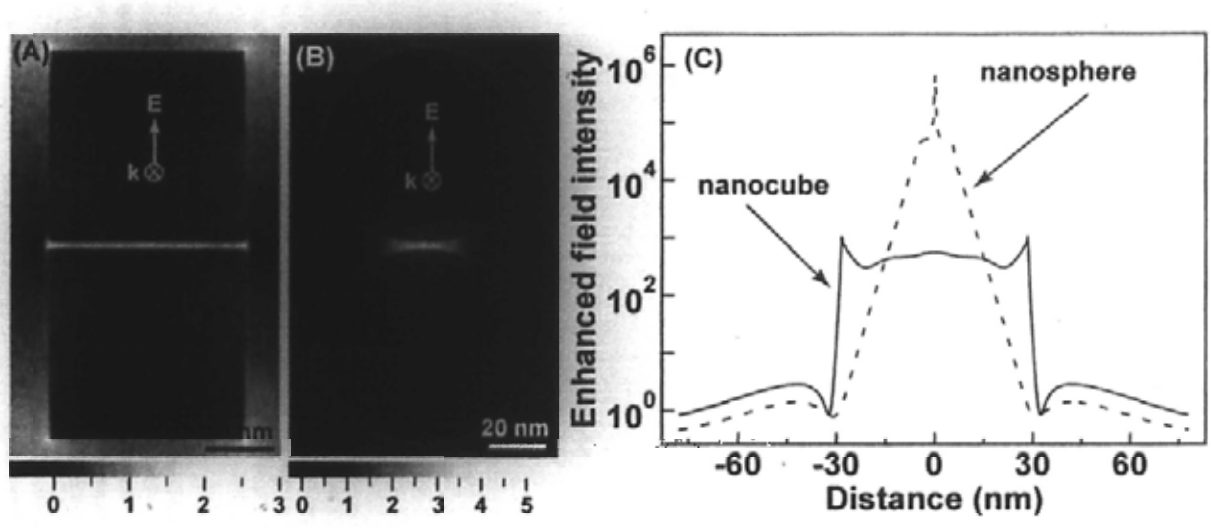


Figure 5.1.1. Electric-field-intensity enhancement contours of (A) a Au nanocube dimer and (B) a Au nanosphere dimer at the logarithmic scale. (C) Field intensity profiles in the middle of the gap along the direction perpendicular to the dimer axis. The edge length of the nanocube is 57 nm, and the interparticle spacing is 1.5 nm for both dimers. The volume of the nanosphere is equal to that of the nanocube. The dimers are excited at their plasmon resonance peak wavelengths, 727 and 694 nm for the nanocube and nanosphere dimer, respectively.

The Au nanocubes were synthesized according to the procedures described in Chapter 3. The yield of the nanocubes in the product is above 90% (Figure 5.1.2A). TEM images (Figure 5.1.2B – D) show that their sizes and shapes are relatively uniform, with an average edge length of (57 ± 2) nm. The edges and corners of these nanocubes are rounded. They are single-crystalline, as revealed by previous structural characterizations [35].

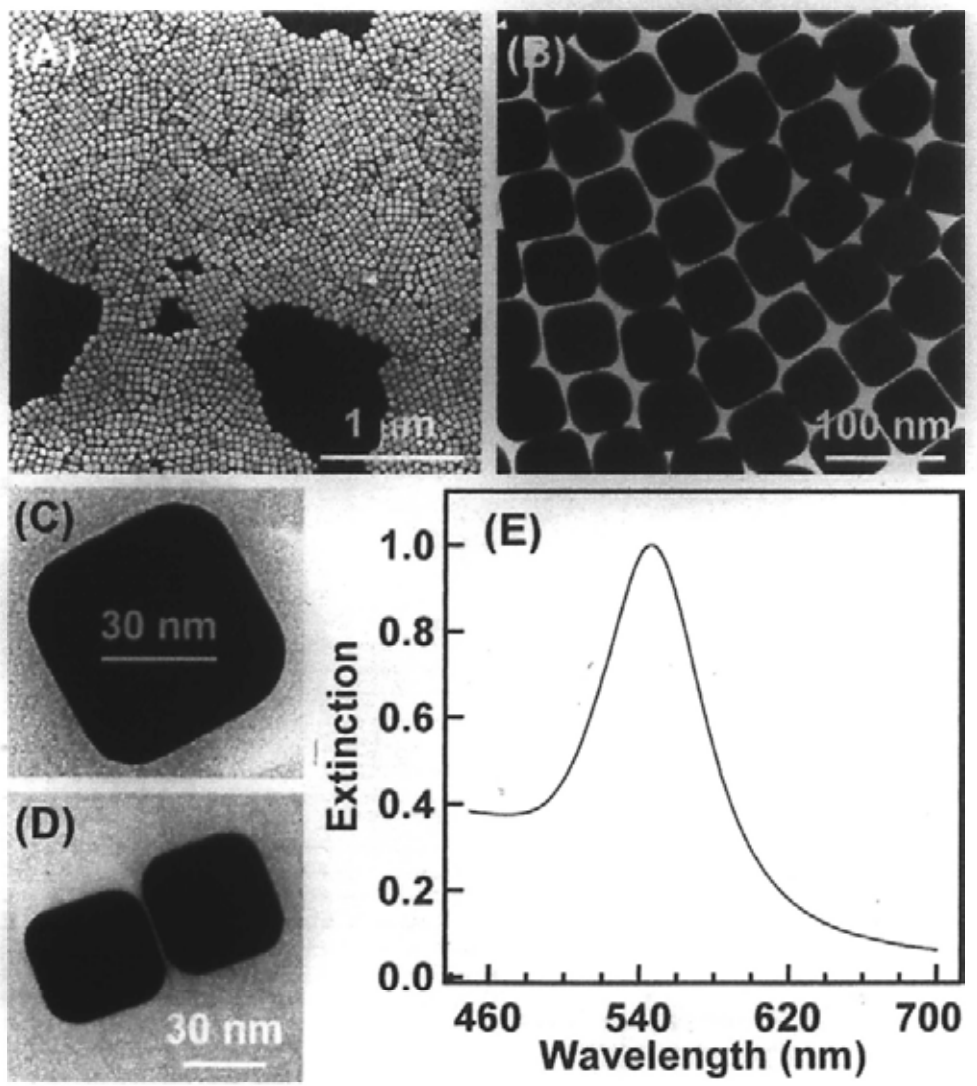


Figure 5.1.2. (A) SEM image and (B) TEM image of Au nanocubes. (C) TEM image of a single

nanocube. (D) TEM image of a nanocube dimer. (E) Normalized ensemble extinction spectrum of the Au nanocubes dispersed in aqueous solutions.

Clusters composed of two-dimensionally ordered Au nanocubes were formed by depositing the aqueous nanocube dispersions on indium tin oxide (ITO)-coated glass substrates and then drying the deposits naturally under ambient conditions [36]. The use of transparent and conductive ITO substrates allows the Au nanocubes to be characterized with both SEM and dark-field imaging simultaneously. The Au nanocubes tend to form patches of varying areas on ITO substrates through the joint actions of the capillary force established by the evaporating solvent and the van der Waals force between CTAB-encapsulated Au nanocubes. The amount of the nanocubes on substrate (the patch area) can be controlled by the concentration of the Au nanocube dispersions. The ITO substrate carrying the Au nanocubes was subjected to ultrasonication after deposition to remove loosely bound nanocubes. Figure 5.1.3A shows a representative SEM image of Au nanocube clusters scattered on the substrate. The number and ordering of nanocubes in each cluster can be revealed under high magnifications, as exemplified by a 2 × 2 cluster in Figure 5.1.3B. The Au nanocubes are observed to generally pack together face to face without sideways shifts in these clusters. Such close packing can be ascribed to the high size uniformity of these nanocubes. When neighboring nanocubes are in face-to-face contact, their contact area is maximized. Therefore the total interaction potential among the nanocubes in a cluster is minimized. A pattern matching method was employed to correlate the ordering of each cluster and its scattering spectrum. This method is illustrated by comparing the SEM image shown in Figure 5.1.3A and the scattering image shown in Figure 5.1.3C. For each bright spot in the scattering image, there is a corresponding nanocube cluster in the SEM image. The spatial distributions of the features in both images are

exactly the same. This observation, together with the fact that there are nearly 20 spots in both images, indicates that the same region is probed by SEM and dark-field imaging. After the correlation between SEM and dark-field images is established, the nanocube ordering (Figure 5.1.3B) and scattering spectrum (Figure 5.1.3D) of each cluster can be unambiguously characterized by SEM and dark-field spectroscopy, respectively.

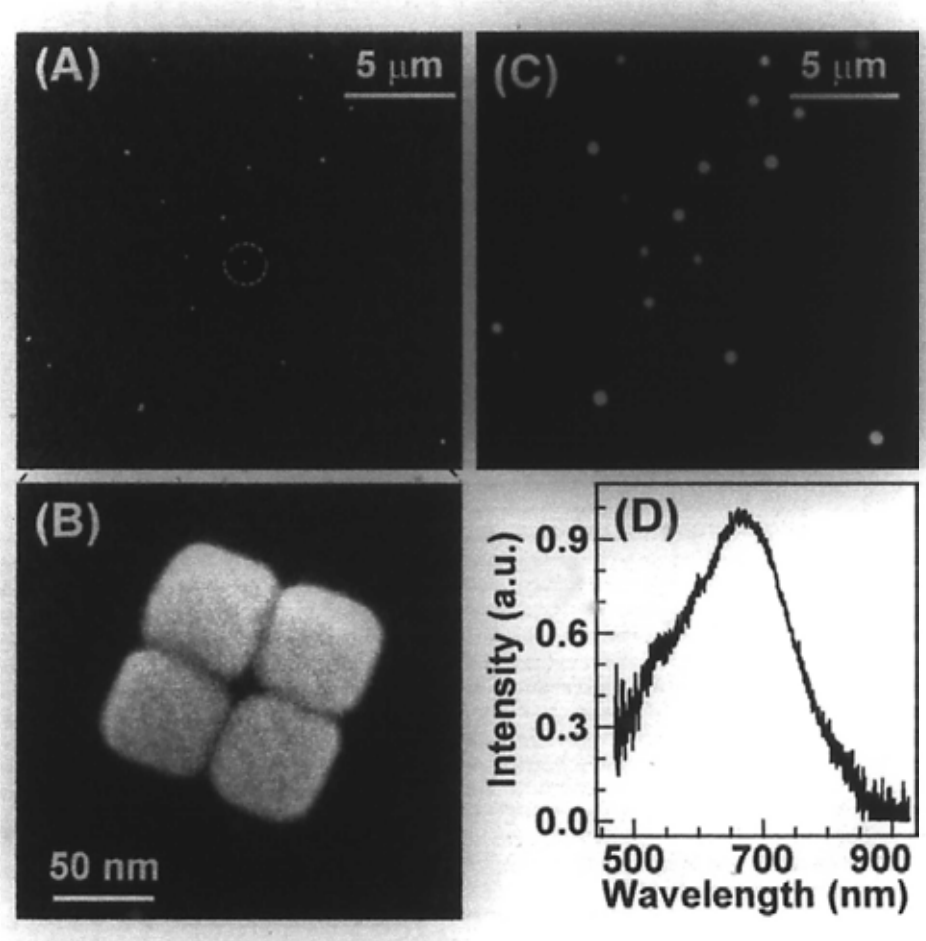


Figure 5.1.3. SEM images of (A) Au nanocube clusters distributed in a large area and (B) one 2 × 2 cluster. (C) Dark-field image corresponding to the SEM image shown in (A). The weak spots arise from the scattering of dust particles. (D) Scattering spectrum of the 2 × 2 cluster.

## 5.2 Plasmonic Properties of Clusters Composed of Two-Dimensionally Ordered Gold Nanocubes

The ordering and scattering spectra of the Au nanocube clusters with the number of nanocubes ranging from 1 to 9 were characterized. Figure 5.2.1A shows the SEM image of a single representative Au nanocube on an ITO substrate. Its scattering spectrum is shown in Figure 5.2.1B. Compared to the ensemble extinction spectrum (Figure 5.1.2E) of the nanocubes dispersed in aqueous solutions, the scattering spectrum of the single nanocube shows two distinct differences. One is the redshift of the plasmon resonance peak from 546 to 553 nm, and the other is the increase in the FWHM from 60 to 81 nm in spite of the inhomogeneous broadening associated with the ensemble spectrum. These differences can be ascribed to the use of ITO substrates to support the Au nanocubes.

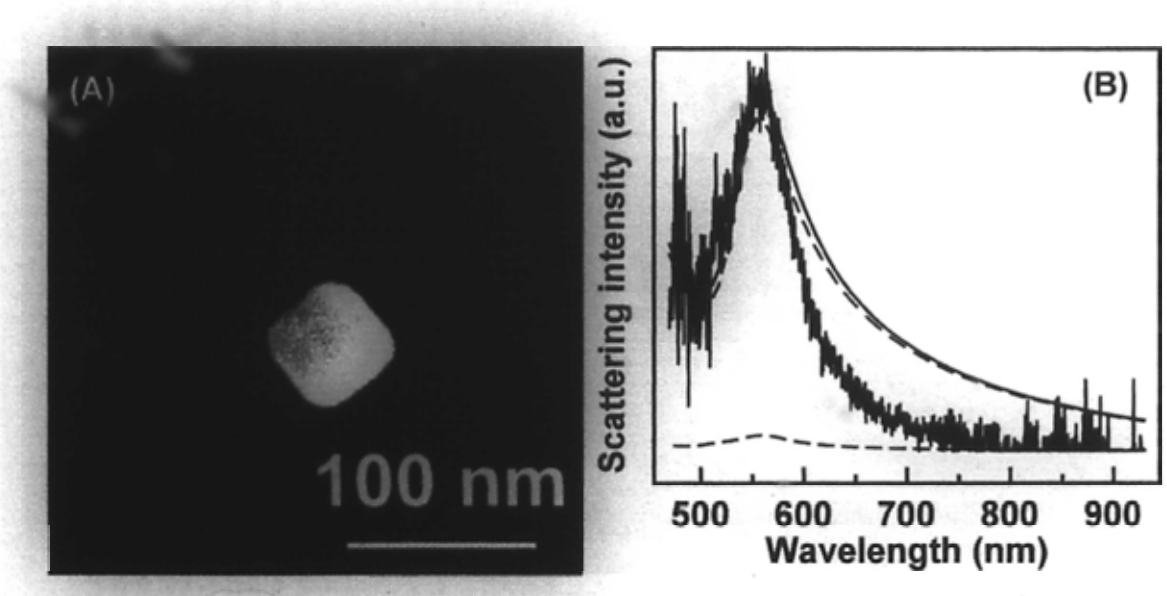


Figure 5.2.1. (A) SEM image of one Au nanocube. (B) Scattering spectrum of the nanocube. The black solid line is the experimental spectrum. The blue and red dashed lines are for the excitation polarized vertically and horizontally (along one edge of the nanocube). The red solid line is the sum

of the blue dashed line and the red dashed line multiplied by 2.

FDTD calculations were performed to understand the effect of the surrounding environment on the plasmon resonance of the Au nanocubes. A single nanocube immersed in water was first considered. The dielectric function of Au was formulated with a combination of the Drude and Lorentz model, with parameters chosen to match the experimental dielectric data as close as possible [37]. In calculation, an electromagnetic pulse with its wavelength ranging from 470 to 930 nm was launched into a box containing the target Au nanostructure to simulate a propagating plane wave interacting with the nanostructure. The Au nanostructure and its surrounding medium inside the box were divided into meshes of 0.5 nm in size. The electric field of the pulse was set parallel to one edge of the nanocube. The refractive index of the aqueous medium was taken to be 1.333. The edge length of the nanocube was set to the average value of 57 nm. In order to match the calculated spectrum with the experimental one, the edges and corners of the nanocube must be rounded. A rounding radius of 10 nm was found to give the best match between the calculated and experimental spectrum of Au nanocubes dispersed in water (Figure 5.2.2). These material and geometrical parameters of Au were then used in all of the following FDTD calculations.

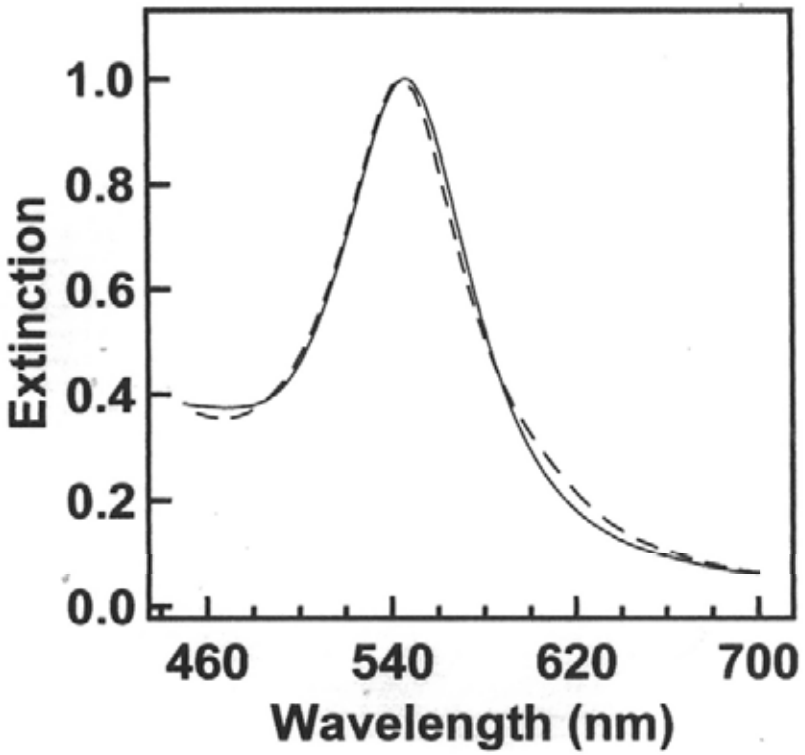


Figure 5.2.2. Experimental (black solid line) and FDTD calculated (red dashed line) extinction spectra of the Au nanocubes in aqueous solutions.

A nanocube sitting on an ITO substrate has a non-uniform surrounding medium. Its top and side faces are surrounded by air and its bottom face is in contact with the ITO substrate. The scattering peak wavelength obtained from the calculation with an index of 1.9 for the ITO substrate was found to be closest to the experimental one (Figure 5.2.1B, the red solid line). This value is in the typical index range reported for ITO thin films [38, 39]. It was subsequently used in our FDTD calculations for all of the nanocube clusters.

The surface area-averaged index of the surrounding medium for the nanocube sitting on the ITO substrate is 1.15, which is smaller than the water index of 1.333. A number of previous studies have shown that the plasmon resonance wavelength of noble metal nanostructures blueshifts with

decreasing indices of their surrounding media [8, 38, 40 – 45]. On the contrary, the calculated plasmon resonance peak of the nanocube on the ITO substrate is redshifted relative to that in water. This result suggests that the ITO substrate plays an important role in the plasmon resonance of the nanocube. The high permittivity of the ITO can induce large image charges, which will screen the Coulombic restoring force of the positive background in the nanocube and lead to the redshift of its LPW. Moreover, the increase in the calculated FWHM of the plasmon resonance peak can probably also be ascribed to the strong effect of the ITO substrate. In addition, the calculated FWHM, 110 nm, is larger than the experimental one (Figure 5.2.1B, the black solid line). This result is probably due to that a constant, real refractive index was employed for the ITO substrate in our FDTD calculations. However, experimental measurements have shown that the refractive index of ITO thin films is often complex, with its real part decreasing with increasing wavelength [38, 39].

FDTD calculations were further performed with different excitation polarizations, because in our experiments, the unpolarized excitation light is directed to the Au nanocubes from the top through a dark-field objective. The electric field can be decomposed into two components, with one perpendicular (vertically-polarized) and the other parallel (horizontally-polarized) to the substrate plane. The calculated spectra corresponding to the two polarization states are shown in Figure 5.2.1B (the red and the blue dashed lines). The scattering in the case of the vertically-polarized excitation is seen to contribute dominantly to the total scattering at the plasmon resonance wavelength. This result is consistent with our above assertion that the ITO substrate plays an important role on the plasmon resonance of the supported Au nanocubes.

A representative 1 × 2 nanocube dimer is shown in Figure 5.2.3A, and its scattering spectral properties are presented in Figure 5.2.3B. Because of the presence of CTAB on the surfaces of the Au nanocubes, there exists a small gap between neighboring nanocubes. Although the gap cannot be

identified clearly under SEM, our TEM imaging clearly shows the presence of a gap in the range of 1 to 2 nm (Figure 5.1.2B and 5.1.3D). When two nanocubes are placed close to each other, their plasmon resonances are coupled together. As a result, the nanocube dimer exhibits two plasmon resonance peaks. One is weaker at 550 nm. The other is stronger at 655 nm. The FDTD calculations indicate that these two plasmon resonance peaks arise from different excitation polarizations (Figure 5.2.3B).

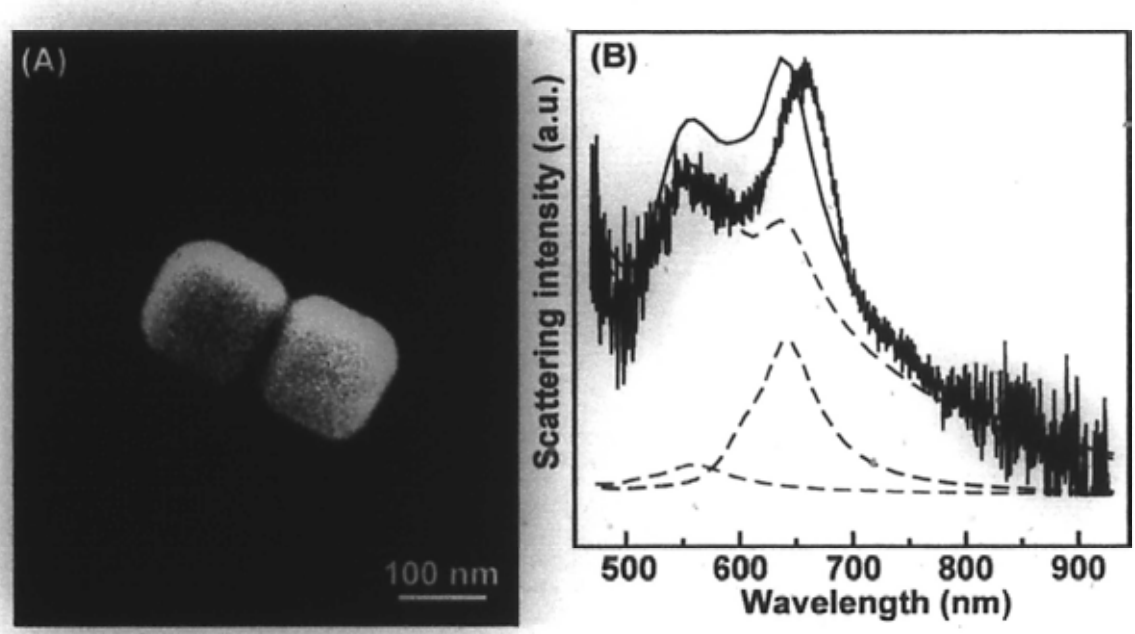


Figure 5.2.3. (A) SEM image of one 1 × 2 nanocube cluster. (B) Scattering spectrum of the nanocube cluster. The black solid line is the experimental spectrum. The colored spectra are obtained from the FDTD calculations. The excitation light is polarized horizontally for the red dashed line (along the dimer axis) and green dashed line (perpendicular to the dimer axis), and vertically for the blue dashed line. The red solid line is their sum.

The peak at 550 nm is predominantly contributed by the plasmon resonance under the

vertically-polarized excitation. The peak at 655 nm is jointly contributed by the plasmon resonance under the vertically-polarized excitation and that under the excitation polarized horizontally and parallel to the dimer axis. The plasmon resonance under the excitation polarized horizontally and perpendicular to the dimer axis makes only a slight contribution to the peak at 550 nm. The appearance of the two peaks under the vertically-polarized excitation can be ascribed to the strong interaction between the dipoles in the dimer and their images in the conductive ITO substrate as the dimer–substrate spacing is very small. Due to the high dielectric constant of the ITO (3.61), the non-uniform near-field around the cluster will induce large image charges. These charges will couple with the plasmonic resonance of the cluster and give rise to new resonance mode. This phenomenon has been observed before both theoretically and experimentally [46 – 50].

The low-energy resonance peak wavelength obtained from the FDTD calculations is 640 nm for the nanocube dimer, which is smaller than the experimental one by 15 nm. This inconsistency is due to that a mesh size of 0.5 nm was used in our FDTD calculations. The gap distance can only be set to the mesh size multiplied by an integer number. The gap distance employed in our calculations is 1.5 nm, by which the calculated low-energy peak wavelength is closest to the experimental one. This value is also used for all of the nanocube clusters during our calculations. If the actual gap distance is smaller than the used one, the experimental peak wavelength will be larger than the calculated one. On the contrary, if the actual gap distance is larger than the used one, the measured peak wavelength will be smaller than the calculated one. We have seen both cases since the actual gap distance between neighboring nanocubes fluctuates among different clusters.

Three Au nanocubes can form two types of clusters. One is 1 × 3 (Figure 5.2.4A), and the other is L type (Figure 5.2.4C). The 1 × 3 cluster exhibits two plasmon resonance peaks of comparable intensities, with one at 545 nm and the other at 780 nm (Figure 5.2.4B, the black line). The addition

of one more nanocube along the axial direction leads to the redshift of the low-energy plasmon resonance. As revealed by the FDTD calculations (Figure 5.2.4B, the colored lines), the respective contributions of the plasmon resonances under different excitation polarizations to the overall scattering spectrum are similar to those for the 1 × 2 cluster.

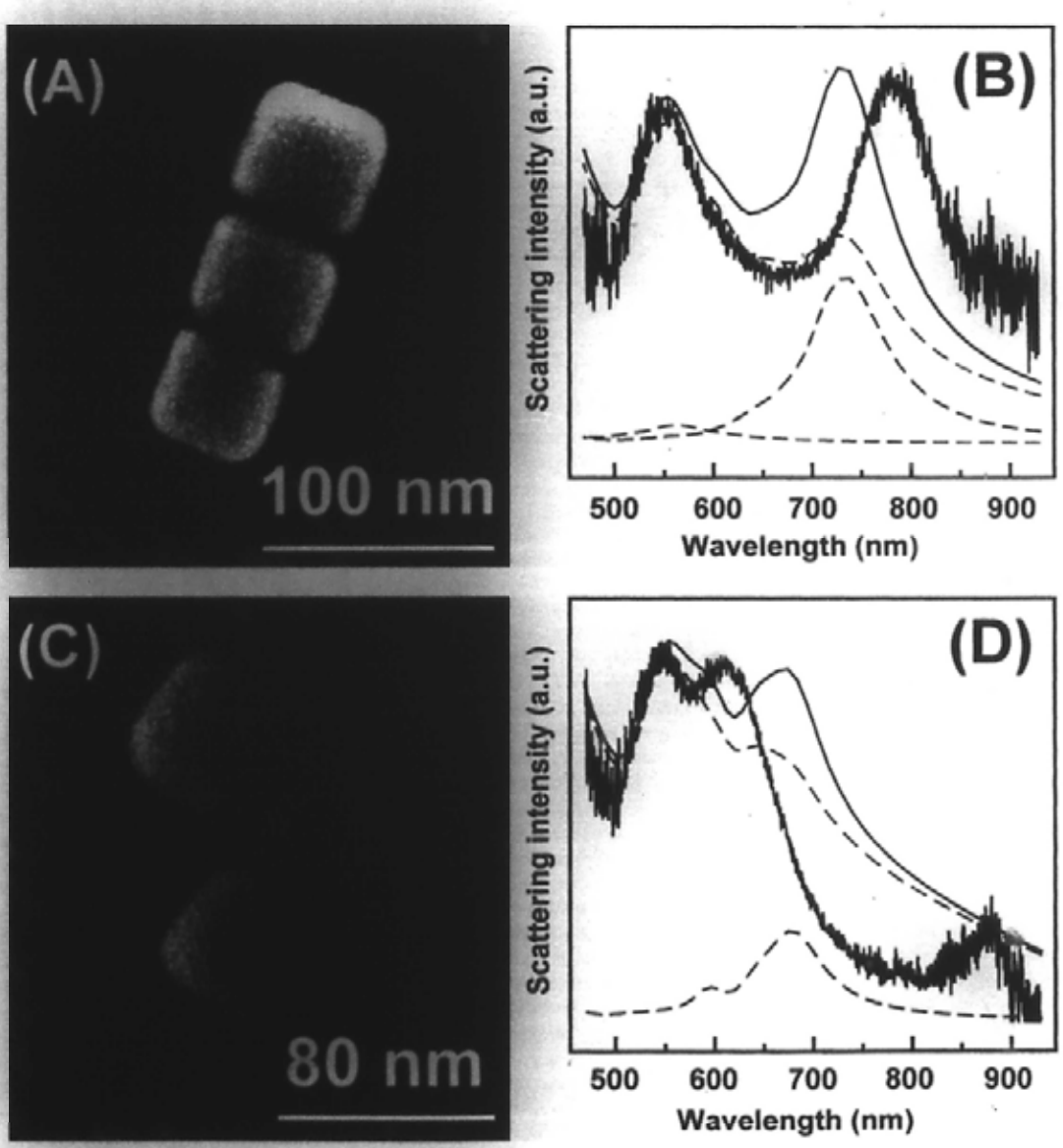


Figure 5.2.4. (A) SEM image of one 1 × 3 nanocube cluster. (B) Scattering spectrum of the 1 × 3 nanocube cluster. The black solid line is the experimental spectrum. The colored spectra are

obtained from the FDTD calculations. The excitation light is polarized horizontally for the red dashed line (along the dimer axis) and green dashed line (perpendicular to the dimer axis), and vertically for the blue dashed line. The red solid line is their sum. (C) SEM image of one 3: L type nanocube cluster. (D) Scattering spectrum of the 3: L type nanocube cluster. The black solid line is the experimental spectrum. The colored spectra are obtained from the FDTD calculations. The excitation polarization is horizontal for the red dashed line (along one edge of the L type cluster) and vertical for the blue dashed line. The red solid line is the sum of them.

The L type cluster also shows two peaks of comparable intensities. The first peak is positioned at 545 nm, and the second one is at 610 nm (Figure 5.2.4D, black line). The FDTD calculations show that the first peak is contributed by the plasmon resonance under the vertically-polarized excitation. The second peak contains joint contributions from the resonance under the vertically-polarized excitation and that under the excitation polarized horizontally and parallel to one edge (Figure 5.2.4D, colored lines). The calculated scattering spectrum under the horizontally-polarized excitation shows two peaks. The lower-energy, stronger one can be ascribed to the two connected nanocubes along the polarization direction, and the higher-energy, weaker one can be ascribed to the third nanocube at the side. The latter is overwhelmed by the neighboring stronger peaks on the experimental spectrum. If these two peaks are compared to those of the 1 × 2 dimer under the two horizontal excitation polarization states (Figure 5.2.3B), both peaks are significantly redshifted. These results, together with the clear difference in the scattering properties between the 1 × 3 and L type cluster, highlight the intriguing dependence of the plasmonic properties on the number and relative position of the Au nanocubes in a cluster.

Four types of ordering have been observed for the clusters containing four nanocubes,

including 1 × 4, 2 × 2 (Figure 5.2.5A), L type (Figure 5.2.5C), and T type (Figure 5.2.5E). The lower-energy plasmon resonance peak wavelength of the 1 × 4 cluster is beyond the upper wavelength limit of our detector. It is therefore not considered here. As shown in Figure 5.2.5B, the scattering spectrum of the 2 × 2 cluster is very broad and strong. The FDTD investigation reveals that it is composed of three peaks. The peak around 550 nm is contributed dominantly by the plasmon resonance under the vertically-polarized excitation. The peak around 670 nm contains joint contributions from the resonance under the vertically-polarized excitation and that under the horizontally-polarized excitation. A weak peak around 600 nm arises mainly from the resonance under the horizontally-polarized excitation.

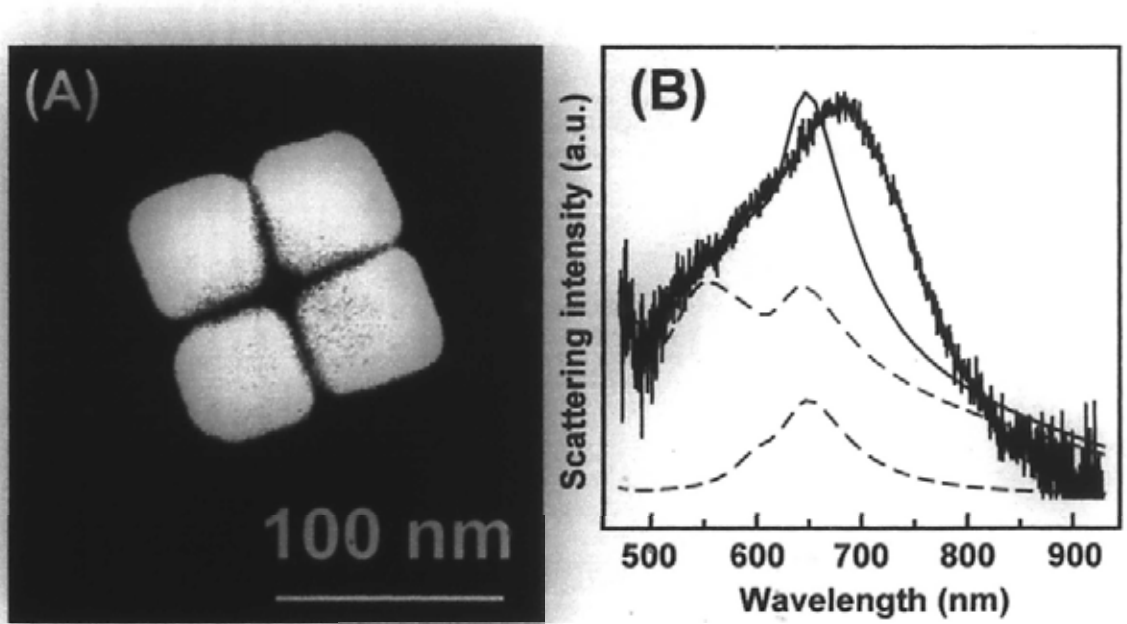

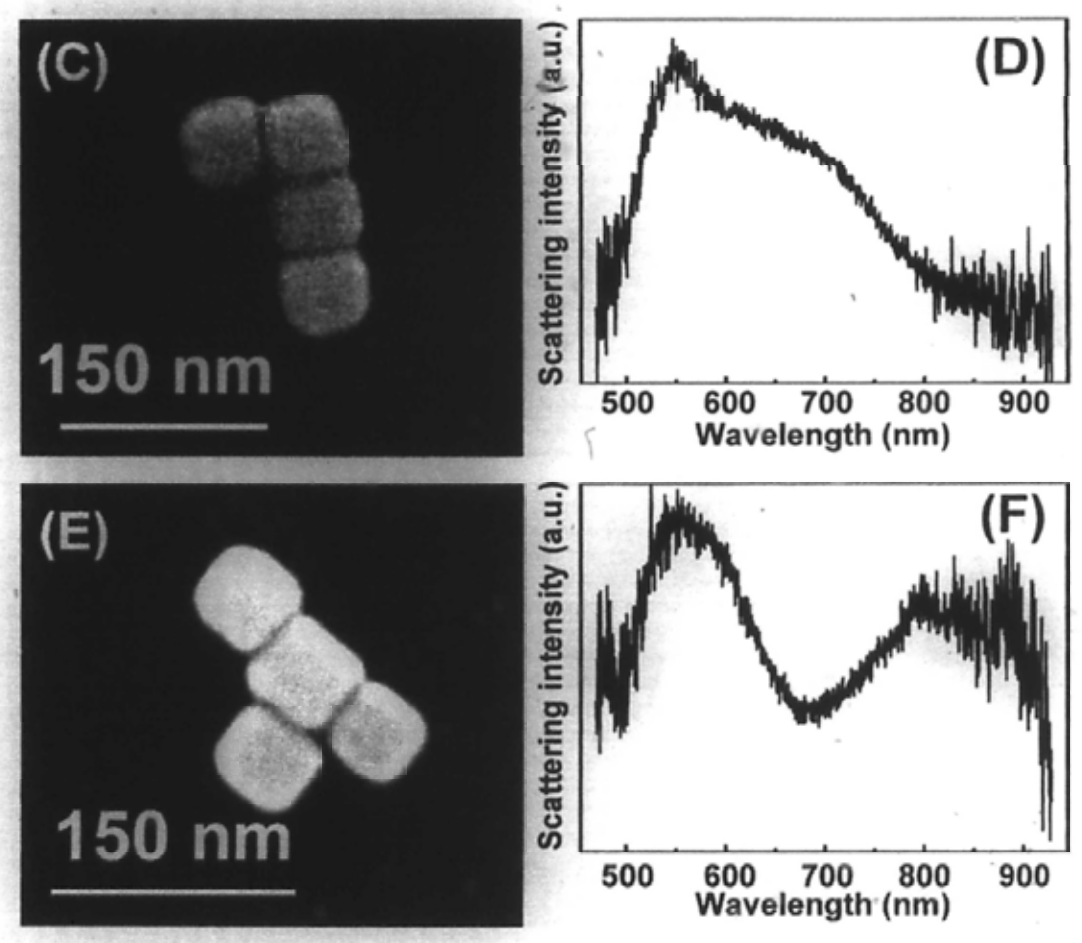


Figure 5.2.5. (A) SEM image of one 2 × 2 nanocube cluster. (B) Scattering spectrum of the 2 × 2 nanocube cluster. The black solid line is the experimental spectrum. The colored spectra are obtained from FDTD calculations. The excitation light is polarized horizontally for the red dashed line (along one edge of the 2 × 2 nanocube cluster) and vertically for the blue dashed line. The red solid line is their sum. (C) SEM image of one 4: L type nanocube cluster. (D) Scattering spectrum of the 4: L type nanocube cluster. (E) SEM image of one 4: T type nanocube cluster. (F) Scattering spectrum of the 4: T type nanocube cluster.

Figure 5.2.5D and F shows the scattering spectra of the L and T type clusters containing four nanocubes. Due to the memory limitation of our computers, the FDTD studies were not carried out

for these two clusters. Both clusters exhibit a strong plasmon resonance peak around 550 nm. The L type cluster has another strong plasmon peak around 700 nm. In comparison, the T type cluster has another strong plasmon peak around 820 nm. Both clusters also have weaker scattering peaks, which are submerged under the stronger scattering peaks.

We further studied the plasmonic properties of some selected clusters that contain from five up to nine nanocubes within the wavelength range limits of our detector. Figure 5.2.6A, B, and C show a five-nanocube, L type cluster, a 2 × 3 cluster, and a six-nanocube, star type cluster, respectively. Their scattering spectra exhibit multiple peaks over the wavelength range from 550 to 850 nm, and their overall shapes vary from cluster to cluster (Figure 5.2.6D).

Figure 5.2.7A shows a seven-nanocube, L type cluster. It scatters light strongly and nearly constantly from 550 to 650 nm, with a decaying tail towards longer wavelengths (Figure 5.2.7D). Figure 5.2.7B shows an eight-nanocube, L type cluster. Its scattering spectrum is similar to that of the seven-nanocube, L type cluster below 700 nm. Above 700 nm, it has a scattering peak around 810 nm (Figure 5.2.7D). Figure 5.2.7C shows a 3 × 3 cluster. Its scattering spectrum exhibits two clear peaks around 550 and 830 nm. The scattering in between these two peaks is considerably strong (Figure 5.2.7D), suggesting the existence of multiple plasmon resonance peaks.

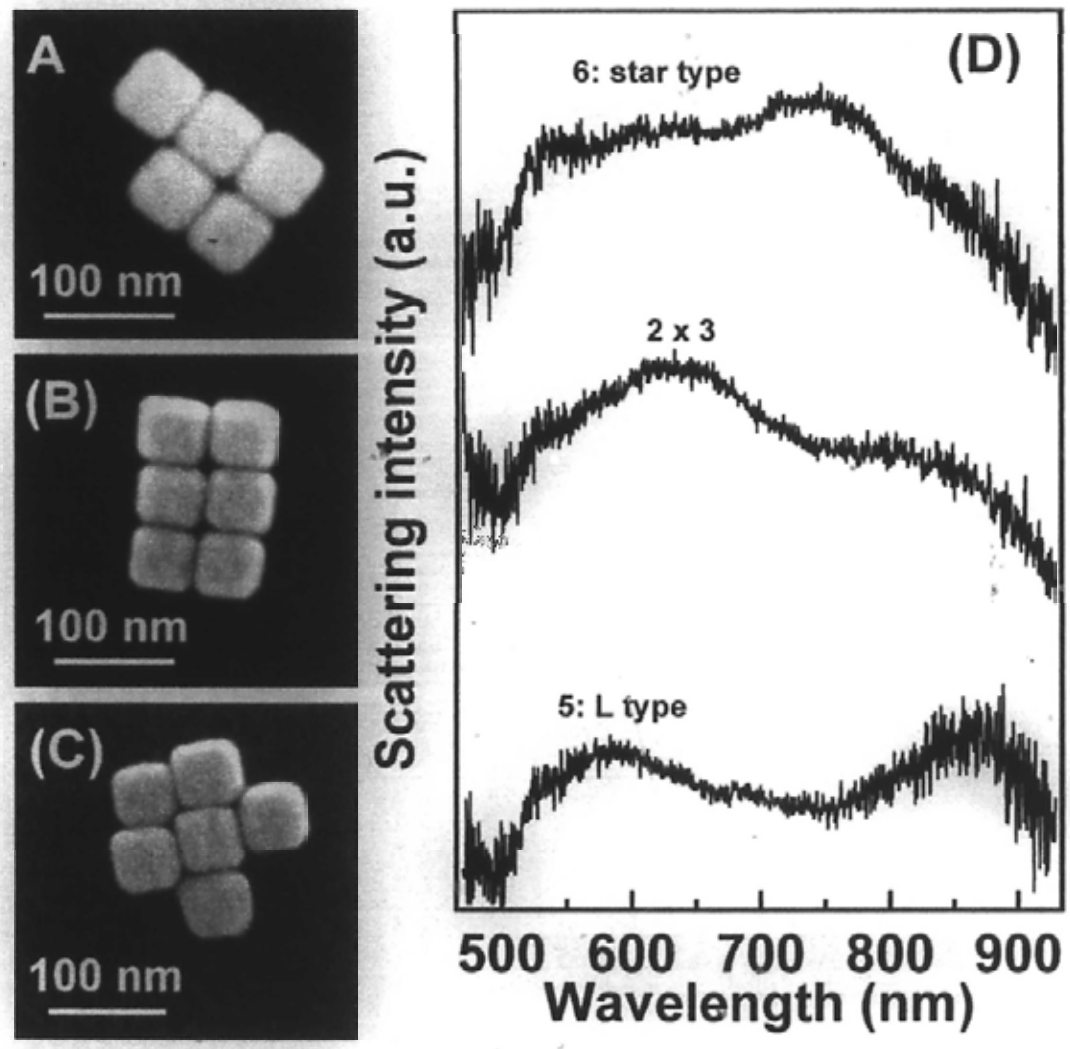


Figure 5.2.6. (A), (B), and (C) SEM images of one 5: L type, 2 × 3, and 6: star type nanocube cluster, respectively. (D) Scattering spectra of the 5: L type, 2 × 3, and 6: star type cluster.

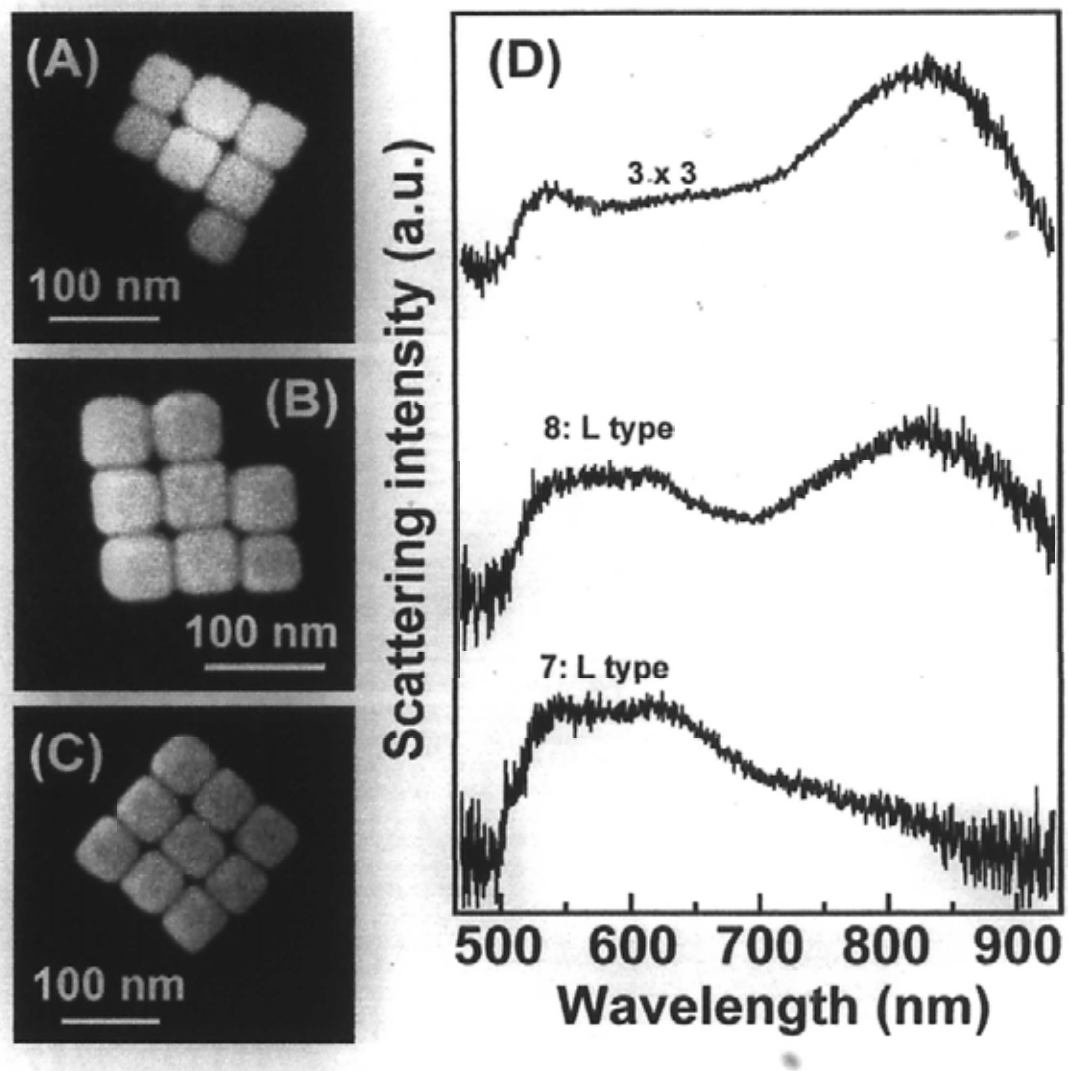


Figure 5.2.7. (A), (B), and (C) SEM images of one 7: L type, 8: L type, and 3 × 3 nanocube cluster, respectively. (D) Scattering spectra of the 7: L type, 8: L type, and 3 × 3 cluster.

Taking together the scattering spectral properties of the clusters with the number of nanocubes ranging from one to nine (see the summary in Figure 5.3.2 below), we see that all the clusters exhibit a strong plasmon resonance peak around 550 nm, irrespective of the nanocube number and arrangement. As revealed by the FDTD calculations, this plasmon resonance peak arises from the vertically-polarized excitation. It can therefore be ascribed to the interaction between the dipole in

the cluster and its image dipole in the ITO substrate. The vertically-polarized excitation induces a dipole in each nanocube, with its magnitude being approximately determined by the thickness of the nanocube. This dipole then induces an image dipole in the ITO substrate. The two dipoles interact strongly with each other owing to the intimate contact of the nanocube with the substrate, resulting in the plasmon resonance at 550 nm. Since the thickness of the nanocube is constant, the plasmon resonance induced by this mechanism is expected to be independent of the nanocube number and arrangement in a cluster.

The dipoles induced by the vertically-polarized excitation in different nanocubes in a cluster are coupled with each other owing to the nanometer-scale spacing between the nanocubes. This coupling also occurs for their image dipoles in the ITO substrate. The interaction among all of these dipoles produces an additional plasmon resonance peak at a longer wavelength. If all the dipoles are treated together as a collective system, the dipole coupling in the entire system will be dependent closely on the number of the nanocubes and their spatial arrangement in the cluster. Moreover, the dipoles induced by the horizontally-polarized excitation are not only coupled together, but also dependent on the in-plane polarization state of the excitation light. As a result from all of these factors taking effect together, the clusters generally exhibit more plasmon resonance peaks towards longer wavelengths as they become larger and more asymmetric (Figure 5.3.2). The scattering peaks also become broader owing to the presence of buried, weak peaks. The positions and relative intensities of different scattering peaks vary strongly as a function of the nanocube number and ordering in the cluster. These results point to a potential way for tailoring the plasmonic properties of noble metal nanostructures by forming clusters and varying the number and ordering of the basic building units in the cluster.

Another noticeable feature is that the overall scattering spectra generally become broader as the

nanocube cluster gets larger. Two factors are believed to cause this spectral broadening. The first one is the inhomogeneous distributions of the nanocube size and gap distance, both of which can cause a broadening in the scattering spectrum. As the number of the nanocubes in a cluster is increased, the effect of the inhomogeneous broadening will become larger. The second one is the appearance of multipolar plasmon resonances. As the overall cluster size is increased, multipolar plasmon resonance modes can be excited due to the phase retardation effect.

## 5.3 Plasmonic Properties of Thermally Treated Clusters Composed of Two-Dimensionally Ordered Gold Nanocubes

An interesting phenomenon encountered in the studies of the plasmon coupling between noble metal nanostructures is the singular behavior associated with the transition from dielectric proximity to conductive contact. Previous experimental and theoretical investigations on Au nanostructure dimers have demonstrated that the coupled plasmon peak jumps abruptly to a lower energy upon touching and subsequently jumps back to higher energies after touching [1, 24]. In order to study and compare the plasmonic properties of the nanocube clusters before and after the formation of conductive contact between neighboring Au nanocubes, we thermally treated the clusters at 200 °C for 9 h. This temperature was chosen because the melting points of Au nanocrystals have previously been found to be significantly lower than the bulk value [51]. After the thermal treatment, the Au nanocubes in the clusters are found to be welded together, but their cubic shape is still largely preserved.

All the clusters studied in the previous section were thermally treated. Their SEM images and scattering spectra are shown below and compared with those of the untreated ones (Figure 5.3.2).

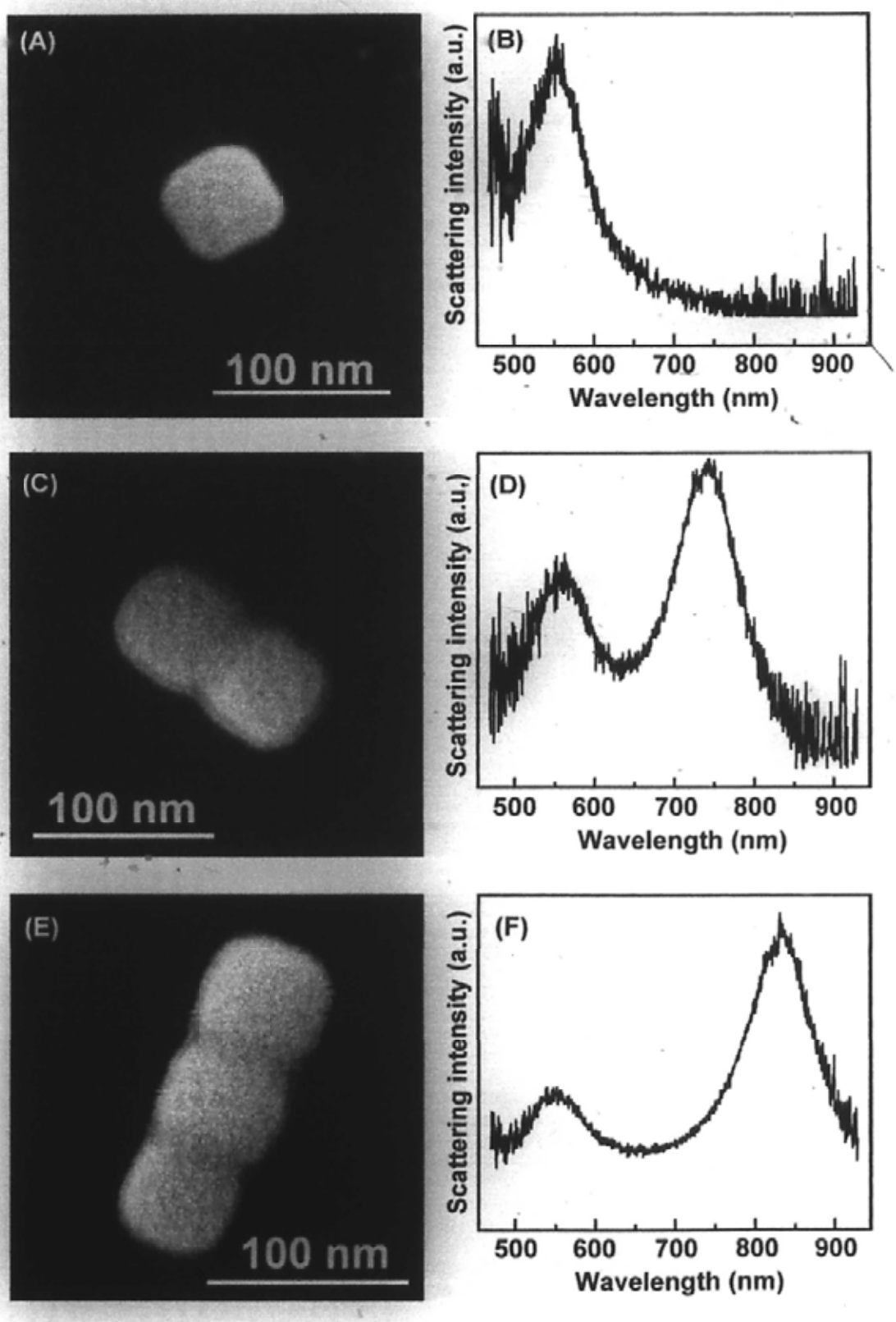
(A)
100 nm
(B)
Scattering intensity (a.u.)
500
600
700
800
900
Wavelength (nm)
(C)
100 nm
(D)
Scattering intensity (a.u.)
500
600
700
800
900
Wavelength (nm)
(E)
100 nm
(F)
Scattering intensity (a.u.)
500
600
700
800
900
Wavelength (nm)

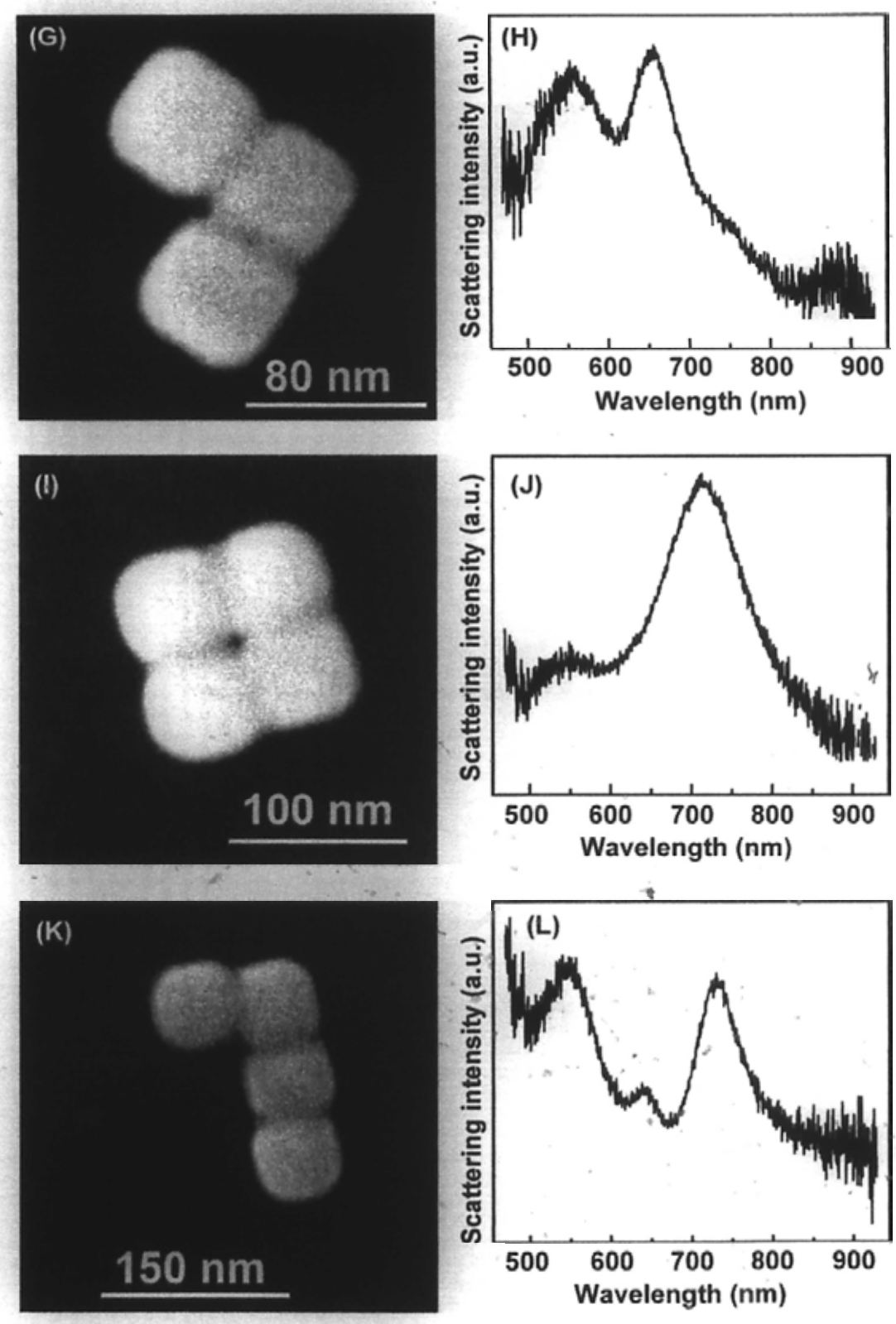
(G)
80 nm
(H)
Scattering intensity (a.u.)
500
600
700
800
900
Wavelength (nm)
(I)
100 nm
(J)
Scattering intensity (a.u.)
500
600
700
800
900
Wavelength (nm)
(K)
150 nm
(L)
Scattering intensity (a.u.)
500
600
700
800
900
Wavelength (nm)

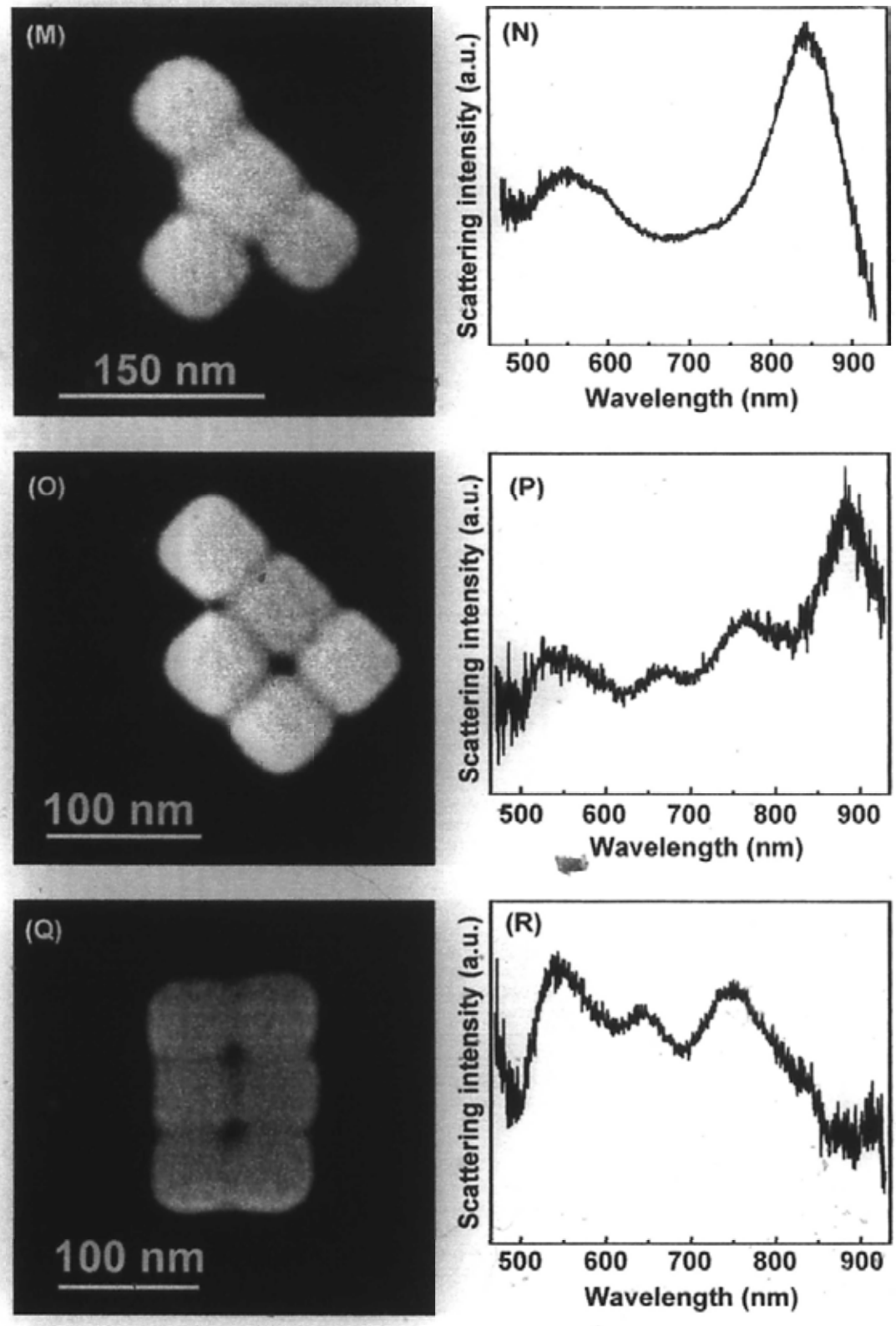
(M)
150 nm
(N)
Scattering intensity (a.u.)
500 600 700 800 900
Wavelength (nm)
(O)
100 nm
(P)
Scattering intensity (a.u.)
500 600 700 800 900
Wavelength (nm)
(Q)
100 nm
(R)
Scattering intensity (a.u.)
500 600 700 800 900
Wavelength (nm)

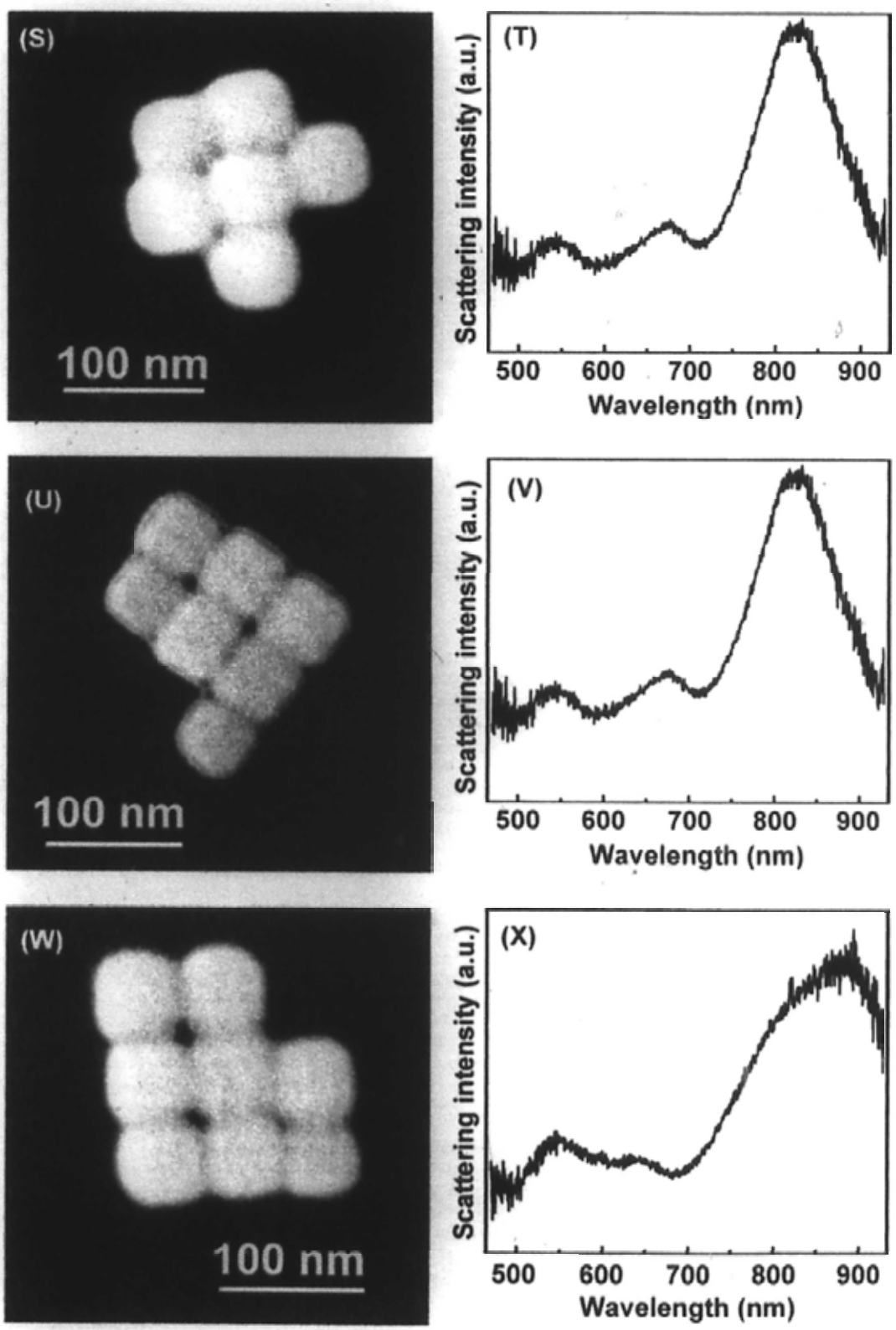
(S)
100 nm
(T)
Scattering intensity (a.u.)
500
600
700
800
900
Wavelength (nm)
(U)
100 nm
(V)
Scattering intensity (a.u.)
500
600
700
800
900
Wavelength (nm)
(W)
100 nm
(X)
Scattering intensity (a.u.)
500
600
700
800
900
Wavelength (nm)

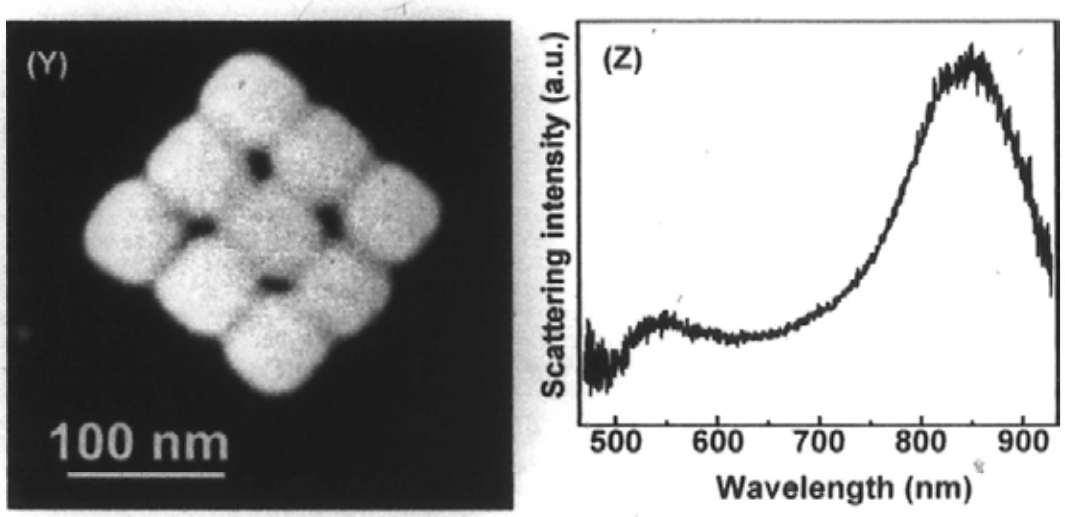


Figure 5.3.1. Left side: SEM images of different nanocube clusters after the thermal welding. Right side: Scattering spectra of different nanocube clusters after thermal welding. (A, B) Single nanocube. (C, D) 1 × 2 nanocube cluster. (E, F) 1 × 3 nanocube cluster. (G, H) 3: L type nanocube cluster. (I, J) 2 × 2 nanocube cluster. (K, L) 4: L type nanocube cluster. (M, N) 4: T type nanocube cluster. (O, P) 5: L type nanocube cluster. (Q, R) 2 × 3 nanocube cluster. (S, T) 6: star type nanocube cluster. (U, V) 7: L type nanocube cluster. (W, X) 8: L type nanocube cluster. (Y, Z) 3 × 3 nanocube cluster.

The corners and edges of the thermally treated Au nanocubes become blunter (Figure 5.3.1A). The scattering spectrum of the single Au nanocube remains almost the same as that before thermal treatment in terms of the peak position and FWHM (Figure 5.3.1B and Figure 5.2.1B). This suggests that the cubic shape is not severely deformed by thermal treatment. Several general features are observed on the scattering spectra of the thermally treated clusters (Figure 5.3.1, right side). First, the peak around 550 nm is preserved for all the clusters. Since the nanocube thickness is not altered by the thermal treatment, this plasmon peak remains nearly unchanged. Second, the overall spectra become sharper. As seen from the SEM images (Figures 5.3.1, left side), the nanocubes in the

clusters are welded together after thermal treatment, which removes the spectral broadening effect owing to the inhomogeneous distribution in the gap distance. Third, the lower-energy peaks on the right side of the 550-nm peak are red-shifted for all of the clusters (Figure 5.3.1: right side, Figure 5.3.2). Buried weak peaks for some of the clusters therefore become resolved after the thermal treatment. Because the lower-energy peaks of the untreated clusters arise from the plasmon coupling among different nanocubes, this result is consistent with the previous observations that the coupled plasmon peaks jump to longer wavelengths after touching [1, 24]. Fourth, for most of the clusters, the intensity ratio between the longest-wavelength peak and that around 550 nm becomes larger after the thermal treatment. This can be ascribed to the dipolar nature of the longest-wavelength peak. The nanocubes in a thermally treated cluster are welded together and the entire cluster becomes a single nanostructure. Its net dipole becomes larger in magnitude compared to that before the thermal treatment. The dipolar resonance therefore becomes stronger. Taken together, these distinct scattering spectral changes also suggest that the Au nanocubes in the clusters are indeed welded together after thermal treatment.

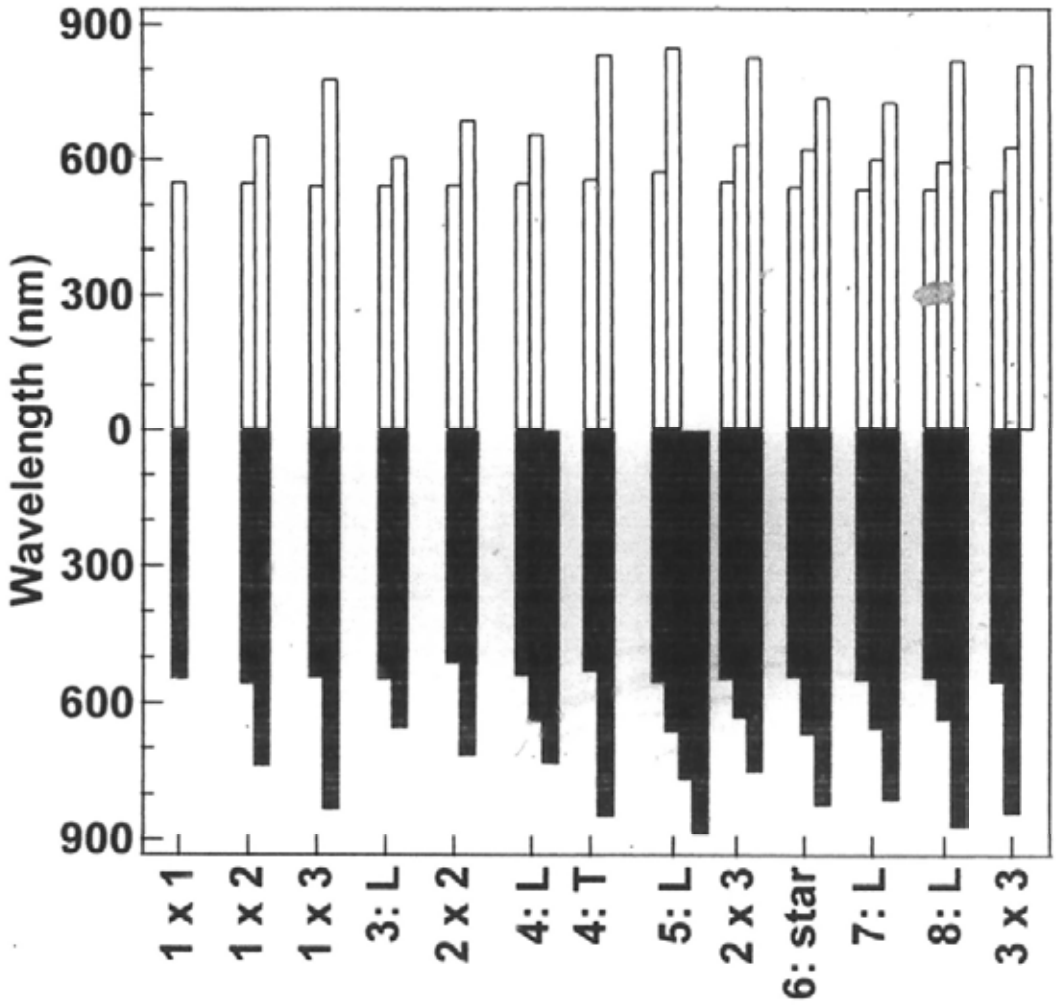


Figure 5.3.2. Summary of the plasmon resonance peak wavelengths of various nanocube clusters. The empty (upper) and grey (lower) bars represent the peak wavelengths of the clusters before and after the thermal treatment, respectively. The number before the colon indicates the number of nanocubes in each cluster.

## 5.4 Summary

In this study, I have prepared clusters of variously-ordered Au nanocubes on ITO substrates and studied their plasmon coupling properties. These nanocube clusters exhibit rich plasmonic

properties that are highly dependent on the number and ordering of the Au nanocubes. In general, more plasmon resonance peaks appear towards longer wavelengths as the cluster gets larger and more asymmetric. These plasmon peaks have been understood from the FDTD calculations to arise from the different plasmon resonance modes under variously-polarized excitations. These nanocube clusters have been further subjected to thermal treatment to weld together the Au nanocubes. In general, the plasmon resonance peaks of the thermally treated clusters become sharper. The lower-energy plasmon resonance peaks are redshifted compared to those before the thermal treatment. These studies offer a potential approach to tailoring plasmonic properties for advanced spectroscopic applications by constructing ordered clusters out of basic repeating units. Moreover, studying the plasmon coupling behavior in clusters of two-dimensionally ordered noble metal nanostructures can help in fundamentally understanding the transition from the localized surface plasmon resonance in isolated metal nanostructures to the propagating surface plasmon resonance on metal–dielectric interfaces.

## References

[1] I. Romero, J. Aizpurua, G. W. Bryant, F. J. García de Abajo, Plasmons in Nearly Touching Metallic Nanoparticles: Singular Response in the Limit of Touching Dimers. *Opt. Express*, 14: 9988, 2006.

[2] P. K. Jain, W. Y. Huang, M. A. El-Sayed, On the Universal Scaling Behavior of the Distance Decay of Plasmon Coupling in Metal Nanoparticle Pairs: A Plasmon Ruler Equation. *Nano Lett.*, 7: 2080, 2007.

[3] C. Sönnichsen, B. M. Reinhard, J. Liphardt, A. P. Alivisatos, A Molecular Ruler Based on Plasmon Coupling of Single Gold and Silver Nanoparticles. *Nat. Biotechnol.*, 23: 741, 2005.

[4] P. K. Jain, M. A. El-Sayed, Noble Metal Nanoparticle Pairs: Effect of Medium for Enhanced Nanosensing. *Nano Lett.*, 8: 4347, 2008.

[5] S. S. Aćimović, M. P. Kreuzer, M. U. González, R. Quidant, Plasmon Near-Field Coupling in Metal Dimers as a Step toward Single-Molecule Sensing. *ACS Nano*, 3: 1231, 2009.

[6] J. Jiang, K. Bosnick, M. Maillard, L. Brus, Single Molecule Raman Spectroscopy at the Junctions of Large Ag Nanocrystals. *J. Phys. Chem. B*, 107: 9964, 2003.

[7] R. F. Aroca, R. A. Alvarez-Puebla, N. Pieczonka, S. Sanchez-Cortez, J. V. Garcia-Ramos, Surface-Enhanced Raman Scattering on Colloidal Nanostructures. *Adv. Colloid Interface Sci.*, 116: 45, 2005.

[8] M. Moskovits, Surface-Enhanced Raman Spectroscopy: a Brief Retrospective. *J. Raman Spectrosc.*, 36: 485, 2005.

[9] Y. Fang, N.-H. Seong, D. D. Dlott, Measurement of the Distribution of Site Enhancements in Surface-Enhanced Raman Scattering. *Science*, 321: 388, 2008.

[10] A. Kinkhabwala, Z. F. Yu, S. H. Fan, Y. Avlasevich, K. Müllen, W. E. Moerner, Large

Single-Molecule Fluorescence Enhancements Produced by a Bowtie Nanoantenna. *Nat. Photonics*, 3: 654, 2009.

[11] K.-H. Su, Q.-H. Wei, X. Zhang, J. J. Mock, D. R. Smith, S. Schultz, Interparticle Coupling Effects on Plasmon Resonances of Nanogold Particles. *Nano Lett.*, 3: 1087, 2003.

[12] P. J. Schuck, D. P. Fromm, A. Sundaramurthy, G. S. Kino, W. E. Moerner, Improving the Mismatch between Light and Nanoscale Objects with Gold Bowtie Nanoantennas. *Phys. Rev. Lett.*, 94: 017402, 2005.

[13] Z. H. Sun, W. H. Ni, Z. Yang, X. S. Kou, L. Li, J. F. Wang, pH-Controlled Reversible Assembly and Disassembly of Gold Nanorods. *Small*, 4: 1287, 2008.

[14] Q.-Q. Wang, J.-B. Han, D.-L. Guo, S. Xiao, Y.-B. Han, H.-M. Gong, X.-W. Zou, Highly Efficient Avalanche Multiphoton Luminescence from Coupled Au Nanowires in the Visible Region. *Nano Lett.*, 7: 723, 2007.

[15] T. Ming, X. S. Kou, H. J. Chen, T. Wang, H.-L. Tam, K.-W. Cheah, J.-Y. Chen, J. F. Wang, Ordered Gold Nanostructure Assemblies Formed by Droplet Evaporation. *Angew. Chem. Int. Ed.*, 47: 9685, 2008.

[16] G. A. Wurtz, P. R. Evans, W. Hendren, R. Atkinson, W. Dickson, R. J. Pollard, A. V. Zayats, Molecular Plasmonics with Tunable Exciton−Plasmon Coupling Strength in J-Aggregate Hybridized Au Nanorod Assemblies. *Nano Lett.*, 7: 1297, 2007.

[17] A. R. Tao, P. Sinsermsuksakul, P. D. Yang, Tunable Plasmonic Lattices of Silver Nanocrystals. *Nat. Nanotechnol.*, 2: 435, 2007.

[18] A. R. Tao, D. P. Ceperley, P. Sinsermsuksakul, A. R. Neureuther, P. D. Yang, Self-Organized Silver Nanoparticles for Three-Dimensional Plasmonic Crystals. *Nano Lett.*, 8: 4033, 2008.

[19] W. L. Barnes, A. Dereux, T. W. Ebbesen, Surface Plasmon Subwavelength Optics. *Nature*, 424:

824, 2003.

[20] E. Ozbay, Plasmonics: Merging Photonics and Electronics at Nanoscale Dimensions. *Science*, 311: 189, 2006.

[21] J. B. Lassiter, J. Aizpurua, L. I. Hernandez, D. W. Brandl, I. Romero, S. Lal, J. H. Hafner, P. Nordlander, N. J. Halas, Close Encounters between Two Nanoshells. *Nano Lett.*, 8: 1212, 2008.

[22] W. Rechberger, A. Hohenau, A. Leitner, J. R. Krenn, B. Lamprecht, F. R. Aussenegg, Optical Properties of Two Interacting Gold Nanoparticles. *Opt. Commun.*, 220: 137, 2003.

[23] D. P. Fromm, A. Sundaramurthy, P. J. Schuck, G. Kino, W. E. Moerner, Gap-Dependent Optical Coupling of Single "Bowtie" Nanoantennas Resonant in the Visible. *Nano Lett.*, 4: 957, 2004.

[24] T. Atay, J.-H. Song, A. V. Nurmikko, Strongly Interacting Plasmon Nanoparticle Pairs: From Dipole−Dipole Interaction to Conductively Coupled Regime. *Nano Lett.*, 4: 1627, 2004.

[25] A. Sundaramurthy, P. J. Schuck, N. R. Conley, D. P. Fromm, G. S. Kino, W. E. Moerner, Toward Nanometer-Scale Optical Photolithography: Utilizing the Near-Field of Bowtie Optical Nanoantennas. *Nano Lett.*, 6: 355, 2006.

[26] P. K. Jain, S. Eustis, M. A. El-Sayed, Plasmon Coupling in Nanorod Assemblies: Optical Absorption, Discrete Dipole Approximation Simulation, and Exciton-Coupling Model. *J. Phys. Chem. B*, 110: 18243, 2006.

[27] P. K. Jain, M. A. El-Sayed, Universal Scaling of Plasmon Coupling in Metal Nanostructures: Extension from Particle Pairs to Nanoshells. *Nano Lett.*, 7: 2854, 2007.

[28] P. K. Jain, M. A. El-Sayed, Surface Plasmon Coupling and its Universal Size Scaling in Metal Nanostructures of Complex Geometry: Elongated Particle Pairs and Nanosphere Trimers. *J. Phys. Chem. C*, 112: 4954, 2008.

[29] B. M. Reinhard, M. Siu, H. Agarwal, A. P. Alivisatos, J. Liphardt, Calibration of Dynamic

Molecular Rulers Based on Plasmon Coupling between Gold Nanoparticles. *Nano Lett.*, 5: 2246, 2005.

[30] B. M. Reinhard, S. Sheikholeslami, A. Mastroianni, A. P. Alivisatos, J. Liphardt, Use of Plasmon Coupling to Reveal the Dynamics of DNA Bending and Cleavage by Single EcoRV Restriction Enzymes. *Proc. Natl. Acad. Sci. U. S. A.*, 104: 2667, 2007.

[31] P. Nordlander, C. Oubre, E. Prodan, K. Li, M. I. Stockman, Plasmon Hybridization in Nanoparticle Dimers. *Nano Lett.*, 4: 899, 2004.

[32] P. Pramon, K. G. Thomas, Plasmon Coupling in Dimers of Au Nanorods. *Adv. Mater.*, 20: 4300, 2008.

[33] A. M. Funston, C. Novo, T. J. Davis, P. Mulvaney, Plasmon Coupling of Gold Nanorods at Short Distances and in Different Geometries. *Nano Lett.*, 9: 1651, 2009.

[34] C. Tabor, D. V. Haute, M. A. El-Sayed, Effect of Orientation on Plasmonic Coupling between Gold Nanorods. *ACS Nano*, 3: 3670, 2009.

[35] X. S. Kou, Z. H. Sun, Z. Yang, H. J. Chen, J. F. Wang, Curvature-Directed Assembly of Gold Nanocubes, Nanobranches, and Nanospheres. *Langmuir*, 25: 1692, 2009.

[36] H. J. Chen, Z. H. Sun, W. H. Ni, K. C. Woo, H.-Q. Lin, L. D. Sun, C. H. Yan, J. F. Wang, Plasmon Coupling in Clusters Composed of Two-Dimensionally Ordered Gold Nanocubes. *Small*, 5: 2111, 2009.

[37] P. B. Johnson, R. W. Christy, Optical Constants of the Noble Metals. *Phys. Rev. B*, 6: 4370, 1972.

[38] Y. Yang, X. W. Sun, B. J. Chen, C. X. Xu, T. P. Chen, C. Q. Sun, B. K. Tay, Z. Sun, Refractive Indices of Textured Indium Tin Oxide and Zinc Oxide Thin Films. *Thin Solid Films*, 510: 95, 2006.

[39] A. Kondilis, E. Aperathitis, M. Modreanu, Derivation of the Complex Refractive Index of ITO

and ITON Films in the Infrared Region of the Spectrum by the Analysis of Optical Measurements. *Thin Solid Films*, 516: 8073, 2008.

[40] H. J. Chen, X. S. Kou, Z. Yang, W. H. Ni, J. F. Wang, Shape- and Size-Dependent Refractive Index Sensitivity of Gold Nanoparticles. *Langmuir*, 24: 5233, 2008.

[41] H. J. Chen, L. Shao, K. C. Woo, T. Ming, H.-Q. Lin, J. F. Wang, Shape-Dependent Refractive Index Sensitivities of Gold Nanocrystals with the Same Plasmon Resonance Wavelength. *J. Phys. Chem. C*, 113: 17691, 2009.

[42] A. D. McFarland, R. P. Van Duyne, Single Silver Nanoparticles as Real-Time Optical Sensors with Zeptomole Sensitivity. *Nano Lett.*, 3: 1057, 2003.

[43] L. J. Sherry, S.-H. Chang, G. C. Schatz, R. P. Van Duyne, B. J. Wiley, Y. N. Xia, Localized Surface Plasmon Resonance Spectroscopy of Single Silver Nanocubes. *Nano Lett.*, 5: 2034, 2005.

[44] L. J. Sherry, R. C. Jin, C. A. Mirkin, G. C. Schatz, R. P. Van Duyne, Localized Surface Plasmon Resonance Spectroscopy of Single Silver Triangular Nanoprisms. *Nano Lett.*, 6: 2060, 2006.

[45] W. H. Ni, H. J. Chen, X. S. Kou, M. H. Yeung, J. F. Wang, Optical Fiber-Excited Surface Plasmon Resonance Spectroscopy of Single and Ensemble Gold Nanorods. *J. Phys. Chem. C*, 112: 8105, 2008.

[46] T. Okamato, I. Yamaguchi, Optical Absorption Study of the Surface Plasmon Resonance in Gold Nanoparticles Immobilized onto a Gold Substrate by Self-Assembly Technique. *J. Phys. Chem. B*, 107: 10321, 2003.

[47] P. Nordlander, E. Prodan, Plasmon Hybridization in Nanoparticles near Metallic Surfaces. *Nano Lett.*, 4: 2209, 2004.

[48] G. Lévêque, O. J. F. Martin, Optical Interactions in a Plasmonic Particle Coupled to a Metallic Film. *Opt. Express*, 14: 9971, 2006.

[49] J. J. Mock, R. T. Hill, A. Degiron, S. Zauscher, A. Chilkoti, D. R. Smith, Distance-Dependent Plasmon Resonant Coupling between a Gold Nanoparticle and Gold Film. *Nano Lett.*, 8: 2245, 2008.

[50] M. W. Knight, Y. P. Wu, J. B. Lassiter, P. Nordlander, N. J. Halas, Substrates Matter: Influence of an Adjacent Dielectric on an Individual Plasmonic Nanoparticle. *Nano Lett.*, 9: 2188, 2009.

[51] K. Dick, T. Dhanasekaran, Z. Y. Zhang, D. Meisel, Size-Dependent Melting of Silica-Encapsulated Gold Nanoparticles. *J. Am. Chem. Soc.*, 124: 2312, 2002.

# Chapter 6

# Plasmon Coupling between Gold Nanocrystals and Substrates

The studies in Chapter 5 indicate that the adjacent substrate can exert great impact on the plasmonic properties of the nanocrystals. Many nowadays applications require the attachment of metallic nanocrystals onto different substrates. For example, Ag nanocrystal arrays have been fabricated on mica substrates for biosensors with high sensing performance [1 – 3]. Ag nanocrystals have been utilized for fabricating plasmon-enhanced solar cells on silicon wafers and GaAs substrates [4 – 7]. Metallic nanoparticles have been arranged in one-dimensional chains on ITO substrates for plasmonic waveguiding [8 – 10], and in two-dimensionally ordered arrays on silica for realizing coherence resonances with extremely sharp linewidths [11, 12]. Moreover, metallic nanostructures with specific geometries, for example, split-ring structures, have been deposited on semiconducting and insulating substrates to fabricate metamaterials with fascinating optical properties, such as negative refraction, cloaking, and plasmon-induced transparency [13 – 16]. Studying and understanding the coupling between metal nanocrystals/nanostructures and different substrates are therefore very important for integrating them with microelectronic processing techniques to fabricate novel plasmonic circuits, which can act as a link between electronic circuits and traditional optical devices.

The influence of the substrate on the plasmonic properties of a metal nanocrystal is mediated

by the electromagnetic field in the substrate. The substrate provides a symmetry-breaking dielectric environment for the nanocrystal [17]. Under the excitation of the localized surface plasmon resonance, the substrate is polarized and can induce a non-uniform electromagnetic field around the nanocrystal. This non-uniform electromagnetic field can excite different higher order plasmon modes of the nanocrystal. The electron oscillations associated with these modes can also interact with the substrate-induced field. As a result, the substrate mediates the interactions among the different plasmon modes of the nanocrystal and gives rise to their hybridization. The hybridization among the different plasmon modes can lead to significantly different optical responses of the nanocrystal compared to those of the free-standing one. Recent comprehensive studies have revealed that new plasmon modes will come up in the scattering/absorption spectrum of a nanocrystal attached onto a metallic or insulating substrate with large dielectric constants [17 – 24]. These findings are very important for sensing applications utilizing plasmon-enhanced spectroscopy (PES), because PES is highly dependent on the position of the plasmon resonance [25, 26]. On the other hand, the substrate can also modify the near-field distributions and far-field scattering properties of the nanocrystal [27 – 29]. The near-field distributions are crucial for the PES and refractive index based plasmonic sensing, while the far-field scattering is one of the pivotal ingredients for the plasmon-enhanced solar cells [7, 27]. Previous studies have shown that the refractive index sensitivity of Au nanodisks can be enhanced by reducing the substrate effect [30], while a silicon substrate can favor the plasmon-enhanced fluorescence [31]. Moreover, substrates can strongly modify the far-field scattering distributions of metal nanocrystals. Donut-shaped images have been reported for Au colloids on a Au film [29].

However, only spherical nanocrystals have so far been considered in these studies. Elongated nanocrystals are known to be superior to their spherical counterparts due to the larger

scattering/absorption cross sections, stronger field enhancements, and flexible tunability of the LPWs [32 – 35]. It is therefore very interesting to study the effect of the substrates on the plasmonic behaviors of elongated nanocrystals. On the other hand, the substrate-induced electromagnetic field is strongly dependent on the dielectric properties of substrates. Therefore substrates with different dielectric properties are expected to have different influence on the plasmonic properties of the metal nanocrystals. In this chapter I will present the studies of the coupling between Au nanocrystals and substrates. In §6.1 I will introduce the effect of the dielectric properties of the adjacent substrates on the far-field scattering patterns of Au nanocrystals. It is found that the appearance of donut-shaped far-field scattering patterns is strongly dependent on the dielectric constants of the substrates. In §6.2 I will further study the scattering spectra of Au nanocrystals with different sizes on silicon substrates. The coupling with silicon substrates can be very strong for nanocrystals of large volumes, giving rise to Fano resonances in their scattering spectra.

## 6.1 Effect of the Dielectric Properties of Adjacent Substrates on the Far-Field Scattering Pattern

A Au nanorod sample with an ensemble LLPW of 648 nm when dispersed in water is chosen for this study. It is obtained from the oxidation of the large nanorods utilized in §4.2. Figure 6.1.1 shows a typical TEM image and the extinction spectrum of the nanorod sample. The nanorods have a uniform size and shape distribution and their average length and width are (89 ± 7) and (42 ± 3) nm, respectively.

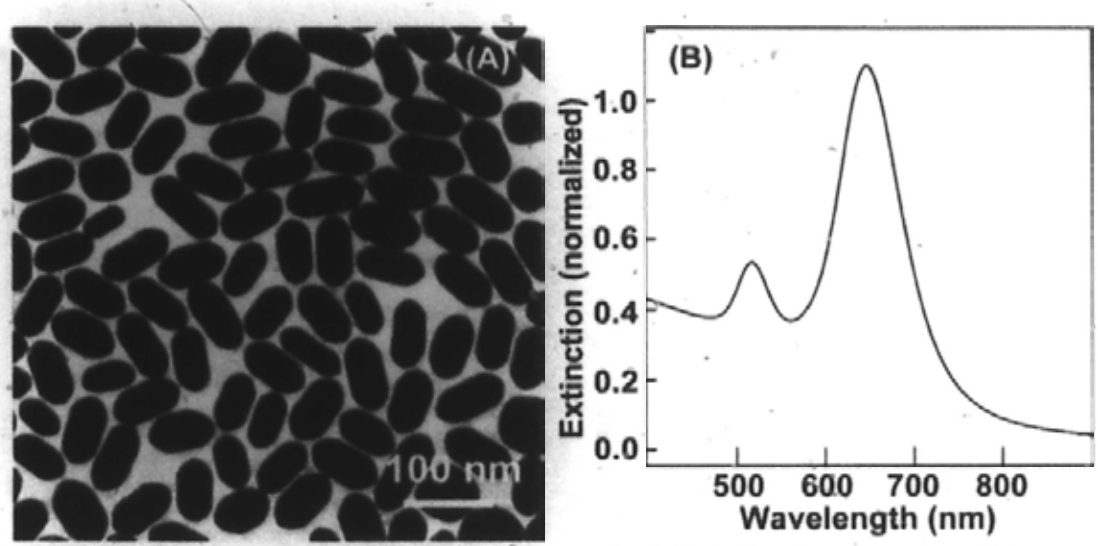


Figure 6.1.1. (A) TEM image of the Au nanorod sample. (B) Extinction spectrum of the Au nanorod in an aqueous solution.

The nanorod sample was then centrifuged twice (6300 g, 10 min) to remove CTAB surfactant and the surplus reactants. The supernatant was then dispersed into DI water for further characterization. Seven substrates, platinum (Pt) film on glass, Au film on glass, silicon wafer (Pure Sil, Inc., USA), glass cover slip (Ted Pella, Inc., USA), ITO (SPI Supplies, USA), single crystalline ZnO substrate (Wafer World, Inc., USA), and mesostructured titania ($mTiO_2$) thin film, were chosen for the following studies. For the fabrication of the metallic substrates, 100-nm Au films and 50-nm Pt films were deposited onto clean glass slides (Ted Pella, Inc., USA) with a magnetron sputtering. A 10-nm chromium layer was deposited as an adhesion layer before the deposition of Pt. The $mTiO_2$ film was fabricated using the evaporation-induced self-assembly technique through dip coating [36]. The precursor solution for the titania films was prepared by first dissolving 0.136 g of poly(ethylene oxide)–poly(propylene oxide)–poly(ethylene oxide) triblock copolymer ($EO_{20}PO_{70}EO_{20}$, P123) in 1.632 g of ethanol. Separately, 0.55 g of tetraethyl orthotitanate (TEOT) was added into concentrated HCl (0.42 g, ~12.1 M) and prehydrolyzed under vigorous stirring at room temperature

for 5 min. The two solutions were thereafter mixed together. The molar composition was 1 TEOT: 0.0097 P123: 6 $H_2O$: 1.8 HCl: 14.7 ethanol. After the precursor solution was stirred at room temperature for 10 min, they were dip coated onto silicon substrates at a speed of 10 mm $min^{-1}$. The dip-coating procedure was repeated several times to make the final thickness of the film to be ~1 μm. The produced films were dried in a refrigerator at 5 °C overnight.

The Au nanorods were then deposited onto the different substrates by drop-casting 10 μL of the aqueous solution onto the substrates and then drying the deposits naturally under ambient conditions. The number density of the nanorods on each substrate was controlled to be 1–3/$\mu m^2$. The substrates coated with the Au nanorods were then placed under the dark-field microscope for taking the scattering spectra and imaging with either a grayscale CCD (Princeton Instruments Pixis 512B) or a color CCD (AxioCam MRC5, Carl Zeiss, Inc, Germany). A general comparison of the far-field scattering patterns of the Au nanorods on the different substrates is shown in Figure 6.1.2. It can be clearly seen that the scattering intensity deistributions of the nanorods lying on the Pt, Au, and silicon substrates exhibit well-defined donut-shaped patterns, while those of the nanorods on the ZnO, ITO, glass, and m$TiO_2$ are normal solid bright spots. Moreover, the colors of these patterns vary significantly among the different substrates. The donut-shaped scattering patterns have also been observed in a previous experiment on Au nanospheres adjacent to Au thin films [29]. These results indicate that substrates with different dielectric properties can have distinct impacts on the scattering patterns of the nanorods. The origins of these impacts will be discussed further in the following.

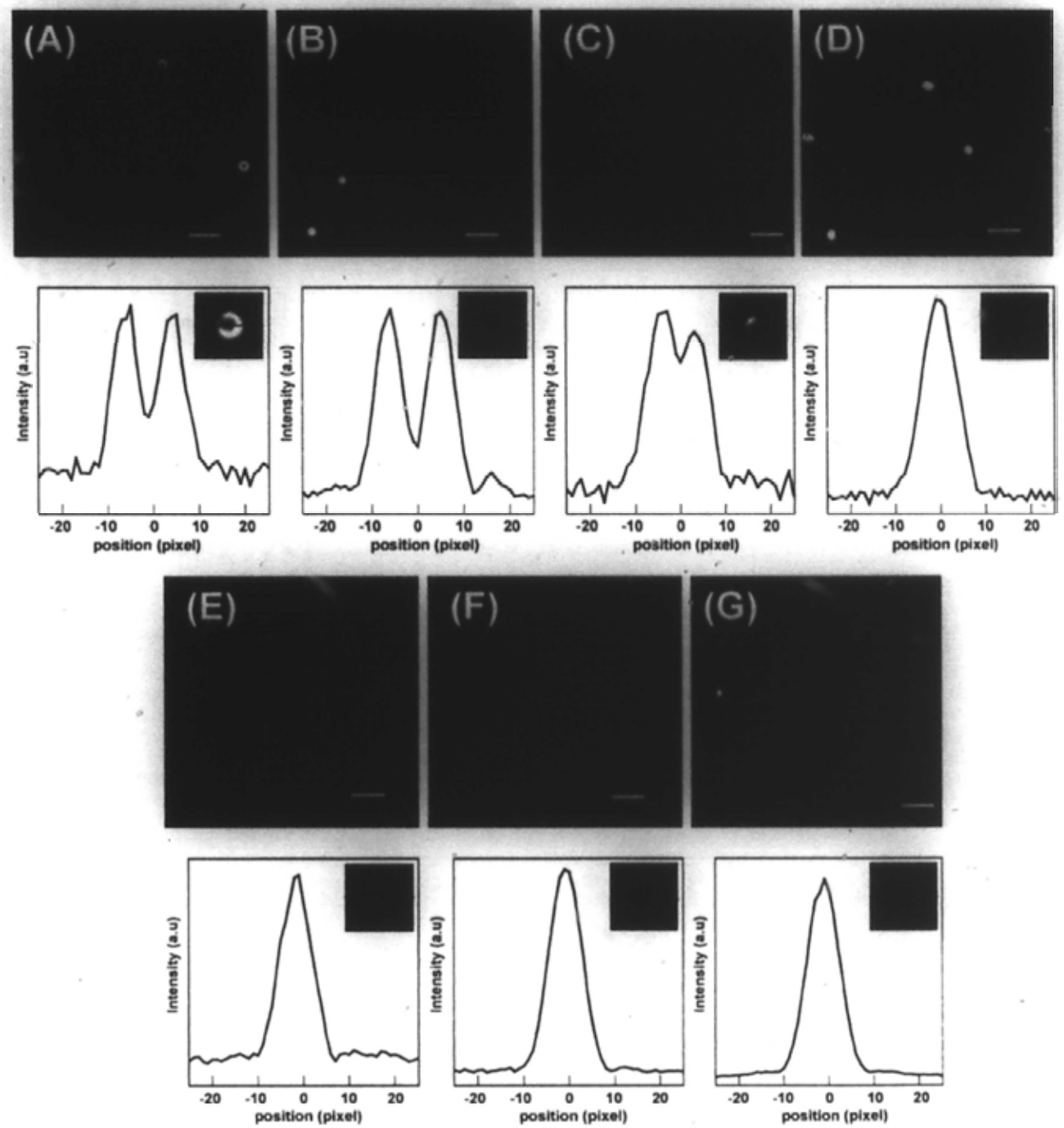


Figure 6.1.2. Colored CCD images and line plots through a typical grey scale scattering pattern. (A) Nanorod on the Pt film. (B) Nanorod on the Au film. (C) Nanorod on silicon. (D) Nanorod on crystalline ZnO. (E) Nanorod on ITO. (F) Nanorod on glass. (G) Nanorod on the $mTiO_2$ film. The scale bars stand for 2 μm.

The size of the nanorods in this study is much smaller than the incident wavelength and thus the nanorods can be regarded as a polarizable electric point dipole. Due to the dark-field excitation scheme in our studies (Figure 3.3.1), the incident electromagnetic field can be decomposed into two components. One is associated with the electric field parallel to the substrate and the other perpendicular to the substrate. These two components can excite the related dipole moments in the nanorods, which is defined as the in-plane dipole (parallel to the substrate) and the normal dipole (perpendicular to the substrate). Due to the presence of the substrates, these two dipole moments can induce their related images in the substrates. The coupling between the dipoles and their images determines the far-field scattering properties of the nanorod–substrate system. Figure 6.1.3 shows the simplified representation of this interaction between the nanorod and the substrate.

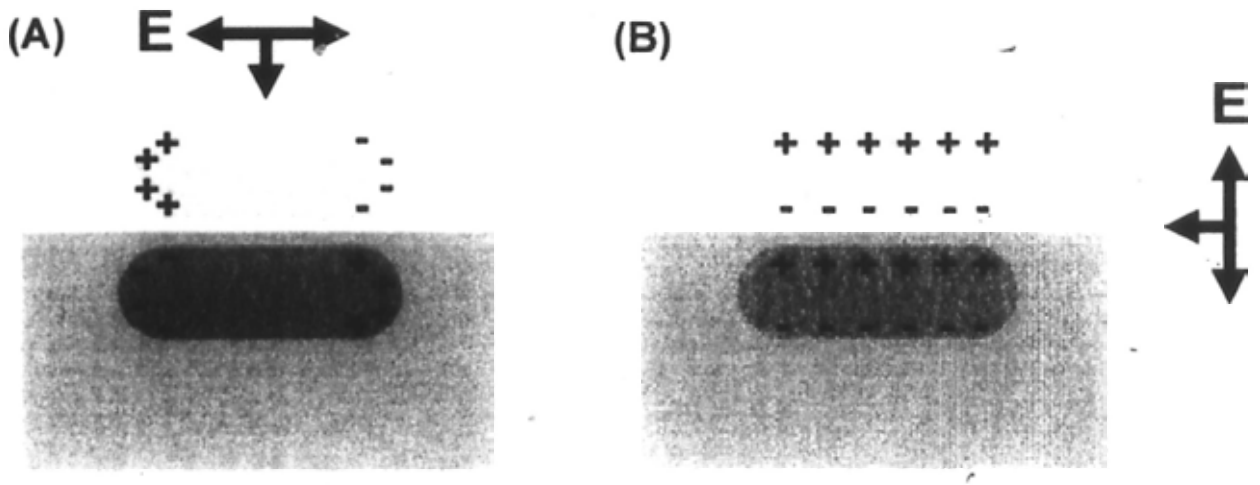


Figure 6.1.3. Simplified representation of the interaction between the nanorod and the substrate. (A) Parallel excitation. (B) Perpendicular excitation.

The scattering power for a dipole radiation is characterized by a $\sin^2\theta$ distribution, where $\theta$ is the angle between the dipole axis and the observation direction [37]. The numerical aperture of our dark-field objective (0.8) leads to a collection angle of ± 54° relative to the optical axis of the

objective. Therefore for the in-plane dipole radiation, $\theta$ is between 36° and 144° and results in a far-field scattering pattern of a solid spot. For the normal dipole radiation, $\theta$ is between −54° and 54° and results in a far-field scattering pattern of a donut shape. The net far-field scattering pattern of the nanorod is the sum of these two contributions. Because for the in-plane dipole the induced image dipole moment is opposite to that in the nanorod (Figure 6.1.3A), these two dipole moments will cancel each other and result in a reduced far-field scattering intensity. On the other hand, the normal dipole moment and its image are parallel to each other and the net dipole oscillation is enhanced. The far-field pattern of the nanorod is strongly dependent on the relative intensity of these two modes of dipole radiation. Because the magnitude of the induced dipole moment is determined by the dielectric properties of the substrate, it is expected that the dielectric function of the substrate will play an important role in the far-field scattering patterns of the adjacent Au nanorods. In the following discussion a simple electrostatic model is employed to reveal the relationship between them.

The problem of the interaction between the nanorod and the substrate can be solved by using electrostatic approximations because the size of the nanorod is much smaller than the incident wavelength [38, 39]. Moreover, only the dipole radiation can effectively couple to the far-field scattering, the multipole contributions have been neglected in the discussion of the scattering pattern. It should be noted that for the in-plane dipole, two modes, which are the TLPW and LLPW, can be excited. Our previous studies have shown that the scattering intensity from the TLPW of the nanorod is much smaller than that from the LLPW [33]. Therefore, only the contribution from the LLPW will be considered. The electric field induced by the in-plane dipole moment ($\mathbf{E}_{prim}$) and its image ($\mathbf{E}_{image}$) can be expressed as [40],

$$\begin{cases} \mathbf{E}_{in,prim} = \dfrac{p}{4\pi\varepsilon_0\varepsilon_1}\left[\left(\dfrac{3x^2}{r^5}-\dfrac{1}{r^3}\right)\mathbf{e}_x, \dfrac{3xy}{r^5}\mathbf{e}_y, \dfrac{3x(z-h)}{r^5}\mathbf{e}_z\right] \\ \mathbf{E}_{in,image} = \dfrac{p}{4\pi\varepsilon_0\varepsilon_1}\left[\left(\dfrac{3x^2}{r'^5}-\dfrac{1}{r'^3}\right)\mathbf{e}_x, \dfrac{3xy}{r'^5}\mathbf{e}_y, \dfrac{3x(z+h)}{r'^5}\mathbf{e}_z\right] \end{cases} \tag{6.1.1}$$

where $p$ is the magnitude of the dipole moment and $x$, $y$, and $z$ are the Cartesian coordinates of the dipoles. The parameter $h$ is the distance between the dipole and the interface, while the parameters $r$ and $r'$ denote the radial distance measured from the center locations of the in-plane dipole and its image, respectively. $\varepsilon_1$ is the dielectric function of the air. The total field in the detection space is,

$$\mathbf{E}_{in} = \mathbf{E}_{in,prim} - \frac{\varepsilon_2-\varepsilon_1}{\varepsilon_2+\varepsilon_1}\mathbf{E}_{in,image} \tag{6.1.2}$$

where $\varepsilon_2$ is the dielectric function of the substrate. For the normal dipole and its image, the results are,

$$\begin{cases} \mathbf{E}_{norm,prim} = \dfrac{p}{4\pi\varepsilon_0\varepsilon_1}\left[\dfrac{3x(z-h)}{r^5}\mathbf{e}_x, \dfrac{3y(z-h)}{r^5}\mathbf{e}_y, \dfrac{3(z-h)^2}{r^5}-\dfrac{1}{r^3}\mathbf{e}_z\right] \\ \mathbf{E}_{norm,image} = \dfrac{p}{4\pi\varepsilon_0\varepsilon_1}\left[\dfrac{3x(z+h)}{r'^5}\mathbf{e}_x, \dfrac{3y(z+h)}{r'^5}\mathbf{e}_y, \dfrac{3(z+h)^2}{r'^5}-\dfrac{1}{r'^3}\mathbf{e}_z\right] \end{cases} \tag{6.1.3}$$

$$\mathbf{E}_{norm} = \mathbf{E}_{norm,prim} + \frac{\varepsilon_2-\varepsilon_1}{\varepsilon_2+\varepsilon_1}\mathbf{E}_{norm,image} \tag{6.1.4}$$

In our studies, the distances between the dipoles and the observer are much larger than $h$, $x$, $y$, and $z$. Therefore the total electric field can be expressed as,

$$\mathbf{E}_{in} \approx \mathbf{E}_{in,prim} - \frac{\varepsilon_2-\varepsilon_1}{\varepsilon_2+\varepsilon_1}\mathbf{E}_{in,prim} = \frac{2\varepsilon_1}{\varepsilon_1+\varepsilon_2}\mathbf{E}_{in,prim} \tag{6.1.5}$$

$$\mathbf{E}_{norm} \approx \mathbf{E}_{norm,prim} + \frac{\varepsilon_2-\varepsilon_1}{\varepsilon_2+\varepsilon_1}\mathbf{E}_{norm,prim} = \frac{2\varepsilon_2}{\varepsilon_1+\varepsilon_2}\mathbf{E}_{norm,prim} \tag{6.1.6}$$

We further make the approximation that $x = 0$, $y = 0$, and $z \approx r$. This approximation is reasonable in our studies. Then the electric field becomes,

$$\mathbf{E}_{in} \approx -\frac{p}{4\pi\varepsilon_0\varepsilon_1}\frac{2\varepsilon_1}{\varepsilon_1+\varepsilon_2}\frac{1}{r^3}\mathbf{e}_x \tag{6.1.7}$$

$$\mathbf{E}_{norm} \approx \frac{p}{4\pi\varepsilon_0\varepsilon_1}\frac{4\varepsilon_2}{\varepsilon_1+\varepsilon_2}\frac{1}{r^3}\mathbf{e}_z \tag{6.1.8}$$

The ratio of the electric field intensity between these two radiations then becomes,

$$K = \frac{|\mathbf{E}_{in}|^2}{|\mathbf{E}_{norm}|^2} = \frac{\varepsilon_1^2}{4|\varepsilon_2|^2} = \frac{1}{4|\varepsilon_2|^2} \tag{6.1.9}$$

This ratio is directly related to the scattering pattern of the Au nanorods observed in our studies, because the far-field scattering intensity is proportional to $|\mathbf{E}|^2$. Figure 6.1.4A shows the dependence of $1/|\varepsilon_2|^2$ on the wavelength for these seven substrates, with their dielectric functions obtained from previous reported data [41]. It can be seen that $1/|\varepsilon_2|^2$ is almost constant in the wavelength range of 550 nm to 900 nm, in which my studies were performed. We therefore utilized the average values over this wavelength range in the following studies.

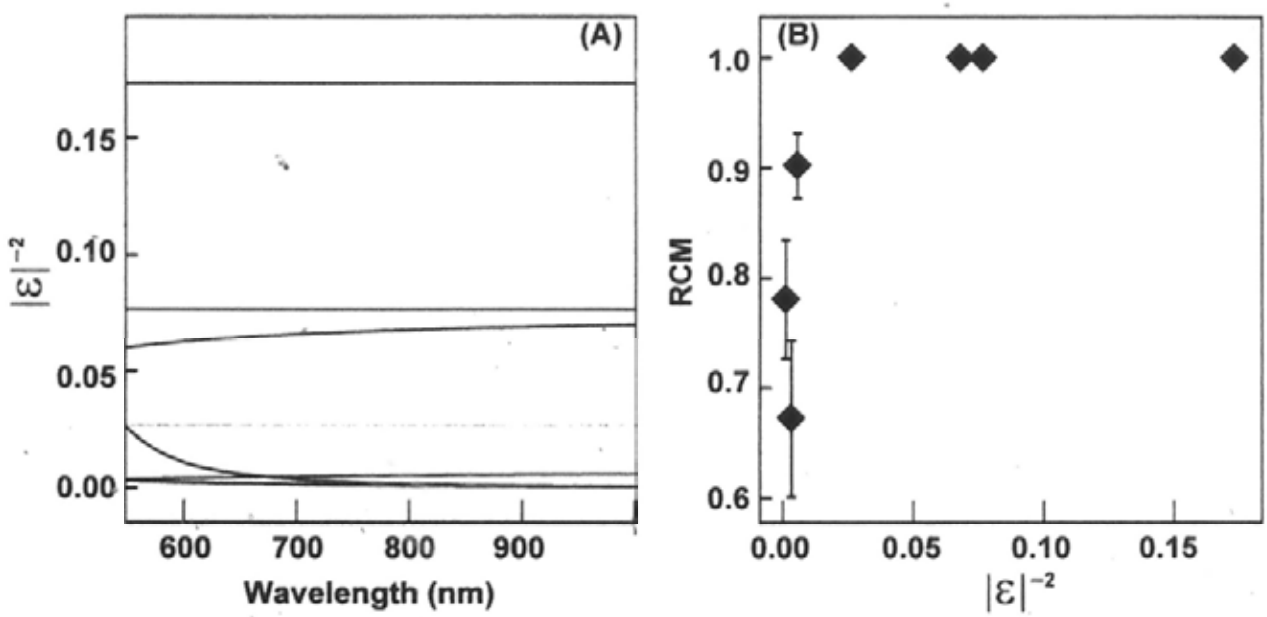


Figure 6.1.4. (A) Dependence of $1/|\varepsilon_2|^2$ on the wavelength of Pt (red), Au (black), Si (blue), $mTiO_2$

(orange), ZnO (purple), ITO (cyan), and glass (green). (B) Plot of the ratio of the central intensity to the maximum intensity on the ring of the scattering patterns of the Au nanorods on the different substrates. Each data point is an average over 20 particles for each substrate and standard error bars are included.

The ratio of the central intensity to the maximum intensity (RCM) of each scattering pattern can be obtained from the cross-section profile passing through the center of the patterns, as those shown in Figure 6.1.2. An empirical relation between the RCM and the $1/|\varepsilon_2|^2$ of the different substrate is shown in Figure 6.1.4B. Clearly within the error bars the RCM increases monotonically and saturates at 1 when $1/|\varepsilon_2|^2$ is larger than 0.02. The abnormal behavior between Pt and Au is believed to originate from the Cr adhesion layer below the Pt film. The presence of this thin Cr layer will modify the dielectric properties of the Pt and lead to a different $1/|\varepsilon|^2$ value compared to that of pure Pt. It is expected that a more accurate calculation of the dielectric function of this Pt–Cr hybrid layer can give a better description of the far-field scattering patterns of the adjacent Au nanorods. These results indicate that when a Au nanorod is deposited onto a substrate with $1/|\varepsilon|^2$ smaller than 0.02, the in-plane dipole will be cancelled nearly completely while the normal dipole is enhanced by their related images, leading to a far-field scattering with a donut-shaped pattern. On the other hand, when the nanorod is deposited onto a substrate with $1/|\varepsilon|^2$ above 0.02, the induced image is not strong enough to cancel the in-plane dipole radiation and therefore the scattering pattern returns to a solid spot. This conclusion can be further confirmed by the following FDTD calculations.

Figure 6.1.5 shows the calculated scattering spectra and related far-field scattering patterns of

the Au nanorods on silicon ($1/|\varepsilon|^2$=0.006) and glass ($1/|\varepsilon|^2$=0.1). The calculations were performed for the electric field parallel to the longitudinal axis of the nanorod (red lines) or perpendicular to the substrate (green lines). Clearly for the nanorod on glass, the total scattering spectra is contributed by a dominant mode induced by the longitudinal excitation and a much weaker mode induced by the perpendicular excitation. The far-field scattering pattern is a solid bright spot (Figure 6.1.5A, B, and C). On the other hand, for the nanorod lying on silicon, the contributions by these two modes are comparable. Therefore the far-field scattering changes into a donut-shaped pattern (Figure 6.1.5D, E, and F).

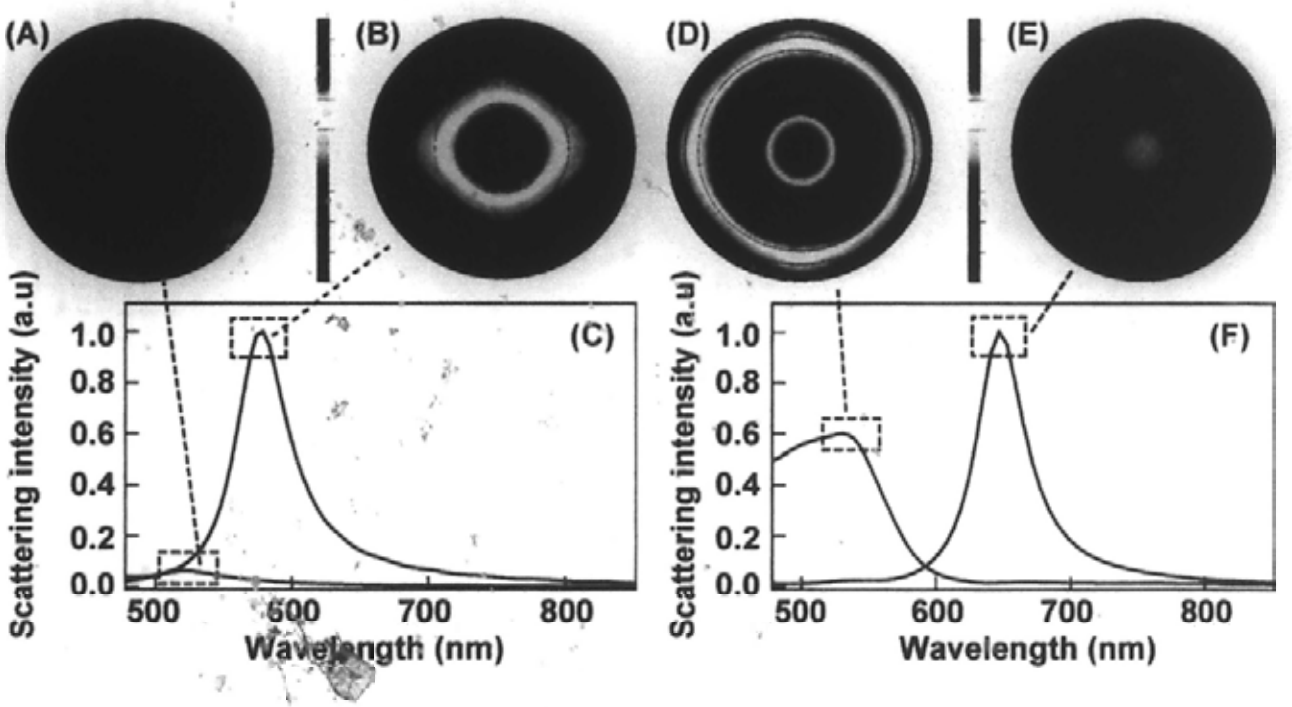


Figure 6.1.5. FDTD calculated far-field scattering spectra and patterns of the Au nanorod. (A) Scattering pattern of the plasmon mode induced by the perpendicular excitation for the Au nanorod on glass. (B) Scattering pattern of the plasmon mode induced by the longitudinal excitation for the Au nanorod on glass. (C) Scattering spectra of the plasmon modes induced by the perpendicular excitation (green) and longitudinal excitation (red) for the Au nanorod on glass. (D) Scattering

pattern of the plasmon mode induced by the perpendicular excitation for the Au nanorod on silicon. (E) Scattering pattern of the plasmon mode induced by the longitudinal excitation for the Au nanorod on silicon. (F) Scattering spectra of the plasmon modes induced by the perpendicular excitation (green) and longitudinal excitation (red) for the Au nanorod on silicon. The scattering intensity increases gradually as the colors in the two color bars change from blue to red.

The donut-shaped scattering pattern is then discussed in greater detail. Equation (6.1.1) and (6.1.3) show that the intensity of the electric field induced by the image dipoles decays approximately as $1/h^6$. It is therefore expected that the scattering pattern will be strongly dependent on the distance between the Au nanorod and the substrate. As nowadays most microelectronic techniques are based on silicon, Au nanorods on silicon are then chosen as a model system for investigating the effect of the separation between them on their far-field scattering patterns. Mesostructured silica films ($mSiO_2$) with three different thicknesses (2.7, 7.6, and 13.7 nm) were coated onto the Si wafers as a separation layer. The mesostructured silica films were fabricated by the same method used for preparing the $mTiO_2$ film described above. The thickness of the films was controlled by using precursors with different concentrations and measured with atomic force microscopy (AFM) (Veeco MultiMode, Veeco Instruments Inc., USA). For coating the films of 13.7-nm thickness, 0.276 g of P123 was first dissolved in 21.6 g of ethanol. 1.04 g of tetraethyl orthosilicate (TEOS) was prehydrolyzed in a solution containing 0.54 g of dilute HCl (pH = 2) and 1.2 g of ethanol by vigorous stirring at room temperature for 30 min. These two solutions were thereafter mixed together. The final molar composition of the precursor solution was 1 TEOS: 0.0095 P123: 6 $H_2O$: 0.001 HCl: 104.4 ethanol. The preparation of the precursor solution for the other two thin films was similar, except that the precursor solution was diluted 4 times and 16 times

by ethanol. After the precursor solutions were stirred for 2 h at room temperature, they were dip-coated onto silicon wafers at a speed of 10 mm/min. The resultant mesostructured silica films were dried at room temperature overnight before used.

The Au nanorods were deposited onto the coated silicon substrates and their scattering patterns were then captured as a function of the $mSiO_2$ thickness. Figure 6.1.6 shows a typical series of colored images. From these images, it can be clearly seen that as the distance between the nanorod and the substrate is increased, the scattering pattern changes gradually from a green donut shape into a red solid bright spot. This behavior is also corroborated by the scattering spectra shown in Figure 6.1.6E. Along with the increase of the separations the intensity of the lower energy resonance associated with the longitudinal excitation increases gradually and becomes dominant in the whole scattering spectrum, while the intensity of the resonance at 550 nm associated with the perpendicular excitation decreases and disappears finally. At a thickness of 13.7 nm the scattering spectrum of the nanorod is similar to that of the nanorod lying on glass substrate. These findings suggest that the donut-shaped scattering pattern is induced by the near-field interaction between the Au nanorod and the substrate. The effective interaction length is found to be around 15 nm for silicon substrate. This should be taken into consideration for the future development of metal nanocrystal-based plasmonic devices onto silicon substrates. On the other hand, it is expected that a simultaneous measurement of the distance-dependent far-field scattering pattern and spectrum can lead to the development of an ultrasensitive sensor for detecting the subtle changes in the separation between metal nanocrystals and the silicon substrates.

The above studies have shown that substrates can affect the scattering spectra of adjacent Au nanocrystals enormously. In the following section I will continue to discuss the scattering spectra of Au nanocrystals on silicon substrates.

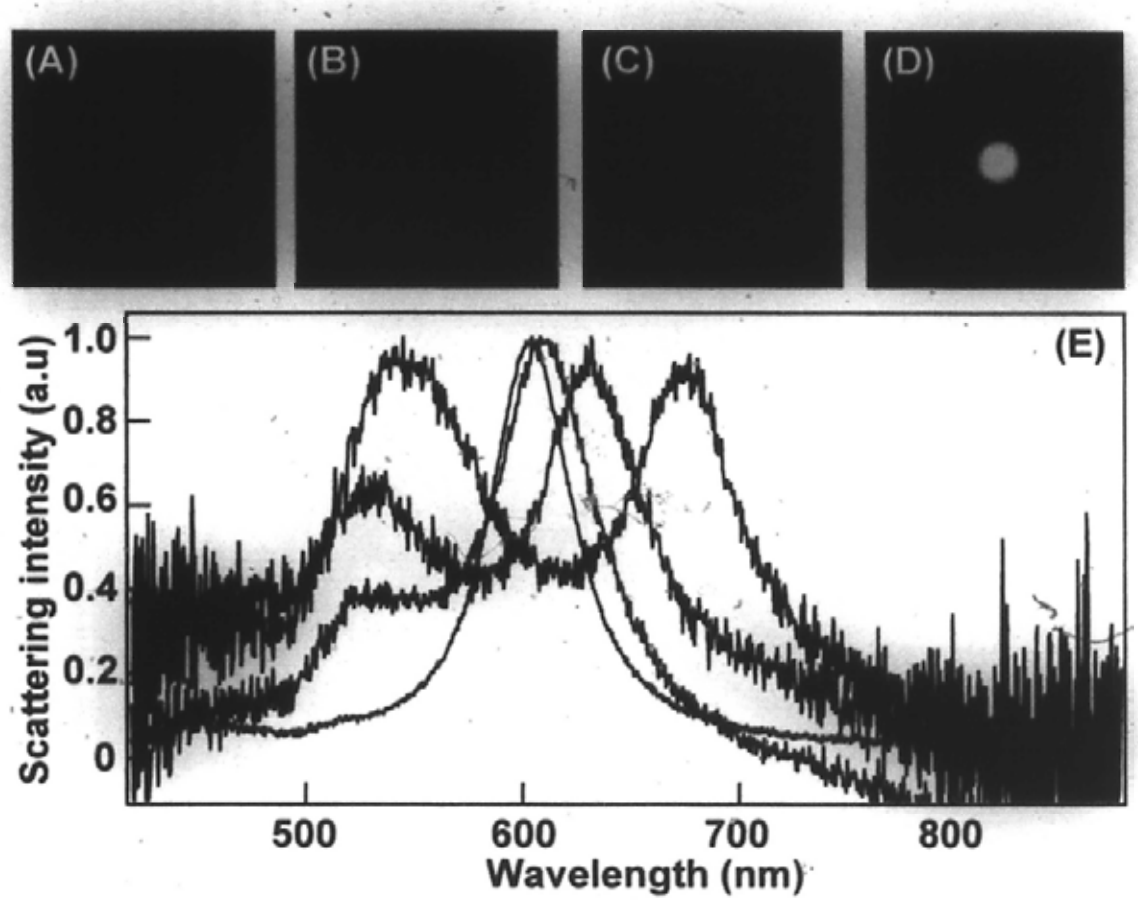


Figure 6.1.6. Far-field scattering patterns and spectra of the Au nanorods lying on a silicon substrate coated with the $mSiO_2$ films of increasing thicknesses. (A) and red curve in (E): 0 nm. (B) and green curve in (E): 2.7 nm. (C) and blue curve in (E): 7.6 nm. (D) and black curve in (E): 13.7 nm.

## 6.2 Dielectric Substrate-Induced Fano Resonance

The presence of substrates introduces symmetry breaking for the electromagnetic field environment surrounding metal nanocrystals. Under external excitation, the substrate can induce a non-uniform electromagnetic field around the nanocrystal. This non-uniform field can excite multipolar resonances in the particle. The electron oscillations associated with these resonances can induce their image charges in the substrate. A specific resonance mode can interact with its own

image as well as images induced by other modes, giving rise to mixtures of different plasmon modes in the nanocrystal. Therefore the substrate "mediates" the hybridization of the different resonance modes of the nanocrystal. This intraparticle hybridization can result in distinct resonance properties compared to those of the isolated nanocrystal. Previous comprehensive studies have shown that the coupling of Au nanostructures with substrates can lead to the broadening of the plasmon resonance spectrum, appearance of new resonance modes, and reshaping of the resonance spectrum [18, 20, 22 – 23]. Moreover, the coupling behaviors are found to be highly dependent on the dielectric constant of the substrate and the size of the nanocrystal [17, 24]. Substrates with higher dielectric constants can induce larger non-uniform electric fields surrounding the particle, while the excitation of multipole resonance modes can be easier in larger nanocrsytals. However, most of these studies are theoretical results and only recently did Knight *et al* observe this large coupling effect in Au nanoshell–dielectric substrate system [17]. In this section I will introduce our systematic studies on the coupling between Au nanocrystals of different sizes and substrates of large dielectric constants. It is found that Fano resonance can occur as a result of the hybridization between the higher order modes in nanocrystals of larger sizes.

Two types of Au nanocrystal samples were chosen. One is the same as those used in §6.1. The other is tetrahexahedral (THH) Au nanocrystals with average lengths and widths of (188 ± 5) nm and (118 ± 7) nm [42]. Its volume is about 17 times that of the Au nanorod. The synthesis of the Au THH nanocrystal samples was similar to that of the large nanorods discussed in §4.2, except that the amount of the added seed solution was changed from 100 μL (10 times diluted) to 10 μL (50 times diluted). Figure 6.2.1 shows the SEM images of these two samples, from which one can see that they both have uniform size and shape distributions.

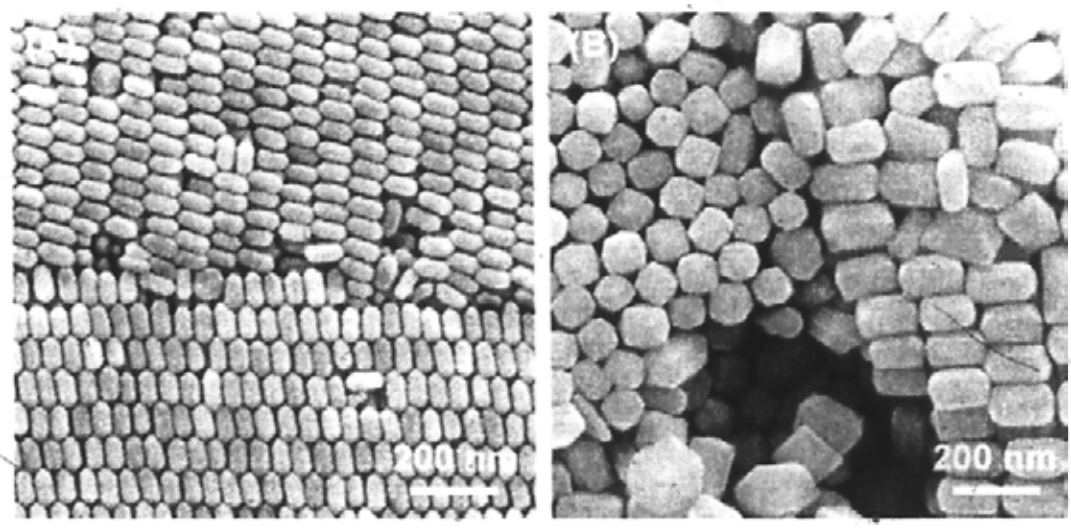


Figure 6.2.1. SEM images of the Au nanorods (A) and Au THH nanocrystals (B).

The Au nanorods and THH nanocrystals were then deposited onto glass and silicon wafers for characterizing their far-field scattering properties. The scattering patterns and spectra of these two samples are shown in Figure 6.2.2. The Au nanorods exhibit only one dominant scattering peak centering at 580 nm when they are deposited onto a glass substrate. On the other hand, when the nanorods are adhered to silicon, their scattering spectra show two resonance modes. One is at 530 nm and the other at 680 nm. I therefore carried out FDTD calculations to reveal the origins of these scattering modes. The calculations were performed from 450 to 900 nm. The refractive index of glass was set to 1.55 and kept as a constant over the above wavelength range. The dielectric constant of silicon at different wavelengths was obtained from previous experimental measurements [41]. The dielectric function of Au was the same as that used in Chapter 5. The sizes and shapes of the nanorods and the THH Au nanocrystals mentioned below were set according to the measurements from their SEM and TEM images. The FDTD calculations were performed with different excitation polarizations. The electric field can be decomposed into three components, with one perpendicular (vertically polarized) and the other two parallel (horizontally polarized) to the substrate plane. One

of the horizontally polarized excitation is along the longitudinal axis (HL polarized) while the other one is along the transverse axis (HT polarized) of the nanocrystal. The total scattering spectrum is obtained by summing up the spectra from all these three components. The calculation results for the Au nanorods on glass and silicon are included in Figure 6.2.2A and B (the colored lines). The calculated spectra can well reproduce the experimental measurements. The scattering intensities of the vertically polarized mode (blue) and the HT polarized mode (yellow) are very small for the nanorod on the glass substrate. The HL polarized mode (green) dominates the total scattering spectrum (red). This is consistent with the solid-spot scattering pattern shown in the inset. On the other hand, the relative intensity of the vertically polarized mode becomes much stronger and comparable with that of the HL polarized mode when the nanorod is deposited onto the silicon substrate. Moreover, the HL polarized mode shows a red-shift of ~100 nm compared to that of the nanorod on glass. These are ascribed to the fact that the dielectric constant of silicon is much larger than that of glass (Figure 6.1.4). A Large dielectric constant can lead to much stronger coupling between the nanorod and the substrate, which is further confirmed by the donut-shaped scattering pattern shown in the inset.

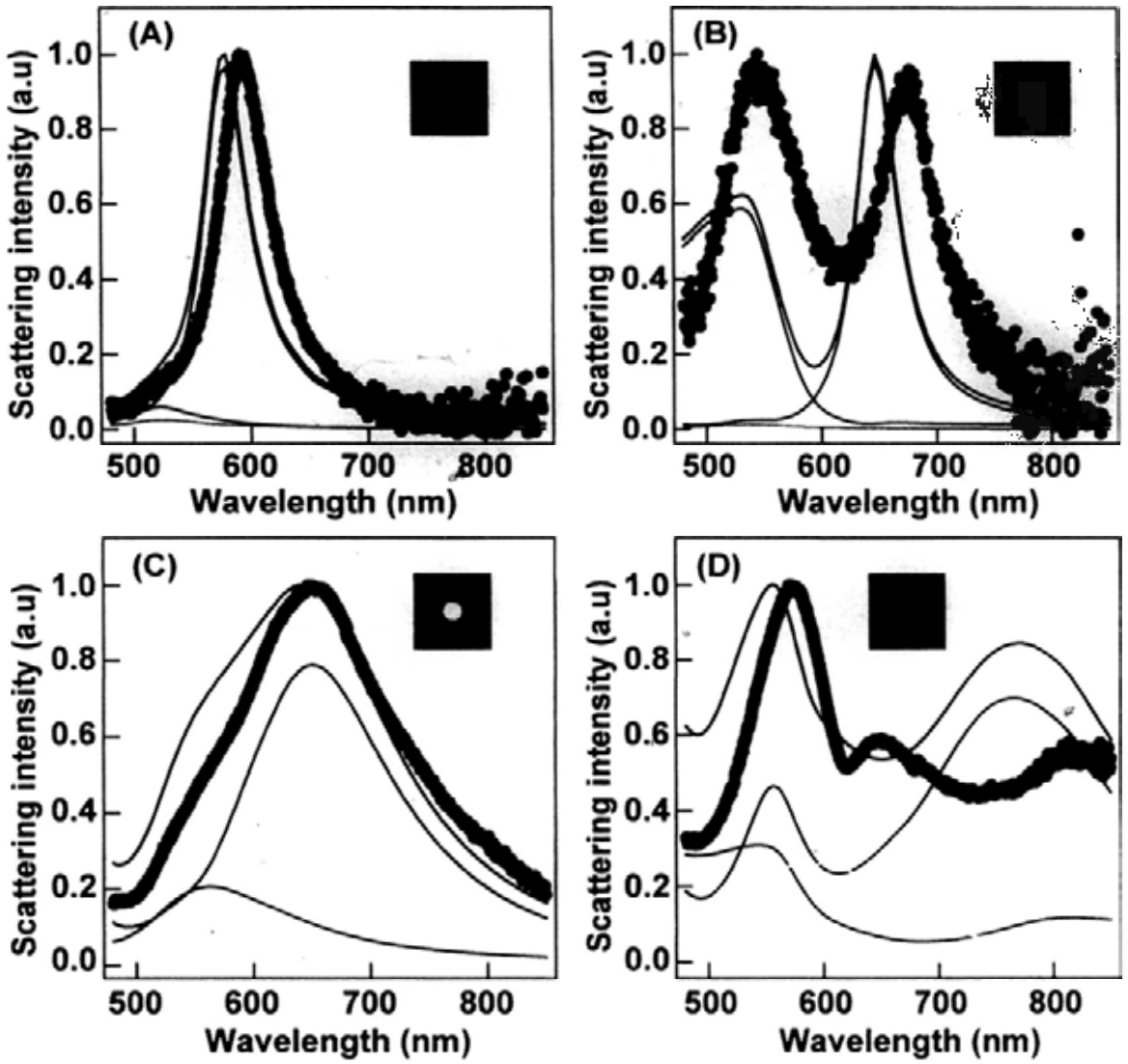


Figure 6.2.2. Experimental (dots) and calculated (colored lines) scattering spectra of the Au nancrystals on the different substrates. (A) Au nanorod on glass. (B) Au nanorod on silicon. (C) Au THH nanocrystal on glass. (D) Au THH nanocrystal on silicon. The green, blue, and yellow lines stand for the HL polarized, vertically polarized, and HT polarized resonance modes. The red line represents their sums. The colored images in the insets are the far-field scattering patterns of the related nanocrystals. All the experiment spectra are typical results taken over 10 nanocrystals for each sample.

For the Au THH nanocrystal with a much larger volume, its scattering spectrum on glass is

similar to that of the nanorod (Figure 6.2.2C). The scattering pattern is also a solid bright spot (the inset in Figure 6.2.2C). The FDTD results indicate that the total spectrum is dominated by the HL polarized mode at 658 nm. Moreover, the scattering spectrum shows significant broadening (120 nm for the HL polarized mode) compared to that of the nanorod (45 nm for the HL polarized mode). This broadening is due to the retardation effect and the increase of the radiation damping as the nanocrystal becomes larger. However, the scattering spectrum of the THH is extremely different from that of the nanorod when they are both deposited onto silicon. Three separated resonance modes can be observed in the experimental scattering spectrum of the THH shown in Figure 6.2.2D. One centers at 580 nm and the other two center at 650 and 830 nm, respectively. More interestingly, a well-defined small dip can be clearly observed between the 580 nm and the 650 nm peak. From the calculation results one can see that the HL polarized excitation can induce two resonance modes, with a broad one centering at 770 nm and a narrow one centering at 560 nm. Their widths are 139 and 39 nm, respectively. From the discussion below the broad resonance can be assigned as a dipole mode while the narrow one is a quadrupole mode arising from the large volume of the Au THH nanocrystal and the large dielectric constant of the substrate. The vertically polarized mode is represented by a relatively broad resonance (84 nm) at 540 nm. The donut-shaped scattering pattern (the inset) suggests that the vertical coupling between the THH and silicon is strong. The HT polarized mode is much broader over the investigated wavelength range and can be considered as a background. The scattering spectra of these three modes are then summed up to make comparison with the measured spectrum (red line in Figure 6.2.2D). However, the calculated spectrum can not reproduce the experimental one, especially the dip structure. These findings suggest that the coupling between the Au nanocrystal and the substrate becomes rather complicated for a large nanocrystal sitting on a substrate with a high dielectric constant.

The scattering spectrum of the Au THH nanocrystal on silicon was then studied in great detail so as to gain a further understanding. The spectra of an individual THH nanocrystal on silicon were firstly obtained for both s-polarized and p-polarized excitation to identify different resonance modes experimentally. For p-polarized excitation, the wavevector of the incident light was oriented ~ 60° from the normal to the substrate according to our dark-field excitation geometry. The scheme of the experiment setup for the polarization-excitation measurements is shown in Figure 6.2.3.

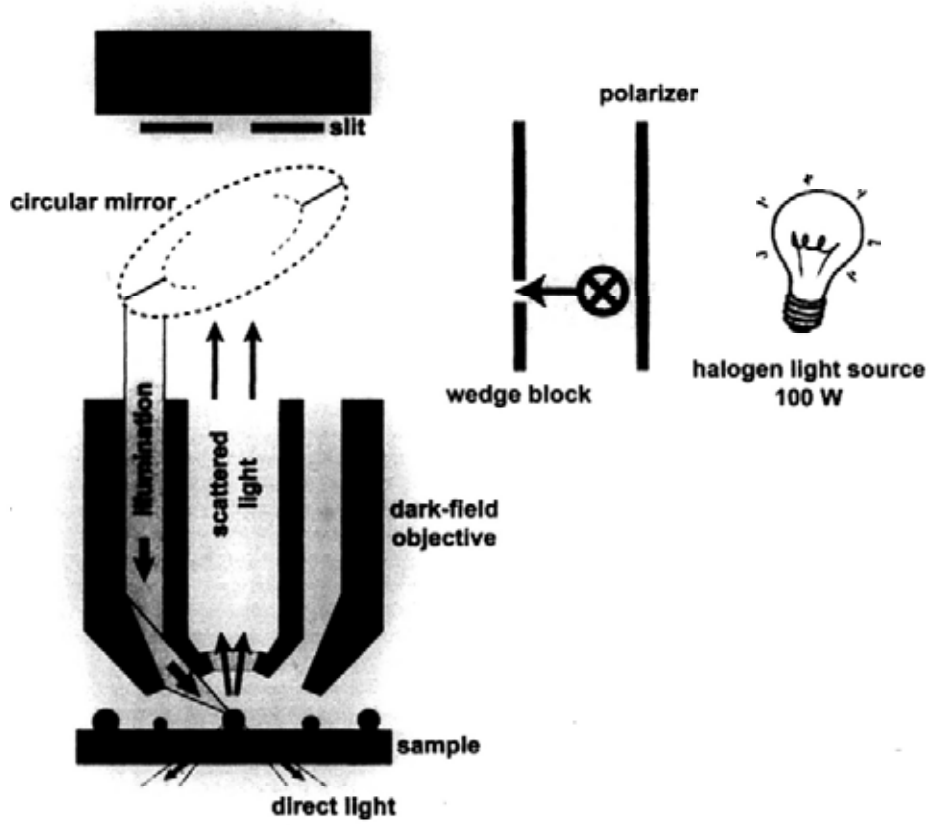


Figure 6.2.3. Scheme of the experiment setup for polarization-dependent dark-field microspectroscopy.

Polarized-excitation dependent spectra were measured on the nanocrystals illuminated by polarized light [43]. A linear polarizer (U–AN360 Olympus, JAPAN) was placed in the optical path

just after the halogen source in order to polarize the incident light. In order to retain a clean polarization at the sample plane, a beam block with a wedge-shaped cutout was placed in the optical path with the polarizer. This wedge was used to select only one portion of the beam that was then reflected by only one region of the circular mirror, thereby selecting one polarization at the sample plane. In our experiment the polarizer–wedge configuration was chosen such that the incident light was s-polarized with respect to the sample substrate (horizontally polarized), allowing for varying the polarization with respect to the nanocrystal by rotating the sample stage. The polarization of the incident light can be changed into p-polarized by rotating the wedge block by 90°. The collected scattering spectra were divided by the white-light scattering spectrum from the polarized halogen lamp for their calibration.

Figure 6.2.4A shows the schemes of the three different polarization excitations utilized in our experiments, including the HL polarized excitation (blue), HT polarized excitation (green), and the p-polarized excitation (red). The related experiment scattering spectra from an individual Au THH nanocrystal on silicon are shown in Figure 6.2.4B. Clearly the HL polarized excitation induces two resonances, with a narrow one (38 nm) centering at 540 nm and a broad one (161 nm) centering at ~870 nm. It should be mentioned that the detection limit of the spectrometer in our dark-field microscope prevents an accurate measurement of the signal in the wavelength range larger than 850 nm. This is why only a half portion of the resonance at 870 nm can be observed. However, this will not affect our conclusions as most interesting phenomena happen below 850 nm in this study. The HT polarized excitation only induces a broad resonance with much lower intensity. These findings are in excellent agreement with those from the FDTD calculations, which are shown in the right side in Figure 6.2.4C. On the other hand, under p-polarized excitation which includes both the vertically and horizontally polarized excitations, the scattering spectrum shows a similar shape as that in

Figure 6.2.2. The FDTD calculation was then performed for p-polarized excitation of the THH nanocrystal. The result is included in the left side in Figure 6.2.4C. The three resonance modes can be well reproduced and a clear dip around 640 nm is also observed in the calculated spectrum. The origins of these three different modes in the unpolarized experimental spectrum will be discussed below. As the contributions from the vertically polarized and the HT polarized resonance are very small when the wavelength is larger than 700 nm, it can be concluded that the resonance at 830 nm in the unpolarized scattering spectrum is mainly originated from the low-energy mode of HL polarized resonance. On the other hand, the relatively complicated scattering spectrum in the range of 530–750 nm is contributed by both the high-energy HL polarized and the vertically polarized resonances.

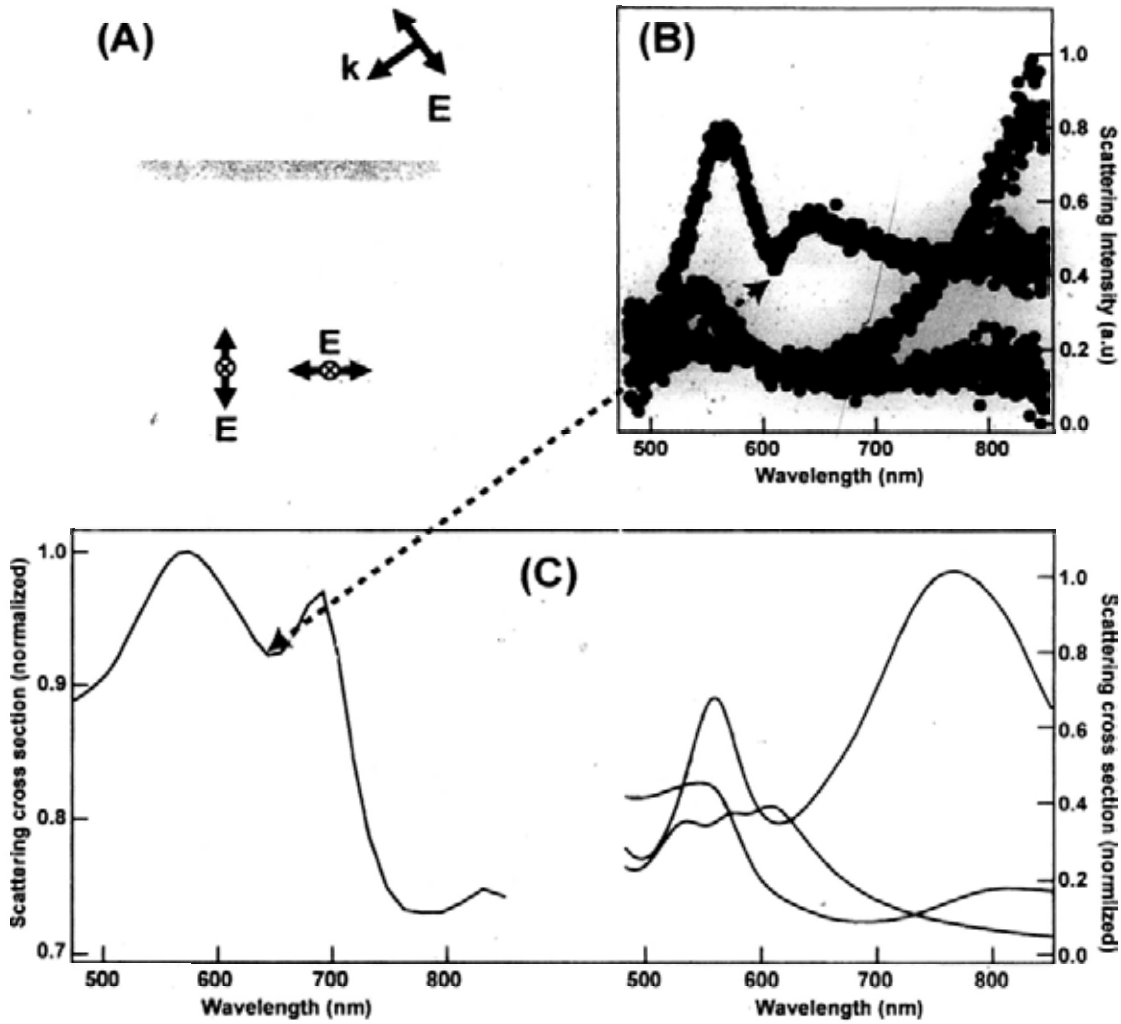


Figure 6.2.4. Polarization dark-field scattering of an individual Au THH nanocrystal on a silicon substrate. (A) Scheme of the three polarization excitations, including the HL polarized (blue), HT polarized (green), and p-polarized (red). (B) Experimental scattering spectra of a Au THH nanocrystal on silicon under the HL polarized (blue), HT polarized (green), and p-polarized (red) excitations. (C) Left side: calculated scattering spectrum of an individual Au THH nanocrystal on silicon under p-polarized excitation. Right side: calculated scattering spectra of Au THH nanocrystals on silicon under HL polarized (blue), HT polarized (green), and vertically polarized (black) excitations.

As it is mentioned above, substrates with large dielectric constants can mediate the interactions

between the different resonance modes of the nanocrystal and lead to their hybridization. This can be seen more clearly by calculating the charge distributions at the different resonance modes in the nanocrystal and the silicon substrate. Figure 6.2.5A shows the charge distributions for the HL polarized resonance and vertically polarized resonance. The HL polarized resonance at 770 nm is a dipole mode and it is assigned as a HLD mode. The HL polarized resonance at 560 nm is a quadrupole mode, which is assigned as a HLQ mode. The vertically polarized resonance at 540 nm is relatively complicated and of an octupole nature. It is assigned as a VO mode. The higher-order resonance modes usually come up in nanocrystals of large volumes because of the retardation effect [44 – 46]. In addition, as the HLQ mode cannot be seen in the calculated spectra for the THH on glass, it can be concluded that the large dielectric constant of silicon is another origin of this mode. Interestingly, all of these three resonance modes induce a similar surface charge distribution of dipolar nature in the substrate. Therefore the surface charges of the substrate can lead to effective hybridizations among these modes via Coulomb interactions. Figure 6.2.5B shows the charge distributions of the nanocrystal–silicon substrate system under p-polarized excitation, which illustrates more clearly how the hybridization occurs. The resonance at 570 nm is of an octupole nature, while the resonance at 690 nm has a quadrupole nature. This result indicates that these two resonances result from the hybridization between the HLQ mode and the VO mode. This finding is consistent with a recent theoretical study, which shows that strong substrate-mediated interaction could lead to hybridization between the dipole mode and quadrupole mode of a Au nanoshell [24]. As the resonance width of the HLQ mode (39 nm) is narrower than that of the VO mode (84 nm), the coupling between a broad mode and a narrow mode with alike energy can induce Fano resonance and give rise to the dip structure in the scattering spectrum (Figure 6.2.2D and Figure 6.2.4B and C) [47 – 53]. The charge distribution of the dip exhibits a quadrupole nature (Figure

6.2.5B).

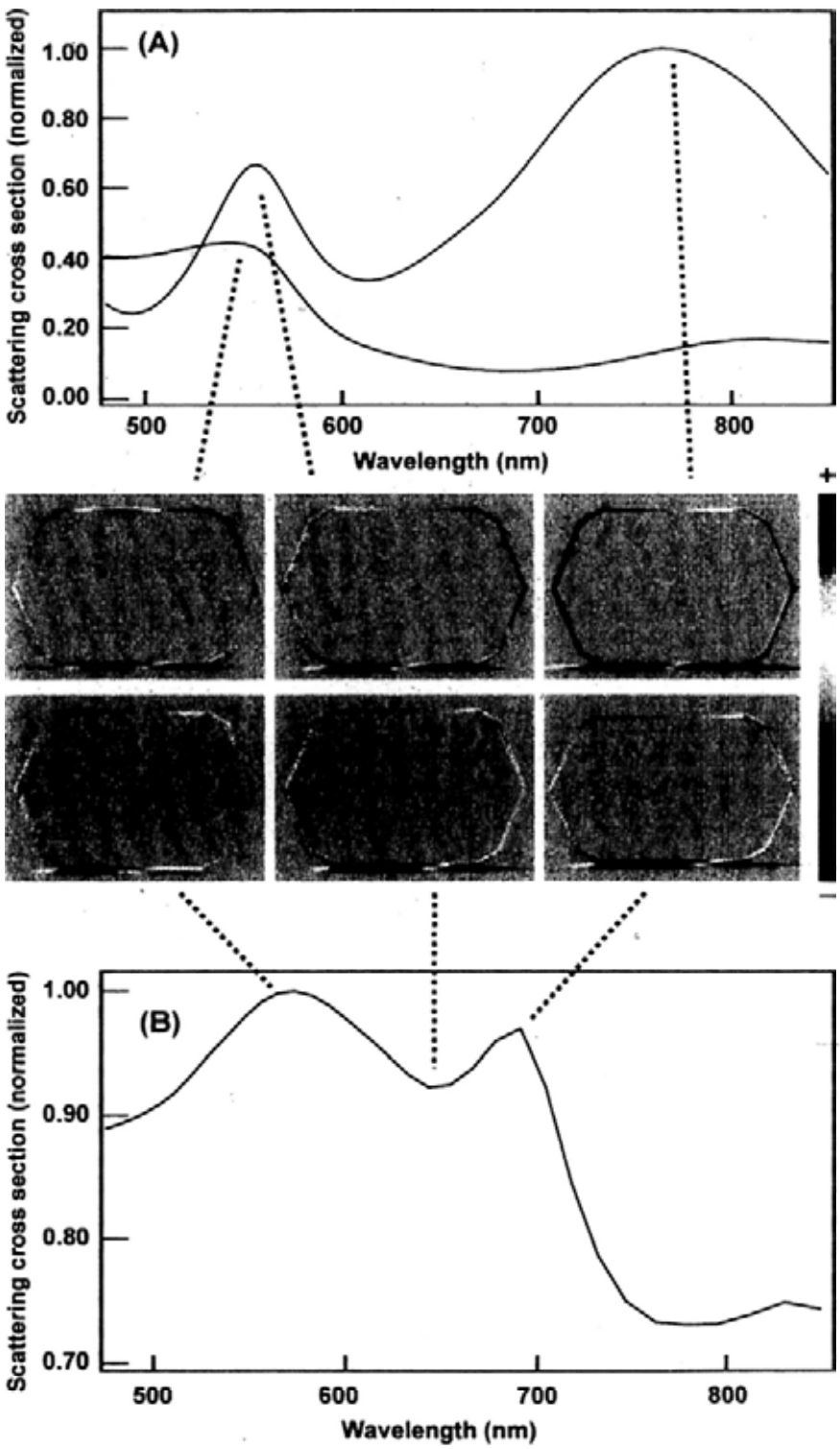


Figure 6.2.5. Charge distributions of the different resonances in an individual Au THH nanocrystal

on silicon. The nanocrystal is under the different polarized excitations. (A) HL polarized (blue) and vertically polarized (black). (B) P-poloarized excitation. The colored figures show the charge distributions of the different resonance modes. They have been linked to the related modes by the black dashed lines.

The Fano resonance can be further corroborated by analyzing the unpolarized scattering spectrum with a phenomenological Fano interference model [48, 51, 54 – 57],

$$S(E) = \left| a_r - \sum_{j=1}^{3} \frac{b_j \Gamma_j \exp(i\phi_j)}{E - E_j + i\Gamma_j} \right|^2 \qquad (6.2.1)$$

where $E$ is the energy of the incident photon, $a_r$ is the constant amplitude of the background, $b_j$ and $\Phi_j$ specify the amplitudes and phases of each resonance, $\omega_j$ and $\Gamma_j$ represent their resonance energies and linewidths. Figure 6.2.6 illustrates the result of the fitting and the individual contributions from each resonance. Excellent agreement is found between the experiment and the model by using the parameters in the caption.

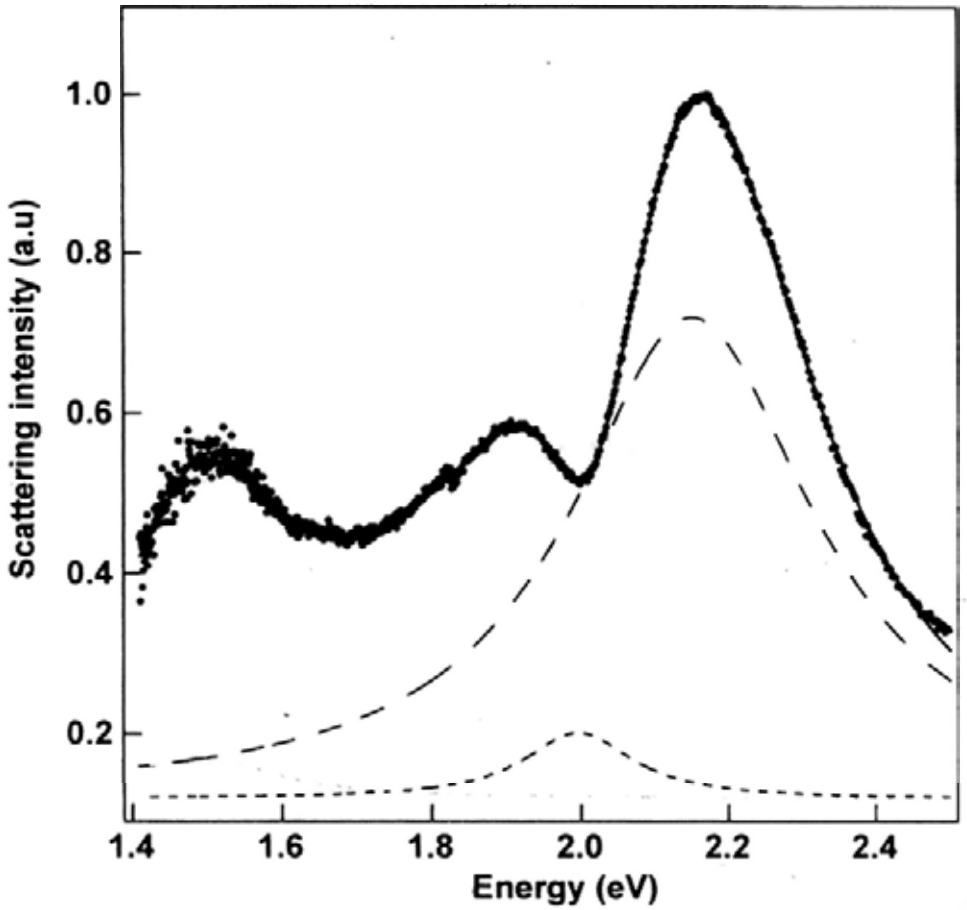


Figure 6.2.6. Fitting of the scattering spectrum of a Au THH nanocrystal on the silicon substrate by using the Fano interference model. The parameters are $a_r$ = –0.34, $b_1$ = 0.29, $\Gamma_1$ = 0.09 eV, $\Phi_1$ = 230°, $E_1$ = 2.00 eV; $b_2$ = 0.78, $\Gamma_2$ = 0.20 eV, $\Phi_2$ = 105°, $E_2$ = 2.15 eV; $b_3$ = 0.23, $\Gamma_3$ = 0.12 eV, $\Phi_3$ = 71°, $E_3$ = 1.49 eV. The blue, green, and orange dashed lines are the individual resonances.

The above model analysis provides important information on the Fano resonance formalism. The dip structure is indeed induced by the coupling between a broad resonance (0.20 eV) of higher energy at 2.15 eV and a narrow (0.09 eV) resonance of lower energy at 2.00 eV. By comparing with the FDTD calculation results shown in Figure 6.2.5, we can assign the higher energy mode at 2.15 eV to the VO resonance and the lower energy mode at 2.00 eV to the HLQ resonance. The deviations from the model fitting and the FDTD calculations in resonance energies and linewidths

are due to the differences between the geometry of the Au THH nanocrystal model incorporated into the calculations and that of the real nanocrystal employed in the dark-field scattering experiments. The relatively large amplitude of the resonance mode at 2.15 eV is caused by the excitation geometry of the dark-field system, in which the perpendicular excitation is larger than the other polarizations.

The studies in §6.1 shows that the far-field scattering pattern of an individual Au nanorod on a silicon substrate is highly dependent on the distance between them. It is also interesting to see whether the distance between the Au THH nanocrystal and the silicon substrate will affect the Fano resonance. The Au THH nanocrystals were deposited onto $mSiO_2$-coated sililcon substrate and their scattering spectra were then collected as a function of the thickness of the $mSiO_2$ film. The results are shown in Figure 6.2.7A. As the separation between the nanocrystal and the substrate becomes large, the dipole mode associated with the HL polarized excitation shifts to high energy gradually. Its intensity also rises and becomes dominant in the total scattering spectrum. On the other hand, the hybridized resonances associated with the HLQ and VO modes further shift into higher energy region and broaden gradually. The dip is submerged into the broad resonance and then disappears when the separation is larger than 7.6 nm. Finally the scattering spectrum of the Au THH nanocrystal changes into the one similar to that of the nanocrystal on glass when the separation reaches 97.0 nm. These findings indicate that the coupling between large nanocrystals and substrates with large dielectric constants is highly sensitive to the separation between them. As the dip structure associated with the Fano resonance only exists when the separation is smaller than 8 nm, it can be inferred that the hybridizations between the different modes in the nanocrystal mediated by the substrate is a near-field interaction. Figure 6.2.7B shows the dependence of the dip position on the thickness of the film. A linear relation with a slope of 40 meV/nm can be found within the

experimental error. The distance sensitivity is about twice of that in a previous study by utilizing a spherical Au nanocrystal–Au film system (20 meV/nm). This finding again unveils the possibility to fabricate ultrasensitive detectors for monitoring the changes in the nanoscale distance by using this strong metal nanocrystal–substrate coupling effect.

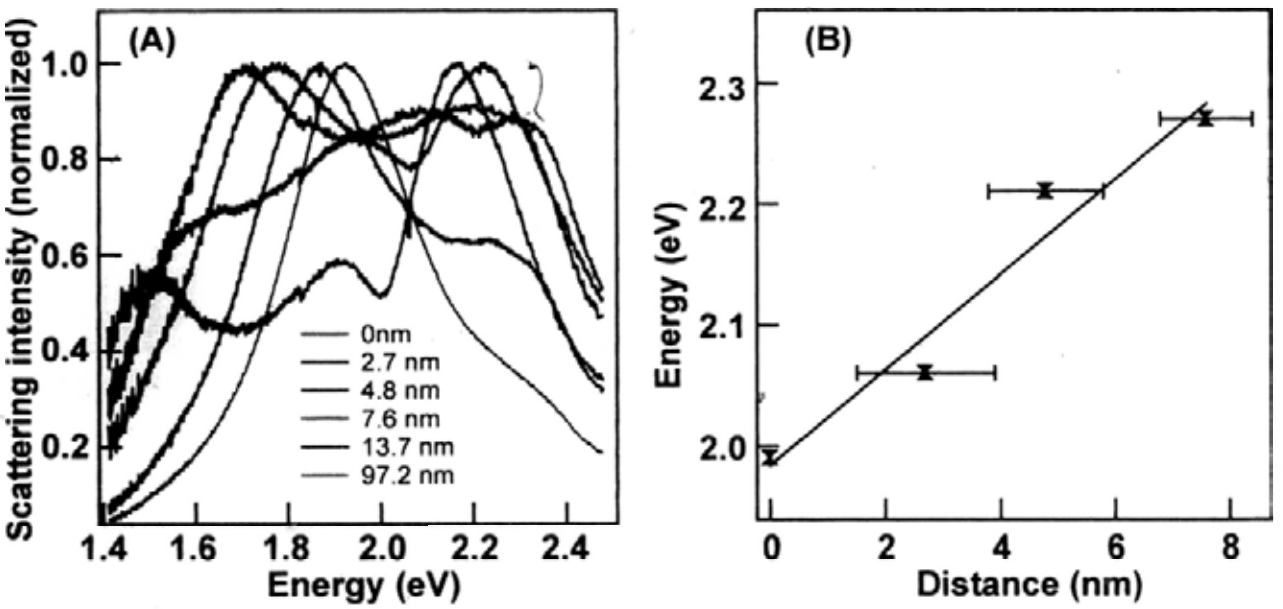


Figure 6.2.7. (A) Scattering spectra of the Au THH nanocrystals on silicon substrate with different $mSiO_2$ film thicknesses. (B) Dependence of the dip position on the thickness of the silica film. The solid red line is the linear fit of the experimental data.

## 6.3 Summary

In this chapter I have discussed the effects of substrates on the localized surface plasmon resonance behaviors of adjacent Au nanocrystals. The coupling between Au nanocrystals and substrates can alter their far-field scattering patterns and spectra enormously. It is found that the scattering pattern of an individual Au nanorod is highly dependent on the modulus of the dielectric constant of the substrate, as well as the separations between the nanorod and the substrate. When the

nanorod is in close proximity to a substrate with a large modulus of the dielectric constant, its horizontal resonance is damped out and a donut-shaped scattering pattern associated with the vertically resonance becomes dominant. Moreover, as the volume of a nanocrystal is increased, silicon substrates of a large dielectric constant can induce multipole-resonance modes in the nanocrystal. These modes can further hybridize together through the substrate and induce Fano resonance. This hybridization is found to be strongly dependent on the distance between the nanocrystal and the substrate. It only takes into effect when the separation is below 8 nm. The results in this chapter have furthered our understanding on the localized surface plasmon resonances of metal nanocrystals in non-uniform dielectric environments. This development will be of great help in analyzing and deducing the resonance properties of future plasmonic devices in which substrates will mostly be utilized. Moreover, the above studies can also lead to the development of ultrasensitive plasmonic sensors that can detect subtle nanoenvironment changes involving induce changes in the separation between the plasmonic nanocrystal and the substrate.

## References

[1] A. J. Haes, R. P. Van Duyne, A Nanoscale Optical Biosensor: Sensitivity and Selectivity of an Approach Based on the Localized Surface Plasmon Resonance Spectroscopy of Triangular Silver Nanoparticles. *J. Am. Chem. Soc.*, 124: 10596, 2002.

[2] A. J. Haes, L. Chang, W. L. Klein, R. P. Van Duyne, Detection of a Biomarker for Alzheimer's Disease from Synthetic and Clinical Samples Using a Nanoscale Optical Biosensor. *J. Am. Chem. Soc.*, 127: 2264, 2005.

[3] J. N. Anker, W. P. Hall, O. Lyandres, N. C. Shah, J. Zhao, R. P. Van Duyne, Biosensing with Plasmonic Nanosensors. *Nat. Mater.*, 7: 442, 2008.

[4] S. Pillai, K. R. Catchpole, T. Trupke, M. A. Green, Surface Plasmon Enhanced Silicon Solar Cells. *J. Appl. Phys.*, 101: 093105, 2007.

[5] K. Nakayama, K. Tanabe, H. A. Atwater, Plasmonic Nanoparticle Enhanced Light Absorption in GaAs Solar Cells. *Appl. Phys. Lett.*, 93: 121904, 2008.

[6] F. J. Beck, A. Polman, K. R. Catchpole, Tunable Light Trapping for Solar Cells Using Localized Surface Plasmons. *J. Appl. Phys.*, 105: 114310, 2009.

[7] H. A. Atwater, A. Polman, Plasmonics for Improved Photovoltaic Devices. *Nat. Mater.*, 9: 205, 2010.

[8] S. A. Maier, P. G. Kik, H. A. Atwater, S. Meltzer, E. Harel, B. E. Koel, A. A. G. Requicha, Local Detection of Electromagnetic Energy Transport below the Diffraction Limit in Metal Nanoparticle Plasmon Waveguides. *Nat. Mater.*, 2: 229, 2003.

[9] S. A. Maier, M. L. Brongersma, P. G. Kik, S. Meltzer, A. A. G. Requicha, H. A. Atwater, Plasmonics – A Route to Nanoscale Optical Devices. *Adv. Mater.*, 13: 1501, 2001.

[10] J. R. Krenn, A. Dereux, J. C. Weeber, E. Bourillot, Y. Lacroute, J. P. Goudonnet,, Squeezing the

Optical Near-Field Zone by Plasmon Coupling of Metallic Nanoparticles. *Phys. Rev. Lett.*, 82: 2590, 1999.

[11] B. Auguié, W. L. Barnes, Collective Resonances in Gold Nanoparticle Arrays, *Phys. Rev. Lett.*, 101: 143902, 2008.

[12] V. G. Kravets, F. Schedin, A. N. Grigorenko, Extremely Narrow Plasmon Resonances Based on Diffraction Coupling of Localized Plasmons in Arrays of Metallic Nanoparticles. *Phys. Rev. Lett.*, 101: 087403, 2008.

[13] H.-T. Chen, W. J. Padilla, J. M. O. Zide, A. C. Gossard, A. J. Taylor, R. D. Averitt, Active Terahertz Metamaterial Devices. *Nature*, 444: 597, 2006.

[14] N. Liu, H. C. Guo, L. W. Fu, S. Kaiser, H. Schwerizer, H. Giessen, Three-Dimensional Photonic Metamaterials at Optical Frequencies. *Nat. Mater.*, 7: 31, 2008.

[15] J. Valentine, S. Zhang, T. Zentgraf, E. Ulin-Avila, D. A. Genov, G. Bartal, X. Zhang, Three-Dimensional Optical Metamaterial with a Negative Refractive Index. *Nature*, 455: 376.

[16] N. Liu, L. Langguth, T. Weiss, J. Kästel, M. Fleischhauer, T. Pfau, H. Giessen, Plasmonic Analogue of Electromagnetically Induced Transparency at the Drude Damping Limit. *Nat. Mater.*, 8: 758, 2009.

[17] M. W. Knight, Y. P. Wu, J. B. Lassiter, P. Nordlander, N. J. Halas, Substrates Matter: Influence of an Adjacent Dielectric on an Individual Plasmonic Nanoparticle. *Nano Lett.*, 9: 2188, 2009.

[18] P. Nordlander, E. Prodan, Plasmon Hybridization in Nanoparticles near Metallic Surfaces. *Nano Lett.*, 4: 2209, 2004.

[19] T. Okamoto, I. Yamaguchi, Optical Absorption Study of the Surface Plasmon Resonance in Gold Nanoparticles Immobilized onto a Gold Substrate by Self-Assembly Technique. *J. Phys. Chem. B*, 107: 10321, 2003.

[20] F. Le, N. Z. Lwin, J. M. Steele, M. Käll, N. J. Halas, P. Nordlander, Plasmons in the Metallic Nanoparticle–Film System as a Tunable Impurity Problem. *Nano Lett.*, 5: 2009, 2005.

[21] V. V. Gozhenko, L. G. Grechko, Electrodynamics of Spatial Clusters of Spheres: Substrate Effects. *Phys. Rev. B*, 68: 125422, 2003.

[22] G. Lévêque, O. J. F. Martin, Optical Interactions in a Plasmonic Particle Coupled to a Metallic Film. *Opt. Express*, 14: 9971, 2006.

[23] G. Lévêque, O. J. F. Martin, Tunable Composite Nanoparticle for Plasmonics. *Opt. Lett.*, 31: 2750, 2006.

[24] Y. P. Wu, P. Nordlander, Finite-Difference Time-Domain Modeling of the Optical Properties of Nanoparticles near Dielectric Substrates. *J. Phys. Chem. C*, 114: 7302, 2010.

[25] Y. Chen, K. Munechika, D. S. Ginger, Dependence of Fluorescence Intensity on the Spectral Overlap between Fluorophores and Plasmon Resonant Single Silver Nanoparticles. *Nano Lett.*, 7: 690, 2007.

[26] C. L. Haynes, R. P. Van Duyne, Plasmon-Sampled Surface-Enhanced Raman Excitation Spectroscopy. *J. Phys. Chem. B*, 107: 7426, 2003.

[27] K. R. Catchpole, A. Polman, Design Principles for Particle Plasmon Enhanced Solar Cells. *Appl. Phys. Lett.*, 93: 191113, 2008.

[28] F. Moreno, B. García-Cámara, J. M. Saiz, F. González, Interaction of Nanoparticles with Substrates: Effects on the Dipolar Behavior of the Particles. *Opt. Express*, 16: 12487, 2008.

[29] J. J. Mock, R. T. Hill, A. Degiron, S. Zauscher, A. Chilkoti, D. R. Smith, Distance-Dependent Plasmon Resonant Coupling between a Gold Nanoparticle and Gold Film. *Nano Lett.*, 8: 2245, 2008.

[30] A. Dmitriev, C. Hägglund, S. Chen, H. Fredriksson, T. Pakizeh, M. Käll, D. S. Sutherland,

Enhanced Nanoplasmonic Optical Sensors with Reduced Substrate Effect. *Nano Lett.*, 8: 3893, 2008.

[31] S.-H. Guo, S.-J. Tsai, H.-C. Kan, D.-H. Tsai, M. R. Zachariah, R. J. Phaneuf, The Effect of an Active Substrate on Nanoparticle-Enhanced Fluorescence. *Adv. Mater.*, 20: 1424, 2008.

[32] P. K. Jain, K. S. Lee, I. H. El-Sayed, M. A. El-Sayed, Calculated Absorption and Scattering Properties of Gold Nanoparticles of Different Size, Shape, and Composition: Applications in Biological Imaging and Biomedicine. *J. Phys. Chem. B*, 110: 7238, 2006.

[33] W. H. Ni, X. S. Kou, Z. Yang, J. F. Wang, Tailoring Longitudinal Surface Plasmon Wavelengths, Scattering and Absorption Cross Sections of Gold Nanorods. *ACS Nano*, 2: 677, 2008.

[34] X. S. Kou, W. H. Ni, C.-K. Tsung, K. Chan, H.-Q. Lin, G. D. Stucky, J. F. Wang, Growth of Gold Bipyramids with Improved Yield and Their Curvature-Directed Oxidation. *Small*, 3: 2103, 2007.

[35] C. Sönnichsen, T. Franzl, T. Wilk, G. Von Plessen, J. Feldmann, Drastic Reduction of Plasmon Damping in Gold Nanorods. *Phys. Rev. Lett.*, 88: 077402, 2002.

[36] P. C. A. Alberius, K. L. Frindell, R. C. Hayward, E. J. Kramer, G. D. Stucky, B. F. Chmelka, General Predictive Syntheses of Cubic, Hexagonal, and Lamellar Silica and Titania Mesostructured Thin Films. *Chem. Mater.*, 14: 3284, 2002.

[37] J. D. Jackson, Classical Electrodynamics, 2nd ed. Wiley, New York, 1975.

[38] U. Kreibig, M. Vollmer, Optical Properties of Metal Clusters. Berlin: Springer-verlag; New York: Springer-Verlag, c1995.

[39] C. Bohren, D. Huffman, Absorption and Scattering of Light by Small Particles. New York: Wiley, 1983.

[40] L. Novotny, B. Hecht, Principles of Nano-Optics, University Press: Cambridge, 2006.

[41] E. D. Palik, Handbook of Optical Constants of Solids, Academic Press, Boston, 1985.

[42] T. Ming, W. Feng, Q. Tang, F. Wang, L. D. Sun, J. F. Wang, C. H. Yan, Growth of Tetrahexahedral Gold Nanocrystals with High-Index Facets. *J. Am. Chem. Soc.*, 131: 16350, 2009.

[43] J. B. Lassiter, J. Aizpurua, L. I. Hernandez, D. W. Brandl, I. Romero, S. Lal, J. H. Hafner, P. Nordlander, N. J. Halas, Close Encounters between Two Nanoshells. *Nano Lett.*, 8: 1212, 2008.

[44] N. Félidj, J. Grand, G. Laurent, J. Aubard, G. Lévi, A. Hohenau, N. Galler, F. R. Aussenegg, J. R. Krenn, Multipolar Surface Plasmon Peaks on Gold Nanotriangles. *J. Chem. Phys.*, 128: 094702, 2008.

[45] F. Hao, E. M. Larsson, T. A. Ali, D. S. Sutherland, P. Nordlander, Shedding Light on Dark Plasmons in Gold Nanorings. *Chem. Phys. Lett.*, 458: 262, 2008.

[46] F. Tam, A. L. Chen, J. Kundu, H. Wang, N. J. Halas, Mesoscopic Nanoshells: Geometry-Dependent Plasmon Resonances beyond the Quasistatic Limit. *J. Chem. Phys.*, 127: 204703, 2007.

[47] U. Fano, Effects of Configuration Interaction on Intensities and Phase Shifts. *Phys. Rev.*, 124: 1866, 1961.

[48] A. Christ, Y. Ekinci, H. H. Solak, N. A. Gippius, S. G. Tikhodeev, O. J. F. Martin, Controlling the Fano Interference in a Plasmonic Lattice. *Phys. Rev. B*, 76: 201405(R), 2007.

[49] G. Bachelier, I. Russier-Antoine, E. Benichou, C. Jonin, N. D. Fatti, F. Vallée, P.-F. Brevet, Fano Profiles Induced by Near-Field Coupling in Heterogeneous Dimers of Gold and Silver Nanoparticles. *Phys. Rev. Lett.*, 101: 197401, 2008.

[50] F. Hao, Y. Sonnefraud, P. V. Dorpe, S. A. Maier, N. J. Halas, P. Nordlander, Symmetry Breaking in Plasmonic Nanocavities: Subradiant LSPR Sensing and a Tunable Fano Resonance. *Nano Lett.*, 8: 3983, 2008.

[51] F. Hao, P. Nordlander, Y. Sonnefraud, P. V. Dorpe, S. A. Maier, Tunability of Subradiant Dipolar and Fano-Type Plasmon Resonances in Metallic Ring/Disk Cavities: Implications for Nanoscale Optical Sensing. *ACS Nano*, 3: 643, 2009.

[52] N. Verellen, Y. Sonnefraud, H. Sobhani, F. Hao, V. V. Moshchalkov, P. V. Dorpe, P. Nordlander, S. A. Maier, Fano Resonances in Individual Coherent Plasmonic Nanocavities. *Nano Lett.*, 9: 1663, 2009.

[53] N. A. Mirin, K. Bao, P. Nordlander, Fano Resonances in Plasmonic Nanoparticle Aggregates. *J. Phys. Chem. A*, 113: 4028, 2009.

[54] C. Ropers, D. J. Park, G. Stibenz, G. Steinmeyer, J. Kim, D. S. Kim, C. Lienau, Femtosecond Light Transmission and Subradiant Damping in Plasmonic Crystals. *Phys. Rev. Lett.*, 94: 113901, 2005.

[55] N. A. Gippius, S. G. Tikhodeev, T. Ishihara, Optical Properties of Photonic Crystal Slabs with an Asymmetrical Unit Cell. *Phys. Rev. B*, 72: 045138, 2005.

[56] S. H. Fan, J. D. Joannopoulos, Analysis of Guided Resonances in Photonic Crystal Slabs. *Phys. Rev. B*, 65: 235112, 2002.

[57] Y. Ekinci, A. Christ, M. Agio, O. J. F. Martin, H. H. Solak, J. F. Löffler, Electric and Magnetic Resonances in Arrays of Coupled Gold Nanoparticle in-Tandem Pairs. *Opt. Express*, 16: 13287, 2008.

# Chapter 7

# Photothermal Conversion Properties of Gold Nanoerystals

Excitation of the localized surface plasmon resonance of Au nanostructures can induce very large light absorption. The absorbed light can be converted to heat, which is thereafter transferred to the surrounding environment to cause a temperature increase. This photothermal conversion effect has been employed to selectively kill cancer cells [1 – 7], controllably release genes [8, 9] and deliver drugs [10, 12], image biological components on the basis of photothermal interference contrast [13, 15], optically record data five-dimensionally [16], and drive and guide liquid flow in microfluidic channels [17]. A critical factor for the successful use of plasmonic Au nanostructures in all of these applications is the photothermal conversion efficiency. Therefore, a thorough understanding of the effects of various experimental parameters on the photothermal conversion efficiency is very important. Several methods have been developed for the characterization of the photothermal conversion effect. The local temperature increases arising from the illumination of Au nanorods embedded in polymer matrices have been visualized with infrared cameras [18]. The photothermal conversion properties of Au nanospheres have been studied by embedding them in ice and measuring the time-dependent Raman signals of ice to monitor the melting process [19]. Thermochromic microcapsules have been utilized to reveal the temperature change by dispersing them together with Au nanospheres in liquids [17]. In addition, the photothermal conversion

properties of Au nanospheres have also been measured experimentally and modeled theoretically on the basis of microliter-scale water droplets that are kept still on the tip of syringe needles [20]. These measurements are either time consuming or complicated. They are therefore difficult to be employed for simple and quick investigation of the photothermal properties of a large number of noble metal nanostructures with varying sizes, plasmon wavelengths, and structural complexities.

Two recent experiments have demonstrated the continuous monitoring of the temperature variations of Au nanostructure dispersions under laser illumination by placing a thermocouple in the dispersions [21, 22]. This direct measurement method is simple and easy to perform. In the first experiment, the temperature changes of $SiO_2$–Au core–shell, $Au_2S$–Au core–shell, and Au nanorod samples that have the same plasmon wavelength have been measured. The photothermal conversion efficiencies have been found to differ by a factor of 3 among the three Au nanostructure samples [21]. In the second experiment, the photothermal properties of lithographically fabricated Au nanopyramids that have two different base diameters, two shell thicknesses, and two shapes have been determined. The Au nanopyramids with thin shells and sharp tips have been found to exhibit the largest photothermal response [22].

In this chapter I report on the systematic studies of the photothermal conversion properties of Au nanocrystals by placing a thermocouple in aqueous Au nanocrystal dispersions to directly monitor the temperature rises under laser illumination. The measurement in aqueous solutions is especially of a relevance to the biotechnological applications of noble metal nanostructures because the tissues and cells in biological systems are essentially in an aqueous environment. In §7.1 I will present the investigation on the effect of the plasmon wavelength on the photothermal conversion properties of Au nanocrystals. In this study, I have grown Au nanorod samples that have longitudinal plasmon wavelengths ranging from 520 to 960 nm and measured their photothermal response. It is

found that the temperature of Au nanocrystal solutions reaches a maximum at ~75 °C when the plasmon resonance wavelength of Au nanocrystals is equal to the illumination laser wavelength. In §7.2 I focus on the effect of the particle volume on the photothermal conversion efficiencies of Au nanocrystals. For this study eight Au nanocrystal samples that have the same plasmon wavelength at 809 nm have been prepared, and their photothermal responses have been measured. The photothermal conversion efficiencies have also been obtained from the modeling based on the energy balance and compared with those obtained from electrodynamic calculations. The results show that for Au nanocrystals with similar shapes, the larger the nanocrystal, the smaller the photothermal conversion efficiency becomes. In many applications, metal nanostructures are required to be coated with different molecules and materials. Assembly and aggregation also occur when they interact with targeted objects. Both the shell coating and assembly can largely change the plasmonic properties of metal nanostructures. I have therefore further measured the photothermal responses of Au–ZnS and Au–$Ag_2S$ core–shell nanostructures and studied the effect of the controlled assembly of one Au nanopolyhedron sample and one Au nanorod sample on the photothermal conversion in §7.3 and §7.4.

## 7.1 Effect of the Plasmon Wavelength

For studying the effect of the plasmon wavelength on the photothermal conversion properties of Au nanocrystals, nanorods were chosen because nanorod samples with varying longitudinal plasmon wavelengths can readily be synthesized. The Au nanorod samples in our experiments were prepared using a seed-mediated growth method together with anisotropic shortening as mentioned before [23, 24]. Specifically, two nanorod samples with LLPWs of 957 and 740 nm were employed as starting nanorods. The TEM images of six representative nanorod samples are shown in Figure 1A–F and the extinction spectra of all of the 20 nanorod samples are provided in Figure 1G. Both

the TEM images and extinction spectra indicate that these nanorod samples have narrow size distributions.

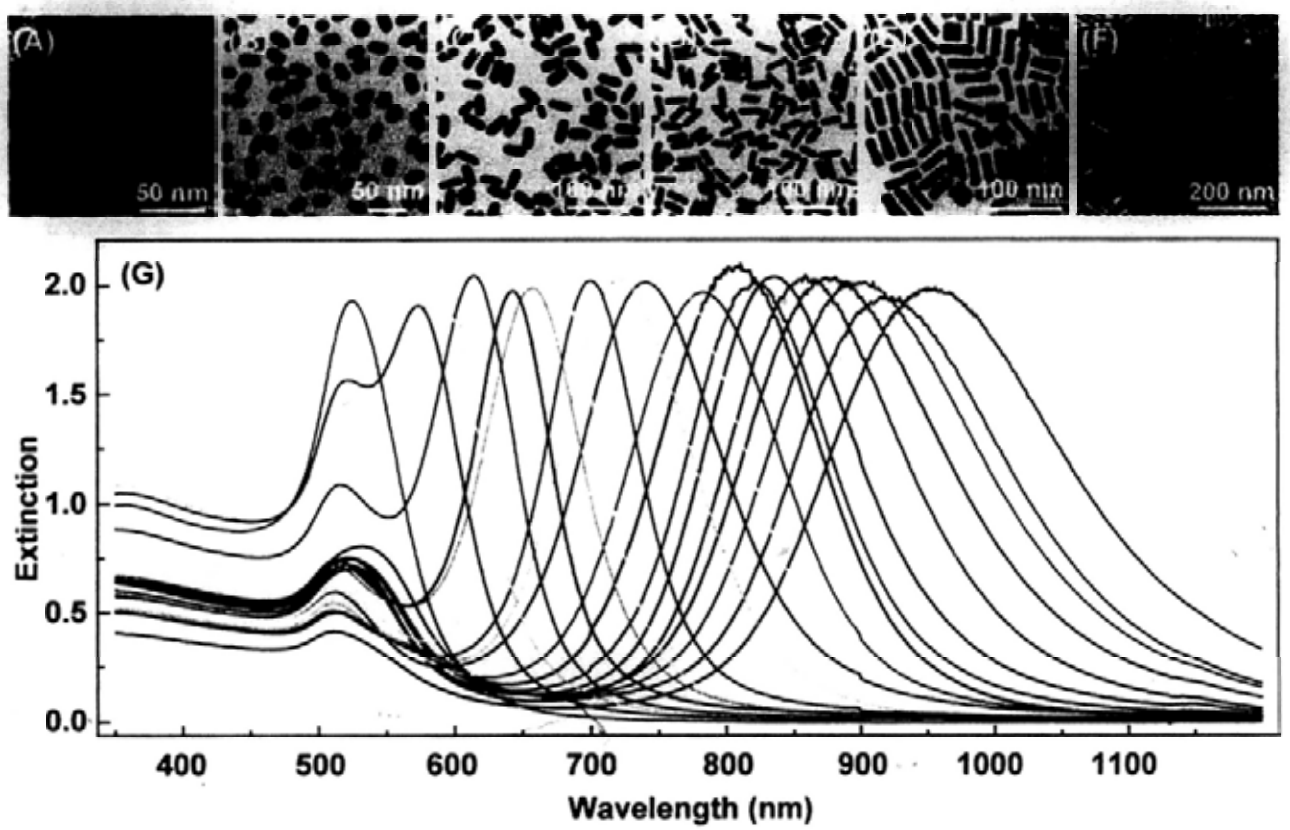


Figure 7.1.1. (A – F) TEM images of the representative Au nanorod samples. Their average lengths/diameters are (21 ± 2)/(17 ± 1), (29 ± 2)/(17 ± 1), (41 ± 3)/(17 ± 1), (43 ± 3)/(13 ± 1), (55 ± 7)/(13 ± 1), and (64 ± 6)/(12 ± 1) nm from (A) to (F), respectively. (G) Extinction spectra of the Au nanorod samples used in the experiment. The longitudinal plasmon wavelengths from left to right are 525, 574, 588, 615, 640, 660, 680, 700, 720, 741, 760, 776, 810, 820, 840, 860, 880, 900, 922, and 957 nm, respectively.

The LLPWs of the nanorod samples range from 520 to 960 nm, with an interval of ~20 nm per

sample. Their lengths and diameters are in the ranges of 20–65 and 10–20 nm, respectively. The extinction intensities at the longitudinal plasmon resonance peak wavelengths were adjusted to be around 2 for all of the nanorod samples for the photothermal measurements. The particle concentrations were therefore estimated to be in the range of 0.3–1.5 nM. They decrease as the nanorod sizes become larger.

The setup for the measurement of the photothermal conversion is shown in Figure 7.1.2. It is composed of a 1-cm path length quartz cuvette containing 2-mL of the Au nanorod solution and covered with a foam cap, a K-type thermocouple connected to a digital thermometer (CIE 305), and a continuous semiconductor diode laser (809 nm, JUM2500/50/20, VDM00036, JENOPTIK, Germany). In order to reduce the heat loss, the cuvette was clamped at its top part above the solution surface, with two pieces of foam inserted between the clamp heads and cuvette walls. The bottom of the cuvette was kept ~5 cm above the magnetic stirrer. The laser light was coupled out through an optical fiber with a power of 1.72 W and illuminated on the Au nanorod solution in the cuvette with a spot diameter of ~5 mm. The use of a 809-nm laser is because biological tissues have a window of high transmission in the spectral range of 650–900 nm. [25] The measurement of the photothermal properties in this transmission window will be of an important relevance to the biotechnological applications of metal nanostructures. The probe head of the thermocouple was completely submerged in the solution and carefully kept away from the illumination laser beam. The temperature was recorded every 30 s for 30 min after the laser was turned on. During the measurement, the solution was kept stirring with a small Teflon-coated magnetic stirring bar.


Figure 7.1.2. Digital photo showing the setup for the measurement of the photothermal conversion properties of the Au nanocrystals.

Figure 7.1.3 shows the temperature rise traces of the 20 nanorod samples under the laser illumination. All of the traces exhibit a similar trend. The temperature first increases rapidly and then reaches a plateau after ~20 min. The end temperature varies with the longitudinal plasmon wavelength, as shown in Figure 7.1.4. The end temperature for the Au nanorod sample with a longitudinal plasmon wavelength of 810 nm is 76 °C, which is the highest among all of the nanorod samples. If we consider the starting temperature of 21 °C, a remarkable maximum net temperature increase of 55 °C is obtained under our measurement conditions. For the nanorod samples with longitudinal plasmon wavelengths either shorter or longer than the illumination laser wavelength, the end temperature is lower. The variation of the end temperature versus the plasmon wavelength can be ascribed to the change in the extinction intensity at the laser wavelength. The extinction of

noble metal nanostructures is contributed by both the absorption and scattering. Only the absorbed light energy can be converted into heat. For Au nanorods, we have previously shown that the absorption-to-extinction ratio decreases nearly linearly with increasing diameters. The 20 nanorod samples employed in this experiment have two different diameters. Those with longitudinal plasmon wavelengths longer than 710 nm were obtained from the nanorod samples with a LLPW of 957 nm and have an average diameter of 12 nm, while those with longitudinal plasmon wavelengths shorter than 710 nm were obtained from the nanorod sample with a LLPW of 740 nm and have an average diameter of 17 nm. This is the reason for the presence of a jump around 710 nm in Figure 7.1.4. When the plasmon resonance peak is shifted away from the laser wavelength, the extinction value and therefore the light absorption at the laser wavelength become smaller, leading to the reduction in the end temperature. In addition, the end temperatures achieved with the nanorod samples with longitudinal plasmon wavelengths between 760–860 nm range from 72–76 °C. The differences from the highest value are less than 5 °C. This result can be ascribed to the large widths of the longitudinal plasmon peaks of the nanorod samples. It allows us to choose Au nanorod samples with plasmon wavelengths over a certain range without being exactly equal to the illumination laser wavelength in the applications involving the photothermal conversion.

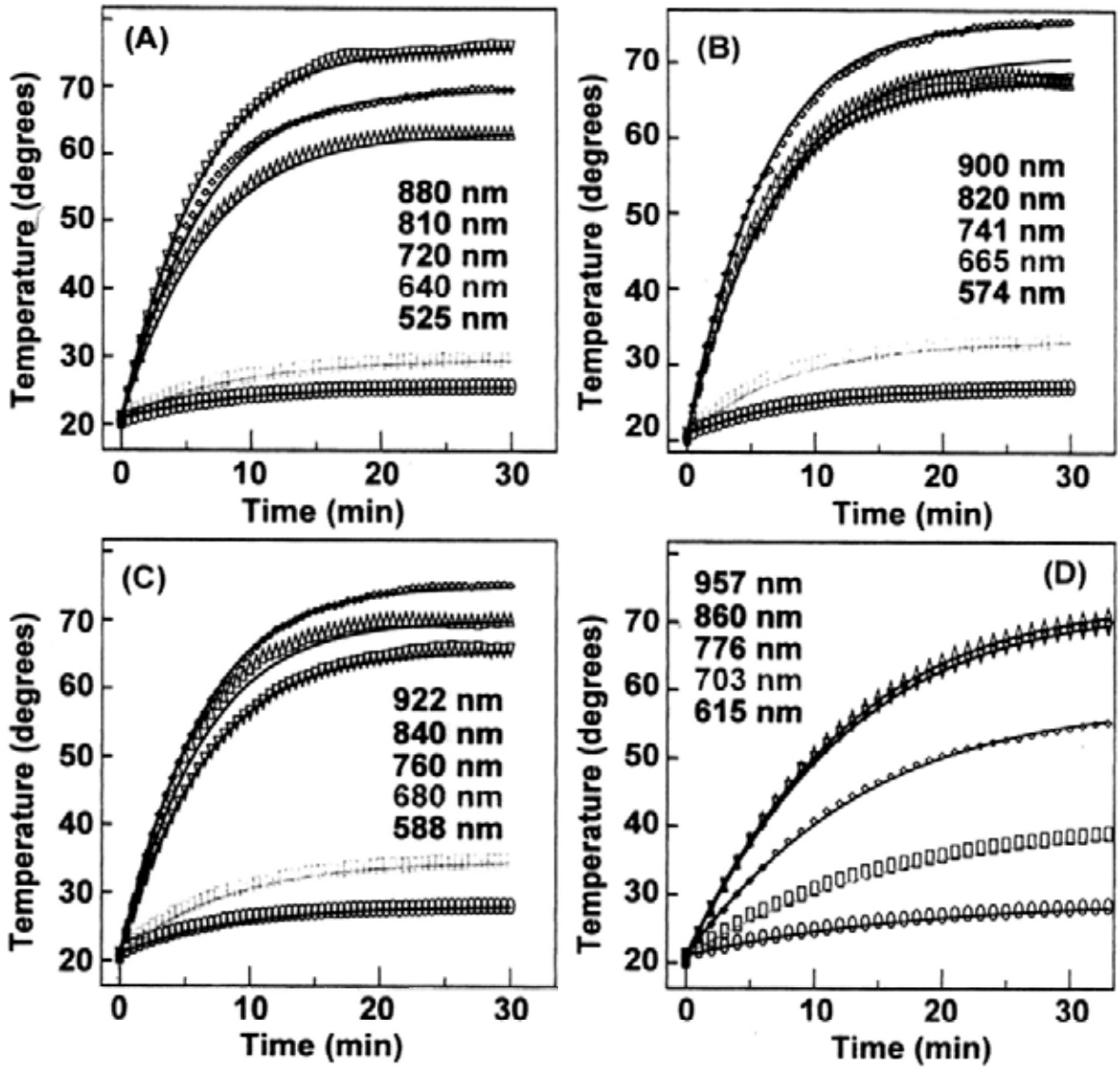


Figure 7.1.3. (A–D) Experimental (symbols) and calculated (solid lines) temperature traces for the 20 Au nanorod samples. The numbers indicate the LLPWs of the nanorod samples.

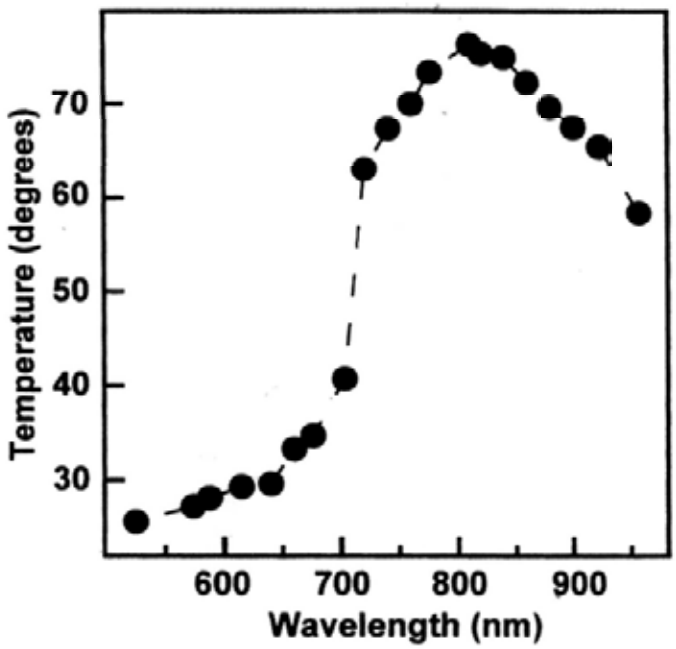


Figure 7.1.4. Dependence of the end temperature on the nanorod LLPW. The end temperature is an average of the last five points for each trace.

We employed a theoretical model to analyze the photothermal conversion process and determine the photothermal conversion efficiency. The model is based on the energy balance of the Au nanorod solution during the photothermal heating process [20, 26]. Because the solution was kept stirring, the temperature is reasonably assumed to be uniform in the solution. The energy balance can therefore be expressed as,

$$\left(m_w c_{pw} + m_c c_{pc}\right)\frac{\mathrm{d}\Delta T}{\mathrm{d}t} = Q_{\text{laser}} - Q_{\text{loss}} \tag{7.1.1}$$

where $m_w$ = 2 g is the mass of the solution, $m_c$ = 4.09 g is the mass of the quartz cell that is in contact with the solution, $c_{pw}$ = 4.187 $J \cdot g^{-1} \cdot K^{-1}$ is the constant-pressure heat capacity of the solution, $c_{pc}$ = 0.839 $J \cdot g^{-1} \cdot K^{-1}$ is the constant-pressure heat capacity of the quartz cell. $\Delta T$ is the difference between the solution temperature $T$ at time $t$ and the starting solution temperature $T_0$, $Q_{\text{laser}}$ is the energy arising from the laser illumination, and $Q_{\text{loss}}$ is the energy dissipated to the surrounding

environment. It should be noted that the validity of Equations 7.1.1 rely on the assumption that there is little thermal gradient within the solution so that the whole solution can be described by the same temperature at any time instant. In order to verify this, we conducted a control experiment in which a typical Au nanorod sample with localized surface plasmon wavelength of 790 nm was chosen. After the temperature rise had reached the plateau, we recorded the temperatures at 6 different points in the solution (Figure 7.1.5). The difference between the highest (74.0 °C) and lowest temperatures (73.2 °C) is just 0.8 °C (1%), suggesting that the thermal gradient is very small in the solution.

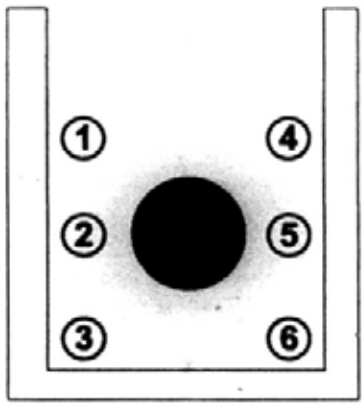


Figure 7.1.5. Illustration of a control experiment showing the temperature distribution in the Au NR solution. The temperatures at the six positions are: ① 73.3 °C, ② 73.6 °C, ③ 73.8 °C, ④ 73.2 °C, ⑤ 74.0 °C, ⑥ 73.9 °C, respectively.

There are two contributions for $Q_{laser}$. One is the light absorption by the Au nanorods in the solution, and the other is the absorption by the cuvette walls and the solution. The second contribution is usually not included in common extinction spectra because of the use of references. It is small, but cannot be neglected, especially when the absorption by the Au nanorods is very small. If the fraction of the laser energy absorbed by the cuvette walls and the solution is assumed to be $\xi$,

the two contributions to $Q_{laser}$ can then be written as,

$$Q_{laser} = I(1-\xi)(1-10^{-E_\lambda})\eta + I\xi \tag{7.1.2}$$

where $I$ = 1.72 W is the incoming laser power, $E_\lambda$ is the extinction value at the illumination laser wavelength, and $\eta$ is the ratio of the absorption to extinction of the Au nanorods. $\eta$ is also known as the photothermal conversion efficiency. The energy dissipation mainly occurs through the heat conduction and thermal radiation. It is usually expanded as a Taylor series of $\Delta T$. In our modeling, the first two terms are employed, which gives,

$$Q_{loss} = B\Delta T + C(\Delta T)^2 \tag{7.1.3}$$

where $B$ and $C$ are two coefficients. Combining Equations 7.1.1–3, we obtain,

$$(m_w c_{pw} + m_c c_{pc})\frac{d\Delta T}{dt} = I(1-\xi)(1-10^{-E_\lambda})\eta + I\xi - B\Delta T - C(\Delta T)^2 \tag{7.1.4}$$

The unknown parameters $B$ and $C$ were determined by switching off the laser when the temperature rise reached the plateau. Under this condition, Equation (7.1.4) becomes,

$$(m_w c_{pw} + m_c c_{pc})\frac{d\Delta T}{dt} = -B\Delta T - C(\Delta T)^2 \tag{7.1.5}$$

By integrating $\Delta T$ with respect to $t$ and fitting the temperature decay curve (Figure 7.1.6A) with the obtained equation, we obtained $B$ = 1.295 $J{\cdot}K^{-1}{\cdot}min^{-1}$ and $C$ = 0.00803 $J{\cdot}K^{-2}{\cdot}min^{-1}$. $C$ is much smaller than $B$, justifying the above use of only two terms in Equation 7.1.3. $\xi$ was determined by replacing the Au nanorod solution with water. In this case, Equation 7.1.4 becomes,

$$(m_w c_{pw} + m_c c_{pc})\frac{d\Delta T}{dt} = I\xi - B\Delta T - C(\Delta T)^2 \tag{7.1.6}$$

When the temperature rise reaches the steady state, the left side of Equation 7.1.6 becomes zero. In this way, $\xi$ was determined from the end temperature (Figure 7.1.6B) to be 0.0411.

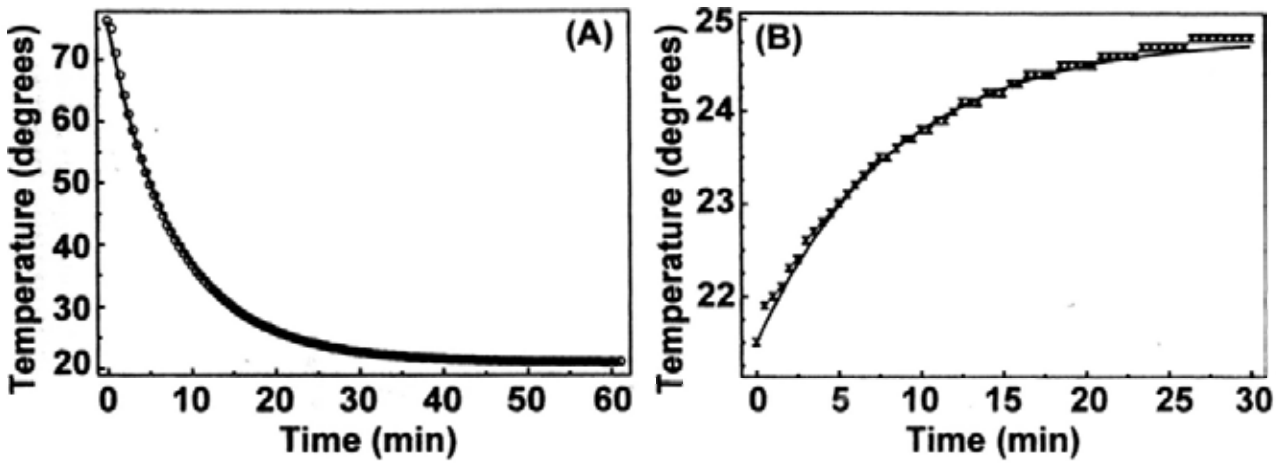


Figure 7.1.6. (A) Experimental (circles) and fitted (solid line) temperature decay of the Au nanorod solution after the laser is switched off. (B) Experimental (symbols) and fitted (solid line) temperature trace of DI water under the illumination of the diode laser.

After the parameters $B$, $C$, and $\xi$ are known, the photothermal conversion efficiency $\eta$ can then be determined by considering the steady state of the Au nanorod solution. At the steady state, the left side of Equation (7.1.4) becomes zero and the temperature reaches $T_{end}$. $\eta$ is therefore given by,

$$\eta = \frac{B(T_{end} - T_0) + C(T_{end} - T)^2 - I\xi}{I(1-\xi)(1-10^{-E_\lambda})} \tag{7.1.7}$$

In order to corroborate the validity of our theoretical model, we further solved Equation (7.1.4) and obtained the temperature as a function of time,

$$T = \frac{b\left[e^{\frac{(b-a)Ct}{mc_p}} - 1\right]}{1 - \frac{b}{a}e^{\frac{(b-a)Ct}{mc_p}}} + T_0 \tag{7.1.8}$$

where the parameters $a$ and $b$ are given by,

$$a = \frac{\frac{B}{C} + \sqrt{\frac{B^2}{C^2} + \frac{4D}{C}}}{2} \tag{7.1.9}$$

$$b = \frac{\frac{B}{C} - \sqrt{\frac{B^2}{C^2} + \frac{4D}{C}}}{2} \tag{7.1.10}$$

$$D = I(1-\xi)(1-10^{-E_\lambda})\eta + I\xi \tag{7.1.11}$$

Equation 7.1.8 was employed to model the photothermal conversion process of the Au nanorod samples with different LLPWs. The calculated temperatures are plotted as solid lines in Figure 7.1.3. No fitting parameters were used in the calculation. The obtained temperature rise traces agree remarkably well with the experimental ones, suggesting that the model is very robust and reliable. It was therefore utilized to analyze the photothermal conversion process in the following studies of the effects of the particle volume, shell coating, and assembly on the photothermal conversion.

## 7.2 Effect of the Particle Volume

For the study of the particle volume effect, I have prepared three Au nanorod samples and five Au nanobipyramid samples by combining the seed-mediated growth together with the anisotropic shortening and transverse overgrowth [23, 24, 27, 28]. Because the photothermal conversion has been found above to be most efficient when the plasmon wavelength of Au nanocrystals is equal to the illumination laser wavelength, the LLPWs of the eight samples were all synthetically controlled to be 809 nm. Figure 7.2.1A–H show the TEM images of the Au nanocrystals in the order of increasing particle volumes. For the purpose of better comparison, the TEM image of one individual nanocrystal is also shown in the insets, and they are all shown at the same magnification and aligned horizontally. The Au nanorods have a cylindrical shape with smooth surfaces, while the Au

nanobipyramids are composed of two pentagonal pyramids with a common base in the middle and the two pyramids pointing to the opposite directions. All of the three nanorod samples and the first three nanobipyramid samples have smooth surfaces, while the surfaces of the last two nanobipyramid samples are rough. These nanocrystal samples possess narrow size distributions. Their average sizes and volumes, together with their given names, are listed in Table 1. The difference in the particle volume between the largest and smallest nanocrystal sample amounts to 200 times.

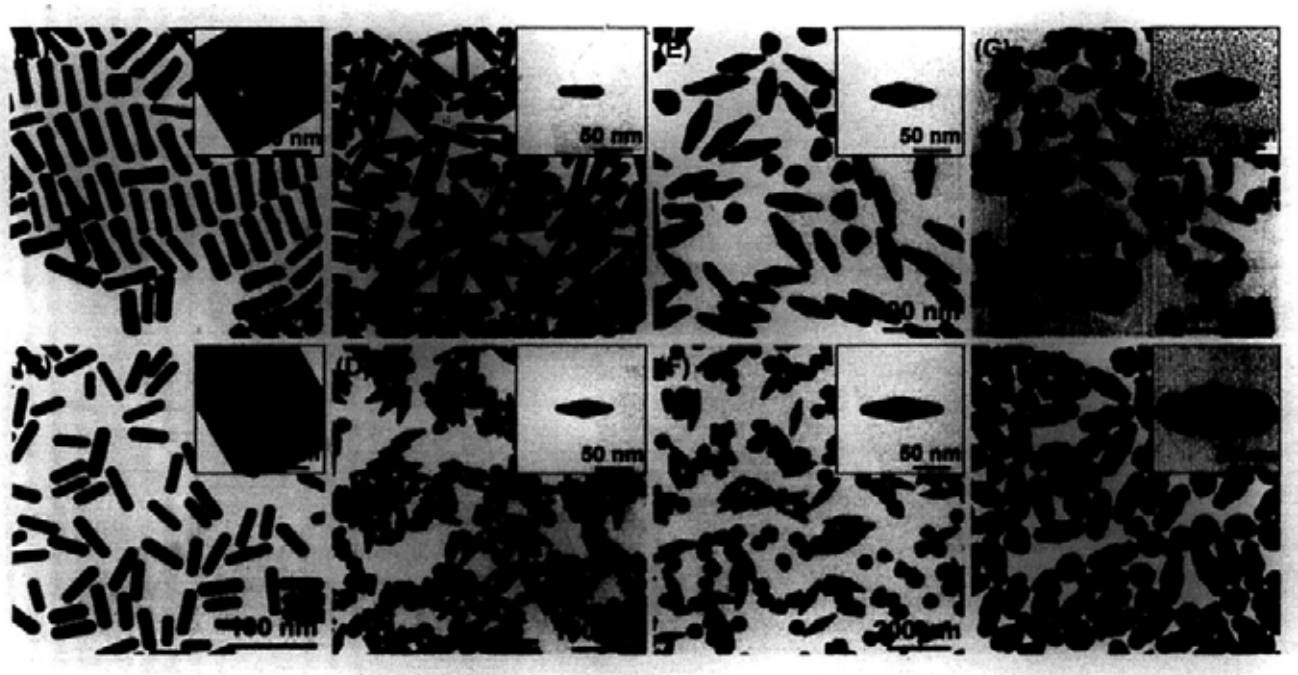


Figure 7.2.1. (A–H) TEM images of ensemble small nanorods, medium nanorods, large nanorods, smallest nanobipyramids, smaller nanobipyramids, medium nanobipyramids, larger nanobipyramids, and largest nanobipyramids, respectively. The inset in each image presents the TEM image of a representative single nanocrystal for each sample. The abrupt variation in the image background is due to that all of the Au nanocrystals are shown in the same orientation and at the same length scale.

Table 7.2.1. Sizes and the end temperatures of the Au nanocrystals with the same longitudinal plasmon wavelengths and different volumes.

| Au nanocrystals | length[a] (nm) | diameter[b] (nm) | volume ($nm^3$) | end temperature (°C) |
|---|---|---|---|---|
| largest nanobipyramids | 173 (16) | 77 (7) | 537100 | 55.4 |
| larger nanobipyramids | 137 (11) | 50 (4) | 132000 | 68.4 |
| medium nanobipyramids | 125 (9) | 39 (2) | 62800 | 71.9 |
| smaller nanobipyramids | 85 (12) | 32 (2) | 32400 | 74.0 |
| smallest nanobipyramids | 74 (8) | 24 (2) | 13400 | 74.3 |
| large nanorods | 63 (7) | 15 (3) | 10300 | 75.3 |
| medium nanorods | 55 (7) | 13 (1) | 6700 | 75.6 |
| small nanorods | 38 (5) | 10 (2) | 2700 | 77.0 |

[a] The numbers in the parentheses are standard deviations. [b] The diameters of the nanobipyramids were measured at the middle.

The variation in the end temperature should arise from the difference in the photothermal conversion efficiency among the Au nanocrystal samples, because their extinction values at the illumination wavelength are the same. The photothermal conversion processes of the eight Au nanocrystal samples were therefore modeled to determine their photothermal conversion efficiencies by using the energy balance equations in §7.1. Excellent agreements between the experimental and calculated temperature traces are obtained (Figure 7.2.2).

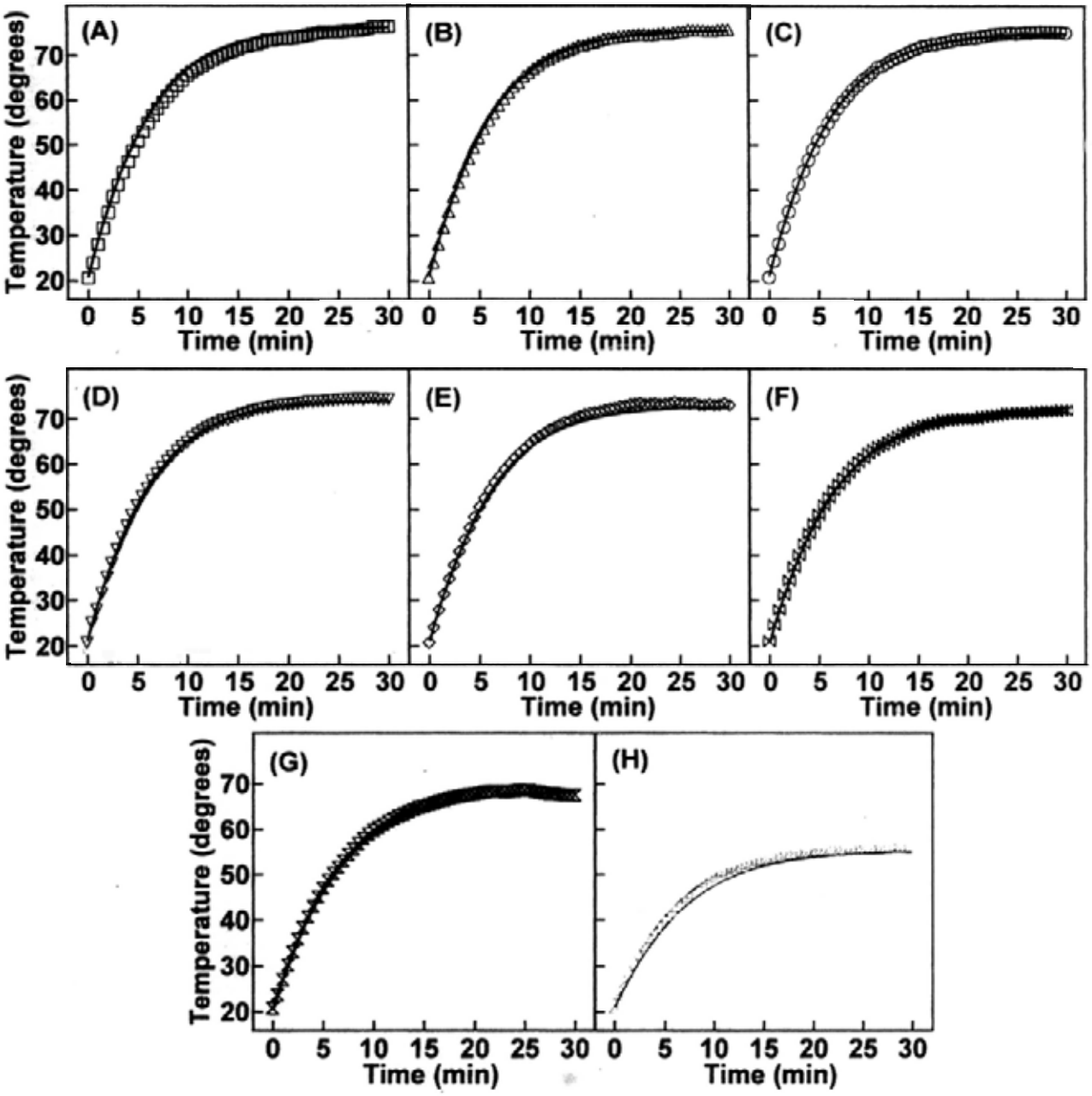


Figure 7.2.2. Experimental (symbols) and calculated (solid lines) temperature traces of the Au nanocrystal samples that have the same LLPW and different particle volumes. (A) Small nanorods. (B) Medium nanorods. (C) Large nanorods. (D) Smallest nanobipyramids. (E) Smaller nanobipyramids. (F) Medium nanobipyramids. (G) Larger nanobipyramids. (H) Largest nanobipyramids.

The photothermal conversion efficiencies are plotted in Figure 7.2.3A as a function of the effective radius, which is calculated from the particle volume by assuming a sphere with the same volume (open symbols). The conversion efficiency ranges from 51% to 95% and decreases as the effective radius is increased. Specifically, the efficiency for small nanorod sample with an effective radius of 8 nm is very close to that of a previous reported value on Au nanospheres sample with a radius of 10 nm [19]. The smaller value in our study is due to the fact that nanorod sample will scatter more light and lead to a reduced absorption ratio compared to the nanospheres sample [29].

Metal nanocrystals can both absorb and scatter light. The sum of the absorption and scattering is the extinction. The photothermal conversion efficiency is determined by the fraction of the absorption in the extinction. Both the absorption and scattering cross sections of metal nanocrystals can be calculated theoretically. We therefore carried out FDTD calculations to compare the theoretical photothermal conversion efficiencies with the experimental ones. The Au dielectric function was formulated according to the Drude model with the parameters chosen to match the experimentally measured dielectric data [30]. The excitation electric field was set to be polarized along the length axis of the nanocrystal. The surrounding medium was taken as water with a refractive index of 1.333. The sizes and shapes of the Au nanocrystals were set to be as close as possible to those measured from the TEM images. Specifically, the nanorod was modeled as a cylinder capped with a semisphere at each end. The nanobipyramid was modeled as two pentagonal pyramids with their two apexes truncated spherically.

The calculated extinction spectra of the eight Au nanocrystals are shown on the right side of Figure 7.2.3B. The calculated longitudinal plasmon wavelengths are all 809 nm, in good agreement with the experimental ones. The larger experimental peak widths arise mainly from the inhomogeneous size distributions of the Au nanocrystals. The calculated photothermal conversion

efficiencies are plotted in Figure 7.2.3A (solid symbols). It is seen to range from 13% to 96% and decrease as the effective radius is increased. This overall trend is consistent with that obtained from the experiments, especially when the effective radius of the nanocrystals is below 20 nm. However, there exists a considerable difference in the conversion efficiency between the experiments and calculations when the effective radius is above 20 nm. In this range, the calculated efficiencies are smaller than the measured ones. We believe that the observed difference between the experiments and calculations can be ascribed to the fact that the scattered light can be re-absorbed by the nanocrystals in the solution. This factor causes the measured conversion efficiency to be larger than the calculated one. Because the contribution of the scattering to the extinction increases rapidly with increasing nanocrystal sizes, the re-absorption of the scattered light becomes more important as the size of the nanocrystal gets larger.

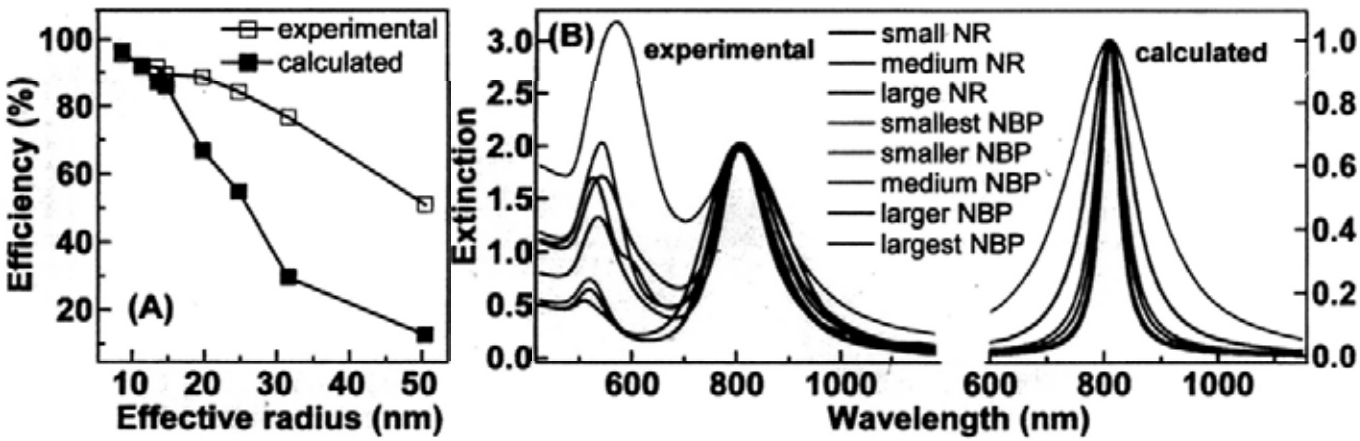


Figure 7.2.3. (A) Dependence of the experimental (open symbols) and calculated (solid symbols) photothermal conversion efficiency on the effective particle radius. (B) Experimental (left) and calculated (right) extinction spectra of the eight Au nanocrystal samples. The abbreviations NR and NBP stand for nanorod and nanobipyramid, respectively.

## 7.3 Effect of the Shell Coating

The plasmon wavelengths of metal nanostructures have been well known to be highly sensitive to the dielectric properties of the surrounding medium. Moreover, the surrounding dielectric layer can be made of semiconductors with appropriate band gaps to enhance the overall light absorption. I therefore carried out the studies on the effect of the shell coating on the photothermal conversion efficiency. Two Au nanocrystal–semiconductor core–shell nanostructures were prepared and their photothermal properties were measured.

The cores are Au nanopolyhedrons and the shells are either ZnS or $Ag_2S$. Their preparation followed our reported procedure [31]. Specifically, the Au nanopolyhedron cores were first grown by the seed-mediated method. The seeds were made by the addition of a freshly prepared, ice-cold $NaBH_4$ solution (0.6 mL, 0.01 M) into a mixture solution composed of $HAuCl_4$ (0.25 mL, 0.01 M) and CTAB (7.5 mL, 0.1 M). The resultant solution was mixed by rapid inversion for 2 min and then kept at room temperature for 1 h before its use. The growth solution was prepared by the sequential addition of CTAB (6.4 mL, 0.1 M), $HAuCl_4$ (0.8 mL, 0.01 M), and AA (3.8 mL, 0.1 M) into water (32 mL). The seed solution was diluted 10 times with DI water. The diluted seed solution (0.02 mL) was then injected into the growth solution. The resultant solution was mixed by gentle inversion for 10 s and then left undisturbed overnight. Figure 7.3.1A shows the SEM image of the uncoated Au nanopolyhedron sample. It has an average diameter of (43 ± 1) nm. When dispersed in aqueous solutions, it has a plasmon wavelength of 545 nm (Figure 7.3.1B).

The core–shell Au nanopolyhedron–semiconductor nanostructures were prepared by mixing together appropriate amounts of the Au nanopolyhedron solution, zinc thiobenzoate, and $AgNO_3$ in aqueous CTAB solutions, followed by a hydrothermal treatment. In a typical preparation, the as-grown Au nanopolyhedrons were precipitated by centrifugation at 8000 g for 10 min and then

redispersed in 0.1 M aqueous CTAB solutions. The extinction intensity of the nanopolyhedron solution at the plasmon resonance peak was adjusted to be 1.6 at an optical path length of 1 cm. For the growth of the core–shell Au nanopolyhedron–$Ag_2S$ nanostructures, a calculated amount of zinc thiobenzoate (2.0 mg, 0.006 mmol) was added in 10 mL of the Au nanopolyhedron solution, followed by the addition of $AgNO_3$ (0.01 M). The concentration of $Ag^+$ in the reaction solution was 0.2 mM. The resultant solution was transferred to a Teflon-lined, stainless-steel, 25-mL autoclave and kept at 140 °C for 3 h. The product was collected by centrifugation, washed with water, and redispersed in DI water for its further characterization. The role of zinc thiobenzoate was to supply sulfur. The sulfur species arising from the decomposition of zinc thiobenzoate preferentially reacted with the $Ag^+$ ions to form the $Ag_2S$ shell.

The above procedure was also utilized to prepare the core–shell Au nanopolyhedron–ZnS nanostructures by increasing the amount of zinc thiobenzoate to 20 mg (0.06 mmol). When the amount of zinc thiobenzoate was increased relative to the amount of $Ag^+$ ions, the shell was mainly composed of ZnS, while only a very thin layer of $Ag_2S$ was formed between the Au nanopolyhedron core and the ZnS shell to act as an adhesion layer.

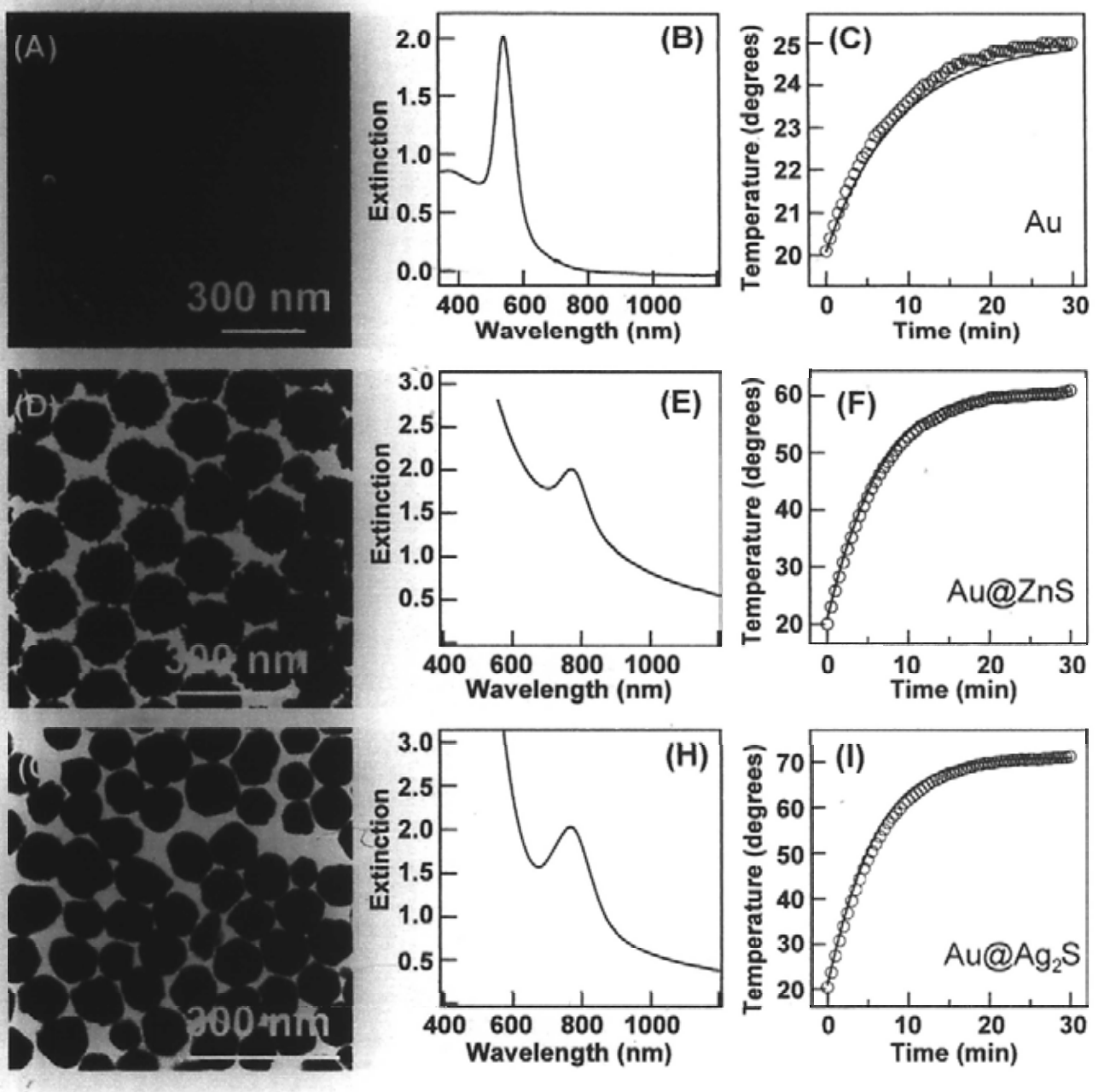


Figure 7.3.1. Effect of the shell coating on the photothermal conversion. (A, D, G) SEM image of the Au nanopolyhedron sample, TEM image of the core–shell Au nanopolyhedron–ZnS nanostructures, and TEM image of the core–shell Au nanopolyhedron–$Ag_2S$ nanostructures. (B, E, H) Extinction spectra of the three samples shown in (A, D, G). The particle concentration of the Au nanopolyhedron sample is estimated to be 0.24 nM. (C, F, I) Experimental (symbols) and calculated (solid lines) temperature traces for the three samples.

Figure 7.3.1D and 7.3.1G show the TEM images of the nanopolyhedron–ZnS and nanopolyhedron–$Ag_2S$ core–shell nanostructures, respectively. The ZnS shell is porous, while the $Ag_2S$ shell is dense. The refractive index of ZnS is ~2, and that of $Ag_2S$ is in the range of 2.5–3.5 in the near infrared spectral region [32, 33]. The shell coating results in large red shifts in the plasmon resonance peak. The plasmon wavelengths of both core–shell nanostructures were controlled to be 770 nm by varying the shell thicknesses during the synthesis [31]. As a result, the overall average diameters of the nanopolyhedron–ZnS and nanopolyhedron–$Ag_2S$ nanostructures are (160 ± 8) and (88 ± 8) nm, respectively. The control of the two types of nanostructures to have the same plasmon wavelength ensures that the effect of the plasmon wavelength on the photothermal conversion efficiency is the same. The extinction intensities at the plasmon resonance peaks were all adjusted to be ~2 for the uncoated Au nanopolyhedron sample and the two nanostructure samples (Figure 7.3.1E and H).

The temperature rise traces for the three samples are compared in Figure 7.3.1C, F, and I. Because the extinction intensity of the uncoated Au nanopolyhedron sample at 809 nm is 0.06, which is very small, the end temperature resulting from the photothermal conversion is only 25 °C. In contrast, the extinction intensities at 809 nm are 1.7 for both of the core–shell nanostructure samples. The measured end temperatures for the nanopolyhedron–ZnS and nanopolyhedron–$Ag_2S$ samples are 60 and 71 °C, respectively. The photothermal conversion processes of the three samples were then analyzed, as shown by the solid curves in Figure 7.3.1C, F, and I, and the obtained conversion efficiencies are 20%, 64%, and 86%, respectively. This result indicates that the photothermal conversion efficiencies of metal nanocrystals can be increased by shifting their plasmon resonances towards the illumination laser wavelength through shell coating. Moreover, even though the extinction intensities at 809 nm are the same for the two nanostructure samples, the

conversion efficiency of the nanopolyhedron–$Ag_2S$ sample is 1.4 times that of the nanopolyhedron–ZnS sample. The difference in the conversion efficiency is ascribed to the different light absorption behaviors of the $Ag_2S$ and ZnS shells at 809 nm. $Ag_2S$ and ZnS are semiconductors. Their band gaps have previously been measured to be 0.9–1.1 and 3.4–3.8 eV, respectively [32, 33]. The former is smaller, while the latter one is larger than the illumination photon energy. Therefore, the ZnS shell is transparent to the illumination laser, while the $Ag_2S$ shell can strongly absorb it. The additional light absorption introduced by the $Ag_2S$ shell causes the conversion efficiency of the Au nanopolyhedron–$Ag_2S$ sample to be higher than that of the nanopolyhedron–ZnS sample. This result suggests that coating metal nanocrystals with strongly light-absorbing materials can increase the photothermal conversion efficiencies.

## 7.4 Effect of the Assembly

I subsequently studied the effects of the assembly of metal nanocrystals on the photothermal conversion efficiency. Such studies are highly relevant to the photothermal killing of cancer cells with metal nanocrystals, because typically a number of metal nanocrystals are aggregated on cancer cells during photothermal therapy [1 – 7]. Two situations were considered. In the first situation, the plasmon resonance wavelength of spatially isolated metal nanocrystals is far away from the illumination laser wavelength, where the extinction intensity is nearly zero. After the assembly, the extinction intensity at the illumination wavelength is greatly increased. In the second situation, the plasmon wavelength of isolated metal nanocrystals is very close to the illumination wavelength. The assembly induces a large red shift of the plasmon resonance peak, which causes a great reduction in the extinction intensity at the illumination wavelength. The Au nanopolyhedron sample and one of the nanorod samples were chosen. Their assembly was realized by the addition of 0.01 M

glutathione in the solutions. The assembly followed reported procedures [34, 35], and the details are stated as follow: The pH of the Au nanocrystal solutions were firstly adjusted to ~3 by the addition of HCl (1.0 M). Glutathione (0.2 mL, 0.01 M) was added into the Au nanocrystal solutions (2 mL each). For the separate monitoring of the assembly process, the mixture solutions were kept at 45 °C and their extinction spectra were taken every minute after the addition of glutathione.

Figure 7.4.1A shows the time-dependent extinction spectra of the nanopolyhedron solution recorded after the addition of glutathione. The plasmon wavelength of the isolated Au nanopolyhedron sample is 545 nm. The addition of glutathione induces the assembly of the nanopolyhedrons. The plasmon resonance peak corresponding to the isolated nanopolyhedrons decreases in intensity. At the same time, a broad peak appears in the spectral region of 700–1100 nm. The occurrence of this broad peak causes a large increase in the extinction intensity at 809 nm. The assembly of the nanopolyhedrons is corroborated by the TEM imaging. The nanopolyhedrons are randomly distributed in the absence of glutathione (Figure 7.4.1B). They are assembled into chains in the presence of glutathione (Figure 7.4.1C).

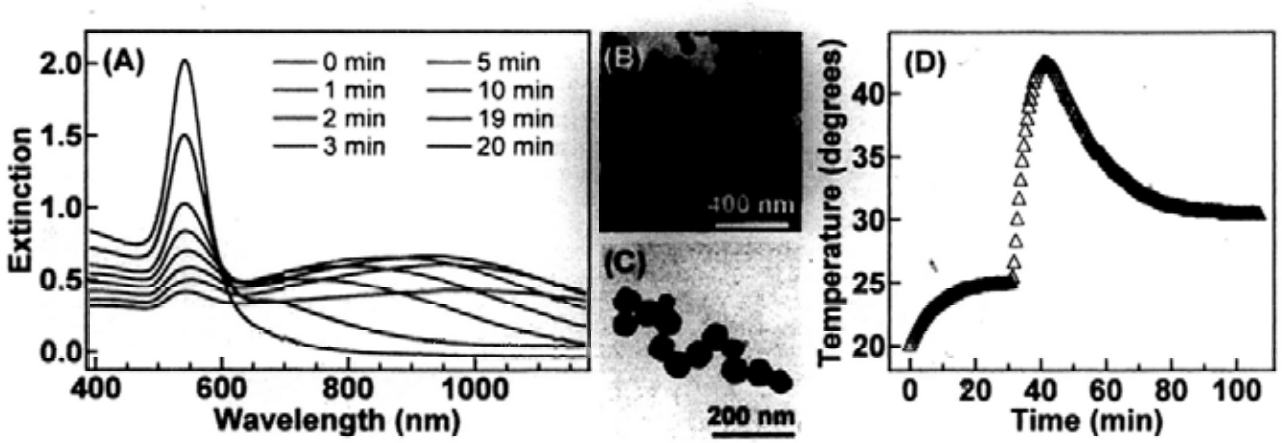


Figure 7.4.1. Effect of the nanocrystal assembly on the photothermal conversion. (A) Extinction spectra of the Au nanopolyhedron sample acquired as a function of the time after the addition of

glutathione. (B) TEM image of the as-grown Au nanopolyhedron sample. Its average diameter is (43 ± 1) nm. (C) TEM image of the Au nanopolyhedrons assembled into a chain. (D) Temperature trace of the Au nanopolyhedron sample. Glutathione was added after 30 min.

The effect of the assembly on the photothermal conversion is revealed by the temperature trace shown in Figure 7.4.1D, where the extinction intensity of the starting nanopolyhedron sample at its plasmon resonance peak wavelength was adjusted to be around 2. The resultant particle concentration is estimated to be ~0.2 nM. At the starting stage without the addition of glutathione, the temperature rise trace of the nanopolyhedron solution appears similar to that indicated with the black circles in Figure 7.3.1B. The quick injection of 20 μL of the glutathione solution at 30 min triggers a rapid temperature increase from 25 to 43 °C within ~10 min. This rapid temperature rise is caused by the increase in the extinction intensity at 809 nm owing to the assembly of the Au nanopolyhedrons in the solution. Because the added volume of the glutathione solution is very small, the temperature drop at 30 min is unobservable. After reaching a maximum at 43 °C, the solution temperature starts to decrease steadily and stabilizes finally at 30 °C. The temperature decrease can be explained by looking at the extinction spectra shown in Figure 4a for the assembly. The extinction intensity at 809 nm reaches a maximum at ~8 min after the addition of glutathione. The time period is approximately the same as that taken for the nanopolyhedron solution to arrive at its maximum temperature. After reaching the maximum, the extinction intensity at 809 nm starts to decrease because the plasmon peak red shifts as more nanopolyhedrons are assembled together. The absorption of less light power induces the reduction in the solution temperature.

The Au nanorod sample with a longitudinal plasmon wavelength of 810 nm was used for the second situation. The extinction intensity at its longitudinal plasmon peak was adjusted to be around

2.0. The resultant particle concentration was estimated to be ~0.4 nM. The addition of glutathione induces a reduction in the extinction intensity at the longitudinal plasmon peak and a concomitant appearance of a new peak in the longer-wavelength region (Figure 7.4.2A). The glutathione-induced assembly of the Au nanorods is corroborated by the TEM imaging. In the absence of glutathione, the nanorods are randomly distributed (Figure 7.4.2B). They are assembled into chains in the presence of glutathione (Figure 7.4.2C). The temperature of the nanorod solution rises to 77 °C after 30 min of the laser illumination (Figure 7.4.2D). It shows a gradual decrease after the addition of glutathione and finally becomes stabilized. This temperature drop can clearly be ascribed to the assembly-induced decrease in the extinction intensity at the illumination laser wavelength. The results obtained from the two assembly situations indicate that the assembly state of metal nanocrystals has a strong effect on the plasmon-based photothermal conversion. This effect should be fully taken into account for the development of highly efficient, plasmon-based phototherapy agents. In addition, target-selective phototherapy agents might be developed if the assembly process of metal nanocrystals can be designed to be triggered by the presence of some specific biological species.

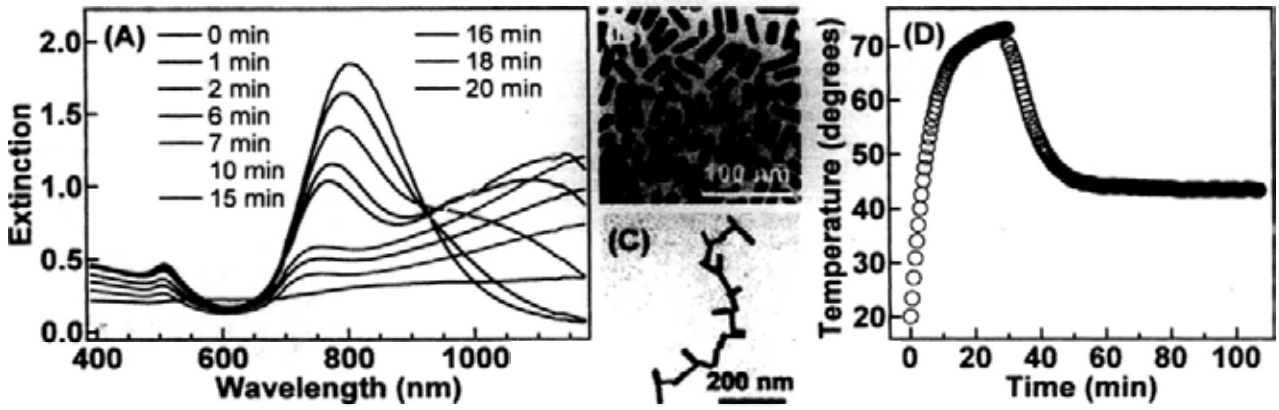


Figure 7.4.2. Effect of the nanocrystal assembly on the photothermal conversion. (A) Extinction spectra of the Au nanorod sample acquired as a function of the time after the addition of glutathione. (B) TEM image of the as-grown Au nanorod sample. It has an average length of (38 ± 5) nm and diameter of (10 ± 2) nm. (C) TEM image of the end-to-end assembled Au nanorods. (D) Temperature trace of the Au nanorod sample. Glutathione was added after 30 min.

## 7.5 Summary

In summary, the photothermal conversion efficiencies of Au nanocrystals have been found to be strongly dependent on the plasmon resonance wavelength, nanocrystal volume, shell coating, and assembly state. The Au nanocrystal solutions reach the highest temperature when the plasmon resonance wavelength is equal to the illumination laser wavelength. The photothermal conversion efficiency decreases as the particle volume of the Au nanocrystals that are similarly shaped gets larger, because the fraction of the excitation light power that is scattered becomes larger. Coating of the Au nanocrystals with appropriate materials can improve the plasmon-based photothermal conversion through two effects. One is the shift in the plasmon resonance wavelength arising from the change in the refractive index of the surrounding medium, and the other is the increase in light absorption resulting from the use of semiconductor coating materials with suitable band gap

energies. Moreover, assembly of Au nanocrystals has been found to be an effective means for controlling their photothermal conversion properties. The results obtained in this chapter are useful not only for understanding the fundamental aspects of plasmon-based photothermal conversion but also for designing metal nanostructure-based phototherapy agents with improved efficiencies and flexibilities.

## References

[1] X. H. Huang, I. H. El-Sayed, W. Qian, M. A. El-Sayed, Cancer Cell Imaging and Photothermal Therapy in the Near-Infrared Region by Using Gold Nanorods. *J. Am. Chem. Soc.*, 128: 2115, 2006.

[2] E. B. Dickerson, E. C. Dreaden, X. H. Huang, I. H. El-Sayed, H. H. Chu, S. Pushpanketh, J. F. McDonald, M. A. El-Sayed, Gold Nanorod Assisted Near-Infrared Plasmonic Photothermal Therapy (PPTT) of Squamous Cell Carcinoma in Mice. *Cancer Lett.*, 269: 57, 2008.

[3] G. von Maltzahn, A. Centrone, J.-H. Park, R. Ramanathan, M. J. Sailor, T. A. Hatton, S. N. Bhatia, SERS-Coded Gold Nanorods as a Multifunctional Platform for Densely Multiplexed Near-Infrared Imaging and Photothermal Heating. *Adv. Mater.*, 21: 3175, 2009.

[4] J. Y. Chen, D. L. Wang, J. F. Xi, L. Au, A. Siekkinen, A. Warsen, Z.-Y. Li, H. Zhang, Y. N. Xia, X. D. Li, Immuno Gold Nanocages with Tailored Optical Properties for Targeted Photothermal Destruction of Cancer Cells. *Nano Lett.*, 7: 1318, 2007.

[5] L. R. Hirsch, R. J. Stafford, J. A. Bankson, S. R. Sershen, B. Rivera, R. E. Price, J. D. Hazle, N. J. Halas, J. L. West, Nanoshell-Mediated Near-Infrared Thermal Therapy of Tumors under Magnetic Resonance Guidance. *Proc. Natl. Acad. Sci. U.S.A.*, 100: 13549, 2003.

[6] C. Loo, A. Lowery, N. J. Halas, J. West, R. Drezek, Immunotargeted Nanoshells for Integrated Cancer Imaging and Therapy. *Nano Lett.*, 5: 709, 2005.

[7] A. M. Gobin, M. H. Lee, N. J. Halas, W. D. James, R. A. Drezek, J. L. West, Near-Infrared Resonant Nanoshells for Combined Optical Imaging and Photothermal Cancer Therapy. *Nano Lett.*, 7: 1929, 2007.

[8] C.-C. Chen, Y.-P. Lin, C.-W. Wang, H.-C. Tzeng, C.-H. Wu, Y.-C. Chen, C.-P. Chen, L.-C. Chen, Y.-C. Wu, DNA−Gold Nanorod Conjugates for Remote Control of Localized Gene Expression by Near Infrared Irradiation. *J. Am. Chem. Soc.*, 128: 3709, 2006.

[9] S. E. Lee, G. L. Liu, F. Kim, L. P. Lee, Remote Optical Switch for Localized and Selective Control of Gene Interference. *Nano Lett.*, 9: 562, 2009.

[10] A. G. Skirtach, C. Dejugnat, D. Braun, A. S. Susha, A. L. Rogach, W. J. Parak, H. Möhwald, G. B. Sukhorukov, The Role of Metal Nanoparticles in Remote Release of Encapsulated Materials. *Nano Lett.*, 5: 1371, 2005.

[11] M. Bikram, A. M. Gobin, R. E. Whitmire, J. L. West, Temperature-Sensitive Hydrogels with $SiO_2$–Au Nanoshells for Controlled Drug Delivery. *J. Controlled Release*, 123: 219, 2007.

[12] M. S. Yavuz, Y. Y. Cheng, J. Y. Chen, C. M. Cobley, Q. Zhang, M. Rycenga, J. W. Xie, C. Kim, K. H. Song, A. G. Schwartz, L. V. Wang, Y. N. Xia, Gold Nanocages Covered by Smart Polymers for Controlled Release with Near-Infrared Light. *Nat. Mater.*, 8: 935, 2009.

[13] D. Boyer, P. Tamarat, A. Maali, B. Lounis, M. Orrit, Photothermal Imaging of Nanometer-Sized Metal Particles among Scatterers. *Science*, 297 : 1160, 2002.

[14] L. Cognet, C. Tardin, D. Boyer, D. Choquet, P. Tamarat, B. Lounis, Single Metallic Nanoparticle Imaging for Protein Detection in Cells. *Proc. Natl. Acad. Sci. U.S.A.*, 100: 11350, 2003.

[15] S. Berciaud, L. Cognet, G. A. Blab, B. Lounis, Photothermal Heterodyne Imaging of Individual Nonfluorescent Nanoclusters and Nanocrystals. *Phys. Rev. Lett.*, 93: 257402, 2004.

[16] P. Zijlstra, J. W. M. Chon, M. Gu, Five-Dimensional Optical Recording Mediated by Surface Plasmons in Gold Nanorods. *Nature*, 459: 410, 2009.

[17] G. L. Liu, J. Kim, Y. Lu, L. P. Lee, Optofluidic Control Using Photothermal Nanoparticles. *Nat. Mater.*, 5: 27, 2006.

[18] C.-H. Chou, C.-D. Chen, C. R. C. Wang, Highly Efficient, Wavelength-Tunable, Gold Nanoparticle Based Optothermal Nanoconvertors. *J. Phys. Chem. B*, 109: 11135, 2005.

[19] H. H. Richardson, Z. N. Hickman, A. O. Govorov, A. C. Thomas, W. Zhang, M. E. Kordesch, Thermooptical Properties of Gold Nanoparticles Embedded in Ice: Characterization of Heat Generation and Melting. *Nano Lett.*, 6: 783, 2006.

[20] H. H. Richardson, M. T. Carlson, P. J. Tandler, P. Hernandez, A. O. Govorov, Experimental and Theoretical Studies of Light-to-Heat Conversion and Collective Heating Effects in Metal Nanoparticle Solutions. *Nano Lett.*, 9: 1139, 2009.

[21] J. R. Cole, N. A. Mirin, M. W. Knight, G. P. Goodrich, N. J. Halas, Photothermal Efficiencies of Nanoshells and Nanorods for Clinical Therapeutic Applications. *J. Phys. Chem. C*, 113: 12090, 2009.

[22] W. Hasan, C. L. Stender, M. H. Lee, C. L. Nehl, J. Lee, T. W. Odom, Tailoring the Structure of Nanopyramids for Optimal Heat Generation. *Nano Lett.*, 9: 1555, 2009.

[23] C.-K. Tsung, X. S. Kou, Q. H. Shi, J. P. Zhang, M. H. Yeung, J. F. Wang, G. D. Stucky, Selective Shortening of Single-Crystalline Gold Nanorods by Mild Oxidation. *J. Am. Chem. Soc.*, 128: 5352, 2006.

[24] W. H. Ni, X. S. Kou, Z. Yang, J. F. Wang, Tailoring Longitudinal Surface Plasmon Wavelengths, Scattering and Absorption Cross Sections of Gold Nanorods. *ACS Nano*, 2: 677, 2008.

[25] R. Weissleder, A Clearer Vision for in vivo Imaging. *Nat. Biotechnol.*, 19: 316, 2001.

[26] D. K. Roper, W. Ahn, M. Hoepfner, Microscale Heat Transfer Transduced by Surface Plasmon Resonant Gold Nanoparticles. *J. Phys. Chem. C*, 111: 3636, 2007.

[27] X. S. Kou, S. Z. Zhang, Z. Yang, C.-K. Tsung, G. D. Stucky, L. D. Sun, J. F. Wang, C. H. Yan, Glutathione- and Cysteine-Induced Transverse Overgrowth on Gold Nanorods. *J. Am. Chem. Soc.*, 129: 6402, 2007.

[28] X. S. Kou, W. H. Ni, C.-K. Tsung, K. Chan, H.-Q. Lin, G. D. Stucky, J. F. Wang, Growth of

Gold Bipyramids with Improved Yield and Their Curvature-Directed Oxidation. *Small*, 3: 2103, 2007.

[29] C. Sönnichsen, T. Franzl, T. Wilk, G. von Plessen, J. Feldmann, Drastic Reduction of Plasmon Damping in Gold Nanorods. *Phys. Rev. Lett.*, 88: 077402, 2002.

[30] P. B. Johnson, R. W. Christy, Optical Constants of the Noble Metals. *Phys. Rev. B*, 6: 4370, 1972.

[31] Z. H. Sun, Z. Yang, J. H. Zhou, M. H. Yeung, W. H. Ni, H. K. Wu, J. F. Wang, A General Approach to the Synthesis of Gold-Metal Sulfide Core-Shell and Heterostructures. *Angew. Chem., Int. Ed.*, 48: 2881, 2009.

[32] S. Lindroos, T. Kanniainen, M. Leskelä, Growth of Zinc Sulfide Thin Films by the Successive Ionic Layer Adsorption and Reaction (Silar) Method on Polyester Substrates. *Mater. Res. Bull.*, 32: 1631, 1997.

[33] T. B. Nasrallah, H. Dlala, M. Amlouk, S. Belgacem, J. C. Bernède, Some Physical Investigations on $Ag_2S$ Thin Films Prepared by Sequential Thermal Evaporation. *Synth. Met.*, 151: 225, 2005.

[34] S. Z. Zhang, X. S. Kou, Z. Yang, Q. H. Shi, G. D. Stucky, L. D. Sun, J. F. Wang, C. H. Yan, Nanonecklaces Assembled from Gold Rods, Spheres, and Bipyramids. *Chem. Comm.*, 1816, 2007.

[35] X. S. Kou, Z. H. Sun, Z. Yang, H. J. Chen, J. F. Wang, Curvature-Directed Assembly of Gold Nanocubes, Nanobranches, and Nanospheres. *Langmuir*, 25: 1692, 2009.

# Chapter 8

# Conclusions

In this thesis I have comprehensively studied the refractive index sensing behaviors, the plasmon coupling, and the photothermal conversion properties of Au nanostructures. Au nanocrystals with different plasmon wavelengths, shapes, and sizes were dispersed into water–glycerol mixtures to measure their refractive index sensitivities. It has been found that Au nanocrystals of longer plasmon resonance wavelength, higher-curvature protrusion, and larger polarizabilities generally exhibit higher refractive index sensitivities. On the basis of these studies, a novel optical fiber-based plasmonic sensor was fabricated by depositing Au nanorods with different longitudinal plasmon wavelengths onto the core surface of an etched commercial optical fiber. The refractive index plasmonic sensing in conjunction with optical fibers can be realized on both the single-particle and ensemble levels. These findings open up the possibility for the development of real-time, low-cost, ultrasensitive, and multiplexed sensors for industrial, environmental, and clinical applications.

To study the plasmon coupling in Au nanocrystals, I fabricated clusters of two-dimensionally ordered Au nanocubes on ITO substrates and studied their plasmon resonance properties using the dark-field scattering technique. These clusters exhibit rich plasmonic properties that are highly dependent on the number and ordering of the Au nanocubes. FDTD calculations show that the low-energy plasmon modes are contributed by both the in-plane coupling among different nanocubes in the cluster and the vertical coupling between the ITO substrate and the entire cluster.

Moreover, the vertical coupling between the ITO substrate and cluster also gives rise to a plasmon mode that is independent on the number and ordering of the nanocubes in the cluster. These studies can further our understanding on the plasmon coupling in metal nanostructures and offer a potential approach to tailoring plasmonic properties for advanced spectroscopic and sensing applications by constructing ordered clusters out of basic repeating units.

I have further investigated the coupling between Au nanocrystals and substrates with different dielectric properties. The substrates utilized included the Pt films, Au films, silicon substrates, glass substrates, ITO, single crystalline ZnO substrates, and mesostructured titania thin films. It is found that the far-field scattering pattern of an individual nanorod would changes gradually from a solid bright spot to a donut-shaped pattern as the spacing between the nanorod and a substrate with a large dielectric constant gets smaller. This transition is due to nearly complete damping of the in-plane dipole resonance in the nanorod by the substrate. Moreover, for a nanocrystal adjacent to a silicon substrate of an even larger dielectric constant ($14.3 + 0.1i$ at 700 nm), its scattering spectra will be altered enormously due to the substrate-mediated hybridization of the different plasmon modes in the nanocrystal. As the nanocrystal becomes large enough, the hybridization among the different modes will be so strong that Fano resonance can come up. These results will be of great use in analyzing and deducing the resonance properties of future plasmonic devices fabricated on different substrates. In addition, the coupling between Au nanocrystals and substrates has been found to be of near-field nature. It becomes effective when the nanocrystal–substrate separations are smaller than 15 nm. This finding can lead to the development of ultrasensitive plasmonic sensors that can detect subtle changes in the separation between metal nanocrystals and substrates.

The photothermal properties of Au nanocrystals and their related nanostructures have been further explored in order to understand their photothermal conversion efficiency. The effects of the

plasmon resonance wavelength, particle volume, shell coating, and assembly on the photothermal conversion efficiencies of Au nanocrystals have been systematically studied by directly measuring the temperature of Au nanocrystal solutions with a thermocouple and analyzed on the basis of energy balance. The temperature of Au nanocrystal solutions reaches a maximum at ~75 °C when the plasmon resonance wavelength of Au nanocrystals is equal to the illumination laser wavelength. For Au nanocrystals with similar shapes, the larger the nanocrystal, the smaller the photothermal conversion efficiency becomes. The photothermal conversion can also be controlled by shell coating and assembly through the change in the plasmon resonance energy of Au nanocrystals. Moreover, coating Au nanocrystals with semiconductor materials that have band gap energies smaller than the illumination laser energy can improve the photothermal conversion efficiency owing to the presence of an additional light absorption channel. These findings not only can further our understanding on the fundamental aspects of plasmon-based photothermal conversion but also are of great value for designing metal nanostructure-based phototherapy agents with improved efficiencies and flexibilities.

# Curriculum Vitae

## EDUCATION

Ph.D. in Physics, July 2010 (expected)

Department of Physics, The Chinese University of Hong Kong, Hong Kong, China

2004–2007, M.S. in Optical Engineering, School of Physics and Engineering, Sun Yat-Sen University, Guangzhou, China

2000–2004, B.S. in Physics, School of Physics and Engineering, Sun Yat-Sen University, Guangzhou, China

## PUBLICATIONS

(1) **Huanjun Chen**, Lei Shao, Tian Ming, Zhenhua Sun, Chunmei Zhao, Baocheng Yang, Jianfang Wang, Understanding the Photothermal Conversion Efficiency of Gold Nanocrystals., ***Small***, revised, 2010.

(2) Lei Zhao, Tian Ming, Guisheng Li, **Huanjun Chen**, Jianfang Wang, Jimmy. C. Yu, Monosteps on the Surfaces of Mesostructured Silica and Titania Thin Films., ***Small***, accepted, (2010).

(3) Lei Shao, Kat Choi Woo, **Huanjun Chen**, Zhao Jin, Hai-Qing Lin, Jianfang Wang, Angle and Energy Resolved Surface Plasmon Coupling between Gold Nanorods., ***ACS Nano***, DOI: 10.1021/nn100180d, (2010).

(4) Weihai Ni, **Huanjun Chen**, Jing Su, Zhenhua Sun, Jianfang Wang, Hongkai Wu, Effects of Dyes, Gold Nanocrystals, pH, and Metal Ions on the Plasmonic and Molecular Resonance Coupling, ***J. Am. Chem. Soc.***, 132, 4806 (2010).

(5) Weihai Ni, Tobias Ambjörnsson, Sten Peter Apell, **Huanjun Chen**, Jianfang Wang, Observing Plasmonic–Molecular Resonance Coupling on Single Gold Nanorods. ***Nano Lett.***, 10, 77 (2009).

(6) Tian Ming, Lei Zhao, Zhi Yang, Huanjun Chen, Lingdong Sun, Jianfang Wang, Chunhua Yan, Strong Polarization Dependence of Plasmon–Enhanced Fluorescence on Single Gold Nanorods. ***Nano Lett.***, 9, 3896 (2009).

(7) **Huanjun Chen**, Lei Shao, Kat Choi Woo, Tian Ming, Hai-Qing Lin, Jianfang Wang, Shape-Dependent Refractive Index Sensitivities of Gold Nanocrystals with the Same Plasmon Resonance Wavelength. ***J. Phys. Chem. C***, 113, 17691 (2009).

(8) **Huanjun Chen**, Zhenhua Sun, Weihai Ni, Kat Choi Woo, Hai-Qing Lin, Lingdong Sun, Jianfang Wang, Chunhua Yan, Plasmon Coupling in Clusters Composed of Two-Dimensionally Ordered Gold Nanocubes. ***Small***, 5, 2111 (2009).

(9) Xiaoshan Kou, Zhenhua Sun, Zhi Yang, **Huanjun Chen**, Jianfang Wang, Curvature-Directed Assembly of Gold Nanocubes, Nanobranches, and Nanospheres. ***Langmuir***, 25, 1692 (2009).

(10) Tian Ming, Xiaoshan Kou, **Huanjun Chen**, Tao Wang, Hoi-Lam Tam, Kok-Wai Cheah, Ji-Yao Chen, Jianfang Wang, Ordered Gold Nanostructure Assemblies Formed by Droplet Evaporation. ***Angew. Chem. Int. Ed.***, 47, 9685 (2008).

(11) Weihai Ni, **Huanjun Chen**, Xiaoshan Kou, Man Hau Yeung, Jianfang Wang, ***J. Phys. Chem. C***, 112, 8105 (2008).

(12) Weihai Ni, Zhi Yang, **Huanjun Chen**, Li Li, Jianfang Wang, Coupling between Molecular and Plasmonic Resonances in Freestanding Dye–Gold Nanorod Hybrid Nanostructures. ***J. Am. Chem. Soc.***, 130, 6692 (2008).

(13) **Huanjun Chen**, Xiaoshan Kou, Zhi Yang, Weihai Ni, Jianfang Wang, Shape- and Size-Dependent Refractive Index Sensitivity of Gold Nanoparticles. ***Langmuir***, 24, 5233 (2008).